Université catholique de Louvain
Institut de la Matière Condensée et des Nanosciences
Bio & Soft Matter

Surface and in-depth molecular characterization of plasma-treated polymers and plasma-polymers using SIMS

Vanina CRISTAUDO

Thèse présentée en vue de l'obtention du grade de Docteur en Sciences de l'Ingénieur

Promoteurs :

Pr Arnaud DELCORTE (UCL/IMCN/BSMA, Belgique)
Pr François RENIERS (Université Libre de Bruxelles, Belgique)

Membres du jury :

Pr Bernard PIRAUX (Président), UCL/IMCN/NAPS, Belgique
Pr Jacques DEVAUX (Secrétaire), UCL/IMCN, Belgique
Pr Didier LÉONARD, Université Claude Bernard Lyon I, France
Pr Antonino LICCIARDELLO, Università degli Studi di Catania, Italie

Mai 2017

Conditio sine qua non.

À mon mari CLAUDE.

Remerciements

En tout premier lieu, je tiens à remercier profondément mes deux promoteurs de thèse, le *Professeur Arnaud DELCORTE* de l'UCL et le *Professeur François RENIERS* de l'ULB, pour m'avoir donné la possibilité de travailler au sein de leurs équipes de recherche et pour la confiance qu'ils m'ont accordée. J'aimerais remercier également les membres de mon comité d'accompagnement, le Professeur Christian BAILLY et le Professeur Rony SNYDERS, ainsi que les membres du jury, les Professeurs Bernard PIRAUX, Jacques DEVAUX, Didier LÉONARD et Antonino LICCIARDELLO, pour avoir contribué à l'amélioration de cette thèse.

Je tiens à remercier particulièrement la Dr Delphine MERCHE et « ma collègue de doctorat à l'ULB » Stéphanie COLLETTE (bientôt Docteur !), sans lesquelles ce travail n'aurait jamais existé ! Merci aussi au Dr Alp OZKAN et Joffrey BANETON du groupe CHANI à l'ULB, et au Professeur Thierry DUFOUR.

Je remercie tous mes précieux collaborateurs, et particulièrement le Professeur Nunzio TUCCITTO et le Dr Bartlomiej CZERWINSKI, sans lesquels cette thèse aurait eu un poids différent (dans tous les sens du terme!). Merci encore au Dr Martin SEAH (NPL) pour l'intérêt montré envers mes résultats, et au Dr Alex SHARD (NPL) pour la participation au VAMAS Study : une opportunité très intéressante de comparaison des résultats SIMS et XPS obtenus au sein de différents laboratoires. Merci au Dr Damien COSSEMENT de Materia Nova (Mons) pour les nombreuses discussions que nous avons tenues sur le SIMS et la PCA à l'occasion des conférences et réunions des utilisateurs ION-TOF. Je tiens aussi à remercier les Professeurs Jacques DEVAUX, Patrick BERTRAND, Alain JONAS, Christian BAILLY et la Professeure Christine DUPONT pour les fructueuses discussions qu'on a eues au cours de ces quatre années de thèse sur des sujets les plus variés (spectroscopie infrarouge, calorimétrie, ellipsométrie, SIMS, entre autres).

Je remercie le Professeur Bernard NYSTEN pour m'avoir donné la possibilité d'effectuer les mesures AFM dans son laboratoire, ainsi que les Professeurs Charles-André FUSTIN et Jean-François GOHY pour les mesures GPC et le traitement UV de certains échantillons. Merci aussi à toutes les personnes qui m'ont apporté leur aide dans les mesures complémentaires réalisées durant ma thèse, notamment Cécile D'HAESE (AFM), Pierre ELOY (XPS), Sabine BEBELMAN (IR), la Dr Delphine MAGNIN (ellipsométrie et XRR), Pascal VAN VELTHEM (DSC), Yasmine ADRIAENSEN (WCA), le

Dr Olivier BERTRAND (GPC) et le Dr Guillaume HAUFFMAN (traitement UV). Merci aussi au Dr Sébastian FANIEL et au Dr Nicolas ANDRÉ de WINFAB, pour m'avoir aidée dans le traitement HF du silicium, la profilométrie et l'ellipsométrie avec grande sympathie et cordialité.

Mes remerciements vont également à mes collègues de laboratoire, particulièrement le Dr Oscar RESTREPO et son épouse (qui m'a accueillie chaleureusement en Belgique), le Dr Roussin LONTIO FOMEKONG, Mohammad ZARSHENAS, Henok MESFIN, Hugues LAMBERT, la Dr Sara MAUQUOY et la Dr Anna BRATEK. Merci à Luigi Cesare MELCHIORRE, que j'ai suivi pendant son mémoire et qui m'a donné beaucoup de satisfactions avec son travail méticuleux ! Merci aussi à tous les membres du pôle BSMA, et plus particulièrement aux secrétaires Françoise BOUVY (déjà à la retraite), Rose-Anne JACOB, Françoise SOMERS et Aurore BECQUEVORT pour leurs gentillesse et disponibilité.

J'exprime toute ma gratitude à mon ancien promoteur de Master Thesis, le Professeur Antonino LICCIARDELLO, et à la Professeure Maria Emanuela AMATO de l'Università degli Studi di Catania, pour m'avoir guidée pendant mes études universitaires, ainsi que suivie (et soutenue) pendant mon long doctorat en Belgique. Votre affection, vos conseils et votre aide ont été essentiels dans ma réussite personnelle et, surtout, professionnelle.

Dans la sphère familiale, je souhaite remercier profondément mon mari pour la grande épreuve de patience démontrée. Je remercie également mes parents Carmen et Matteo, mes « petits » frères Alfredo et Bruno, la abuela Lucia, la abuela Maria y el abuelo Bruno, de même que la famille de mon époux - ma belle-mère Anne-Marie, ma belle-sœur Marián, mon beau-frère Thierry et ses enfants -, pour leur soutien inconditionné. J'aimerais remercier aussi ma tante María et mes cousines, spécialement María Alejandra.

Enfin, mes remerciements vont à toutes ces personnes qui, liées par un lien d'amitié ou d'affection, sont restées à mon côté pendant cette longue période de thèse, et qui m'ont encouragée à l'aboutissement de l'une des plus importantes étapes de ma vie.

Table of contents

CHAPTER 1

CHAPTER 2

List of abbreviations

AA: Acrylic Acid
AC: Alternating Current
AFM: Atomic Force Microscopy
APPJ: Atmospheric Pressure Plasma Jet
AR-XPS: Angle-Resolved X-ray Photoelectron Spectroscopy
ATR: Attenuated Total Reflectance
ATR-FTIR: Attenuated Total Reflectance - Fourier-Transform Infrared Spectroscopy
BA-C6: Poly (bisphenol A hexane ether)
CAP: Competition Ablation - Polymerization
DBD: Dielectric Barrier Discharge
DC: Direct Current
DMF: Dimethylformamide
DSC-S: Dual Source Column - Sputtering
DVB: Divinylbenzene
EDX: Energy Dispersive X-ray Spectrometry
ESR: Electron Spin Resonance Spectroscopy
FHC: Fused Hollow Cathode
FT-IR (or FTIR): Fourier-Transform Infrared Spectroscopy
FWHM: Full Width at Half Maximum
GCIB: Gas Cluster Ion Beam
GPC: Gel Permeation Chromatography
HDPE: High Density Polyethylene
IR: Infrared
LB: Langmuir-Blodgett
LDPE: Low Density Polyethylene
LF: Low Frequency
LIF: Laser Induced Fluorescence
LIS: Low Inertia Sensor
LMIG: Liquid Metal Ion Gun
MCP: Multi-Channel Plate
MD: Molecular Dynamics
MS: Mass Spectrometry
MSE: Mean Square Error
MVA: Multivariate Analysis
NEXAFS: Near Edge X-ray Absorption Fine Structure
OES: Optical Emission Spectroscopy

P2VP: Poly (2-vinylpyridine)
P4MS: Poly (4-methyl styrene)
PAMS: Poly (α-methyl styrene)
PC: Polycarbonate
PC: Principal Component
PCA: Principal Component Analysis
PDMS: Poly (dimethylsiloxane)
PE: Polyethylene
PECVD: Plasma Enhanced Chemical Vapor Deposition
PEG: Poly (ethylene glycol)
PEO: Poly (ethylene oxide)
PET: Poly (ethylene terephthalate)
PETI: Poly (ethylene terephthalate-ethylene isophthalate)
PFA: Perfluoroalkoxy Copolymer
PI: Primary Ions
PIB: Polyisobutylene
PMMA: Poly (methyl methacrylate)
poly(EHA-co-GMA): Copolymer of 2-Ethylhexyl Acrylate and Glycidyl Methacrylate
PP: Polypropylene
PP2VP: Plasma-Polymerized 2-Vinylpyridine
PPG: Poly (propylene glycol)
pp-PS: plasma-polymerized Polystyrene
PPS: Plasma-Polymerized Styrene
PPVF: Plasma-Polymerized Vinylferrocene
PS: Polystyrene
PTFE: Polytetrafluoroethylene
PVC: Polyvinyl chloride
PVP: Polyvinylpyrrolidone
PVP: Poly (4-vinylphenol) = Poly (4-hydroxy styrene)
QCM: Quartz Crystal Microbalance
RAE: Rotating Analyzer
RF: Radiofrequency
RPE: Rotating Polarizer
RSGP: Rapid Step-Growth Polymerization
S/A: Sputtering/Analysis
SE: Spectroscopic Ellipsometer
SEM: Scanning Electron Spectroscopy
SI: Secondary Ion

SIMS: Secondary Ion Mass Spectrometry
SNMS: Sputtered Neutral Mass Spectrometry
SPS: Sulfonated Polystyrene
SSIMS: Static Secondary Ion Mass Spectrometry
ToF: Time-of-Flight
ToF-SIMS: Time-of-Flight Secondary Ion Mass Spectrometry
ToF-SSIMS: Time-of-Flight Static Secondary Ion Mass Spectrometry
UHV: Ultra High Vacuum
UV: Ultraviolet
VUV: Vacuum-Ultraviolet
WCA: Water Contact Angle
XPS: X-ray Photoelectron Spectroscopy
XRR: X-ray Reflectivity

CHAPTER 1
Introduction

Non-equilibrium plasmas are widely used for the treatment of polymer surfaces or the deposition of (ultra)thin polymer layers from volatile precursors, in order to modify the surface chemistry without altering the bulk properties or, only in the latter case, to prepare functional films with desired properties on selected substrates. The respective processes are known as plasma treatment and plasma polymerization. Plasma technologies for the surface modification or the synthesis of polymers find applications in several sectors, such as medicine, microelectronics and food industry, just to name a few. Indeed, compared to the chemical methods of surface modification of polymers and the conventional polymerization techniques, plasma processes appear to be more attractive, mostly because they require fewer steps and do not use solvents.

Historically, plasma processes were conducted under low pressure, but in the last decades an increasing interest arose towards plasma technologies at (near) atmospheric pressure, both for the synthesis and the treatment of polymer-based materials. In addition to the many advantages offered by low-pressure plasma techniques, atmospheric plasmas permit to avoid the constraints of the vacuum, so that they can be easily upgraded to the industrial scale. An extensive amount of work was already conducted on the more traditional plasma processes at low pressure, providing a relatively good knowledge of the underlying physics. On the other hand, the chemical and physical properties of the polymers, treated or synthesized by the recently developed plasma technologies under atmospheric pressure, need to be better understood.

As a matter of fact, both plasma-treated and plasma-synthesized polymers are complex systems to study. The chemical and structural modifications of polymers exposed to plasmas generally affect the (sub)surface region, ranging from a few nm to tens of nm. On the other hand, plasma-deposited polymers (named plasma-polymers) differ from their conventional counterparts because of the absence of a repeat unit, accompanied by a relatively high content of cross-linking, branching and unsaturation. Additionally, in the case of plasma-polymers, the chemical structure can be homogeneous along the whole depth or exhibit gradients, depending on the control of the precursor injection. An important point in both cases of plasma treatment and plasma polymerization consists in the possibility to finely tune the chemical and structural properties of the resulting polymer material by simply varying the external plasma parameters, e.g. the plasma power. Thus, adequate characterization tools are required, in order to elucidate the specific chemical and structural features of these systems, to investigate their dependence on the plasma parameters, and finally to better understand the processes occurring under atmospheric pressure.

Because atmospheric plasma technologies involve ultrathin films or ultra-shallow surface modifications, X-ray photoelectron spectroscopy (XPS) is the most commonly used chemical analysis technique for the investigation of these materials. The complementary surface technique time-of-flight secondary ion mass spectrometry (SIMS) is generally considered as more exotic. This is probably due to the extensive fragmentation of the polymer chains upon primary ion bombardment, so that the extraction of chemical and structural features from the SIMS spectra is not straightforward, and sometimes extremely time-consuming. Historically, several structural SIMS indicators, empirically defined and given by ratios or normalized sums of secondary ion intensities, were developed to extract the desired information from the SIMS spectra for plasma-polymers and plasma-treated surfaces. However, their evolution as a function of the plasma parameters depends strongly on the chemical/structural nature of the precursor(s) and their blind use can lead to contradictory results. The application of statistical methods, such as principal component analysis (PCA), alleviated this issue, permitting to focus only on the main variation trends of the SIMS intensities. Furthermore, for a long time SIMS was limited to the surface analysis of polymers, due to the loss of distinctive structure-related information during the erosion of the sample. In the late 1990s, the advent of cluster-SIMS paved the way for the polymer *molecular* depth-profiling. However, it was not until the development of massive Ar cluster ion beams as sputter sources that molecular depth-profiling of polymers could be performed universally, including also polyolefins and aromatic polymers. This explains the small amount of in-depth SIMS characterization of plasma-treated and plasma-deposited polymers currently reported in the literature.

This thesis focuses on the development of new methodologies for the surface and in-depth chemical characterization of plasma-treated and plasma-synthesized polymers under atmospheric pressure, by means of the application of the combined ToF-SIMS/PCA protocol and the use of large Ar cluster sputtering. Preliminary fundamental studies on polymer SIMS organic depth-profiling are performed on two conventionally-polymerized model polymers, i.e. poly (methyl methacrylate) (PMMA) and polystyrene (PS). In particular, the effects of the polymer molecular weight, the thickness of the film, and the nature of the substrate, on the sputtering efficiency of massive Ar cluster ions are elucidated. Important insights given by these fundamental contributions are used at a later stage in the characterization of plasma-polymers. Two different and challenging case studies involving plasma-treated and plasma-polymer films, respectively, were defined for the development of novel characterization protocols:

1) Polyethylene films exposed to an atmospheric Ar-H_2O post-discharge. This recent typology of plasma treatments represents a promising route of oxidative functionalization for industrial and medical applications. However, tracing the reactivity of H_2O with the polyolefin is challenging, due to the inevitable intervention of the atmospheric water vapor. Thus, exploiting the isotope sensitivity and selectivity of SIMS, deuterated water vapors were employed to investigate the H-D exchange, oxygen/nitrogen-uptake, unsaturation, branching and/or cross-linking, as a function of the parameters “treatment time” and “sample-torch distance”. For the first time, the surface chemical characterization could be correlated with the in-depth modifications, and rationalized on the basis of the lifetime of the reactive species present in the post-discharge.

2) Polystyrene-like films deposited from the styrene precursor near atmospheric pressure by means of a dielectric barrier discharge (DBD). This plasma-polymer is generally used in the preparation of electronic devices, as protective films and in medical applications. The peculiar chemical and structural features of the deposited aromatic coatings, after exposure to the ambient air, were investigated in the inner layers as a function of the plasma power. This expedient permits to perform ex-situ characterization even in presence of adventitious surface contamination and, more importantly, post-polymerization oxidation. It is shown that SIMS can provide information about the unsaturation, branching and/or cross-linking, as well as the aromatic and aliphatic content of the plasma deposited films. Insights about the polymerization degree can be derived thanks to the fundamental studies on SIMS molecular depth-profiling of PS.

It is worth noticing that the SIMS characterization carried out on these two selected polymers (plasma-treated and plasma-synthesized, respectively) brings not only information about the chemical structure itself, but also about the physico-chemical interactions between the plasma (or post-discharge) and the polymer substrate. The latter can indirectly provide some peculiar insights related to the plasma medium, that could be out of reach of the plasma diagnostics.

This thesis starts with some information about the theoretical background on non-equilibrium plasmas for surface treatments and synthesis of polymers, in addition to the SIMS technique (Chapter 2). The SIMS instrumentation, as well as profilometry and ellipsometry, will be described in Chapter 3. The main results about the fundamental studies on polymer SIMS depth-profiling with large Ar clusters will be presented in Chapter 4, including a published paper. The study of the plasma-treated polyethylene will be given in Chapter 5 in the form of two published articles, while that concerning the plasma-polymerized polystyrene will be presented in Chapter 6. Finally, general conclusions and perspectives will be drawn in Chapter 7.

CHAPTER 2
Theoretical background

2.1. Plasma state

Plasma is considered the 4th state of matter, the others being solid, liquid, and gas.[1] Plasma is the most abundant form of ordinary matter in the Universe, most of which is in the rarefied intergalactic regions, and in the stars, including the Sun. Everyday examples related to plasma phenomena are the neon signs, electric sparks, and lightening.

Plasma is described as a fully or partially-ionized gas, composed by negative and positive ions, electrons, and neutrals (atoms, molecules, and radicals in their ground or excited state). Additionally, plasmas are globally electrically neutral despite the local presence of charged particles, which make them conductor and strongly influenced by electrical and magnetic fields. The electroneutrality is verified above the Debye length (λ_D), that defines the influence area of an ion:

$$\lambda_D = \sqrt{\frac{\varepsilon_0 . k_B . T_e}{n_e . e^2}} \tag{1}$$

where ε_0: vacuum permittivity (8.85 x 10^{-12} C^2 J^{-1} m^{-1}); k_B: Boltzmann constant (1.38 x 10^{-23} J K^{-1}); e: electron charge (1.602 x 10^{-19} C); T_e: electron temperature (K); and n_e: electron density (m^{-3}).

In non-equilibrium situation, the different plasma particles (that are electrons, ions and neutral species) exhibit different velocities depending on their mass (electrons are much smaller than ions and neutrals). Thus, they show different average kinetic energies. The energy distribution function of each plasma species is known to approximate to a Maxwell-Boltzmann (or Maxwellian) distribution, so that a specific temperature can be attributed to each plasma particle (T_e, T_i, T_g for electrons, ions and neutral gas species, respectively).[1] For instance, the electron temperature (T_e) for such an energy distribution can be defined as:

$$T_e = \frac{2}{3} . m_e . \frac{\langle v \rangle^2}{2 . k_B} \tag{2}$$

where m_e is the mass of the electron (9.1095 x 10^{-31} kg), $\langle v \rangle^2$ is the root mean square velocity of the electron (in m s^{-1}), and k_B is the Boltzmann constant (1.38 x 10^{-23} J K^{-1}).

Plasmas can be classified on the basis of the ionization degree (α), defined as follows:

$$\alpha = \frac{n}{n_0 + n} \tag{3}$$

where n represents the electron density, that is equal to the density of ions, while n_0 is the density of the neutral species present in the plasma. Thus, plasmas can be distinguished in weakly ionized ones, when $10^{-7} < \alpha < 10^{-4}$ (an example is given by the glow discharges), and strongly ionized ones if $\alpha > 10^{-4}$ (like for instance in the case of the Sun). Another important concept of the plasma state concerns the mean free path (λ), which determines the collision frequency of particles (as a function of the pressure):

$$\lambda = \frac{k_B . T}{\sqrt{2} . \sigma . p} \tag{4}$$

Here, k_B is the Boltzmann constant (1.38 x 10^{-23} J K^{-1}), T is the temperature of the particle (K), σ is the effective collision cross section (m^2), which depends on the energy involved in the inelastic collision events, and p is the pressure (N m^{-2}).

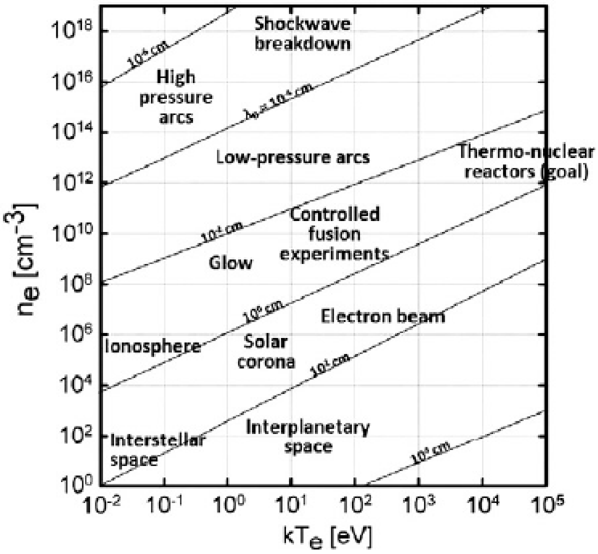

Figure 1. *Classification of plasmas in terms of density and energy for different Debye lengths (λ_D).*[2]

Plasmas are distinguished by their intrinsic properties, such as densities of electrons, ions, and neutrals, Debye length (function of electron density and energy), temperatures of electrons and heavy particles (i.e. ions and neutral species). Based on the electron density (n_e) and energy ($k_B.T_e$) for different Debye lengths (λ_D), plasmas are classified as illustrated in **Figure 1**.

In addition, plasmas are commonly discriminated in thermal and non-thermal (or cold) plasmas, as a function of the temperatures of electrons and (neutral) heavy gas particles, T_e and T_g (related to their respective energies). This reflects the macroscopic temperature of the plasma. The distinction is represented in **Figure 2**, that reports the trend in electron and neutral temperatures with pressure for a mercury plasma discharge.[3,4,5]

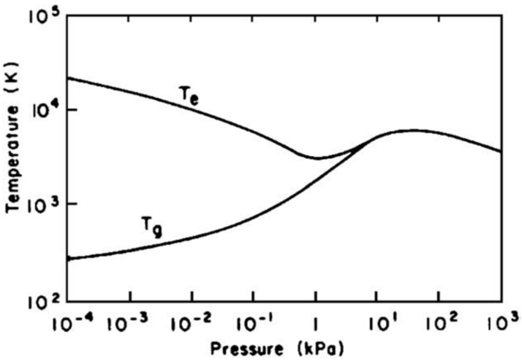

Figure 2. *Evolution of the plasma temperature (electrons and heavy particles) with the pressure in a mercury plasma arc.*[5]

Non-thermal plasmas are characterized by high T_e (up to 100 000 K, 1 eV = 11 600 K), and relatively low T_g (the macroscopic temperature ranges from 300 to 1 000 K), so that $T_e >> T_i \sim T_g$ (T_i: ion temperature). Indeed, the electron energy is transferred to the neutral gas in order to mainly induce ionization processes. Since non-thermal plasmas are generally operated at low pressure, the mean free path of the particles is longer and a lower fraction of energy is transferred. As a consequence, cold plasmas (like for instance glow discharges) possess a higher population of neutrals than ion species (i.e. low α values). An example of non-thermal plasma offered by the nature is the Aurora Borealis. Conversely, in thermal plasmas, the high gas pressure determines an augmentation of the collisions between particles, so that the system thermalizes ($T_e = T_i \sim T_g$). Thermal plasmas possess high ionization degrees (close to 1), so that they are also referred as "hot" plasmas in opposition to the "cold" plasmas characterized by very small fractions of ionized gas ($10^{-7} < \alpha < 10^{-4}$). Typical examples are the Sun, reactors for nuclear fusion and arcs, among others. Plasmas utilized in "plasma technology" are usually cold plasmas. This thesis will only deal with cold plasmas at atmospheric pressure (non-thermal) for surface modification and deposition of polymer-based materials. Only those will be detailed in the next pages.

Glow discharge

The glow discharge is a type of non-thermal plasma as the dielectric barrier discharge (DBD), a variant that enables to work under atmospheric pressure.[6] A glow discharge is achieved by applying a current through a gas between two electrodes. **Figure 3** reports the characteristics current-voltage (I-V) of a direct current (DC) plasma initiated between two planar electrodes (2-cm diameter, inter-electrode distance of 50 cm) in a tube (pressure of 1 torr). Three different zones can be discriminated in the I-V curve of Figure 3: the dark discharge before the "breakdown" point (from A to C); then, the glow discharge (D-I) and the arc (J).

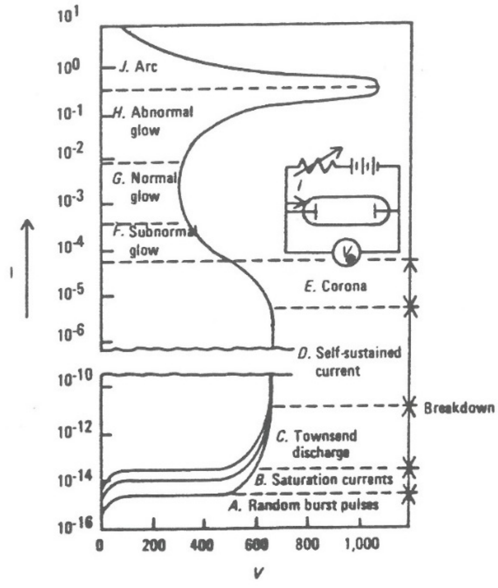

Figure 3. *Evolution of the voltage as a function of the current in a glow discharge.*[7]

At low voltage (region A), the current evolution is determined by the electrons formed by the cosmic irradiation (the density of free electrons in the atmosphere is ~10^{-15} cm^{-3}). Then, the system reaches saturation (B), since the electron energy is not any more sufficient to cause ionization. The region C is characterized by the Townsend regime, where the electrons acquire energy from the application of the electric field to induce further ionization. Thus, the current increases exponentially until reaching the “breakdown” point, indicated in the graph of Figure 3 with a dotted line. After the breakdown point, the discharge is self-maintained, that is the current increases without increasing the voltage. The system is now in the glow discharge region. After the subnormal and normal glows (signified with F and G, respectively), the system evolves towards the abnormal discharge. In this region (H), the current increases linearly with increasing voltage. This is typically the region utilized in this thesis for a better control of the plasma. A further augmentation of the current leads to the transition to the arc (appearance of thermal plasma as a consequence of the presence of a very high electron density).

Five different areas can be distinguished in the inter-electrode region, as represented in **Figure 4.** They are the cathode space, the negative glow, the Faraday space, the positive column, and the anode space.[6]

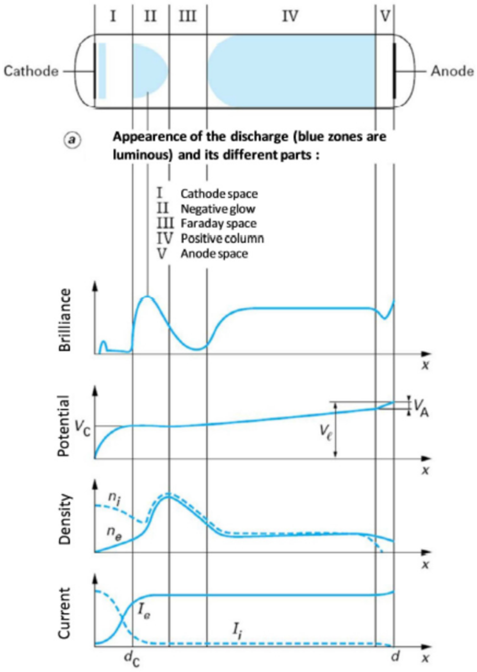

Figure 4. *Different areas of a glow discharge.*[8]

I. In the *cathode (or cathodic) space*, the drop of voltage induces the acceleration of the positive ions towards this electrode, determining the emission of secondary electrons by ion bombardment. The latter are accelerated producing gas ionization. The observed luminosity in this area of the tube is ascribable to the radioactive recombination of ions and electrons.

II. The *negative glow* is characterized by the highest brilliance along the inter-electrode distance, due to radioactive relaxation phenomena of the excited species (atoms or molecules), formed by the interactions with high-energy electrons accelerated by the electric field.

III. In the *Faraday zone*, no photons are emitted because of the prevalence of inelastic collisions that take place in the negative glow. Thus, the electrons have lost part of their energy to be able to ionize any atoms or molecules. Furthermore, an excess of negative charges is built in this space, which prevents the electrons to be accelerated to the anode.

IV. In the *positive column*, the electroneutrality condition is found. This represents the zone where the plasma is formed. The fraction of charged particles is very low, ranging from 1/100 000 to 1/1 000 000.

V. In the *anode space*, no ions are created. The drop of voltage determines the acceleration of the electrons (and their consequent collection), that leads to ionization processes in the positive column previously mentioned.

In the past, plasmas were usually operated under low pressure. The control of the atmosphere inside the chamber was aimed to gain a better understanding of the physics underlying the observed phenomena. More recently, plasma technologies working under atmospheric pressure start to be developed. They permit to overcome the disadvantages of vacuum operations, which is more interesting for the industrial applications.[5] The difficulties of sustaining a glow discharge under these conditions is discussed in the next section.

Atmospheric pressure plasmas

The main difficulties for obtaining atmospheric-pressure cold plasmas consist in: 1) formation of arcs between the electrodes and further transition to a thermal plasma, and 2) higher voltages are needed for gas breakdown at 760 torr.[2,9,10]

The transition of a glow discharge to an arc plasma as a function of the time is represented in **Figure 5**. This can be explained by the much higher collision frequency under atmospheric conditions than at low pressure, as suggested by **Equation (4)** (i.e. $\lambda \propto 1/p$), that leads to the heating of the gas (represented in Figure 2). In order to avoid the arcing between the electrodes, a possible approach consists in reducing the duration of the discharge, so that the number of collisions caused by the electrons accelerated by the electric field is limited (see Figure 5).[2] Another expedient consists in applying pulses to the electrodes (pulsed voltage, AC or DC), by alternating the polarities of the electrodes with a high frequency generator.[2] An additional technical trick concerns the placement of a dielectric barrier (i.e. an insulating layer) between the electrodes. The discharge obtained in this way is called dielectric barrier discharge (DBD),[2] and it is a variant of the glow discharge. The role of the dielectric is to accumulate the electrons at one electrode, decreasing the apparent ΔV and so the electric field responsible for the electron acceleration, which in turn reduces the collisions. In this case an AC current is needed to avoid the discharge stops.

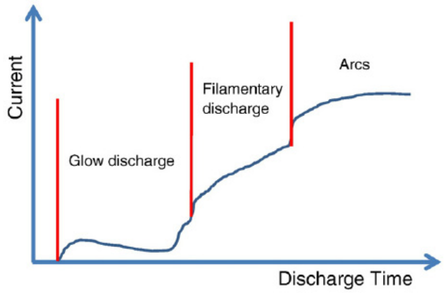

Figure 5. *Schematic illustration of a discharge current as a function of the duration of the discharge.*[2]

The second major drawback of atmospheric pressure plasmas compared to low pressure discharges is that they require higher breakdown voltages for similar inter-electrode distances. The dependence of the breakdown voltage (V_b) on the pressure and distance is given by the Pashen law:[10]

$$V_b = \frac{B.p.d}{C + \ln(p.d)} \tag{5}$$

where *d* represents the inter-electrode spacing, *p* is the pressure, *B* and *C* are constants that depend on the gas nature and the electrode material.

Figure 6 shows the typical breakdown voltage curves for different gases between two parallel plate electrodes. A minimum breakdown can be observed for a given *p x d* product, generally below *p x d* = 10 cm x torr. For instance, V_b of argon is estimated to be 2 500 V at 760 torr and 5-mm gap.[10] As a consequence, narrower gaps of the order of a few mm are necessary for the sustainment of atmospheric-pressure plasmas, imposing certain limitations to the reactor geometry. These curves also suggest the use of noble gases to reduce the energy consumption, since they exhibit much lower V_b values with respect to the air.

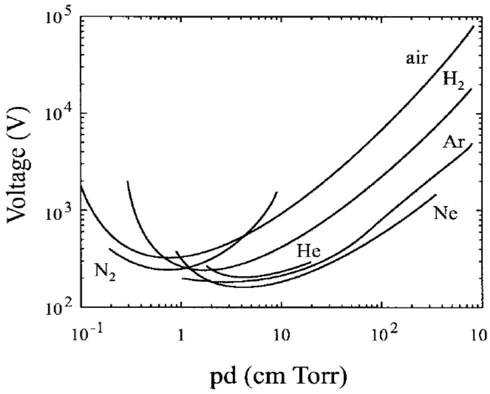

Figure 6. *Typical breakdown voltage curves for different gases between two parallel plate electrodes. p = pressure and d = electrode separation.*[10]

Traditional atmospheric-pressure plasma sources include transferred arcs, plasma torches, corona discharges, and dielectric barrier discharges. Arcs and torches are typically used in metallurgy because of their high gas temperature, that can exceed 3000 °C, and high density of charged particles (10^{16}-10^{19} cm^{-3}).[10] Plasma torches can also produce non-thermal plasmas with gas temperature close to the room temperature.[5] On the other hand, corona and dielectric barrier discharges produce cold plasmas, weakly ionized, and with a gas temperature between 40 °C and 400 °C.[10] In this thesis, only the second typology of plasma torches and the dielectric barrier discharge will be described as they were used for surface treatment of polymers and plasma polymerization, respectively.

Plasma torch and dielectric barrier discharge

The atmospheric pressure plasma jet (APPJ)[5,9,10] is the type of plasma source used in this thesis for the surface modification of polyolefin films of Chapter 5. The APPJ is a small (typical length < 20 cm) RF plasma torch, that works at low power. It was developed in the mid-1990s by J. Y. Jeong et al. (UCLA, University of California, Los Angeles) in collaboration with J. Park et al. (Los Alamos National Laboratory). This device can operate under atmospheric conditions (760 torr and temperatures between 75 °C and 150 °C). In addition, the plasma jets exhibit very low breakdown voltages of 0.05-0.2 kV, comparable to those characteristic of low-pressure discharges of 0.2-0.8 KV, and lower than those of dielectric barrier discharges (5-25 kV).[10]

The system consists of two concentric electrodes through which the working gas flows. The plasma is ignited by applying a RF power to the inner electrode (13.56 MHz and its harmonics; radio-frequencies between 1 and 1000 MHz are required, so that only the electrons follow the oscillations of the electric field)[5], at a voltage between 100 and 150 V. The gas, ionized by the inelastic collisions of the electrons driven by the electric field, exits through a nozzle. The low injected power enables the torch to produce a stable, homogeneous discharge and avoids the arc transition. The research team of Park and coworkers (UCLA) also designed a rectangular version of the APPJ.[11] Here, the upper electrode is connected to the RF power supply, while the lower electrode is grounded (both electrodes are perforated planar aluminum plates). Both sources are commercialized by SurfX Technologies[12]. The specific model of atmospheric plasma torch utilized in this thesis, that is an Atomflo™ 250D, is presented in detail in §5.2.3.1 and §5.3.3.1.

A dielectric barrier discharge is a system of two electrodes, separated by a distance of a few mm, where at least one of them is covered by a dielectric layer (see **Figure 7**). The dielectric barrier avoids the arc transition, which is due to the extensive ionization occurring at high pressure as a consequence of very short mean free paths. In a DBD system the charged particles, accelerated towards the opposite-sign electrode, starts accumulating on the insulating material. This leads to a diminution of the applied electric field, since another one of same intensity but opposite direction is created. This should cause the extinction of the discharge, that justifies the need to apply an AC voltage for its sustainment. The main characteristic properties of DBDs can be found in the work of Kogelschatz et al.[13] Furthermore, the plasma source used for the polymerization of the styrene precursor of Chapter 6 is a home-made DBD system, and it will be fully described in §6.2.2.

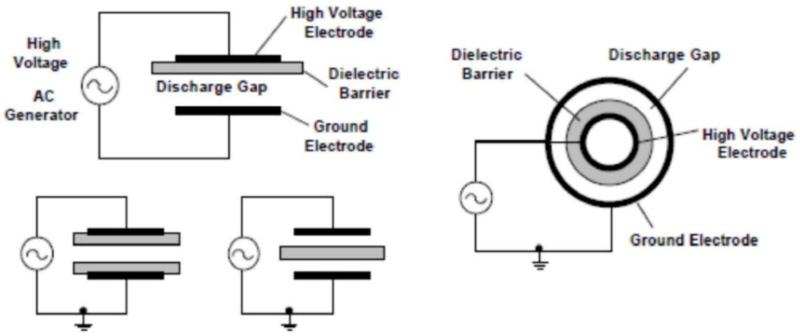

Figure 7. *Common dielectric-barrier discharge electrode configurations.*[14]

Two distinct types of discharge can be discriminated in a DBD: filamentary and diffused discharges.[15] The filamentary dielectric-barrier discharge is characterized by the local propagation of ionization fronts, named streamers, followed by the formation of filaments through the inter-electrode spacing, from the cathode to the anode. These thin conductive channels possess a diameter of around 100 μm, that become wider once they enter in contact with the dielectric layer. Furthermore, they are separated from each other by as much as 2 cm.[10] They last for 10-100 ns and are randomly distributed in space and time, thus this discharge mode can also be utilized for surface treatment as the diffuse discharges.[10,16] In filamentary discharges, the distribution of active species is axial, so that only the surface in contact with the filaments is treated by ions and electrons (neutrals and UV radiation are responsible of the surface modifications outside those areas). Homogeneous diffuse discharges can also be obtained in DBD configurations, even at atmospheric pressure.[14] A diffuse discharge is characterized by an isotropic distribution of the plasma species in the positive column. The prevalent formation of metastable species in the plasma gas is demonstrated in this case, that can induce Penning effect (i.e. the ionization that follows the collision of two species - atoms or molecules - , one being in an excited state whose energy is higher than the ionization potential of the second species in the ground state)[i]. In this thesis, argon is

---

[i] Penning ionization can be represented as follows: $A^* + X \rightarrow X^{+\bullet} + A + e^-$, where A^* is an excited-state species and X is the target atom or molecule in the ground state.

the carrier gas used in the plasma polymerization conducted in the DBD device, as well as the plasma treatment with the torch. This noble gas (electronic configuration: [Ne] $3s^2\ 3p^6$) exhibits two metastable electronic states, which are not capable to ionize O_2 and N_2: the first one is Ar ($^3P_2$) having an energy of 11.55 eV, while the second Ar ($^3P_0$) state exhibits an energy of 11.72 eV.[17]

2.2. Plasma surface modification of polymers

2.2.1. Basics of plasma surface modification

The modification process of the surface properties and the surface morphology of polymer-based materials induced by the exposure to glow discharges (or post-discharges) is known as plasma treatment of polymers.[18,19] Indeed, plasma contains numerous active species, such as electrons, ions and radicals (as well as photons), the latter being produced by the collisions between electrons and the gas molecules present in the plasma zone. The interactions of these electrons, ions, and radicals with the solid surface of the polymer lead to chemical and physical reactions, i.e. formation of radicals, implantation of atoms (better known as grafting of functional groups), and etching. The prevalence of one of these processes is mainly determined by the nature of treated polymer and the plasma gas (like e.g. Ar, He, H_2, O_2, N_2), in addition to the energy level of the plasma.

When a polymer surface is treated by plasma, the generation of radicals has been evidenced a long time ago by means of electron spin resonance (ESR) spectroscopy.[19] Radicals are formed in several ways, such as hydrogen abstraction from polymer chains by electrons or other radicals, or C-C bond scission upon electron or ion bombardment. Yasuda et al. demonstrated in 1973 that radicals remain trapped and stable in plasma-treated polyethylene.[20] Furthermore, a slow decay of the radical concentration was observed within the first 20 hours after the exposure of the polymer to nitrogen plasma at an RF power of 75 or 100 W (13.56 MHz) and a pressure of 0.12 torr. Yasuda hypothesized that UV radiations were responsible for the radical generation in the bulk of the material, whereas the electron impact could only form radical species at the surface of the polymer. The recombination reactions of the radicals generated at the polymer surface with the radicals derived from the activation of the gas molecules (e.g. O_2 and N_2) lead to the implantation or grafting process. The implantation reaction by plasma treatment is considered the most important process for the surface modification of polymers. The grafting of specific chemical functional groups, such as hydroxyl, carbonyl, amino, and amido groups, induces changes of surface properties like, for instance, the transition of a polymer surface from hydrophobic to hydrophilic in order to improve adhesion and wettability abilities (refer to §2.2.3).[21] Radicals can also initiate two types of degradation reactions in the polymer materials, chain scission and cross-linking.[19,22] Both processes take place under high energy irradiation of polymers, such as γ-rays and accelerated electrons and ions and, to a minor extent, under plasma exposure because of the low energy levels of the activated species (electrons and ions). Chain scission and cross-linking are competitive processes, so that the predominant one is dictated by the chemistry of the polymer material, which intervene in the stabilization by resonance of the radicals obtained under irradiation. Generally, polymers possessing a repeating unit $-(CH_2-CHR)_n-$ (i.e. containing a tertiary carbon atom) undergo mainly chain scission, producing volatile products. On the other hand, polymers with repeating unit $-(CH_2-CRR')_n-$ (note the presence of a quaternary carbon atom) undergo cross-linking reactions. Polyolefins like PE and PP[ii] tend to give predominantly cross-linking, while polyacrylates give mostly chain scission.[19] Bond scissions of polymers as a consequence of the degradation mechanism upon irradiation and interaction with the activated species of the plasma during adequate times, lead to a chemical etching process, which in turn determines weight loss (or plasma susceptibility). Weight loss rate is strongly dependent on the polymer nature and the plasma energy levels. Generally, polyolefins show low plasma susceptibilities, such as 1.2 and 0.8 mg/cm^2.min for PE and PP, respectively, when using a 30 W and 13.56 MHz He plasma; whereas polymers containing oxygen functionalities (ester, ethers, carboxylic acids) exhibit greater weigh losses, like for instance 15.4 PMMA.[19,23] The etching is considered a degradation process of the polymer surface. Indeed, after plasma-induced etching, polymer surfaces functionalized by specific plasma treatment tend to show typical elemental composition, chemical structure, and degree of polymerization of the pristine polymer. In addition to the above-mentioned chemical etching, physical etching can occur when polymers are exposed to plasmas (refer to the sputtering process in SIMS, §2.4.1). However, ion energies of a few keV are required, much higher of those possessed by the ions in plasma. Thus, sputtering yields are low in plasma treatment of polymers.

[ii] PE: Polyethylene; PP: Polypropylene

2.2.2. Applications of plasma-treated polymers

Plasma technology is widely used for surface modification of polymers in many fields of application, such as microelectronics, biomedical, automotive, chemical and food industries. In this section, some applications of plasma-treated polymers are presented, with particular reference to the biomedical[17] and food packaging[24] sectors.

In the medical field, plasma treatments are given to polymers to mainly achieve bio/blood compatibility and antimicrobial properties. Cell attachment and growth are influenced by the surface wettability, surface free energy, and charge of the polymer-based biomaterial. In order to improve the blood compatibility of selected polymers (e.g. nylon, polyester, polyethylene, polypropylene), one possible solution consists in the immobilization of proteins with antithrombogenic or thrombolytic properties on their surfaces. An example is provided by the study conducted by Lahann and collaborators,[25] who investigated the surface modification of a poly (2-chloroparaxylylene) layer by treatment with a sulfur dioxide plasma, in order to obtain a more hydrophilic surface with new functional groups. The results demonstrated a significant influence of the surface treatment on the adsorption of the human blood protein, fibrinogen, and consequently, a net improvement of the haemocompatibility. Kim et al. developed an interesting protocol for the immobilization of insulin and heparin on poly (ethylene terephthalate) (PET) films to improve the blood compatibility.[26] More precisely, the polymer film was exposed to oxygen plasma glow discharge to produce peroxides on its surface. These peroxides were then used as catalysts for the polymerization of acrylic acid (AA). At this point, poly (ethylene oxide) (PEO) was grafted on to PET-AA, thanks to the carboxylic acid groups introduced. Finally, this step was followed by the reactions of the PET-AA first with insulin, and then heparin. Beyond the biocompatibility, another serious issue in the development of medical devices is related to the adhesion of bacteria to the polymer surface leading the formation of biofilms, which are resistant to antibiotics. A possible solution to this problem consists in the coating of the “medical” polymer with antibacterial agents, in order to either prevent the bacteria adherence or kill the bacteria as they come in contact with the surface. In this respect, Zhang et al. proposed to coat PE surfaces with triclosan and bronopol.[27] The polymer surface was made more hydrophilic by O_2 plasma treatment, followed by Ar and H_2 plasma treatment, to enhance the coating of the two antibacterial agents. Results revealed that non-reactive argon plasma was better than reactive hydrogen plasma in improving the antibacterial properties of PE.

Bio/blood compatibility and antimicrobial properties imparted to polymer surfaces by plasma treatment are essential for the use of polymeric biomaterials in various medical applications, such as implants (from simple catheters to artificial lungs or kidneys) and biosensors. For instance, Wang et al. proposed to make hydrophilic the surface of a hydrophobic polypropylene (PP) membrane, on one side, by plasma treatment in presence of ammonia gas.[28] The modified PP membrane was coupled to urease and used to construct a urea sensor, which gave electrode response time only half that of the conventional urea sensor. Another case of successful application of plasma treatment to biomaterials is given by the work of Eloy et al. on poly (methyl methacrylate) intraocular lenses.[29] Indeed, they demonstrated that CF_4 plasma surface modification of the polymer was able to significantly reduce the adhesion of proteins, the appearance of inflammatory cell responses, and the formation of cellular debris.

Surface functionalization, sterilization, etching and deposition are the main purposes of plasma treatments of polymer-based food packaging. For the past few decades, food industries have been replacing traditional packaging materials, including glass, metals and paper, with polymeric materials because of a series of advantageous properties, such as greater flexibility, chemical inertness, transparency, low specific weights, among many others. The most used polymers are PE, PP, and PET, which together account for more than the 80% of the food packaging polymers.[24] However, in most cases polymer surfaces need to be functionalized in order to improve for instance their wettability, sealability, printability, adhesion to other polymers or materials.[24] An example of improvement in printability of PE surfaces is given in the review published by Bárdos and Baránková, where the polymer surface is exposed to He-FHC (fused hollow cathode) plasma.[30] Very short treatment times (only 5 s) were necessary to observe a dramatic increase in the spreadability of the ink. The control of the microbiological requirements for packaging polymer-based materials is a crucial point in the food industry. Cold plasma sterilization seems to be a convenient approach to this issue. However, relatively long treatment times represent a limiting factor to the industrial application of this approach. Recently, Schneider et al. demonstrated the scalability of the plasma sterilization technique for industrial applications.[31] Tests were carried out on PET foils and treatment times of 5 s, showing that the spore reduction kinetics reproduced by a low-pressure microwave plasma source designed for industrial applications demonstrated the easy scalability of the approach. Other approaches, presented in the review of Appendini et al.,[32] are based on the immobilization of antimicrobial peptides by plasma treatment, like in the case of medical applications, and bioactive functional compounds, such as e.g. glucose oxidase, nisin, lysozyme, sodium benzoate.

2.2.3. Review of literature related to surface modification of polyethylene induced by atmospheric plasma torches

Atmospheric-pressure plasma torches, as those commercialized by SurfX Technologies LLC, were developed for plasma enhanced chemical vapor deposition (PECVD)[33,34] and plasma treatment of polymer surfaces for improving, for example, their adhesion properties[35]. Considering the extensive amount of studies conducted with these plasma sources on a large variety of systems, this section will only present the most outstanding works (both experimental and plasma diagnostics), that can be assimilated to the plasma treatment of polyethylene by an atmospheric Ar-H_2O (and Ar-D_2O) post-discharge described in Chapter 5. The selected studies were all conducted in the research group of Professor F. Reniers. They are related to two specific configurations of atmospheric plasma torches, linear and showerhead (the latter being the one used in Chapter 5), and provide important insights in the SIMS characterization of the plasma-modified polyethylene films performed in this thesis.

In 2012, Dufour and collaborators[36] conducted the characterization of the flowing post-discharge of an RF plasma torch supplied with He (carrier gas) and O_2 (reactive gas), by means of mass spectrometry (MS), optical emission spectroscopy (OES) and electrical measurements. The plasma source used in these experiments was a torch with “linear” geometry (Atomflo™ 400L-Series from SurfX Technologies), since the size of the slit permitting the gas exit is 20 x 0.8 mm. The influences of the O_2 flow rate, the He flow rate, and the distance separating the torch from a copper plate located downstream were investigated. First of all, the intervention of atmospheric N_2 and O_2 is found inevitable, even after increasing the He flow rate. Consequently, they need to be taken into account in the plasma diagnostics. OES characterization identified the different species, excited and positive, present in the post-discharge. Penning ionization of O_2 and N_2 is pointed out. The resulting species seem to be responsible of a DC current of 1-20 μA measured in the post-discharge, that mainly depends on the O_2

flow rate. O_2^+ ions are mostly involved in the DC current, since the Penning ionization is more efficient than for N_2 (leading to N_2^+ ions).

In 2014, Dufour et al.[37] carried out the chemical characterization of high density polyethylene (HDPE) surfaces treated with the atmospheric He-O_2 post-discharge, thoroughly investigated in 2012 (obtained with the linear plasma torch). The RF power was fixed at 120 W. The He and O_2 flow rates were 15 L/min and in the range 0-200 L/min, respectively. The sample-torch distance was varied between 1 mm and 25 mm. The purpose of this work was to evaluate the changes in surface hydrophilicity by dynamic contact angle measurements, and to correlate them to the O-based functional groups grafted onto the surface (namely C-O, C=O, O-C=O, determined by XPS) and their variation along the top 9 nm by angle-resolved XPS (AR-XPS). In addition, the ageing behavior of the polymer surfaces treated in different conditions was studied. In the case of O_2 flow rate of 200 L/min, the treatment time slightly influences the AR-XPS depth-profiles of the oxidized groups, while the sample-torch gap strongly affects them: with increasing distance the effectiveness of the plasma treatment decreases in favor of the interaction with atmospheric impurities. Furthermore, MD simulations were conducted to elucidate the formation mechanism of the different O-containing functional groups, permitting to explain the XPS results. Concerning the ageing study, the instability of the treatment over time is explained by simulations with the ejection of low molecular weight oxidized species, such as formaldehyde, rather than chain re-orientation.

Duluard and co-workers[38] investigated in 2013 the influence of ambient air on the flowing post-discharge of an RF plasma torch supplied with Ar (carrier gas) and O_2 (reactive gas), as a function of the sample-torch distance. The feedstock gas He was replaced with Ar, because commercially more attractive. Additionally, H_2O vapor was injected downstream of the two electrodes. In this study, the previous plasma torch was replaced with the Atomflo™ 250D model (SurfX Technologies), that instead possesses a "showerhead" configuration (the discharge is produced between two perforated parallel electrodes of 2.5-cm diameter). The Ar and O_2 flow rates were 30 L/min and in the range of 0-30 L/min, respectively. The H_2O vapor mass flow rate carried by Ar in the bubbling system was ~9 mg/min. The power was fixed at 80 W. A silicon substrate was placed downstream at a distance varying from 2 to 13 mm. Optical emission and absorption spectroscopy were employed in this work. In addition, both spatially resolved mass spectrometry and laser induced fluorescence (LIF) on OH radicals were implemented to trace the air intrusion in the region between the torch and the substrate as a function of the distance. No air is detected for distances < 5 mm, while for gaps > 9 mm the observed decays of the Ar 4p and $N_2(C)$ populations is ascribed, at least in part, to the increasing collisional quenching rates by atmospheric O_2 and N_2.

In 2014, Abou Rich at al.[39] used atmospheric Ar and Ar-O_2 post-discharges, previously investigated by Duluard and co-workers,[38] for the surface modification of low density polyethylene films (LDPE), in order to improve their adhesion abilities by changing hydrophilicity, morphology, and composition. A "showerhead" plasma source (Atomflo™ 250D) was utilized. The Ar flow rate was maintained at 30 L/min, while the O_2 flow rate was varied between 0 and 25 L/min. The sample-torch gap was varied too, going from 2 to 30 mm. The correlation of WCA, XPS and AFM results point out a better functionalization and roughness, hence a higher wettability, when working in presence of O_2. This is strongly dependent on the distance of the polymer substrate from the torch. Furthermore, plasma-induced modifications of the surface, in terms of oxygen concentration and roughness, as a function of the distance from the plasma source (as well as the O_2 flow rate) could be explained by the competition between etching and functionalization processes. An OES study of the plasma phase permitted to identify O and NO as possible responsible species of the polymer ablation. In addition, the ageing study shows that the hydrophobic recovery is completed after 30 days, independently of the O_2 flow rate, when the WCA values reach a plateau of ~80° (vs ~94° of native LDPE). However, the effect of the plasma treatment remains, to some extent, due to the permanence of the surface roughness and a certain concentration of polar groups. A second publication of Abou Rich et al. (2014)[40] focused on the in-depth oxygen diffusion induced either by atmospheric Ar or Ar-O_2 post-discharge in LDPE films. The showerhead plasma torch permitted to apply the following parameter conditions: power between 60 and 90 W; Ar flow rate between 20 and 40 L/min; and O_2 flow rate between 0 and 25 L/min. Instead, the sample-torch distance was fixed at 9 mm. The combination of AR-XPS and ToF-SIMS with 750 eV Cs^+ sputtering points out a maximal penetration depth of oxygen of ~40 nm, by tuning opportunely the treatment conditions. OES measurements suggest that O and NO are the main reactive species responsible both of the surface activation and the oxygen diffusion.

More recently, Abou Rich and collaborators[41] compared the plasma treatments of LDPE films performed by using the post-discharges of two different atmospheric plasma torches with linear and showerhead configurations, respectively. The first plasma source was supplied with He as carrier gas, whereas the second with Ar (as suggested by the manufacturer). Additionally, O_2 was used as reactive gas for the plasma modification of the polyolefin films. Several sample-torch gaps, treatment times, and oxygen flow rates were tried for both systems. The plasma treatments were evaluated in terms of chemical surface composition, roughening and etching effects, which were determined by XPS, AFM, and mass loss (as well as WCA for the estimation of the wettability). The experimental results were correlated with the OES studies conducted on those plasma systems by Dufour et al. (2012),[36] and Duluard et al. (2013)[38]. The main conclusions are the following: 1) for applications aimed to improve the wettability, the choice of the torch is not relevant, if O_2 is used; instead, higher hydrophilicity states are achieved with the linear torch, when no reactive gas is added, and 2) if the main goal is related to the texturization of the polyethylene surface, both configurations cause roughening effects, but to different extents.

In 2016, Collette and co-workers carried out the characterization of the flowing post-discharge of an RF plasma torch (showerhead configuration) supplied with Ar and H_2O as reactive gas, by means of mass spectrometry, optical emission spectroscopy and electrical measurements.[42] The replacement of O_2 with H_2O was justified by the fact that milder treatment conditions were demonstrated in the second case.[43] The results of this investigation were correlated with those from the experimental study of Duluard et al.[38] and the simulations of Atanasova et al.[44], both obtained with the same plasma source. In this study the power was fixed at 80 W. The main Ar flow rate was 30 L/min. A secondary Ar flux supplied a bubbler containing H_2O with flow rates of 0, 2, 4 and 6 L/min, respectively. The resulting H_2O flow rates, introduced in the inner post-discharge (inside the plasma torch device), were 0, 0.7, 1.3 and 2 mL/s, respectively. The increase of the H_2O flow rate determines a diminution of the DC current intensity measured in the post-discharge by placing a copper plate downstream at a distance of 10 mm. This is indirectly explained by the consumption of Ar metastables by the H_2O molecules, so that Ar_2^+ and Ar^+ species cannot be any more formed. The latter species were evidenced by the simulations of Atanasova in the post-discharge, and produced especially through dissociative recombination.[44] The intervention of ambient air was pointed out by the detection in OES of molecular nitrogen. In addition, the absence of Penning ionization of O_2 and N_2 was demonstrated, conversely to the case of a He post-discharge. Plausible pathways for the production of O, OH, O radicals and H_2O_2 were also proposed. The study of the reactivity of H_2O at the interface between an atmospheric Ar plasma torch and LDPE surfaces is one of the main subjects of the Ph.D. thesis of S. Collette, that will be defended in 2017.

2.3. Plasma polymerization

2.3.1. Basics of plasma polymerization

The terminology "plasma polymerization" designates a process of thin polymer film formation directly on the substrate of interest. The polymerization of gaseous or vaporized (liquid) precursor(s) is initiated with the assistance of energetic plasma particles, i.e. electrons, ions and radicals. Unlike conventional polymerization, this process does not require monomers with polymerizable groups (e.g. double bonds), so that alkanes, silanes, and aromatics can be utilized.[45] The resulting polymer films, called plasma-polymers[46],[iii] possess a thickness ranging from hundreds of Å to a few μm.

Plasma-deposited polymers show a series of differences with respect to the conventionally polymerized counterparts.[47] Indeed, plasma-polymers do not contain regular repeat units, since the resultant polymer chains are highly cross-linked and/or branched (refer to Tibbitt et al. for the structure of a plasma-deposited ethylene film)[48]. As a consequence, they are generally insoluble in the usual organic solvents, thermally stable (T_g increases), and chemically inert. Furthermore, the high cross-linking content reduces the ageing effects compared to conventional polymers. Also the permeability properties of plasma-polymers can differ greatly from those of the conventional ones, consequently to the cross-linking and the reduced segmental mobility of the polymer chains.[49] All plasma-polymers contain free radicals as well, determining post-polymerization O-uptake. Another main characteristic of plasma-polymers concerns the adhesion ability, thanks to the substrate activation by plasma leading to an actual grafting process of the polymer chains in growth.[49]

[iii] Plasma-polymers are not polymers in the strict meaning of the word. Indeed, "polymers" are defined as macromolecules built up by the linking together of large numbers (hundreds, thousands, tens of thousands) of much smaller molecules, which are termed "monomers". Additionally, the reaction by which the monomers combine is called polymerization. As a consequence, polymers are characterized by the presence of a repeat unit, while plasma-polymers do not. Hence, the starting molecule of a plasma-polymer is more accurately identified as "precursor" instead of "monomer". However, in the plasma field, the use of the terms polymer, monomer and polymerization is customary, even if not completely appropriate to the process, and so it will be done in this thesis.

Nowadays, the application of plasma polymerization processes is expanding tremendously, and in many scientific fields, for the obtainment of functional polymers with a controlled density of specific chemical groups, and complex structures (refer to §2.3.2 and §2.4.5.2), such as polymer multilayers, gradient polymer layers, and even hybrid systems (with inorganic layers and/or inclusions).[2]

The plasma polymerization process can be described by the CAP-model (competition ablation-polymerization) proposed by Yasuda,[50] and illustrated in **Figure 8**. The main reaction pathways are shown with double arrows (i.e. the polymerization), whereas the side pathways are in back (including the ablation by formation of gaseous by-products). Polymerization occurs either in the plasma phase or on the substrate, after the monomer absorption, activation, and diffusion (a plasma-induced process). The prevalence of one specific reaction pathway on the others is determined by the given experimental conditions and plasma system.

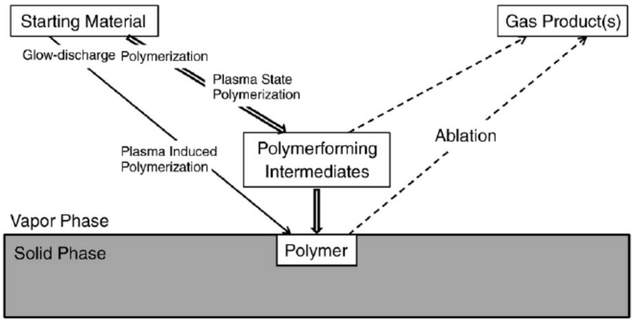

Figure 8. *CAP-model for plasma polymerization.*[51]

A generally accepted polymerization mechanism was defined by Yasuda,[47,52] and based on the thermal initiation of the parylene polymerization. The mechanism is termed rapid step-growth polymerization (RSGP), and it is represented in **Figure 9**. Two different pathways are identified: cycle I, that is a mono-functionalization process ($M^\bullet$), and cycle II, a pathway based on di-functionally activated species ($^\bullet M^\bullet$). The subscripts i, j, and k indicate the size of the different species involved. The termination reaction can occur by radical recombination or cyclization of the chains, although a relatively high content of radicals remains trapped in the polymer structure.[47] It is worth noticing that the RSGP model proposed for the plasma polymerization at low pressure considers the radicals (obtained by electron impact of the monomer M_i) as the most important species in the formation of the deposits. However, it does not take into account the additional intervention of ions (originated by reaction with high-energy metastable species from the plasma gas), which play an important role in the processes conducted especially at atmospheric pressure. More recent mechanisms for plasma polymerization have been proposed by O'Toole et al.[53] and Beck et al.[54], where the role of ions for plasmas at low pressure is pondered. A critical review of the mechanisms for plasma polymerization was recently presented by Friedrich.[55]

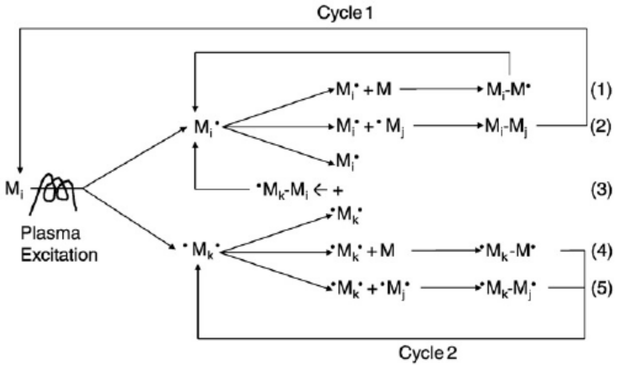

Figure 9. *Schematic representation of the rapid step-growth polymerization (RSGP) mechanism in plasma polymerization.*[47,52]

The chemical structure of the plasma-synthesized polymers depends strongly on the internal plasma parameters (e.g. n, T_e, and T_i), in addition to the external parameters, such as reactor geometry and size, location of the electric energy input, discharge power, frequency, total pressure, partial pressure of the monomer, flow rates, among others.[56,57] Since the external parameters influence the internal parameters, which are very complex to control, the properties of the coatings can be tailored by an appropriate choice of the external parameters. Only, plasma power and monomer flow rate are here discussed. With increasing the applied power (W), the electron energy increases, determining an increase of the plasma density (n), and the temperatures of electrons (T_e) and ions (T_i). This causes a more pronounced fragmentation and re-arrangement of the precursor chemical structure, leading frequently to polymers that are more branched and/or cross-linked. Instead, with increasing the monomer flow rate (F), the retention time of the molecules in the polymerization chamber decreases, so that the monomer undergoes less fragmentation and re-arrangement. The resulting deposits exhibit a more regular structure and higher retention of the original chemical/structural features of the precursor. Hence, "soft" conditions of plasma polymerization can be assumed to be low powers and high monomer flow rates. The combination of these two parameters is given by Yasuda's factor (E):[47,58]

$$E = \frac{W}{F \cdot M} \tag{6}$$

where W is expressed in J/s, while F in mol/s. M represents the molecular weight of the monomer (kg/mol). E is consequently an apparent input energy per monomer molecule (J/kg). Hence, E is proportional to the concentration of activated monomer. Based on the W/F.M parameter, three different domains of plasma polymer deposition can be identified, as depicted in **Figure 10**. For low ratios (low discharge power and high flow rate), or in the monomer- sufficient region, the power supplied to the monomer molecules is relatively low, thus films with higher structural retention are formed. Moreover, the deposition rate increases with increasing this ratio, since the concentration of activated species is lower than the one of the monomers, and new radical species can be obtained. Conversely, for high ratios polymer films more disordered (more fragmentation of the precursor) and less functionalized are formed. This is the monomer-deficient region, where the monomer concentration is low and the ablation process dominates, leading to a decrease of the deposition rate. Usually the polymerization is carried out in the first region of Figure 10.

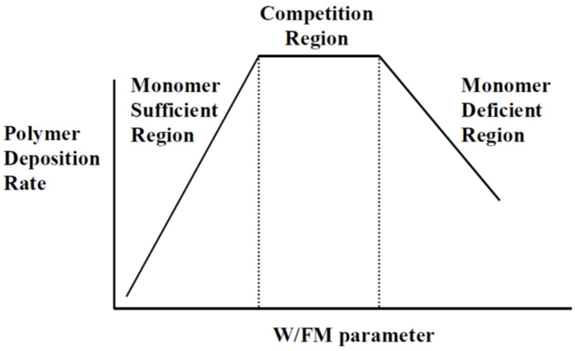

Figure 10. *Domain of plasma-polymer deposition.*[59]

2.3.2. Applications of plasma-polymers

At the present, plasma-deposited polymers find application in a multitude of fields, such as medicine,[60,61] bio-engineering,[61] material science,[58] just to name a few. Two are the main goals of using plasma polymerization in these topics: 1) modification of the surface properties of a given substrate, and 2) obtainment of specific bulk properties of the plasma-polymer films.

A major portion of the research of biomaterials concerns the regulation of the biomolecule-surface interactions, without compromising the substrate bulk properties. This is achieved, for instance, by deposition of thin layers of selected plasma-polymers on those substrates. A typical example is given by the absorption of proteins,[61] which mainly depends on the wettability and the charge density of the target surface. It was demonstrated that a careful control of the conditions of plasma deposition permits to alter the surface in such a way that the protein absorption is favored or, conversely, is significantly reduced (anti-fouling). In that respect, a well-established procedure for the preparation of biologically non-fouling surfaces consists in utilizing a wide range of glycol monomers to synthesize PEO-like coatings.[61] For instance, Nisol and collaborators developed two methods of deposition of such coatings at atmospheric pressure, where tetra (ethylene glycol) dimethyl ether (tetraglyme) is injected, as a liquid or as a vapor, into the post-discharge of an RF torch.[62] The choice of the plasma parameters permits to tailor the surface by varying the density of ethylene oxide groups in the deposited film. On the other hand, the high retention of reactive functional groups, mostly achieved under pulsed polymerization,[63] is the key for the chemisorption of target molecules via derivatization reactions. This approach has been widely employed.[64] In particular, Timmons and Wang[65] patented a method of molecular tailoring of surfaces based on the plasma deposition of brominated films, that successively are involved in reactions of nucleophilic displacement with amino acids or peptides, permitting to the latter to covalently attach the surface.

Non-biologically fouling and non-wettability applications can be expected from plasma-synthesized (super-)hydrophobic surfaces (water contact angles ranging from 105° to 130°). An example is provided by the work carried out by Qiu,[66] who employed saturated perfluoroalkane precursors to prepare polymer films with water contact angles >170°, and surface energies as low as 1.5 mN/m. A second example is given by Hubert et al.,[67] who compared three different methods to produce super-hydrophobic surfaces and/or to enhance their hydrophobicity. One of the approaches consists in the plasma deposition of fluorinated coatings by a DBD at (near) atmospheric pressure, from perfluoro-2-methyl-2-pentene (C_6F_{12}) and perfluorohexane (C_6F_{14}). In all the applied methods, the nature of the plasma gas appears to be a crucial parameter for the desired property.

Super-hydrophobic poly (tetrafluoro ethylene)-like thin films were also prepared by Henry and co-workers by using a plasma-based hybrid process, that consists in sputtering a carbon target in an Ar/CF_4 atmosphere.[68] Another application of the plasma polymerization, as mean of surface modification, concerns the preparation of thin polymer layer adhesives. In this case, it is worth mentioning the study conducted by Tarducci et al.,[69] who demonstrated the possibility of strong adhesion between two surfaces containing epoxide groups (deposited by pulsed plasma onto two solid supports) after application of a drop of diamine dissolved in dioxane, followed by annealing.

As mentioned at the beginning of this section, some applications of the synthesis of plasma-polymers capitalize on their bulk properties, rather than on the surface modification. This is the case, for instance, of the preparation of electrically conductive polymers. A number of heteroaromatic precursors are known to provide such materials by conventional polymerization (high electrical conductivity of ~10 S/m), like e.g. pyrrole, thiophene, and aniline. However, several studies pointed out the feasibility to prepare conductive polymers by pulsed plasmas. In this respect, Qiu and collaborators[70] demonstrated the possibility to polymerize the pyrrole in films with a long-term electrical conductivity, that is ascribed to the higher retention of the rings, and consequently a more linear and polyconjugated structure. In this context, another example is given by the synthesis of polypropylene (PP)-g-sulfonated polystyrene (SPS) composite electrolyte membranes for direct fuel cells.[71] Their preparation is conducted by grafting PS on microporous PP membranes by means of plasma polymerization, and successive sulfonation reaction. The ion conductivity and methanol permeability of these membranes were tested as a function of the grafting reaction time. A two-steps atmospheric plasma process was developed by Merche et al. to build membrane-catalyst-electrode assemblies for fuel cell applications (refer to §2.4.5.2 for the SIMS characterization of the assembly).[72] First, a Pt colloidal solution (i.e. the catalyst) is sprayed into the post-discharge of an RF atmospheric plasma torch on gas diffusion layers and on glassy carbon (model material for the SIMS depth-profiling). Then, a plasma-deposited sulfonated PS layer is synthesized by means of a DBD near atmospheric pressure, by co-injection of styrene and trifluoromethane sulfonic acid as precursors. This polymer-based coating plays the role of an ion-exchange membrane in miniaturized fuel cells using H_2 and CH_3OH. In addition, multilayer polymer coatings are synthesized by plasma e.g. for Al protection purposes, as proposed by Khelifa and collaborators.[73] In this particular assembly, the first layer is a hexamethyldisiloxane-based plasma-polymer film, while the second one is obtained via the polymerization of the 2-ethylhexyl acrylate monomer (initiated from the free radicals trapped on the surface of the plasma-polymer during its growth). Then, a copolymer of 2-ethylhexyl acrylate and glycidyl methacrylate, poly(EHA-co-GMA), is deposited by spin-coating to increase the corrosion resistance of the coating. A 3-fold improvement in the anti-corrosion properties compared to the uncoated Al substrate is observed for this multilayer system.

2.3.3. Review of literature related to the plasma polymerization of styrene

An extensive body of studies was conducted on the plasma polymerization of the styrene monomer at low pressure conditions since the 1960s, spanning a variety of different plasma sources (pulsed and not, high frequency, radio-frequency, microwaves), reactor geometries, and carrier gases (even in absence of them).[74,75,76] This section will present exclusively a few selected works of the last two decades.

In 1995, Chen and co-workers investigated an RF styrene plasma (low pressure and absence of carrier gas) by means of optical emission spectroscopy (OES).[77] Correlations among the emission intensities of CH and $C_4H_2^+$ species, the polymer deposition rate, and the polymeric structure of the deposited films were found out. For instance, with increasing distance between the substrate position and the lower electrode, the deposition rate and the aromaticity, both at the polymer surface and in the bulk, decrease (the latter being determined by XPS and IR, respectively). In 1998, the same team reported a work on the plasma polymerization of the styrene monomer with controlled particle energy. To this purpose Chen et al. developed a discharge reactor divided in two parts: RF glow discharge in the upper part, and polymer deposition in the lower part.[78] The two sections were separated by a screen grid unit, that served to control the energy of the extracted ions and electrons from the upper part thanks to the application of a grid voltage. The resultant films were characterized by IR and XPS. The results indicate a significant influence of the polarity and magnitude of the grid bias voltage on the deposition rate and structural features of the polymer films. The aromaticity of the plasma films is better preserved when positive bias voltages are applied.

In the 2000s, the German research team of Unger focused on the study of different plasma polymerization processes (e.g. asymmetrical pulsed RF plasmas) and different monomers, such as styrene, acetylene, ethylene, butadiene, among others.[79,80,81,82] Generally, a multi method approach (XPS, near edge X-ray absorption fine structure or NEXAFS, and FT-IR) was applied for a comprehensive chemical characterization of the plasma deposits. Among all the precursors investigated in the pulsed plasma processes, only the styrene monomer provides films with spectral features strongly similar to the conventional PS.[79] Oran et al. published in 2004 a ToF-SSIMS study of pulsed plasma-deposited styrene films before and after exposure to air (refer to §2.4.5.1).[81] Correlations between the chemical structure of the polymer deposits (aromaticity, unsaturation, cross-linked and/or branched contents) and the external plasma parameters, i.e. power, duty cycle and pressure, are determined. The O-incorporation taking place after exposure to the atmosphere is related to the irregularity degree of the polymer obtained.[82] Additionally, in the range of deposition conditions applied, the fragmentation of the precursor constitutes a minor process, being the radical chain propagation the prevalent one.[81]

Haïdopoulos et al. (2006) compared the chemical and morphological properties of plasma films produced on stainless steel substrates from the styrene monomer in capacitively (pPS_{capa}) and inductively (pPS_{ind}) coupled reactors, respectively.[83] Additionally, the ageing effect was studied after 15 min and 1 week. Different analytical techniques were employed in the investigation, including FT-IR, XPS, ToF-SIMS (surface analysis), WCA, AFM, and SEM (scanning electron microscopy). pPS_{capa} and pPS_{ind} aged in air for 15 min show similar wettability, surface chemical composition, and bulk chemical structure. ToF-SIMS analyses of the polymer surfaces (sampling depth of 1-3 nm) point out a strong intensity increase of the monomer signal ($m/z = 105$), in addition to the increased counting rate, with respect to the reference conventional PS. This is interpreted by the high presence of oligomers at the surface of the plasma films. The two kinds of plasma-polymers only differed by their microstructure. The ageing over an entire week leads to no modifications of such a microstructure and bulk chemical structure. The exposure to the air induces oxidation of the surface with an estimated depth < 3 nm, and more pronounced in the pPS_{capa} films. More recently, Haïdopoulos et al. investigated the influences of external plasma parameters (power, pressure and deposition time) and the effects of the nature and topography of the substrates (stainless steel, gold and glass) on the morphology of inductively plasma-deposited styrene films, by using SEM and AFM.[84] Additional work was performed by Li et al. in 2015 to further characterize the chemical composition of the pulsed plasma-polymerized styrene films by FTIR and XPS, depending on the external plasma parameters.[85] Diagnostics of the gas phase by OES were also performed to find a correlation between the plasma gas and the character of the deposited films.

Several studies proposed the use of Ar as carrier gas for the plasma polymerization of the styrene monomer, in order to increase the cross-linked degree of the resulting film.[2] However, a certain amount of work explored the possibility of using other carrier gases[86] or gas mixtures. In that respect, Kim and collaborators investigated the effects on the chemical structure of the plasma-deposited styrene when a reactive gas, precisely CH_4, was mixed to the Ar gas.[87] The mixture ratio was varied, resulting in an increase of the deposition rate and diminution of the cross-linking degree when increasing CH_4 content in the mixture gas. This study assesses the feasibility to improve the retention degree of the precursor functional groups by simply adding a reactive gas to the argon.

Another branch of research focused on the polymerization of the styrene using plasmas near atmospheric conditions, which are currently very convenient for industrial applications.[2] Nevertheless, the development of technologies for the plasma deposition of polymers at atmospheric pressure occurred much more recently compared to those working at low pressure. Consequently, only a few works concerning plasma-polymerized styrene can be mentioned in this domain.

Kurosawa and collaborators developed a novel fabrication method based on microplasma polymerization for the localized synthesis of polymer films onto a substrate at atmospheric pressure, without employing masks.[88,89] Potential applications of their work were chemical and bio-sensors. Micro-discharges were originated by a micro-plasma jet operating at very high frequency (438 MHz) inside a quartz capillary. The styrene monomer was used as model precursor, and supplied with He (or Ar) carrier gas. The investigation of the effects of the microplasma polymerization was carried out by varying the experimental conditions and comparing the resulting films with those obtained from the conventional method (plasma polymerization in 100 Pa, 13.56 MHz).[90] FT-IR, EDX (energy dispersive X-ray spectrometry), WCA were employed for the characterization of the plasma films, as well as quartz crystal microbalance (QCM) for the estimation of the deposition rates.[90]

In 2009, two different works were published on the plasma polymerization of styrene by a DBD device. The first was carried out by Topala et al. at atmospheric pressure, and in presence of He as carrier gas.[91]

Aim of this study was the synthesis of stable hydrophobic coatings of plasma-deposited styrene onto silicon and glass substrates. Water contact angles >130° are achieved, being significantly higher than those characteristic of the conventional PS (~90°). The discharge current parameters, i.e. voltage waveform, inter-electrode distance, and gas flow rates, are optimized. Voltage waveform (ramp wave or sin wave) and its rise time are found to have more influence, than the gap and the He flow rate, on the maximum of the discharge current. The second investigation was conducted by Merche and collaborators.[34] The goal of the work was to prepare and characterize plasma-deposited PS films, obtained from the styrene monomer, by an HF homemade DBD system, and in the post-discharge of a commercial atmospheric RF plasma torch. For the DBD, two carrier gases were utilized, Ar and He; while in the second device only Ar was employed. In addition, the polymer was deposited onto a variety of substrates: PTFE (polytetrafluoroethylene), HDPE, stainless steel, glass and silicon wafers. The characterization of the films was performed by XPS, FT-IR, SSIMS, WCA, and optical microscopy. The plasma phase was investigated by OES. XPS, FT-IR and SIMS point out the retention of a series of characteristic features of the conventional PS. However, some differences are evidenced: i) the films are oxidized, and the O-uptake is more pronounced in those synthesized with the plasma torch (atmosphere less controlled); ii) they are branched and/or cross-linked, and unsaturated with respect to the native PS. Furthermore, FT-IR and SSIMS analyses show higher degrees of unsaturation, branching, and cross-linking, as well as lower aromatic contents in the plasma films obtained using Ar than He (both in DBD and torch). The optical microscopy shows a worm-like structure (closely interconnected), compatible with the cross-linked character of these plasma-polymers.

2.4. SIMS characterization of plasma-treated and plasma-deposited polymers

2.4.1. Fundamental of SIMS

Secondary ion mass spectrometry (SIMS) is a solid surface analysis technique. It is based on the mass analysis of secondary ionized species coming from the sample surface, which is bombarded by a primary ion beam having an energy in 1-100 keV range.[92,93] The fraction of ionized species, emitted consequently to the ion-surface interaction, is typically <1%. The analysis of these secondary ions provides information about the chemical composition, elemental and molecular, of the outermost layers of the specimen. This information can be resolved both spatially, by using focused ion beams, and in-depth, when the erosion of the sample is promoted by the use of sufficiently high beam currents to expose the inner layers. A variant of SIMS is the “sputtered neutral mass spectrometry” (SNMS), based on the post-ionization of the sputtered neutral species in the gaseous phase by irradiation with photons, electrons or exposure to plasma.

When the sample surface is hit by an ion beam, the ions penetrate the solid, generating sequences of atomic collision events. Energy transfer by electronic processes play a minor role in the typical SIMS experimental conditions. Hence, the primary ions gradually lose their energy till they implant at a certain average depth. The projected range of the ion, or penetration depth along the incidence direction, is directly proportional to the initial kinetic energy and it decreases with increasing the ion mass (for atomic ions). Other important parameters are the incidence angle and the nature of the material, where density is fundamental. In the solid sample, the collision of atomic and small cluster projectiles with the target atoms triggers a collision cascade, as shown in **Figure 11**. Thanks to the collision cascade, target atoms sufficiently close to the air-solid interface and with energy exceeding the surface binding energy, can be ejected from the material, a process known as sputtering. The sampling depth of SIMS depends on the sputtering conditions (primary ion nature, energy, target properties). Generally, the mean free path of neutral or ionized atoms moved by the collision process is of the order of magnitude of a few interatomic distances. Thus, the secondary ions derive from the topmost layers of the sample.

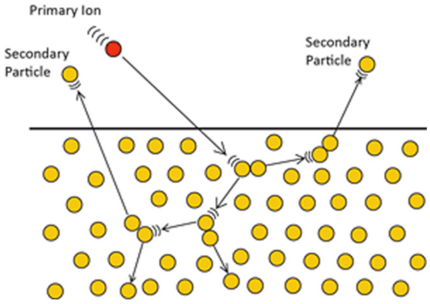

Figure 11. *Collision cascade and sputtering process (adapted image)*[94].

The SIMS technique is intrinsically destructive. However, in the early 1970s Benninghoven and his team in Münster developed the concept of "static-SIMS" (SSIMS) as an important tool for the study of surfaces.[95] The experimentally observed exponential decrease of the SIMS molecular signals as a function of fluence can be expressed as $I = I_0 \exp(-F \cdot \sigma)$, where F is the ion fluence (ions/cm^2) and σ (cm^2) is the damaged cross-section, i.e. the average size of the surface modified by a single ion impact. It was found that $\sigma = 10^{-13}$-10^{-14} cm^2 (in the case of amino acids deposited on metal supports[96]) with a fluence at least 100 times lower than $1/\sigma$, the degradation of the molecular signals can be considered as negligible, so that operating in that range of fluence was called "static SIMS" analysis. Statistically, in the static SIMS regime, a large majority of the primary ions hit an undisturbed surface region.[97] The SSIMS mode was employed to characterize both inorganic and organic materials, in particular polymers.[98,99,100,101,102,103] Indeed, the static conditions avoid the accumulation of chemical damage in the organics due to the degradation reactions triggered by the interaction with the ion projectile, that alter the original molecular information. In contrast, "dynamic-SIMS" applies to primary ion fluences much higher than the static limit of 10^{12} ions/cm^2 in order to perform erosion of the sample (depth-profiling). Then, the signal intensities of the emitted species are followed as a function of time, or equivalently, of depth. However, the depth-profiling of polymer-based materials with the traditional monoatomic primary ions (e.g. a few keV Ar^+) is limited by the cumulative effects of the chemical damage, that cannot be neglected any longer like in SSIMS. This leads to the loss of the molecular ions, so that only the elemental information is kept.

From the instrumental point of view, time-of-flight type mass analyzers (ToF) appear to be the most suitable to perform SSIMS, thanks to their parallel acquisition and their high transmission. Currently, the development of particular expedients to conduct depth-profiling, i.e. the "dual ion beam" mode (refer to §3.1.6), allows the ToF-SIMS to be also competitive in the field of the dynamic-SIMS with instrumentation using continuous beams with magnetic sector analyzer or, to a minor extent, quadrupole analyzers.[104]

2.4.2. Operating modes of SIMS

The analytical capabilities of ToF-SIMS[105] include: A) surface mass spectrometry, B) 2D imaging, C) depth-profiling, and D) 3D analysis by combination of the imaging and depth-profiling modes. They will be briefly introduced in this section, in addition to the retrospective analysis of the ToF-SIMS raw data (point E).

A. Surface mass spectrometry

Molecular surface analysis is permitted under static conditions. Elemental and molecular information concerning the outermost sample layers are obtained with a series of benefits: i) high sensitivity in the range of the ppm/ppb, thus the detection of material contamination and trace elements is feasible; ii) high resolving power (M/ΔM) up to 10000 for m/z 28 (so that the mass contributions $^{28}Si^+$, CO^+, CH_2N^+ and $C_2H_4^+$ can be discriminated); iii) large mass range up to 10000 amu, where molecular compounds can be detected and identified; iv) high isotope sensitivity and selectivity, both as element ions and in molecular fragments and parent ions.

B. Imaging

Imaging is performed in the microprobe mode with ION.TOF instruments such as the one used in this thesis (see §3.1). This operating mode consists in rastering a highly focused ion beam (for instance Bi_3^{++}) onto a given area in order to obtain chemical maps (see **Figure 12.a**). A ToF-SIMS image is a 2D intensity distribution map of a selected secondary ion or a sum of secondary ions, as shown in **Figure 12.b**.

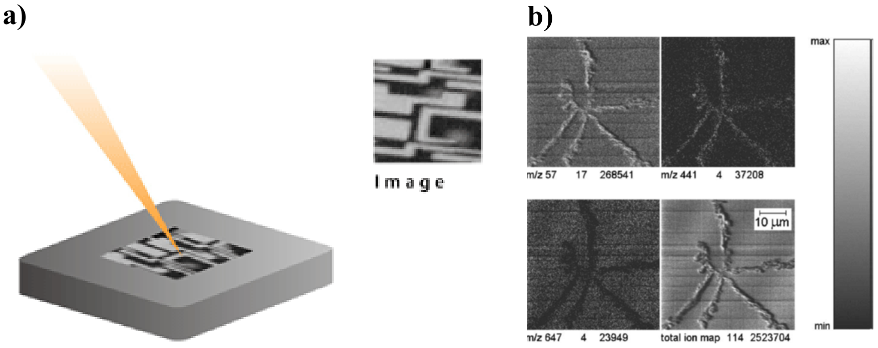

Figure 12. *Imaging in microprobe mode (a),*[105] *and ToF-SIMS mass resolved images of an Irgafos 168 crystal on an additive covered PETI*[iv] *surface (b).*[106]

Characteristic features of the ToF-SIMS imaging mode are high lateral resolution (below 60 nm), and field of view ranging from μm^2 to cm^2.[105]

[iv] PETI: Poly (ethylene terephthalate-ethylene isophthalate) copolymer.

However, a drawback consists in the image shift when the operator changes from positive to negative ion polarities. Therefore, it is difficult to collect positive and negative ion data from the exact same area.

C. Depth-profiling

In ToF-SIMS, the most efficient protocol to perform depth-profiling consists in the use of two distinct keV ion beams (refer to §3.1.6 for the "dual beam" mode, as well as the "single beam" mode). The "dual beam" mode is illustrated in **Figure 13**. The first beam is used with a very low current (typically 1 pA) to analyze the bottom of the crater (analysis beam). The most popular analysis beams are micro-focused Ar^+, Ga^+, Cs^+, Au_n^+, and Bi_n^+ ion beams. The second beam is used with relatively high current (1-10 nA) to erode the sample, and it is called sputter beam. Current sputter sources either use monoatomic (e.g. Ar^+ and Cs^+ beams), polyatomic (like C_{60}^+ beams), or massive cluster ion beams.

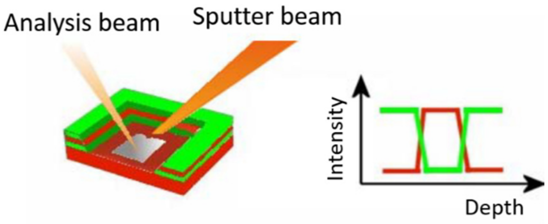

Figure 13. *Depth-profiling experiment carried out in "dual ion beam" mode.*

D. 3D analysis

Reconstruction of the 3D structure of a sample is possible by combining the information derived from the mass spectra, imaging, and depth-profiling.

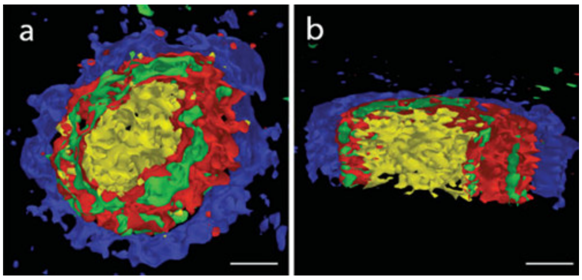

Figure 14. *3D image of a high pressure frozen, freeze-fractured, and freeze-dried thyroid tumor cells (Na^+ is shown in blue, K^+ in green, m/z = 86 in yellow, and the phosphocholine headgroup $C_5H_{15}PNO_4^+$ at m/z = 184 in red).*[107]

This constitutes an ideal analytical tool for the investigation of complex biological systems, like for instance tumor cells (3D image shown in **Figure 14**).

E. Retrospective analysis

The ToF-SIMS instrumentation is equipped with a powerful software for the control of the system and the data analysis. As shown in **Figure 15**, for each voxel analyzed (volume element of coordinates x, y, z) and for each primary ion pulse a complete mass spectrum is recorded (time of flight and intensity of the detected secondary ions). At the end of the measurement, the software is able to process the resulting 3D or 4D data matrix from mapping or depth-profiling, respectively, to give a series of possibilities: the total spectrum reconstruction by summing all individual spectra; the spectrum of a certain surface zone (region of interest) by summing punctual spectra of the investigated area; the surface intensity distribution maps for selected masses (SIMS imaging); the in-depth intensity distribution maps for selected masses (SIMS depth-profiling); the in-depth intensity distribution maps for a selected area; the 3D image of the investigated material.

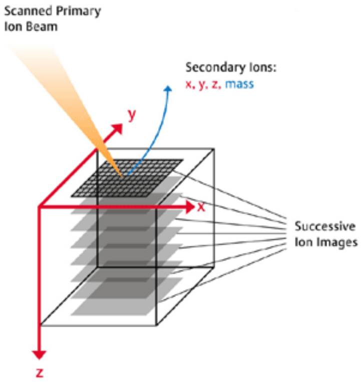

Figure 15. *Retrospective analysis.*[105]

2.4.3. Cluster-SIMS for molecular depth-profiling of polymers

For a long time, the application of SIMS depth-profiling to organic systems was strongly limited by the low secondary ion yields and the extensive alteration of the chemical structure of the material induced by the interaction with keV primary ions (usually monoatomic or biatomic). The advent of polyatomic primary ion beams as sputter sources (cluster-SIMS)[108], such as C_{60}^+, Au_3^+, SF_5^+, Bi_3^+ and more recently massive argon clusters Ar_n^+ (from hundreds to thousands Ar atoms, n), finally opens the possibility of molecular depth-profiling of organic/polymer systems. The main benefits of the use of cluster ion sources with respect to the traditional atomic ion beams were found out for the first time in the early 1960s by the observation of a non-linear increase of the sputter yield.[109] However, in the mid-1980s polyatomic ion sources started to be sporadically employed in the SIMS surface investigation of organics. In 1987, Appelhans and Delmore used SF_6 beams for the characterization of PMMA, PET and PTFE, finding secondary ion yields 3-4 times higher compared to those obtained when employing atomic ion beams of equivalent energy.[110] In 1998, Gillen and Roberson reported the first example of molecular depth-profiling on PMMA with SF_5^+ projectiles.[111] From then on an impressive amount of contributions were focused on the cluster-SIMS investigation of organic and polymer-based specimens.[108]

Several studies of molecular dynamics (MD) simulations have been conducted in order to elucidate the erosion mechanism of organic molecules, and in particular polymers, with monoatomic and polyatomic primary ions.[112,113,114] In this respect, an interesting study was conducted by Delcorte and Garrison in 2007, which shows the comparison of the collision cascades generated by 5 keV C_{60}^+ versus 5 keV Ar^+ primary projectiles on a tetrameric PS sample.[115] **Figure 16** demonstrates a deeper penetration of the Ar^+ compared to the C_{60}^+, consequently the damaged layer is thicker in the first case. On the other hand, the energy deposited by the fullerene projectile is nearer to the surface (around 2-nm depth), explaining an increase of the sputter yield.

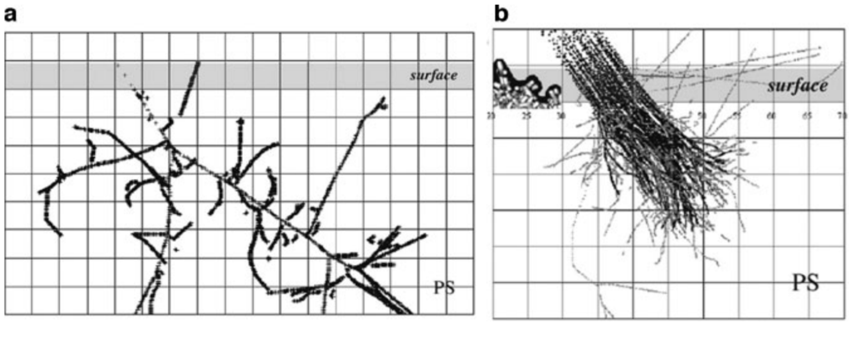

Figure 16. *Collision cascades in a polystyrene tetramer sample induced by 5 keV Ar^+ bombardment (a), and 5 keV C_{60}^+ bombardment (b). The successive positions of the projectile and recoil atoms with more than 10 eV of kinetic energy are represented as a function of time up to 200 fs. Each square of the grid is 5 x 5 A^2. Adapted from reference [115].*

An important model of the erosion produced by ionic bombardment was proposed by Gillen and collaborators in 1990,[116] and later refined by Cheng et al. in 2006[117] and Wucher in 2008[118]. The model is shown in **Figure 17**.

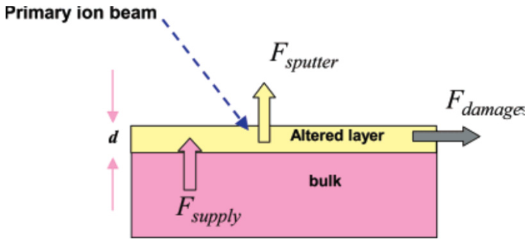

Figure 17. *Schematic diagram of the erosion model.*[117]

F_{supply} represents the entering intact molecular flow, while $F_{sputter}$ is the exiting molecular flow (composed of intact molecules and fragments). On the other hand, F_{damage} represents the sample damage, in terms of bond breaking and cross-linking, with *d* being the damaged depth of the material. According to this model, molecular depth-profiling can be performed in a steady state condition, if $F_{sputter}$ equals F_{supply}, so that the damage is removed before starting to accumulate. In other words, the probed thickness of the material should be equal to the damaged one, so that the uncovered surface can preserve the original molecular information. This condition is verified with the advent of cluster-SIMS. When bombarding a surface with polyatomic ions C_n^+, such as for instance C_{60}^+, they split into *n* constituent atoms possessing a fraction of the initial kinetic energy *E*. Thus, the penetration depth of the constituent atoms is lower compared to that of monoatomic primary ions, and consequently collision cascades and related chemical damage are more confined near the surface (decrease of $F_{altered}$, see Figure 16). Furthermore, conversely to monoatomic ion bombardment, which gives stochastic collision cascade events, polyatomic projectiles determine collective processes.[114] Thus, a non-linear increase of the sputter yield (higher than the total sputter yield of $n{\cdot}C^+$ projectiles with energy *E/n*) is observed in the latter case, leading to a more effective removal of the damage (increase of $F_{sputter}$). Thanks to the combination of these two aspects, the cluster-SIMS constitutes a powerful tool for the molecular depth-profiling of organics and polymer materials without the rapid signal decay typically observed when the static limit is exceeded during ion bombardment (see **Figure 18** for the cases of unsuccessful and successful organic depth-profiling). The profilability of several polymers (such as PMMA, PPG, PEG)[v] has been tested. However, other polymer materials, like PS, PE and PC,[vi] rapidly lose their molecular information during depth-profiling experiments with SF_5^+ and C_{60}^+ ion sputtering.[108] This can be explained by the fact that the chemistry of the material and the projectile plays a fundamental role in the degradation mechanism induced by the ion bombardment.

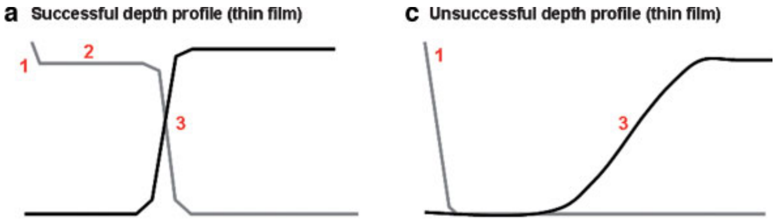

Figure 18. *Limit situations in molecular depth-profiling of thin polymer films. Three different regions can be discriminated in a successful depth-profile: 1) initial drop in signal intensity often defined by the disappearance cross section of the material,[117] 2) a steady state region, and 3) interfacial region. Adapted from reference [108].*

Indeed, ion irradiation of polymers induces the formation of radicals, and as a consequence different competitive degradation mechanisms can take place. Two distinct categories of polymers can be defined as a function of their radiochemical behavior (so also upon ion bombardment), i.e. type I and type II polymers.[119] Type I polymers undergo prevalently cross-linking. They are usually polymers like polyolefins (with low branching degree) or possessing a certain aromatic content (e.g. PS). The presence of aromatic rings leads to the stabilization by resonance of the charges created upon irradiation, so that the molecular structure tends to be preserved, and radical recombination is promoted. Other degradation processes determine the formation of double bonds and cyclization (thus, an increase of the unsaturation degree). All these reactions, leading in the extreme case to an amorphous carbon material, prevent the preservation of the molecular information along the depth. On the contrary, processes of main chain scission and unzipping (or depolymerization) are predominant in type II polymers. Some examples are given by PMMA, PIB[vii], and other polymers highly branched or containing

---

[v] PMMA: Poly (methyl methacrylate); PPG: poly (propylene glycol); PEG: poly (ethylene glycol)

[vi] PS: Polystyrene; PE: Polyethylene; PC: polycarbonate

[vii] PIB: Polyisobutylene

potential breaking points along the backbone (such as ether or carbonyl groups). In these cases, the degradation mechanism produces small volatile fragments, that favor further the erosion process produced by the impinging primary ions.

The radical nature of the degradation processes occurring upon ion bombardment has been evidenced by Licciardello and his team.[120,121,122,123] They performed NO-dosing (nitric oxide) during C_{60}-organic depth-profiling of challenging type I polymers (such as for instance PS).[124] It was demonstrated that the profilability of these polymers is feasible only if the radical recombination resulting in the cross-linking process is inhibited by a radical scavenger like the NO[125]. The possibility to influence the ion-beam triggered reactions during polymer depth-profiling was also pointed out in different experimental conditions. Indeed, Houssiau and co-workers performed molecular depth-profiling of polymers, namely PC, PS, PMMA and PET[viii], by using ultra-low energy Cs^+ ions (250 eV).[126,127,128,129,130] In positive ion polarity, the emission of characteristic ions MCs_n^+ is observed (M is a polymer fragment), whereas in negative ion mode, the analogues M^- ions are obtained. The success of ultra-low energy Cs^+ sputtering of type I polymers is due to: 1) the low energy of the primary ion (similarly to the case of polyatomic ions in the cluster-SIMS), combined to its high mass, determines the deposition of high energy density near the surface; 2) the charge-exchange between the alkaline metal and the polymer fragments provokes an augmentation of probability of formation of M^- ions (or MCs^+ ions), increasing the detection of the non-damaged fraction of the material; 3) in the case of type I polymers like PS, radicals produced by the ion bombardment react with the implanted Cs atoms, leading to the formation of stable anions or R-Cs species and consequently inhibiting the cross-linking.[129] The latter mechanism can be assimilated to that of the NO gas dosing.

Massive cluster beams were introduced in organic surface analyses in the 1990s. Mahoney and collaborators utilized massive supersonic water/glycerol clusters with energy less than 1 eV/nucleon to produce secondary ion mass spectra of peptides.[131] Beuhler and Friedman were conducting studies of sputtering of carbon, gold, and copper surfaces with smaller 240 keV water ion clusters,[132] when Yamada was developing Ar cluster ion beams for inorganic materials modification and smoothing at Kyoto University.[133] The application of the gas ion beam clusters (GCIB)

[viii] PET: Poly (ethylene terephthalate)

technology[134] in SIMS sputtering represented a great progress for the molecular depth-profiling of organics, and especially type I polymer thin films. The most commonly used GCIB are constituted by hundreds to thousands of argon atoms. Their preparation consists in a two-steps process: the isolated atoms in the gas phase collapse in neutral clusters by effect of the cooling in a supersonic expansion, then they are ionized by electron impact, and accelerated (refer to §3.1.2). In order to explain the success of large Ar cluster ion sputtering of organic/polymer surfaces, theoretical studies using MD simulations were conducted in several research groups.[135,136,137] The main difference with smaller polyatomic projectiles (like the fullerene) is that massive Ar ion clusters fragment into a far greater number of atoms. The energy of the constituent atoms is only a few eV, and this value is close to the chemical bond breaking energy (e.g. C-H: 3.3, C-C: 6.3, C=C: 7.6, C≡C: 10.0, C=O: 11.2)[138]. These atoms transfer their energy to the topmost layers of the target with limited bond breaking, inducing a much limited damaged layer and the emission of larger number of molecules via collective emission mechanisms.[139]

In 2008 Hashinokuchi and co-workers carried out molecular depth-profiling of PMMA by using large 5 keV Ar clusters with average cluster sizes of 700, 1000 and 1350 atoms/ion.[140] An increase of the secondary ion yields of high m/z ion fragments (such as 125, 300, 500, 800 amu) compared with the monoatomic Ar sputtering was observed. Moreover, these yields increase with increasing cluster size. Indeed, an important feature of GCIB with respect to the cluster predecessors is that energy E and/or cluster size n (thus E/n) can be tuned to find the optimal etching conditions. A significant amount of fundamental studies has taken advantage of that opportunity. In 2009, Moritani et al. demonstrated the feasibility to induce the fragmentation of PS in specific sites of the polymer chain, tuning the energy per atom of the Ar cluster ions by simple selection of the size of the projectiles.[141] For instance, fragment ions from the aliphatic backbone are emitted above an E_{atom} threshold of ~3 eV, while the fragmentation of the phenyl rings takes place at values >5 eV. Using GCIB, Ninomiya et al. reported high quality molecular depth-profiles from PMMA, but also PS and PC, not profilable with the traditional C_{60}^+ or SF_5^+ primary ions.[142] In 2013, Rading and co-workers compared potentials and limitations of C_{60} and massive Ar cluster sputtering in the molecular depth-profiling of polymer materials (PS, PMMA, and PC).[143] To this purpose, ion beams with varying energy per atom were employed (between 2 and 10 eV/atom in the case of Ar_n^+, 167 and 667 eV/atom for the C_{60}^+). In the context of this study, a linear relation was found between sputter yield volume and energy per atom. Furthermore, the sputter yield increased with increasing cluster size at a given energy/atom, whereas keeping the beam energy constant, the yield decreased with increasing cluster size. In 2013, Seah published an empirical equation for the Ar gas cluster sputtering yields (Y) of inorganic and organic materials as a function of the beam energy, E, and the cluster size, n.[144] For inorganic materials, such as Si, Au and SiO_2, the universal equation is expressed as follows: $Y/n = (E/An)^q/[1 + (E/An)^{q-1}]$, where the parameters A and q are obtained by fitting. In the case of organic materials, like PS, PC and PMMA (data provided by Rading et al., 2013),[143] an extra parameter B is included, whose physical meaning is discussed in the paper. The equation also shows that the sputtering effect are linearly additive (linearity above a certain threshold), i.e. doubling n at constant E/n doubles the sputter yield. In 2015, Seah analyzed the effect of the polymer molecular weight (M_w) on the fitting parameter A, based on the data of sputter yields of PS and PMMA as a function of M_w reported in this thesis.[145] The angle dependence of the universal equation for argon gas cluster sputtering yields was also analyzed by Seah and collaborators in 2015, permitting to clarify some discrepancies between sputter yield data estimated by experiments and MD simulations.[146] The angle dependence was also predicted by MD simulations for small organic molecules[147] and polymers.[148]

The extended body of work performed with GCIB sputtering over almost two decades suggests that massive Ar cluster ions fully overcome the limitations of C_{60}^+ projectiles in the polymer depth-profiling. However, it is worth noticing that the sputtering yield on inorganics is almost null.[144] At the moment, this represents the most important limit to the more universal application of GCIB to the depth-profiling of inorganic and hybrid materials (for instance, multilayer structure where organic layers alternate inorganic ones).

2.4.4. Principal component analysis for SIMS data treatment

Principal component analysis (PCA) is the most commonly used method of multivariate analysis (MVA) in the processing of ToF-SIMS data.[149] PCA was formulated in 1901 by K. Pearson, and further developed to its present stage by H. Hotelling in 1933.[150] Since then, the utility of PCA has been gradually discovered in many scientific fields, such as electric engineering, image analysis, chemistry, and geology.[150] The main goal of PCA consists in the feature reduction, i.e. reducing a large number of variables (representing specific features of the phenomenon under study) in a few latent variables.

A general introduction to the PCA is given by Jackson (1980),[151] Wold (1987),[150] and more recently by Bro and Smilde (2014)[152]. PCA is a multivariate analysis that looks at the overall variance within a data set. In the simplest case of the data processing of ToF-SIMS mass spectra (in positive or negative ion polarity), the data set is represented by a matrix where the rows contain the samples (objects), while the columns represent the selected SIMS peaks (variables), so that each cell is given by the ion intensity. Thus, PCA consists in the application of the covariance matrix of the ToF-SIMS data set. It generates three new matrices containing the scores, the loadings, and the residuals.[150] However, PCA can also be explained graphically, as shown in **Figure 19**.

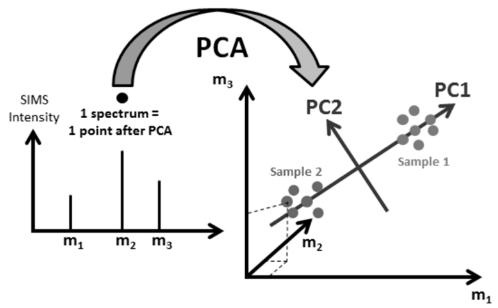

Figure 19. *Graphical representation of PCA applied to a SIMS spectrum (adapted from Henry's Ph.D. thesis[153])[154].*

A single ToF-SIMS mass spectrum, containing from hundreds to thousands peaks *y* (especially in the case of high resolution mass spectra and/or isotopic labelling) can be represented in a hyperspace of *y* dimensions (m_1, m_2, m_3…, m_y in Figure 19). Thus, for a data set of *x* samples (sample 1 and 2 in Figure 19), where each one is represented by several mass spectra containing *y* peaks, each spectrum can be represented by a point in a hyperspace of *y* dimensions.[ix] PCA is geometrically an axis rotation that alligns the new set of axes, called principal components (PCs), with the maximal direction of variance within the data set.[149] In other words, a new hyperspace is found with *n* dimensions ($n < y$), which describes the most of the variations of the

---

[ix] Since PCA is a statistically based method, in SIMS it is recommended to collect at least from 3 to 5 mass spectra per sample across at least 2 samples for homegeneuous surfaces in order to retrieve relevant results.

data set.[155] Generally, only the first few PCs collect variance with physical meanings and PCs of higher rank contain more and more noise.[152] The original data points are described by their projections onto the PCs, which correspond to the scores. The scores plots show the separation (in terms of spreading and clustering) of the samples (or their mass spectra).[149] The loadings correspond to the direction cosines between the new n axes (PCs) and the initial y axes.[156] The loadings plots provide the contribution of the SIMS fragment ions to the separation observed in the corresponding scores plot (related to the same PC). Additionally, there is a positive correlation between loadings and scores of the same mathematical sign, and vice versa. In simpler terms, a SIMS ion associated to a high value of positive loading presents higher relative intensity in the mass spectra related to the samples showing positive scores, and lower relative intensity for those with negative scores.

The input data matrix for PCA needs a series of pre-processing, i.e. normalization, mean centering, scaling and transformation.[149] The peak selection, done in different ways (mass binning,[157] automated or manual selection), can be considered as the first crucial data pre-processing step. Indeed, each data pre-processing procedure implies specific assumptions, which are critical in determining the physical relevance of the PCA output.[158,159] The aim of the data pre-treatment is the removal of the variance not due to chemical differences between the samples. Thus, the normalization permits to eliminate variance in the data that, for instance, is produced by the sample charging and/or instrumental conditions. The normalization consists in dividing each secondary ion intensity (variable) by a scalar value, such as the total intensity of the spectrum or the sum of the intensities of selected peaks.[160] Another step is given by the mean-centering by subtracting the mean-value for a variable from that variable in each spectrum. This ensures that differences in samples are due to variations around the means and not the variance of the means. A more exhaustive explanation is provided elsewhere.[149,159,161,162]

Now, a problem arising in the interpretation of a SIMS molecular depth-profile is linked to the huge amount of data (raw data) obtained from a single experiment: each point of the profile corresponds to a mass spectrum, which in turn is composed by hundreds or thousands of peaks. Thus, methods to manage these giant raw data sets are required, in order to successively apply PCA for the extraction of the most significant information. Tuccitto et al. published in 2016 an attractive data processing method based on the application of wavelet transform[163] directly to a given depth-profiling raw data for their compression and noise removal.[164] Only a few applications of the wavelet filtering to ToF-SIMS data have been reported in literature, specifically for the data treatment of ToF-SIMS images.[165,166] The approach proposed by the authors is schematized in **Figure 20**, and it is called Wavelet-PCA method. First, the mass spectrum related to each single scan is extracted from the whole profile raw data to be successively compressed to the proper level of approximation by means of the appropriate wavelet function. Hence, the PCA data matrix is given by the wavelet compression coefficients (variables) calculated at each depth scan (objects). Finally, the depth profiles are reconstructed from the scores values of the most important PCs, while the mass spectra (more properly, "pseudo-spectra") are calculated by the inverse-wavelet transform applied to the loadings values. The Wavelet-PCA method presents several benefits beyond the reduced computation storage. Indeed, in comparison with the "classical" unit mass-binning compression,[162] retention of the mass resolution is achieved. Additionally, peak-picking procedures or manual peak integration are not anymore required, saving a considerable amount of time to the researcher.

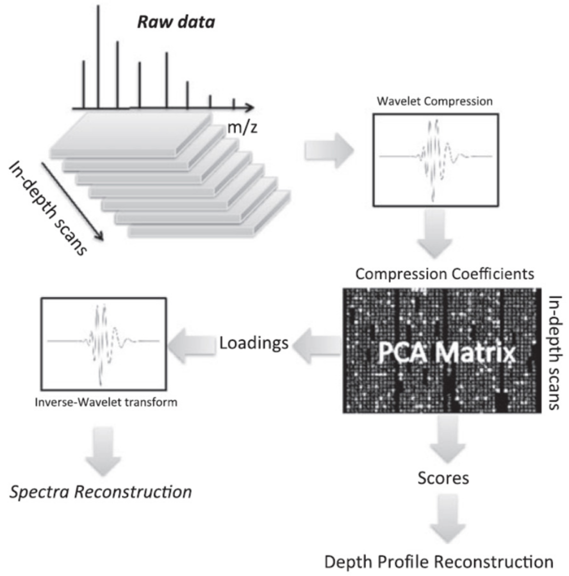

Figure 20. *Scheme of the Wavelet-PCA method applied to the data processing of SIMS depth-profiles. Image reproduced from Tuccitto et al. (2016).*[164]

2.4.5. State of art

2.4.5.1. Static-SIMS of plasma-treated and plasma-deposited polymers

The potential of static-SIMS as a surface characterization technique for the direct interrogation of plasma-treated and plasma-deposited polymer structures was soon foreseen. Often, SSIMS characterization was presented as a complement to other analytical techniques, such as XPS. However, pioneering studies conducted over the 1980s and the early 1990s were strongly limited by the low mass resolution offered by the quadrupole mass analyzers.[167,168] Indeed, distinct molecular fragment ions with the same nominal mass were impossible to distinguish, considerably limiting the interpretation of the surface characterization performed. At the beginning of the nineties, a series of SSIMS studies was carried out by Chilkoti et al. employing isotopically-labelled precursors, in order to investigate plasma-polymers prepared from carbonyl containing volatile organic compounds.[169,170] Indeed, the use of deuterated precursors constitutes a valuable expedient for structural assignments in the case of quadrupole-SIMS, in particular to distinguish the oxygen-containing secondary ions from the hydrocarbon ones. In 1995, plasma-polymerized styrene thin films were studied by means of SSIMS and XPS by Leggett et al., finding out that SIMS analysis is very sensitive to the cross-linked and unsaturated contents of the plasma-deposits.[171] Leggett et al. established by SIMS a structural comparison between the conventional PS and the one obtained by plasma polymerization: plasma-deposited styrene films were more unsaturated along the backbone, even if a good retention of the PS structure was observed. The ageing of the plasma-polymer was also investigated by SIMS, pointing out an increase of the cross-linked character to the detriment of the unsaturation over a 24-hours period of exposure to air, and correlated with the XPS determination of the oxygen incorporation.

An example of SSIMS application to the study of the plasma-induced surface modifications of polymers is provided by the work of De Puydt et al. in 1992.[172] They studied the effects of N_2, O_2 and Ar plasmas on polypropylene and the model compound hexatriacontane (a linear saturated hydrocarbon). Both oxygen and nitrogen incorporations were assessed by quadrupole-SIMS measurements on the basis of the oxidized ion peaks at m/z 31 and 45, and the N-containing peak at m/z 68. Additionally, their dependence on the plasma treatment time was determined. Information about the unsaturation and cross-linking was derived from SIMS structural indicators (refer to the review proposed by Delcorte et al.)[173], such as the sum of the aromatic ion intensities (∑arom).[174] The study of the model hydrocarbon compound treated by Ar and O_2 radio-frequency plasmas led to the hypothesis of a more pronounced ablation of the polymer film with the latter. The plasma-induced etching was thought to be competitive with the oxidative functionalization of the surface.

The mass resolution limitations imposed by quadrupoles were finally alleviated by the introduction of time-of-flight mass analyzers. Petrat and collaborators carried out in 1994 a study on the surface modifications of PS induced by Ar, O_2 and N_2 microwave plasmas, by combination of SSIMS (with a ToF-SIMS instrument developed by Benninghoven's group) and XPS in-situ analyses.[175] The characterization revealed the appearance of a considerable amount of new functional groups in the cases of O_2 and N_2 plasmas, but not for Ar plasma that instead led to small amounts of oxygen contamination. The oxidative functionalization produced by the plasma treatments was assessed by the $C_2H_3O^+$ and COH^+ ions, distinguishable thanks to a typical $M/\Delta M$ of 5000. In this work, the destruction of the aromaticity was pointed out by the $C_7H_7^+/C_4H_7^+$ signal ratio in SIMS, and verified by the ratio of aromatic to aliphatic carbon in the XPS C 1s signal. In 1996, Léonard and collaborators revisited the SIMS investigation of the O_2 post-discharge microwave plasma treatment of polyolefins (in particular, high density polyethylene or HDPE) and hexatriacontane by means of a ToF-SIMS instrument.[176] Now, subtle evolutions of the different ion families could be identified and related to the effects of the sample-discharge distance and the treatment time in terms of the degradation vs functionalization mechanism. The effects of the external plasma parameters on the chemical structure of plasma-deposited polymers have been widely investigated by ToF-SIMS surface analysis. In 1995, Ward and Short studied by SSIMS and XPS plasma-coatings deposited from different alkyl methacrylate precursors and their unsaturated analogues as a function of the injected power and the monomer flow rate.[177] High functional group retention and structural retention from the monomers were achieved in the plasma polymerization at low power and high monomer flow rate. This constitutes a frequent observation in the SIMS surface characterization of plasma-polymers.[178,179] A ToF-SIMS investigation of the chemical character of plasma-deposited films from ethylene and styrene at low pressure, and as a function of the external plasma parameters, was conducted by Oran et al.[180] The unsaturated character of the plasma-deposited ethylene samples versus the duty cycle (for instance) was evaluated by application of the aforementioned parameter ∑arom (in positive ion polarity) and the C^-/CH_2^- intensity ratio (in negative ion mode). The unsaturation degree increases with the increase of these two SIMS indicators. Additionally, the cross-linked content was established by means of the total positive secondary ion yield (its decrease is related to an increase of the cross-linking). The branching was also described by the sum of the normalized intensities of all $C_4H_x^+$ ions. Additional SIMS structural indicators were employed in the surface characterization of plasma-synthesized films from the styrene, allyl alcohol, and allylamine precursors, which were also correlated to the different deposition conditions.[59] In general, harder plasma conditions, such as higher power or lower monomer flow rate, result in higher irregularity of the plasma films (because of a decreased retention of the monomer functionalities and/or higher cross-linked/branched/unsaturated contents). From the study of the ageing of the plasma deposited films, it could be said that the lower the irregularity of the film, the higher is the post-oxidation and vice versa.[81]

Multivariate analysis was employed in the SSIMS studies of plasma-treated and plasma-synthesized polymers, in order to readily extract a higher amount of chemical and/or structural information. The potentialities of combining ToF-SIMS and multivariate analysis for the characterization of ultra-thin films were demonstrated, among others, by von Gradowski and co-workers in 2005.[181] Carbon fluorinated films were obtained with a pulsed Ar/CHF_3 plasma at different deposition times on Si and PET substrates. The surface structure and the influence of the deposition time were successfully understood interpreting the most important variation trends of the ToF-SIMS ion intensities pointed out by PCA. These results were correlated to those from XPS analysis. Furthermore, higher fluorination with increasing deposition time were found for both sets of samples, whereas films on PET possessed much higher cross-linked contents. In 2013, the combined ToF-SIMS/PCA approach was employed in the investigation of the effects of Ar and Ar/O_2 plasmas on amorphous and semi-crystalline poly (bisphenol A hexane ether) (BA-C6) thin films.[182] PCA indicated that the aromatic segments of BA-C6 were more resistant to the oxygen attack than the aliphatic moieties. The introduction of Ar to an O_2 plasma determined a plasma density decrease and an increase of the atomic oxygen concentration. The combination of these two factors led to a decrease in physical sputtering and an increase of the oxidation degree, independently on the crystallinity degree. As a result, aromatic ions and aliphatic ions with long chain lengths but H deficiency were observed in the SIMS spectra of the Ar/O_2 plasma-treated specimens. Furthermore, the crystalline BA-C6 presented higher resistance to the plasma etching compared to the amorphous surface. A recent publication of Cossement et al. (2015)[183] reviewed the work conducted by their group in Mons on the application of PCA to the ToF-SIMS mass spectra of plasma-polymers, in order to extract the relative cross-linking degree.[184,185,186,187,188,189] The evaluation of this peculiar feature is considered much more challenging in SIMS than the study of the polymer chemistry. Three different plasma polymers were prepared as model systems from allylamine (NH_2- groups), ethyl lactate (COOR- functionalities), and propanethiol (SH- groups) precursors, respectively. Additionally, the applied radio-frequency power was varied. In the SIMS of the three plasma-polymer models, the scores of the first principal component (PC1) highlighted significant differences in the chemical composition, also supported by XPS. The most important fragments contributing to PC1 (loadings > 90%) were used to estimate an average C/H ratio, index of the cross-linked degree in the polymers under study. This indicator permitted to verify an increase of the cross-linking as a function of the power injected in the plasma medium, except for the films deposited from the propanethiol monomer. In all the cases, the SIMS/PCA results were validated by independent methods. For instance, in the case of the NH_2-films the assessment of the cross-linking content was cross-checked by the evaluation of the dissolution behavior that the plasma deposits presented in ethanol.

2.4.5.2. Dynamic-SIMS of plasma-treated and plasma-deposited polymers

Thanks to the recent development of molecular depth-profiling of organics, either with very low energy Cs^+ ions or massive Ar clusters (see §2.4.3), ToF-SIMS appears to be a suitable in-depth diagnostic tool for the specific cases of plasma-polymers and polymer surfaces modified by plasma. While large Ar cluster beams are essentially recommended for the sputtering of organic and polymer materials, low energy Cs^+ ion sources are helpful in the investigation of hybrid systems.[130] These two possibilities of analysis permit to study a large spectrum of plasma-related samples, going from plasma-treated polymers, characterized by composition gradients along the depth (see §5.3.4.2), to plasma-synthesized gradient layers (obtained by control of the precursor injection), to polymer multilayers and, finally, hybrid systems where inorganic layers and/or inclusions can be found as well. Last, but not least, the possibility to apply multivariate analysis methods to the depth-profile data processing facilitates their interpretation and, more importantly, eliminates any bias from the manual ion selection. The success of the dynamic-SIMS/PCA approach has already been demonstrated in other application fields, such as the control of the degradation of Li-ion battery electrodes.[190,191] In this section, a few works have been chosen as significant examples of the dynamic-SIMS application to the in-depth investigation of plasma-synthesized polymer-based systems and plasma-modified polymers, respectively.

Merche et al. used SIMS depth-profiling with low energy (500 eV) Cs^+ sputtering to control the membrane-(catalyst-)electrode assembly obtained by a two-steps atmospheric plasma process.[72] This synthesis method is proposed by the authors as a useful tool for building miniaturized fuel cells using H_2 or CH_3OH. Briefly, catalyst nanoparticles were grafted on carbon substrates by spraying a Pt colloidal solution in the post-discharge of an RF atmospheric plasma torch. Then, the resulting decorated electrodes were covered by plasma-synthesized sulfonated polystyrene membranes in a DBD device. These polymer layers were deposited from the styrene and trifluoromethane sulfonic acid monomers, in the presence of a carrier gas (Ar or He). SIMS depth-profiling (carried out in negative ion mode) permitted to access both the membrane-catalyst and catalyst-carbon interfaces. The resulting polymeric film (~2-μm thick) was homogeneous, since the sulfonic groups (verified by the $C_6H_5SO_3^-$ and $C_8H_7SO_3^-$ ions) were uniformly grafted along the entire depth of the layer. Unreacted polymer precursor (m/z = 149) was found along the polymer layer, and mostly adsorbed at the interface with the Pt nanoparticles. This second observation was attributed most likely to the injection of the two monomers before the plasma ignition in the DBD. During the erosion of the Pt nanoparticles, the CNO^- ion was detected and explained by the presence of the capping agent (i.e. polyvinylpyrrolidone or PVP) in the colloidal solution. At the end of the profile, the catalyst-carbon interface was clearly revealed by a net increase of the C^- ion signal.

In 2013, Hubert and collaborators demonstrated the feasibility of synthesizing chlorinated films by a dielectric barrier discharge at atmospheric pressure from two different monomers, differing in the Cl/C ratio and H concentration: C_4Cl_6 and $C_2H_2Cl_4$.[192] The in-depth characterization of the chlorinated films was performed by SIMS depth-profiling with massive Ar cluster sputtering. A 10 keV Ar_{2800}^+ beam was rastered over an area of 700 x 700 μm^2. A 30 keV Bi_5^+ beam was employed to provide mass spectra from a 200 x 200 μm^2 area in the center of the sputtered crater. The mass spectra interpreted in this study were acquired from the middle of the depth-profiles to avoid issues of surface contamination. The depth-profiling experiments permitted to ascertain the homogeneity of the plasma films down to the interface with the Si substrate. Indeed, the signals of characteristic fragment ions of the chlorinated polymer layer, such as $C_8Cl_6^+$ or $C_{11}HCl_7^+$, were stable along the entire profile. Furthermore, the detection of high m/z fragments was interpreted as a sign of polymerization. The SIMS analysis also pointed out the perchlorination of both plasma films via hydrogenated carbons/carbon intensity ratios (i.e. CH^+, CH_2^+ and CH_3^+ compared to C^+), that was found to be characteristic of non-hydrogenated polymers like PTFE. However, SIMS indicated more hydrogenated components in the film obtained from $C_2H_2Cl_4$, whereas the film synthesized from C_4Cl_6 was characterized by higher mass fragments, interpreted on the basis of the polymerization degree. The differences of chemical structure of the two polymers found out in SIMS were correlated with the results from other techniques (namely XPS, WCA, ellipsometry), and ascribed to the difference in bond dissociation energies of the C=C, C-Cl and C-H bonds.

Low energy Cs^+ sputtering was instead employed by Abou Rich and collaborators (2014) to study the in-depth diffusion of oxygen into low density polyethylene (LDPE) induced either by an Ar or Ar-O_2 atmospheric post-discharge.[40] In particular, SIMS depth-profiles were performed by using a 750 eV Cs^+ beam for the sputtering, and a 15 keV Ga^+ beam for the analysis. The SIMS analysis was exclusively carried out in negative ion polarity. The chemical and structural properties of the polymer surface and bulk were investigated in terms of the external plasma parameters, and precisely the treatment time, power and reactive gas flow rate (O_2). The intensity ratio OH^-/CH^- was applied to assess the in-depth oxidation and to compare, at a later stage, the SIMS results with the O/C ratio from AR-XPS analysis. SIMS depth-profiling demonstrated that times > 30 s, powers > 60 W, and O_2 flow rate > 5 mL/min led to oxygen penetration depth, and thus oxygen gas diffusion, up to ~40 nm below the surface. These observations were in rather good agreement with the results from AR-XPS, and also ATR-FTIR.

2.5. Aim and originality of this thesis

In the context of the SIMS characterization of plasma-treated and plasma-deposited polymer films at low pressure, previously presented both at the surface (§2.4.5.1) and along the depth (§2.4.5.2), *the aim of this thesis* *consists in the development of new combined SIMS/PCA protocols for the surface and in-depth chemical analysis of polymers exposed or deposited to/by plasmas under atmospheric pressure conditions.* In order to achieve this goal, sputtering with massive Ar cluster ions (a few tens of keV) was envisaged for the in-depth molecular characterization, being considered as the "universal" sputter source for polymer-based materials, recently introduced in SIMS (§2.4.3). Preliminary, fundamental studies on SIMS molecular depth-profiling of polymers with large Ar clusters were required in order to elucidate the impact of some sample parameters on the sputtering efficiency, such as the influence of the polymer molecular weight, for experimental planning and depth calibration. These fundamental contributions are presented in Chapter 4.

A first case study of *"open air" plasma treatment* of polyolefins was envisaged for the chemical characterization of the ultra-shallow surface modification induced in the specimens. This investigation is proposed in Chapter 5. In particular, low density polyethylene films were treated by an Ar-H_2O post-discharge of an atmospheric plasma torch. However, tracing the reactivity of H_2O with the polyolefin constitutes an arduous task because of the inevitable intervention of the environmental humidity. So, owing to the high sensitivity and selectivity of SIMS to the H isotopes (refer to §2.4.2 point A, and §2.4.5.1), H_2O vapors were replaced with deuterated water vapors to investigate the H-D exchange, as well as the oxygen-uptake, unsaturation, branching and/or cross-linking, as a function of the parameters "treatment time" and "sample-torch distance". For the first time, the Wavelet-PCA approach (§2.4.4) was applied to molecular depth-profiles of plasma-treated polymers, so that the surface chemical characterization could be correlated with the in-depth modifications along the first tens of nm of the films, and rationalized on the basis of the lifetime of the reactive species present in the post-discharge (refer to §2.2.3 for the plasma diagnostics).

A second case study of *plasma polymerization* was conceived for the ex-situ SIMS molecular characterization. Polystyrene-like films were deposited near atmospheric pressure by means of a DBD, as a function of the plasma power. This investigation is presented in Chapter 6. Conversely to the SIMS literature reported in §2.5.4.1 (where plasma-polymers obtained at low pressure were analyzed in static mode only), in this thesis, the chemical and structural features of the deposited aromatic coatings, after exposure to the ambient air, were investigated in the inner layers by SIMS depth-profiling and successive PCA application. Indeed, this expedient permits to perform ex-situ characterization even in presence of post-polymerization oxidation, as well as segregation of the inhibitors of the utilized precursor towards the surface (and additives present in the conventionally synthesized PS references), chain re-orientation at the air/polymer interface, and surface contamination. Information about the peculiar spectral features of the plasma-deposited styrene films, as well as the aromatic and aliphatic contents, and the oxidation as a function of the injected power, were additionally compared with XPS and IR results. A more complete and consistent picture of the variation of the chemical structure of the plasma-polymer when varying the applied power was obtained. Insights about the polymerization degree could be derived thanks to the fundamental studies on SIMS molecular depth-profiling of Chapter 4.

Finally, it is necessary to make clear that the interpretations about the plasma-induced modifications of the polyethylene films (Chapter 5), and the variation of the chemical structure of the plasma deposits as a function of the power (Chapter 6), were uniquely done on the physical basis, without going into the details of the chemical reactions involved in the two plasma processes (i.e. plasma treatment and plasma polymerization).

2.6. References

[1] H. V. Boenig, Fundamentals of Plasma Chemistry and Technology, Technomic Publishing Company, Lancaster, **1988**.

[2] D. Merche, N. Vandencasteele, F. Reniers. Atmospheric plasmas for thin film deposition: A critical review. *Thin Solid Films* **2012**, *520*, 4219.

[3] A. Bogaerts, E. Neyts, R. Gijbels, J. van der Mullen. Gas discharge plasmas and their applications. *Spectrochimica Acta Part B* **2002**, *57*, 609.

[4] S. F. Denes, S. Manolache. Macromolecular plasma-chemistry: An emerging field of polymer science. *Prog. Polym. Sci.* **2004**, *29*, 815.

[5] C. Tendero, C. Tixier, P. Tristant, J. Desmaison, P. Leprince. Atmospheric pressure plasmas: A review. *Spectrochimica Acta Part B: Atomic Spectroscopy* **2006**, *61*, 2, and references herein.

[6] H. V. Boenig, Fundamentals of Plasma Chemistry and Technology, Technomic Publishing Company, Lancaster, **1988**, Chapter 3, and references herein.

[7] H. V. Boenig, Fundamentals of Plasma Chemistry and Technology, Technomic Publishing Company, Lancaster, **1988**, Chapter 3, 31.

[8] A.-M. Pointu, J. Perrin, J. Jolly, Traite de Genie Electrique, Techniques de l'Ingenieur, **1998**.

[9] L. Bárdos, H. Baránková. Cold atmospheric plasma: Sources, processes, and applications. *Thin Solid Films* **2010**, *518*, 6705.

[10] A. J. Y. Schütze, S. E. Babayan, J. Park, G. S. Selwyn, R. F. Hicks. The atmospheric-pressure plasma jet: A review and comparison to other plasma sources. *IEEE Trans. Plasma Sci.* **1998**, *26*, 1685, and references herein.

[11] J. Park, I. Henins, H. W. Herrmann, G. S. Selwyn, J. Y. Jeong, R. F. Hicks, D. Shim, C. S. Chang. An atmospheric plasma source. *Appl. Phys. Lett.* **2000**, *76*, 288.

[12] SurfX Technologies website: http://www.surfxtechnologies.com/

[13] U. Kogelschatz, B. Eliasson, W. Egli. Dielectric-barrier discharges. Principle and applications. *Journal de Physique IV* **1997**, *07*, C4-47.

[14] U. Kogelschatz, B. Eliasson, Fundamentals and applications of dielectric barrier discharges, HAKONE VII Int. Symp. on High Pressure Low Temperature Plasma Chemistry, Greifswald, **2000**.

[15] U. Kogelschatz. Dielectric-barrier discharges: Their history, discharge physics, and industrial applications. *Plasma Chemistry and Plasma Processes* **2003**, *23*, 1.

[16] F. Massines, G. Gouda. A comparison of polypropylene-surface treatment by filamentary, homogeneous and glow discharges in helium at atmospheric pressure. *Journal of Physics D: Applied Physics* **1998**, *31*, 3411.

[17] N. Gomathi, A. Sureshkumar, S. Neogi. RF plasma-treated polymers for biomedical applications. *Current Science* **2008**, *94*, 1478.

[18] J. M. Grace, L. J. Gerenser. Plasma treatment of polymers. *Journal of Dispersion Science and Technology* **2003**, *24*, 305.

[19] N. Inagaki, Plasma Surface Modification and Plasma Polymerization, Technomic Publishing Company, Lancaster, **1996**, Chapter 2, 21-41.

[20] H. Yasuda. Plasma for modification of polymers. *Journal of Macromolecular Science-Chemistry* **1976**, *10*, 383.

[21] E. M. Liston, L. Martinu, M. R. Wertheimer. Plasma surface modification of polymers for improved adhesion: A critical review. *Plasma Surface Modification of Polymers* **1993**, *7,* 1091.

[22] L. Reich, S. Stivala, Elements of Polymer Degradation, McGraw-Hill, New York, **1971**, Chapter 1.

[23] H. Yasuda, C. E. Lamaze, K. Sakaoku. Effect of electrodeless glow discharge on polymers. *Journal of Applied Polymer Science* **1973**, *17*, 137.

[24] S. K. Pankaj, C. Bueno-Ferrer, N. N. Misra, V. Milosavljević, C. P. O'Donnell, P. Bourke, K. M. Keener, P. J. Cullen. Applications of cold plasma technology in food packaging. *Trends in Food Science & Technology* **2014**, *35*, 5.

[25] J. Lahann, D. Klee, H. Thelen, H. Bienert, D. Vorwerk, H. Höcker. Improvement of haemocompatibility of metallic stents by polymer coating. *Journal of Materials Science: Materials in Medicine* **1999**, *10*, 443.

[26] Y. J. Kim, I.-K. Kang, M. W. Huh, S.-C. Yoon. Surface characterization and in vitro blood compatibility of poly (ethylene terephthalate) immobilized with insulin and/or heparin using plasma glow discharge. *Biomaterials* **2000**, *21*, 121.

[27] W. Zhang, P. K. Chu, J. Ji, Y. Zhang, R. K. Y. Fu, Q. Yan. Antibacterial properties of plasma-modified and triclosan or bronopol coated polyethylene. *Polymer* **2006**, *47*, 931.

[28] Y. J. Wang, C. H. Chen, M. L. Yeh, G. H. Hsiue, B. C. Yu. A one-side hydrophilic polypropylene membrane prepared by plasma treatment. *Journal of Membrane Science* **1990**, *53*, 275.

[29] R. Eloy, D. Parrat, T. M. Duc, G. Legeay, A. Bechetoille. In vitro evaluation of inflammatory cell response after CF_4 plasma surface modification of poly (methyl methacrylate) intraocular lenses. *Journal of Cataract & Refractive Surgery* **1993**, *19*, 364.

[30] L. Bárdos, Ladislav, H. Baránková. Cold atmospheric plasma: Sources, processes, and applications. *Thin Solid Films* **2010**, *518*, 6705, and references herein.

[31] J. Schneider, K. M. Baumgärtner, J. Feichtinger, J. Krüger, P. Muranyi, A. Schulz, M. Walker, J. Wunderlich, U. Schumacher. Investigation of the practicability of low-pressure microwave plasmas in the sterilisation of food packaging materials at industrial level. *Surface and Coatings Technology* **2005**, *200*, 962.

[32] P. Appendini, J. H. Hotchkiss. Review of antimicrobial food packaging. *Innovative Food Science & Emerging Technologies* **2002**, *3*, 113.

[33] B. Nisol, C. Poleunis, P. Bertrand, F. Reniers. Poly (ethylene glycol) films deposited by atmospheric pressure plasma liquid deposition and atmospheric pressure plasma-enhanced chemical vapour deposition: Process, chemical composition analysis and biocompatibility. *Plasma Processes and Polymers*, **2010**, *7*, 715.

[34] D. Merche, C. Poleunis, P. Bertrand, M. Sferrazza, F. Reniers. Synthesis of polystyrene thin films by means of an atmospheric-pressure plasma torch and a dielectric barrier discharge. *IEEE Transactions on Plasma Science* **2009**, *37*, 951.

[35] P. Leroy, S. A. Rich, F. Reniers. Ageing of LDPE surfaces modified by low temperature plasma torch, 20th International Symposium on Plasma Chemistry (ISPC 20), Philadelphia, USA, **2011**.

[36] T. Dufour, J. Hubert, N. Vandencasteele, F. Reniers. Chemical mechanisms inducing a dc current measured in the flowing post-discharge of an RF He-O_2 plasma torch. *Plasma Sources Science and Technology* **2012**, *21*, 045013.

[37] T. Dufour, J. Minnebo, S. A. Rich, E. C. Neyts, A. Bogaerts, F. Reniers. Understanding polyethylene surface functionalization by an atmospheric He/O_2 plasma through combined experiments and simulations. *Journal of Physics D: Applied Physics* **2014**, *47*, 224007.

[38] C. Y. Duluard, T. Dufour, J. Hubert, F. Reniers. Influence of ambient air on the flowing afterglow of an atmospheric pressure Ar/O_2 radiofrequency plasma. *Journal of Applied Physics* **2013**, *113*, 093303.

[39] S. A. Rich, T. Dufour, P. Leroy, L. Nittler, J. J. Pireaux, F. Reniers. LDPE films treated by an atmospheric Ar-O_2 post-discharge: Functionalization, etching, degradation and partial recovery of the native wettability state. *J. Phys. D: Appl. Phys*. **2014**, 47, 065203.

[40] S. Abou Rich, P. Leroy, T. Dufour, N. Wehbe, L. Houssiau, F. Reniers. In-depth diffusion of oxygen into LDPE exposed to an Ar-O_2 atmospheric post-discharge: A complementary approach between AR-XPS and ToF-SIMS techniques. *Surface and Interface Analysis* **2014**, *46*, 164.

[41] S. Abou Rich, T. Dufour, P. Leroy, F. Reniers, L. Nittler, J. J. Pireaux. LDPE surface modifications induced by atmospheric plasma torches with linear and showerhead configurations. *Plasma Processes and Polymers* **2015**, *12*, 771.

[42] S. Collette, T. Dufour, F. Reniers. Reactivity of water vapor in an atmospheric argon flowing post-discharge plasma torch. *Plasma Sources Science and Technology* **2016**, *25*, 025014.

[43] L. Liu, D. Xie, M. Wu, X. Yang, Z. Xu, W. Wang, X. Bai, E. Wang. Controlled oxidative functionalization of monolayer graphene by water-vapor plasma etching. *Carbon* **2012**, *50*, 3039.

[44] M. Atanasova, E. Carbone, D. Mihailova, E. Benova, G. Degrez, J. J. van der Mullen. Modelling of an RF plasma shower. *Journal of Physics D: Applied Physics* **2012**, *45*, 145202.

[45] M. Kaiser, M. Walker, K.-M. Baumgärtner, E. Räuchle, K. Kharitonov, M. Hauser. Transparent and fluorescent plasma polymers from aromatic hydrocarbons. *Surface and Coatings Technology* **1998**, *105*, 165.

[46] H. Yasuda. Glow discharge polymerization. *Journal of Polymer Science: Macromolecular Reviews* **1981**, *16*, 199.

[47] H. Yasuda, Plasma Polymerization, Academic Press Inc., London, **1985**.

[48] J. M. Tibbitt, M. Shen, A. T. Bell. Structural characterization of plasma-polymerized hydrocarbons. *Journal of Macromolecular Science-Chemistry* **1976**, *10*, 1623.

[49] H. Yasuda. Plasma polymerization for protective coatings and composite membranes. *Journal of Membrane Science* **1984**, *18*, 273.

[50] H. Yasuda, T. Yasuda. The competitive ablation and polymerization (CAP), Principle and the plasma sensitivity of elements in plasma polymerization and treatment. *Journal of Polymer Science Part A: Polymer Chemistry* **2000**, *38*, 943.

[51] H. Biederman, Y. Osada, Plasma Polymerization Processes, Elsevier, Amsterdam, **1992**.

[52] H. Yasuda, C. E. Lamaze. Polymerization of styrene in an electrodeless glow discharge. *Journal of Applied Polymer Science* **1971**, *15*, 2277.

[53] L. O'Toole, A. J. Beck, A. P. Ameen, F. R. Jones, R. D. Short. Radiofrequency-induced plasma polymerisation of propenoic acid and propanoic acid. *Journal of the Chemical Society, Faraday Transactions* **1995**, *91*, 3907.

[54] A. J. Beck, R. F. Jones, R. D. Short. Mass spectrometric study of the radiofrequency-induced plasma polymerisation of styrene and propenoic acid. *Journal of the Chemical Society, Faraday Transactions* **1998**, *94*, 559.

[55] J. Friedrich. Mechanisms of plasma polymerization-reviewed from a chemical point of view. *Plasma Processes and Polymers* **2011**, *8*, 783.

[56] H. V. Boenig, Fundamentals of Plasma Chemistry and Technology, Technomic Publishing Company Inc., Lancaster, **1988**, 96.

[57] H. Biederman, Plasma Polymer Films, Imperial College Press, London, **2004**, 18.

[58] D. Thiry, S. Konstantinidis, J. Cornil, R. Snyders. Plasma diagnostics for the low-pressure plasma polymerization process: A critical review. *Thin Solid Films* **2016**, *606*, 19.

[59] U. Oran. Surface chemical characterization of plasma-chemically deposited polymer films by time of flight static secondary ion mass spectrometry. Ph.D. Thesis, Free University, Berlin, **2005**.

[60] M. F. Maitz. Applications of synthetic polymers in clinical medicine. *Biosurface and Biotribology* **2015**, *1*, 161.

[61] R. Förch, A. N. Chifen, A. Bousquet, H. L. Khor, M. Jungblut, L.-Q. Chu, Z. Zhang, I. Osey-Mensah, E.-K. Sinner, W. Knoll. Recent and expected roles of plasma-polymerized films for biomedical applications. *Chemical Vapor Deposition* **2007**, *13*, 280, and reference herein.

[62] B. Nisol, G. Oldenhove, N. Preyat, D. Monteyne, M. Moser, D. Perez-Morga, F. Reniers. Atmospheric plasma synthesized PEG coatings: Non-fouling biomaterials showing protein and cell repulsion. *Surface and Coatings Technology*, **2014**, *252*, 126.

[63] H. Biederman, Plasma Polymer Films, Imperial College Press, London, **2004**, Chapter 6, 217.

[64] J. G. Calderon, R. B. Timmons. Surface molecular tailoring via pulsed plasma-generated acryloyl chloride polymers: Synthesis and reactivity. *Macromolecules* **1998**, *31*, 3216.

[65] R. B. Timmons, J.-H. Wang. Molecular tailoring of surfaces. U.S. Patent No 5,876,753, **1999**.

[66] H. Qiu. Controlled chemical and morphological surface modifications via pulsed plasma polymerizations: Synthesis of ultrahydrophobic surfaces. Ph.D. Thesis, University of Texas at Arlington, **2001**.

[67] J. Hubert, J. Mertens, T. Dufour, N. Vandencasteele, F. Reniers Synthesis and texturization processes of (super)-hydrophobic fluorinated surfaces by atmospheric plasma. *Journal of Materials Research* **2015**, *30*, 3177.

[68] F. Henry, F. Renaux, S. Coppée, R. Lazzaroni, N. Vandencasteele, F. Reniers, R. Snyders. Synthesis of superhydrophobic PTFE-like thin films by self-nanostructuration in a hybrid plasma process. *Surface Science* **2012**, *606*, 1825.

[69] C. Tarducci, E. J. Kinmond, J. P. S. Badyal, S. A. Brewer, C. Willis. Epoxide-functionalized solid surfaces. *Chemistry of Materials* **2000**, *12*, 1884.

[70] H. Qiu, F. S. Sanchez-Estrada, R. B. Timmons. Molecular tailoring of surfaces via pulsed plasma polymerization. *Journal of Photopolymer Science and Technology* **2000**, *13*, 29.

[71] B. Bae, D. Kim. Sulfonated polystyrene grafted polypropylene composite electrolyte membranes for direct methanol fuel cells. *Journal of Membrane Science* **2003**, *220*, 75.

[72] D. Merche, T. Dufour, J. Hubert, C. Poleunis, S. Yunus, A. Delcorte, P. Bertrand, F. Reniers. Synthesis of membrane-electrode assembly for fuel cells by means of (sub)-atmospheric plasma processes. *Plasma Processes and Polymers* **2012**, *9*, 1144.

[73] F. Khelifa, S. Ershov, M.-E. Druart, Y. Habibi, D. Chicot, M.-G. Olivier, R. Snyders, P. Dubois. A multilayer coating with optimized properties for corrosion protection of Al. *Journal of Materials Chemistry A* **2015**, *3*, 15977.

[74] R. Denaro, P. A. Owens, A. Crawshaw. Glow discharge polymerization-styrene. *European Polymer Journal* **1968**, *4*, 93.

[75] L. F. Thompson, K. G. Mayhan. The plasma polymerization of vinyl monomers. II. A detailed study of the plasma polymerization of styrene. *Journal of Applied Polymer Science* **1972**, *16*, 2317.

[76] G. W. Prohaska, E. D. Johnson, J. F. Evans. Preparation and characterization of plasma-polymerized styrene thin films. *Journal of Polymer Science: Polymer Chemistry Edition* **1984**, *22*, 2953.

[77] M. Chen, T. C. Yang, Z. Ma. Investigation on RF styrene plasma by emission spectroscopy. *IEEE Transactions on Plasma Science* **1995**, *23*, 151.

[78] M. Chen, T. Yang, Z. Ma. Plasma polymerization of styrene with controlled particle energy. *Journal of Polymer Sciences A, Polymer Chemistry* **1998**, *36*, 1265.

[79] I. Retzko, J. F. Friedrich, A. Lippitz, W. E. S. Unger. Chemical analysis of plasma-polymerized films: The application of X-ray photoelectron spectroscopy (XPS), X-ray absorption spectroscopy (NEXAFS) and Fourier transform infrared spectroscopy (FTIR). *Journal of Electron Spectroscopy and Related Phenomena* **2001**, *121*, 111.

[80] S. Swaraj, U. Oran, A. Lippitz, R.D. Schulze, J. Friedrich, W. Unger. Surface analysis of plasma-deposited polymers films, 2: Analysis of post-plasma air reacted plasma polymerized styrene by X-ray photoelectron spectroscopy and X-ray absorption spectroscopy. *Plasma Processes and Polymers* **2004**, *1*, 134.

[81] U. Oran, S. Swaraj, J. F. Friedrich, W. E. S. Unger. Surface analysis of plasma-deposited polymer films, 1. *Plasma Processes and Polymers* **2004**, *1*, 123.

[82] U. Oran, S. Swaraj, J. F. Friedrich, W. E. S. Unger. Surface analysis of plasma-deposited polymer films by Time of Flight Static Secondary Ion Mass Spectrometry (ToF-SSIMS) before and after exposure to ambient air. *Surfaces and Coatings Technology* **2005**, *200*, 463.

[83] M. Haïdopoulos, J. Larrieu, M. Horgnies, L. Houssiau, J. J. Pireaux. A comparative study between inductively and capacitively coupled plasma deposited polystyrene films: Chemical and morphological characterizations. *Surfaces and Interfaces Analysis* **2006**, *38*, 1266.

[84] M. Haïdopoulos, F. Mirabella, M. Horgnies, C. Volcke, P. A. Thiry, P. Rouxhet, J. J. Pireaux. Morphology of polystyrene films deposited by RF plasma. *Journal of Microscopy* **2007**, *228*, 227.

[85] Z. Li, X. Gillon, L. Houssiau, J. J. Pireaux. Investigation in the synthesis process of plasma polymerisation: New polystyrene. *Materials Research Innovations* **2015**, *19*, S5-1117.

[86] H. L. Luo, J. Sheng, Y. Z. Wan. Plasma polymerization of styrene with carbon dioxide under glow discharge conditions. *Applied Surface Sciences* **2007**, *253*, 5203.

[87] J. T. Kim, K. B. Lim, D. C. Lee. The influence of CH_4 carrier gas in plasma polymerized styrene film. *Surface and Coatings Technology* **2004**, *182*, 1.

[88] S. Kurosawa, H. Harigae, H. Aizawa, J. W. Park, H. Suzuki, and K. Terashima. Synthesis and characterization of microplasma-polymerized styrene and propargyl alcohol films. *Journal of Photopolymer Science and Technology* **2005**, *18*, 273.

[89] H. Aizawa, T. Makisako, S. M. Reddy, K. Terashima, S. Kurosawa, M. Yoshimoto. On-demand fabrication of microplasma-polymerized styrene films using automatic motion controller. *Journal of Photopolymer Science and Technology* **2007**, *20*, 215.

[90] S. Kurosawa, H. Harigae, H. Aizawa, H. Suzuki, K. Terashima. Gas recognition films fabricated by microplasma technology. *Journal of Photopolymer Science and Technology* **2006**, *19*, 253.

[91] I. Topala, M. Asandulesa, D. Spridon, N. Dumitrascu. Hydrophobic coatings obtained in atmospheric pressure plasma. *IEEE Transaction on Plasma Science* **2009**, *37*, 946.

[92] D. Briggs, M. P. Seah, Practical Surface Analysis, Volume 2 - Ion and neutral spectroscopy, John Wiley & Sons, Chichester, **1992**.

[93] J. C. Vickerman, D. Briggs, ToF-SIMS: Materials analysis by mass spectrometry, Second Edition, IM Publications LLP and SurfaceSpectra Limited, Chichester, **2013**.

[94] SIMS introduction (Heidelberg University). http://www.rzuser.uni-heidelberg.de/~hb6/labor/sims/index_en.html.

[95] A. Benninghoven. Die Analyse monomolekularer Festkörperoberflächenschichten mil Hilfe der Sekundärionenemission. *Z. Physik* **1970**, *230*, 403.

[96] W. Sichtermann and A. Benninghoven. Secondary ion formation from amino acids by proton and cation transfer. *Int. J. Mass Spectrom. Ion Phys.* **1981**, *40*, 177.

[97] D. Briggs, M. P. Seah, Practical Surface Analysis, Volume 2 - Ion and neutral spectroscopy, John Wiley & Sons, Chichester, **1992**, Chapter 6, 304.

[98] J. A. Gardella Jr, D. M. Hercules. Static secondary ion mass spectrometry of polymer systems. *Analytical Chemistry* **1980**, *52*, 226.

[99] D. Briggs, A. B. Wootton. Analysis of polymer surfaces by SIMS. 1. An investigation of practical problems. *Surface and Interface Analysis* **1982**, *4*, 109.

[100] D. Briggs, M. J. Hearn. Interaction of ion beams with polymers, with particular reference to SIMS. *Vacuum* **1986**, *36*, 1005.

[101] M. J. Hearn, D. Briggs. Analysis of polymer surfaces by SIMS. 12. On the fragmentation of acrylic and methacrylic homopolymers and the interpretation of their positive and negative ion spectra. *Surface and Interface Analysis* **1988**, *11*, 198.

[102] W. J van Ooij, R. H. G. Brinkhuis. Interpretation of the fragmentation patterns in static SIMS analysis of polymers. Part I. Simple aliphatic hydrocarbons. *Surface and Interface Analysis* **1988**, *11*, 430.

[103] D. Briggs. Analysis of polymer surfaces by SIMS. Part 14. Aliphatic hydrocarbons revisited. *Surface and Interface Analysis* **1990**, *15*, 734.

[104] J. C. Vickerman, D. Briggs. ToF-SIMS: Materials analysis by mass spectrometry. IM Publications and SurfaceSpectra, Chichester & Manchester, Second edition, **2013**, Chapter 23, 616.

[105] TOF-SIMS technique. https://www.iontof.com/tof-sims-secondary-ion-mass-spectrometry.html

[106] N. Médard, A. Benninghoven, D. Rading, A. Licciardello, A. Auditore, Tran Minh Duc, H. Montigaud, F. Vernerey, C. Poleunis, P. Bertrand. Antioxidant segregation and crystallisation at polyester surfaces studied by ToF-SIMS. *Applied Surface Science* **2003**, *203*, 571.

[107] A. Bodzon-Kulakowska, P. Suder. Imaging mass spectrometry: Instrumentation, applications, and combination with other visualization techniques. *Mass Spectrometry Reviews* **2016**, *35*, 147.

[108] C. M. Mahoney. Cluster secondary ion mass spectrometry of polymers and related materials. *Mass Spectrometry Reviews* **2010**, *29*, 247.

[109] F. Gronlund, W. J. Moore. Sputtering of silver by light ions with energies from 2 to 12 keV. *J. Chem. Phys.* **1960**, *32*, 1540.

[110] A. D. Appelhans, J. E. Delmore. Focused, rasterable, high-energy neutral molecular beam probe for secondary ion mass spectrometry. *Anal. Chem.* **1987**, *59*, 1685.

[111] G. Gillen, S. Roberson. Preliminary evaluation of an SF_5^+ polyatomic primary ion beam for analysis of organic thin films by secondary ion mass spectrometry. *Rapid Commun. Mass Spectrom*. **1998**, *12*, 1303.

[112] A. Delcorte, B. J. Garrison. High yield events of molecular emission induced by kiloelectronvolt particle bombardment. *The Journal of Physical Chemistry B* **2000**, *104*, 6785.

[113] A. Delcorte. Modeling keV particle interactions with molecular and polymeric samples. *Nuclear Instruments and Methods in Physics Research Section B: Beam Interactions with Materials and Atoms* **2005**, *236*, 1.

[114] B. Czerwiński, R. Samson, B. J. Garrison, N. Winograd, Z. Postawa. Desorption of organic overlayers by Ga and C_{60} bombardment. *Vacuum* **2006**, *81*, 167.

[115] A. Delcorte, B. J. Garrison. keV fullerene interaction with hydrocarbon targets: Projectile penetration, damage creation and removal. *Nuclear Instruments and Methods in Physics Research Section B: Beam Interactions with Materials and Atoms* **2007**, *255*, 223.

[116] G. Gillen, D. S. Simons, P. Williams. Molecular ion imaging and dynamic secondary-ion mass spectrometry of organic compounds. *Analytical Chemistry* **1990**, *62*, 2122.

[117] J. Cheng, A. Wucher, N. Winograd. Molecular depth profiling with cluster ion beams. *The Journal of Physical Chemistry B* **2006**, *110*, 8329.

[118] A. Wucher. A simple erosion dynamics model of molecular sputter depth profiling. *Surface and Interface Analysis* **2008**, *40*, 1545.

[119] A. Chapiro, Radiation Chemistry of Polymeric Systems, John Wiley & Sons, New York & London, **1962**, 712.

[120] N. Tuccitto, G. Zappalà, V. Spampinato, A. Licciardello, C_{60} depth profiling of polymer-based multilayers, SIMS XVII, Toronto, Canada, **2009**.

[121] V. Cristaudo. Influenza dei gas reattivi nel SIMS dinamico di polimeri. Bachelor Thesis, Università degli Studi di Catania, **2010**.

[122] V. Cristaudo. Metodologie per l'ottenimento di profili di profondità di multistrati polimerici. Master Thesis, Università degli Studi di Catania, **2012**.

[123] D. Sapuppo. Chemical effects in cluster SIMS depth profiling of polymer-based materials. Ph.D. Thesis, Università degli Studi di Catania, Academic Year **2011-2012**.

[124] R. Havelund, A. Licciardello, J. Bailey, N. Tuccitto, D. Sapuppo, I. S. Gilmore, J. S. Sharp, J. L. S. Lee, T. Mouhib, A. Delcorte. Improving secondary ion mass spectrometry C_{60}^{n+} sputter depth profiling of challenging polymers with nitric oxide gas dosing. *Analytical Chemistry* **2013**, *85*, 5064.

[125] R. Wilken, A. Holländer, J. Behnisch. Surface radical analysis on plasma-treated polymers. *Surface and Coatings Technology* **1999**, *116*, 991.

[126] N. Mine, B. Douhard, J. Brison, L. Houssiau. Molecular depth-profiling of polycarbonate with low-energy Cs^+ ions. *Rapid Communications in Mass Spectrometry* **2007**, *21*, 2680.

[127] N. Mine, B. Douhard, L. Houssiau. MCs_n^+ cluster formation on organic surfaces: A novel way to depth-profile organics? *Applied Surface Science* **2008**, *255*, 973.

[128] L. Houssiau, B. Douhard, N. Mine. Molecular depth profiling of polymers with very low energy ions. *Applied Surface Science* **2008**, *255*, 970.

[129] L. Houssiau, N. Mine. Molecular depth profiling of polymers with very low energy reactive ions. *Surface and Interface Analysis* **2010**, *42*, 1402.

[130] C. Noël, L. Houssiau. Hybrid organic/inorganic materials depth profiling using low energy cesium ions. *Journal of The American Society for Mass Spectrometry* **2016**, 27, 908.

[131] J. F. Mahoney, J. Perel, S. A. Ruatta, P. A. Martino, S. Husain, T. D. Lee. Massive cluster impact mass spectrometry: A new desorption method for the analysis of large biomolecules. *Rapid Communications in Mass Spectrometry* **1991**, *5*, 441.

[132] R. J. Beuhler, L. Friedman. Mass distributions of ions sputtered by cluster impacts on carbon, copper and gold targets. *International Journal of Mass Spectrometry and Ion Processes* **1989**, *94*, 25.

[133] I. Yamada. Investigation of ionized cluster beam bombardment and its applications for materials modification. *Radiation Effects and Defects in Solids* **1992**, *124*, 69.

[134] I. Yamada, J. Matsuo, N. Toyoda, A. Kirkpatrick. Materials processing by gas cluster ion beams. *Materials Science and Engineering: R: Reports* **2001**, *34*, 231.

[135] B. J. Garrison, Z. Postawa. Computational view of surface based organic mass spectrometry. *Mass Spectrometry Reviews* **2008**, *27*, 289.

[136] A. Delcorte, O. A. Restrepo, B. Czerwinski, Cluster SIMS of organic materials: Theoretical Insights, Chapter 2 in Cluster Secondary Ion Mass Spectrometry: Principles and Applications, First Edition, John Wiley & Sons, New Jersey, **2013**.

[137] A. Delcorte, V. Cristaudo, V. Lebec, B. Czerwinski Sputtering of polymers by keV clusters: Microscopic views of the molecular dynamics. *International Journal of Mass Spectrometry* **2014**, *370*, 29.

[138] F. S. Denes, S. Manolache. Macromolecular plasma-chemistry: An emerging field of polymer science. *Progress in Polymer Science* **2004**, *29*, 815.

[139] B. Czerwinski, Z. Postawa, B. J. Garrison, A. Delcorte. Molecular dynamics study of polystyrene bond-breaking and crosslinking under C_{60} and Ar_n cluster bombardment. *Nuclear Instruments and Methods in Physics Research Section B: Beam Interactions with Materials and Atoms* **2012**, *303,* 23.

[140] M. Hashinokuchi, K. Moritani, J. Nakagawa. T. Kashiwagi, N. Toyoda. Secondary ion mass spectrometry using size-selected gas cluster ion beam. *Journal of Surface Analysis* **2008***,* *14*, 387.

[141] K. Moritani, G. Mukai, M. Hashinokuchi, K. Mochiji. Site-specific fragmentation of polystyrene molecule using size-selected Ar gas cluster ion beam. *Applied Physics Express* **2009**, *2*, 046001.

[142] S. Ninomiya, K. Ichiki, H. Yamada, Y. Nakata, T. Seki, T. Aoki, J. Matsuo. Precise and fast secondary ion mass spectrometry depth profiling of polymer materials with large Ar cluster ion beams. *Rapid Commun. Mass Spectrom.* **2009**, *23*, 1601.

[143] D. Rading, R. Moellers, H.-G. Cramer, E. Niehuis. Dual beam depth profiling of polymer materials: Comparison of C_{60} and Ar cluster ion beams for sputtering. *Surface and Interface Analysis* **2013**, *45*, 171.

[144] M. P. Seah. Universal equation for argon gas cluster sputtering yields. *The Journal of Physical Chemistry C* **2013**, *117*, 12622.

[145] M. P. Seah. Argon cluster size-dependence of sputtering yields of polymers: Molecular weights and the universal equation. *Surface and Interface Analysis* **2015**, *47*, 169.

[146] M. P. Seah, S. J. Spencer, A. G. Shard. Angle dependence of argon gas cluster sputtering yields for organic materials. *The Journal of Physical Chemistry B* **2015**, *119*, 3297.

[147] B. Czerwinski, L. Rzeznik, R. Paruch, B. J. Garrison, Z. Postawa. Effect of impact angle and projectile size on sputtering efficiency of solid benzene investigated by molecular dynamics simulations. *Nuclear Instruments and Methods in Physics Research Section B: Beam Interactions with Materials and Atoms* **2011**, *269*, 1578.

[148] A. Delcorte, O. A. Restrepo, B. Czerwinski, B. J. Garrison. Surface sputtering with nanoclusters: the relevant parameters. *Surface and Interface Analysis* **2013**, *45*, 9.

[149] D. J. Graham, D. G. Castner. Multivariate analysis of ToF-SIMS data from multicomponent systems: Why, when, and how. *Biointerphases* **2012**, *7*, 49.

[150] S. Wold, K. Esbensen, P. Geladi. Principal component analysis. *Chemometrics and Intelligent Laboratory Systems* **1987**, *2*, 37.

[151] J. E. Jackson. Principal components and factor analysis: Part I - Principal components. *Journal of Quality Technology* **1980**, *12*, 201.

[152] R. Bro, A. K. Smilde. Principal component analysis. *Analytical Methods* **2014**, *6*, 2812.

[153] M. Henry. Development of biocompatible polymeric membranes for bioartificial pancreas. Ph.D. Thesis, Université catholique de Louvain, Louvain-la-Neuve, **2008**, 17.

[154] V. Lebec. Interaction of proteins with chemically controlled surfaces for biosensor development. Ph.D. Thesis, Université catholique de Louvain, Louvain-la-Neuve, **2014**.

[155] X. Vanden Eynde, P. Bertrand. ToF-SIMS quantification of polystyrene spectra based on principal component analysis (PCA). *Surface and Interface Analysis* **1997**, *25*, 878.

[156] D. J. Graham, M. S. Wagner, D. G. Castner. Information from complexity: Challenges of TOF-SIMS data interpretation. *Applied Surface Science* **2006**, *252*, 6860.

[157] J. C. Vickerman, D. Briggs, ToF-SIMS: Materials analysis by mass spectrometry, Second Edition, IM Publications LLP and SurfaceSpectra Limited, Chichester, **2013**, Chapter 17, 453.

[158] M. S. Wagner, D. J. Graham, D. G. Castner. Simplifying the interpretation of ToF-SIMS spectra and images using careful application of multivariate analysis. *Applied Surface Science* **2006**, *252*, 6575.

[159] M. S. Wagner, D. J. Graham, B. D. Ratner, D. G. Castner. Maximizing information obtained from secondary ion mass spectra of organic thin films using multivariate analysis. *Surf. Sci.* **2004**, *570*, 78.

[160] M. S. Wagner, D. G. Castner. Characterization of adsorbed protein films by time-of-flight secondary ion mass spectrometry with principal component analysis. *Langmuir* **2001**, *17*, 4649.

[161] X. Vanden Eynde. Polymer surfaces studied by ToF-SIMS, (Time-of-flight secondary ion mass spectrometry), Molecular weight effects and quantification. Ph.D. Thesis, Université catholique de Louvain, Louvain-la-Neuve, **1999**.

[162] J. C. Vickerman, D. Briggs, ToF-SIMS: Materials analysis by mass spectrometry, Second Edition, IM Publications LLP and SurfaceSpectra Limited, Chichester, **2013**, Chapter 17.

[163] S. G. Mallat. A theory for multiresolution signal decomposition: the wavelet representation. *IEEE Transactions on Pattern Analysis and Machine Intelligence* **1989**, *11*, 674.

[164] N. Tuccitto, G. Zappalà, S. Vitale, A. Torrisi, A. Licciardello. A wavelet-PCA method saves high mass resolution information in data treatment of SIMS molecular depth profiles. *Surface and Interface Analysis* **2016**, *48*, 317.

[165] S. G. Nikolov, H. Hutter, M. Grasserbauer. De-noising of SIMS images via wavelet shrinkage. *Chemometr. Intell. Lab. Syst.* **1996**, *34*, 263.

[166] B. Tyler. Interpretation of TOF-SIMS images: multivariate and univariate approaches to image de-noising, image segmentation and compound identification. *Appl. Surf. Sci.* **2003**, *203*, 825.

[167] F. Garbassi, E. Occhiello, F. Polato, A. Brown. Surface effect of flame treatments on polypropylene. *J. Mater. Sci.* **1987**, *22*, 1450.

[168] E. Ochiello, M. Morra, G. Morini, F. Garbassi, P. Humphrey. Oxygen-plasma-treated polypropylene interfaces with air, water, and epoxy resins: Part I. Air and water. *J. Appl. Polym. Sci.* **1991**, *42*, 551.

[169] A. Chilkoti, B. D. Ratner, D. Briggs. Static SIMS investigation of the surface structure of plasma deposited films prepared from stable isotope-labeled carbonyl precursors. *Polym. Mater. Sci. Eng.* **1990**, *62*, 135.

[170] A. Chilkoti, B. D. Ratner, D. Briggs. Static secondary-ion mass spectrometric investigation of the surface structure of organic plasma-deposited films prepared from stable-isotope-labeled precursors. 1. Carbonyl precursors. *Anal. Chem.* **1991**, *63*, 1612.

[171] G. J. Leggett, B. D. Ratner, J. C. Vickerman. Characterization of plasma-deposited styrene films by XPS and static SIMS. *Surface and Interface Analysis* **1995**, *23*, 22.

[172] Y. De Puydt, D. Léonard, P. Bertrand, Metallized Plastics 3: Fundamental and Applied Aspects, A static SIMS study of the chemical modifications induced by plasma and flame treatments at the surface of polyolefins. K. L. Mittal, Plenum Press, New York, **1992**, 225.

[173] A. Delcorte, V. Cristaudo, M. Zarshenas, D. Merche, F. Reniers, P. Bertrand. Chemical analysis of plasma-treated organic surfaces and plasma polymers by secondary ion mass spectrometry. *Plasma Processes and Polymers* **2015**, *12*, 905.

[174] W. J. Van Ooij, R. H. Brinkhuis. Interpretation of the fragmentation patterns in static SIMS analysis of polymers. Part I. Simple aliphatic hydrocarbons. *Surface and Interface Analysis* **1988**, *11*, 430.

[175] F. M. Petrat, D. Wolany, B. C. Schwede, L. Wiedmann, A. Benninghoven. Comparative in situ ToF-SIMS/XPS study of polystyrene modified by argon, oxygen and nitrogen plasmas. *Surface and Interface Analysis* **1994**, *21*, 402.

[176] D. Léonard, P. Bertrand, A. Scheuer, R. Prat, J. Hommet, J. Le Moigne, J. P. Deville. Time-of-flight SIMS and in-situ XPS study of O_2 and O_2-N_2 post-discharge microwave plasma-modified high-density polyethylene and hexatriacontane surfaces. *J. Adhesion Sci. Technol.* **1996**, *10*, 1165.

[177] A. J. Ward, R. D. Short. A tofsims and xps investigation of the structure of plasma polymers prepared from the methacrylate series of monomers: 2. The influence of the WF parameter on structural and functional group retention. *Polymer* **1995**, *36*, 3439.

[178] A. P. Ameen, R. D. Short, R. J. Ward. The formation of high surface concentrations of hydroxyl groups in the plasma polymerization of allyl alcohol. *Polymer* **1994**, *35*, 4382.

[179] S. Eufinger, W. J. van Ooij, K. D. Conners. DC-plasma polymerization of hexamethyldisiloxane. Part II. Surface and interface characterization of films deposited on stainless-steel substrates. *Surface and Interface Analysis* **1996**, *24*, 841.

[180] U. Oran, S. Swaraj, J. F. Friedrich, W. E. S. Unger. Surface analysis of plasma-deposited polymer films by Time of Flight Static Secondary Ion Mass Spectrometry (ToF-SSIMS) before and after exposure to ambient air. *Surface and Coatings Technology* **2005**, *200*, 463.

[181] M. von Gradowski, B. Jacoby, H. Hilgers, J. Barz, M. Wahl, M. Kopnarski. ToF-SIMS characterisation of ultra-thin fluorinated carbon plasma polymer films. *Surface and Coatings Technology* **2005**, *200*, 334.

[182] X. Ren, L.-T. Weng, K.-M. Ng, C.-M. Chan. Effects of Ar-and Ar/O_2-plasma-treated amorphous and crystalline polymer surfaces revealed by ToF-SIMS and principal component analysis. *Surface and Interface Analysis* **2013**, *45*, 1158.

[183] D. Cossement, F. Renaux, D. Thiry, S. Ligot, R. Francq, R. Snyders. Chemical and microstructural characterizations of plasma polymer films by time-of-flight secondary ion mass spectrometry and principal component analysis. *Applied Surface Science* **2015**, *355*, 842, and references herein.

[184] L. Denis, D. Cossement, T. Godfroid, F. Renaux, C Bittencourt, R. Snyders, M. Hecq. Synthesis of allylamine plasma polymer films: Correlation between plasma diagnostic and film characteristics. *Plasma Processes and Polymers* **2009**, *6*, 199.

[185] L. Denis, F. Renaux, D. Cossement, C. Bittencourt, N. Tuccitto, A. Licciardello, M. Hecq, R. Snyders. Physico-chemical characterization of methyl isobutyrate-based plasma polymer films. *Plasma Processes and Polymers* **2011**, *8*, 127.

[186] L. Denis, D. Thiry, D. Cossement, P. Gerbaux, F. Brusciotti, I. Van De Keere, V. Goossens, H. Terryn, M. Hecq, R. Snyders. Towards the understanding of plasma polymer film behaviour in ethanol: A multi-technique investigation. *Progress in Organic Coatings* **2011**, *70*, 134.

[187] S. Ligot, F. Renaux, L. Denis, D. Cossement, N. Nuns, P. Dubois, R. Snyders. Experimental study of the plasma polymerization of ethyl lactate. *Plasma Processes and Polymers* **2013**, *10*, 999.

[188] S. Ligot, E. Bousser, D. Cossement, J. Klemberg-Sapieha, P. Viville, P. Dubois, R. Snyders. Correlation between mechanical properties and cross-linking degree of ethyl lactate plasma polymer films. *Plasma Processes and Polymers* **2015**, *12*, 508.

[189] D. Thiry, R. Francq, D. Cossement, M. Guillaume, J. Cornil, R. Snyders. A detailed description of the chemistry of thiol supporting plasma polymer films. *Plasma Processes and Polymers* **2014**, *11*, 606.

[190] D. Heller, B. Hagenhoff, C. Engelhard. Time-of-flight secondary ion mass spectrometry as a screening method for the identification of degradation products in lithium-ion batteries-A multivariate data analysis approach. *Journal of Vacuum Science & Technology B* **2016**, *34*, 03H138.

[191] V. Cristaudo, S. Collette, N. Tuccitto, C. Poleunis, L. C. Melchiorre, A. Licciardello, F. Reniers, A. Delcorte. Molecular surface analysis and depth-profiling of polyethylene modified by an atmospheric Ar-D_2O post-discharge. *Plasma Processes and Polymers* **2016**, *13*, 1106.

[192] J. Hubert, C. Poleunis, A. Delcorte, P. Laha, J. Bossert, S. Lambeets, A. Ozkan, P. Bertrand, H. Terryn, F. Reniers. Plasma polymerization of C_4Cl_6 and $C_2H_2Cl_4$ at atmospheric pressure. *Polymer* **2013**, *54*, 4085.

CHAPTER 3
Experimental

In this chapter, the ToF-SIMS (time-of-flight secondary ion mass spectrometry) instrumentation used for the surface and in-depth molecular characterization of plasma-treated (Chapter 5) and plasma-deposited polymers (Chapter 6), as well as model polymer thin films (Chapter 4), will be presented in §3.1. In addition, the principle of two other techniques, i.e. profilometry and ellipsometry, employed for the thickness measurement of the thin polymer films investigated by SIMS will be described in §3.2.

3.1. SIMS instrumentation

A ToF-SIMS instrument is essentially composed of one or more pulsed primary ion sources, a sample manipulator, a time-of-flight (ToF) mass analyzer, and a detector of secondary ions (SI). Moreover, in order to permit the analysis of insulating samples, a system of charge compensation is required. It is typically a source of low energy electrons (electron flood gun). The overall analytical system operates in conditions of UHV (pressure ≥ 10^{-8} mbar). In this thesis, a TOF.SIMS 5 spectrometer is utilized. The instrument is designed and manufactured by ION-TOF GmbH, Münster, Germany. The location of the main units of the TOF.SIMS 5 spectrometer are depicted in **Figure 1**.

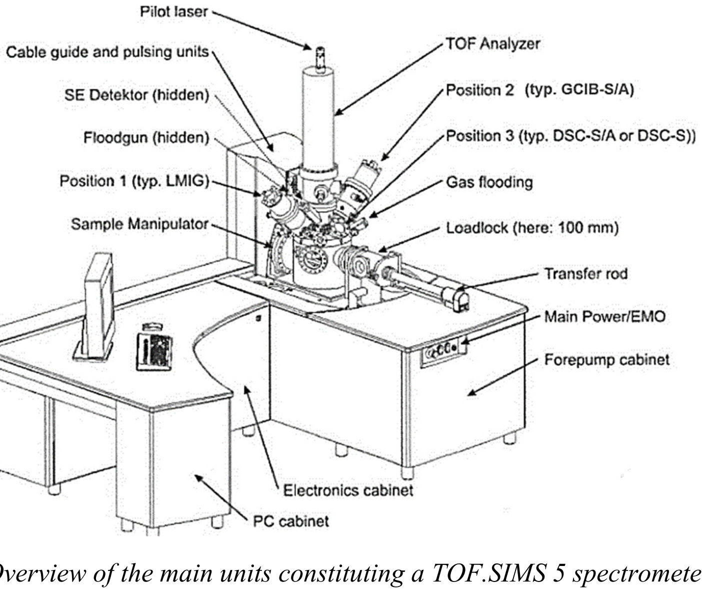

Figure 1. *Overview of the main units constituting a TOF.SIMS 5 spectrometer.*[1]

In particular, the ToF-SIMS instrument installed at UCL is equipped with three different types of primary ion sources. These are the "Bi Nanoprobe", that represents the latest generation of LMIG (liquid metal ion gun; in position 1), the GCIB-S/A (gas cluster ion beam; in position 2, that works either in sputtering or in analysis mode, S/A), and the DSC-S (dual source column - sputtering; in position 3). The LMIG produces monoatomic and cluster Bi ions, the GCIB massive Ar cluster ions, whereas the DSC provides low energy O_2^+ or Cs^+ DC ion beams. In this work, the analysis both in static-SIMS and dynamic-SIMS characterization of polymer samples was performed by using LMIG, while the GCIB was used for sputtering during the depth-profiling experiments. So, in the next sections, a particular attention will be given to these two ion sources.

3.1.1. Analysis ion beam

The 30 keV Bi Nanoprobe-LMIG is the analysis source employed in this work, which uses the patented Bi-Mn emitter technology.[2] The source produces several ion species Bi_x^{m+} and Mn_y^{n+} by thermoionic emission, such as Bi^+ monoatomic ions as well as Bi_3^+, Bi_3^{++} and Bi_5^+ ion clusters. In this study, a 30 keV Bi_5^+ cluster ion beam is used for the analysis of polymer-based materials, since it allows to obtain both high total secondary ion yield and larger relative yields of the highest mass secondary ions.[3]

The schematic overview of the Bi Nanoprobe column is reported in **Figure 2**.[4] Firstly, the primary ions are produced by the application of an extraction electric field (~10 V/nm) to a tungsten tip covered by a thin layer of the liquid Bi-Mn alloy (melting point ≤ 270 °C).[5,6] Then, the image of the source is created at the target by means of three different lens systems: source lens, magnification lens, and target lens. So, the maximum transmitted current is determined by the beam-defining aperture at the exit of the source lens system. Then, the magnification lens is used to tune the solid angle that is transmitted. Finally, the target lens system focuses the beam in the target plane. Furthermore, in order to align the beam through the LMIG column, the source is equipped with two current measurement apertures (aperture 1 and aperture 2). In order to center the beam through them, a deflection system (x-y source, x-y magnification) is located in front of each aperture. The beam is pulsed by scanning it over the aperture 1 (pre-chopper), and the blanking aperture (chopper). For the analysis, the pulse width is generally of the order of 1 ns after the buncher. Both systems are also used as a time-of-flight mass filter to select a certain ion species from the beam, like for instance Bi_5^+ in this work. The final diameter of the ion beam at the exit of the column is ~2-3 µm, when working in "high current bunched" mode (used to achieve high mass resolution).

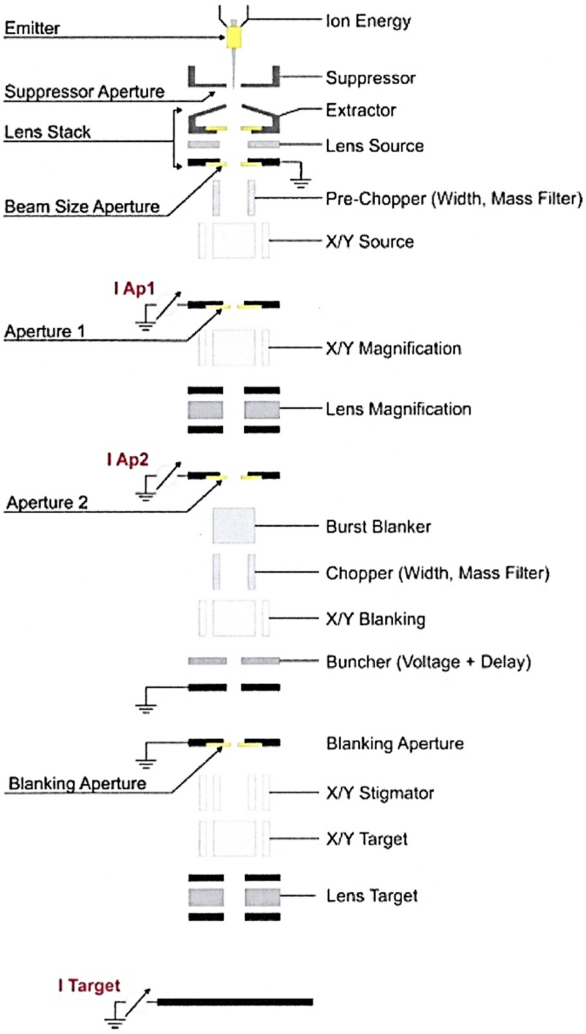

Figure 2. *Schematic of the LMIG column.*[4]

3.1.2. Sputter ion beam

In this thesis, the sputter ion beams used for the different in-depth characterizations of polymers are composed of massive argon cluster ions, with cluster size ranging from 1000 to 5000 atoms and energy of 10 keV. These large Ar cluster beams are produced by a GCIB column, illustrated in

Figure 3.[7] In addition to the sputter mode, conducted in single or dual beam (it will be explained in §3.1.6), the GGIB can be utilized in analysis mode.

The GCIB ion source is placed before the GCIB ion column (cf. Figure 3). The cluster ion formation is a two-stage process.[8] Firstly, argon clusters are formed by an adiabatic expansion, through a small nozzle, from a stagnation region at high pressure (typically 30 bar) into a low vacuum pumped region (10^{-3} bar). Gas clusters are created by the gas cooling, occurring thanks to the expansion. As the gas expands into the vacuum, atoms relative velocity is strongly reduced and a directed, supersonic jet with a fairly wide cluster distribution is formed. A skimmer is placed after this cluster formation region and selects the (cluster-containing) core of the jet from the molecular flow. This aperture also serves as a pressure step between the nozzle chamber (vacuum source, 10^{-3} bar) and the subsequent ion column (high vacuum column at 10^{-5}-10^{-6} bar). Once the cluster beam has passed the skimmer, it enters the ionization chamber. Here, the clusters are ionized by electron bombardment, which is operated in an energy range from 70-100 eV.[9] As soon as cluster ions are formed, they are accelerated into an ion column (applied voltage of 2.5-20 kV), which contains a Wien filter for the separation of the low mass species from the cluster distribution. Furthermore, the GCIB source is tilted of around 3° with respect to the GCIB column to remove the neutrals.

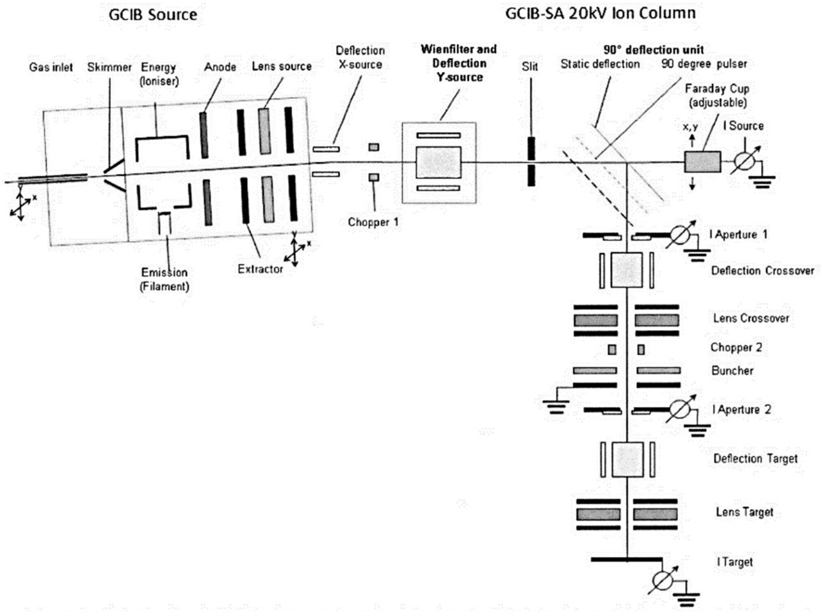

Figure 3. *Schematic of the GCIB ion source and column.*[7]

Then, a 90° deflection unit is used to cut ion pulses of variable length from the DC ion beam of the source. At this point, a gate valve is located to insulate the source from the instrument during maintenance. Finally, the alignment of the GCIB for a given mass range and the determination of the width of the cluster distribution is made thanks to a time-of-flight mass filter, constituted by the choppers 1 and 2. The final diameter of the cluster ion beam at the exit of the column is 20-30 µm.

3.1.3. Surface charging compensation

Insulating samples suffer a charge buildup, due to the imbalance between the primary ion, secondary ion and emitted electron fluxes. The electric charge generated on the sample surface causes instability of the signals, as well as peak broadening or drifting. This problem can be avoided by the use of a charge compensation system, consisting in a pulsed low-energy electron source. In this way, all types of solid samples can be analyzed, conductors and insulators. However, polymer-based materials can be chemically damaged by electron irradiation. Thus, the tuning of the parameters of the flood gun, especially the electron energy and fluence, are very important.[10,11,12] Furthermore, Retzko has reported that plasma polymers, such as polystyrene, are semi-conductive materials[13,14] and, therefore, charge compensation might not be needed, especially for thin plasma polymer films. Nevertheless, in the case of the plasma-polymerized styrene films analyzed in Chapter 6, the use of the electron flood gun was required, which was presumably due to the rather large thickness of the polymer layer on the Si wafer (several µm).

The schematic of the electron flood gun used in the TOF.SIMS 5 spectrometer is reported in **Figure 4**, where one can observe the position of the electrodes. The electron energy is typically 20 eV, and is determined by the potential of the filament.

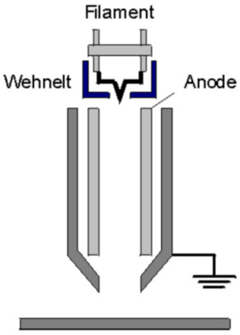

Figure 4. *Schematic of the pulsed low-energy electron source used for surface charge compensation.*[15]

The shielding of the filament is a lens called Wehnelt. The pulsing of this source is achieved by switching the potential from the anode to the Wehnelt unit. The secondary ion extraction field is switched off during the electron pulse. For the analysis of negative secondary ions, a slight negative retarding field at the analyzer extractor lens prevents the electrons to reach the detector.

3.1.4. Time-of-flight (ToF) mass analyzer

After secondary ions are produced by the impinging primary ion beam (30 keV Bi_5^+), they are extracted from the sample by a 2 kV electric potential. More specifically, positive potentials are applied to extract negative secondary ions, and vice versa. The distance between the specimen surface and the extractor lens is optimized at 1.5 mm. The extracted secondary ions, ideally possessing constant kinetic energy (determined by the product of their charge z, typically equal to 1, by the extraction potential *V*), enter in a field-free drift tube. Over a flight path of typically 2 m (*L*), and at constant kinetic energy, lighter ions reach the detector in shorter times compared to heavier ones (see **Figure 5.a**). Hence, the measurement of the flight time (*t*) of an ion permits to determine its mass to charge ratio (*m/z*), thanks to the following **Equation (1):**[16]

$$\frac{m}{z} = \frac{2.V.t^2}{L^2} \tag{1}$$

It is worth noticing that, because of the sputtering physics, the secondary organic molecular ions possess an angular distribution, as well as a rather large energy distribution, with a maximum around 2-3 eV and FWHM of a few electronvolts.[17,18] The angular distribution is compensated by the extractor lens design. The energy spread of the secondary ions leads to a diminution of the mass resolution (M/ΔM), since ions with the same mass are detected at different times because of the difference in kinetic energy (cf. **Figure 5.b**). In order to alleviate this issue, the secondary ions are forced to travel upwards to an ion mirror (use of an electric field), named reflectron, where they are reflected downwards to the detector. This is illustrated in **Figure 5.c**. So, for secondary ions of constant mass, the reflectron increases the flight path of ions with higher kinetic energy and decreases it for the ones with lower energy (refer to Figure 5.c). The detector is placed at the point where the ions are refocused in time. This allows to compensate the energy spread of the secondary ions, and a resolving power M/ΔM above 10000 for m/z 28 (Si^+) can be achieved.

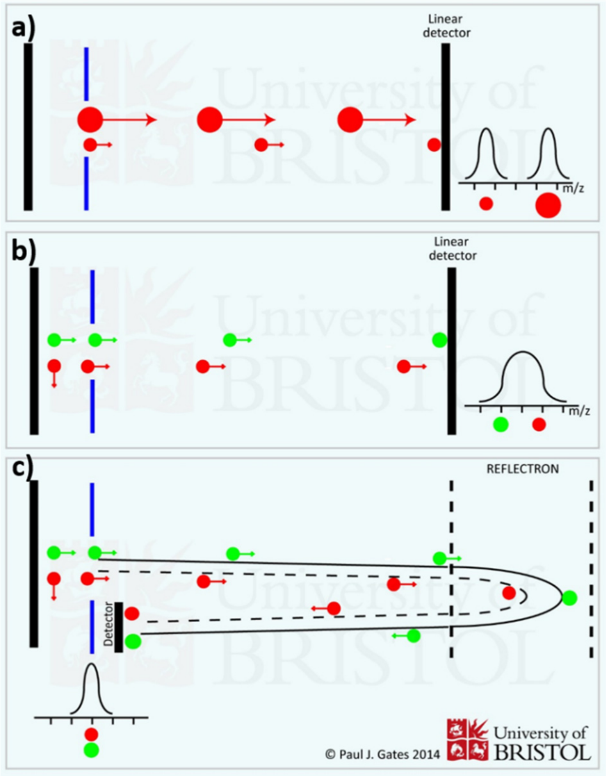

© Paul J. Gates 2014

Figure 5. *Principle of correction of the energy spread of the secondary ions by a reflectron-type ToF mass analyzer, resulting in an increase of the mass resolution.*[19]

Beyond the high mass resolution, ToF mass analyzers offer a series of advantages compared to quadrupole and magnetic sector type analyzers, such as higher transmission (number of ions that reaches the detector over 100 in entrance) up to ~70%, parallel detection of all masses and unlimited mass range.[20] The parallel detection of the masses is very important for depth-profiling and imaging experiments. Indeed, it is not necessary to choose beforehand a certain number of masses to monitor, but they can be selected afterwards by retrospective analysis of the SIMS raw data. However, for depth-profiling ToF analyzers show a lower sensitivity with respect to the magnetic sector analyzers, due to the fact that most of the emitted secondary ions during the sputtering phase are not analyzed. In the ToF analyzer, the measurement of the flight time of the secondary ions starts when the pulse of primary ions is sent to the sample surface. Thus, the duration of the pulse must be negligible compared to the flight time, in order to avoid degradation of the time resolution, and consequently mass resolution. In addition, the drift tube must be totally evacuated from the first secondary ion bunch, before receiving a second one, which is a constraint on the duty cycle. Supposing a flight path of 2 m and an extraction potential of 2 kV, the time required by the ion H^+ to reach the detector is a few μs, while for ions of thousands amu the time is a few hundreds of μs. Generally, duty cycles of ~100 μs are applied.

3.1.5. Secondary ion detector

The detection system is a single ion counting device.[21] It consists in the sequential combination of a multi-channel plate (MCP), a scintillator, and a photomultiplier, coupled with a very fast electronic pulse counting system. This detection system has been developed for the decoupling of the high energy secondary ions with respect to the low operating voltage of the electronics.

In particular, after being forced through the time-of-flight tube, secondary ions are post-accelerated onto the MCP by a 10 kV potential, where they are converted in electrons. The post-acceleration serves to increase the efficiency of the process (that depends on the velocity of the particle), especially in the case of ions with high masses and, thus, lower velocities. The electrons generated in the microchannels are then accelerated towards a scintillator coated with a conducting Al film. There, the electron to photon conversion occurs. The photon detection is operated by the photomultiplier tube.

In general, the SIMS signal intensity of an ion fragment of mass m can be rationalized using **Equation (2)**:

$$I_m = I_p.C_m.Y_m.\alpha_m^{\pm}.\eta \tag{2}$$

where:

I_m is the secondary ion current for the species m (ions/s),

I_p is the primary ion current (or primary particle flux in ions/s),

C_m is the fractional concentration of m in the surface layer,

Y_m is the sputter yield of m,

$\alpha_m^{\pm}$ is the ionization probability of m in positive or negative ions, and

η represents the instrumental factors, that include the analyzer transmission and the detector efficiency.

The two fundamental parameters are $\alpha_m^{\pm}$ and Y_m. The ionization probability of the species m ($\alpha_m^{\pm}$) is defined as the fraction of emitted ions, positive or negative, with respect to the total number of species m, charged and neutral, emitted in the sputtering process. This parameter varies strongly as a function of the nature of the species m, its chemical environment (matrix effect), the pressure of residual gases (for instance, oxygen), and the nature of the projectile. Thus, $\alpha_m^{\pm}$ can severely influence I_m.

Y_m is the total yield of sputtered particles of the species m, neutral and ionic, per primary ion. The total sputter yield, Y, is defined as the number of removed atoms (isolated or contained in molecules, fragments or clusters, independently from their charge), per incident primary ion. Often in the case of polymer materials like those investigated in this thesis (e.g. PMMA, PS, pp-PS), the sputter yield is preferably expressed in terms of eroded volume per incident primary ion (nm^3/PI).[22] In addition, the sputter rate is defined as the eroded thickness per time unit (nm/s). The sputter yield volume can be easily estimated by measuring the thickness of the polymer film (in nm), and the total fluence needed to sputter the given thickness (in PI/nm^2) during SIMS depth-profiling. The fluence is defined as the number of sputter primary ions (current x time) per area unit. Hence, the sputter yield volume is simply given by the sputtered volume to the total fluence ratio. The thickness can be determined by ellipsometry, if the optical properties of the polymer are known, or by profilometry. In the latter case, SIMS crater depth can be directly measured. Both of these techniques will be explained in §3.2, since they are used in this work for the estimation of sputter yield volume, Y, of polymer thin films.

3.1.6. Interlaced and non-interlaced mode

In order to obtain a ToF-SIMS depth-profile, either the “single beam” or “dual beam” mode can be adopted.[23] In both modes, the analyzed area needs to be significantly smaller compared to the sputtered area (being both a few hundreds of μm^2), in order to avoid crater edge effects. In the “single beam mode” the ion gun is continuously switched to perform the pulsed analysis and the DC sample erosion during a few seconds for each phase. However, because of the switching of the primary ion gun, reasonable sputter rates, effective data rate, and current stability are difficult to ensure. Instead, in the “dual ion beam mode”, the parameters of analysis and sputtering are totally decoupled. Indeed, it consists in using two different ion beams. A first beam is utilized at relatively high currents of 1-10 nA to erode the sample, called sputter beam. A second beam with relatively low current (close to 1 pA), called analysis beam, is used to analyze the center of the crater bottom created by the sputter beam. The temporal scheme of the so-called “interlaced mode” for dynamic-SIMS is provided in **Figure 6**.[23] The cycle time, i.e. the time between two consecutive analysis pulses throughout the secondary ions travel in the ToF analyzer, is ~100 µs. The cycle time is adjusted according to the highest masses that need to be detected. The analysis pulse is very short, typically <1 ns. The secondary ions extractor is activated after the sub-ns pulse of the analysis gun only for a few µs (e.g. 10 µs). Then, after a short delay, the sputtering starts, and lasts for 15-90 µs (60 µs in the timing diagram). In case of insulating samples, the flood gun is activated simultaneously to ensure the charge neutralization. Then, the sputter ion pulse and the charge compensation are interrupted, and the cycle can start again. This operational mode optimizes the data rates, the sampling being quasi-continuous, and the detection limits.

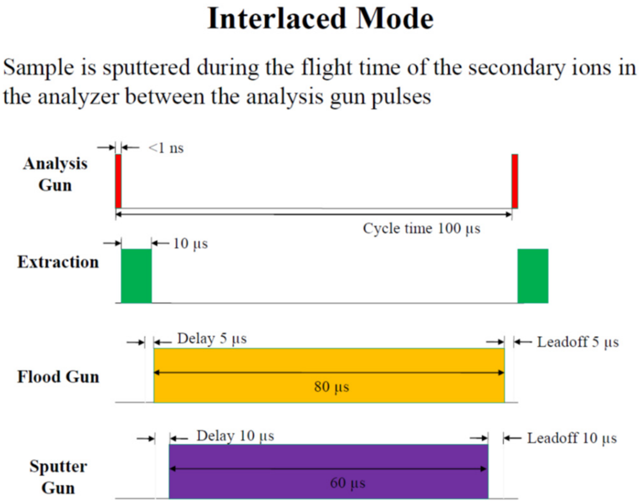

Figure 6. *Temporal diagram of the dual beam interlaced mode for ToF-SIMS depth profiling, including the charge compensation of the sample performed by an electron flood gun.*[24]

However, when the charging of the sample induced by the analysis and/or the sputter beams is high, especially in the case of thick, non-conductive polymer films, another approach exists. This is the so-called “non-interlaced” mode, in which the interruption of the analysis and sputtering is identical to the single beam mode. This approach has been applied in most of the SIMS depth-profiling experiments conducted in this thesis. The timing diagram of the non-interlaced mode is illustrated in **Figure 7**. It can be observed that the analysis sequence, that lasts for 1.64 s in the schematic, is made by pulsing the analysis gun and, then, extracting the emitted secondary ions after each one for few µs. The charge neutralization is carried out also during the analysis sequence in the remaining part of each cycle time (not shown in Figure 7). Then, the DC sputtering sequence follows together with the flood gun, until it stops leaving a pause time with only electron irradiation of the sample. This permits a more effective neutralization of the charge buildup during the ion bombardment. At the end of these three sequences of analysis, sputtering, and flood gun, a new analysis sequence can restart.

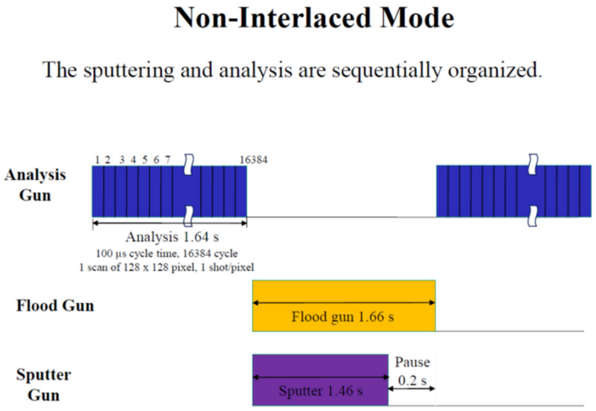

Figure 7. *Temporal diagram of the dual beam non-interlaced mode for ToF-SIMS depth profiling.*[24]

3.2. Techniques for thickness determination of thin polymer films

Two different techniques were mainly used in this thesis for the thickness determination of thin polymer films (from a few nm to several µm), in order to estimate the sputter yield volume of the investigated materials (refer to §3.1.5, 4.3, 6.6.3.4), i.e. the stylus profilometry and the ellipsometry. In the latter case, measurements of polymer single-layers were conducted on a spectroscopic ellisometer, while the more complex bi-layered structures were characterized by a single-wavelength ellipsometer. The principles of both techniques and a few details about the instrumentation utilized in the present work are provided hereafter.

Profilometry

A profilometer is an instrument used to profile the surface topography and waviness. Two different categories of profilers exist: contact versus non-contact profilometers.

In a contact profiler, a diamond stylus is moved vertically in contact with the sample surface. A schematic of a stylus profilometer is provided in **Figure 8.a.** The instrument can measure small surface variations in vertical stylus displacement as a function of position, typically ranging from a few nm to 1 mm. This is done mechanically with a feedback loop, that monitors the force from the sample pushing up against the stylus during the surface scan. A feedback system is employed to keep the force applied to the arm constant. The stylus height position creates an analogic signal, that is then converted into a digital signal, and stored for diplay and analysis. The stylus can be moved along the sample for a specified distance and contact force to perform a line scan, but also laterally across the sample to realize 3D mappings of the specimen surface. In contrast, a non-contact (or optical) profilometer uses light instead a physical probe, such as the low coherence interferometry.

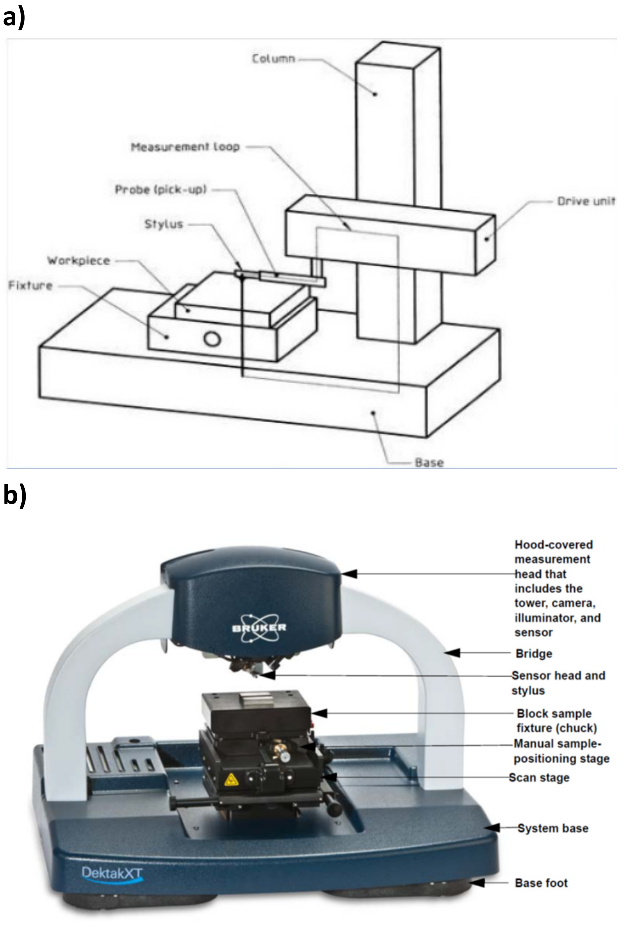

Figure 2-1: DektakXT Stylus Profiler with the Standard Manual X-Y Sample-Positioning Stage

Figure 8. *a) Schematic representation of a contact profiler.*[25] *b) DektakXT® stylus profiler used in this thesis for the thickness determination of thin polymer films.*

The optical profilers offer a series of advantages, like for instance higher speed of measurement (mainly dictated by the light reflected from the surface and the acquisition speed of the electronics), and higher reliability on the surface profile, since the sample is not touched by a physical probe that may damage it. However, contact profilometers show important advantages for the applications required in this thesis (mostly thickness determination, as already mentioned). Indeed, the method is not sensitive to surface reflectance or color, and consequently it is not influenced by the possible presence of surface contaminants. In general, better resolutions are achieved by using a stylus profilometer (strongly dependent on the tip geometry). And, more importantly, it is a direct technique, meaning that no modeling is required, conversely to the optical profilometry and the spectroscopic ellipsometry. This is the main reason of the use of a contact profilometer in this thesis for the confirmation of the thickness measurements conducted by ellipsometry, in addition to the more specific application to SIMS crater depth measurements.

In this work, a DextakXT® stylus surface profiler was employed as measurement tool of thin and thick film step height.[26] The DextakXT system is depicted in **Figure 8.b**. It also measures roughness in the nanometer range. In addition, it provides a step-height repeatability <0.6 nm, thanks to an automatic x-y and theta stage (not reported in Figure 8.b). A diamond-tipped stylus is used to profile the samples, with forces ranging from 0.01 to 0.15 mN depending on the application to soft or hard surfaces. The instrument is additionally equipped with the N-Lite+ Low Inertia Sensor (LIS) option, a system that permits to adjust the stylus force down to 0.0003 mN. This is particularly important for specific applications to polymer-based thin films, in order to use sub-micron styli without damaging the sample. The majority of the tips terminates in a 45° cone with an end radius from 25 μm down to 0.2 μm.

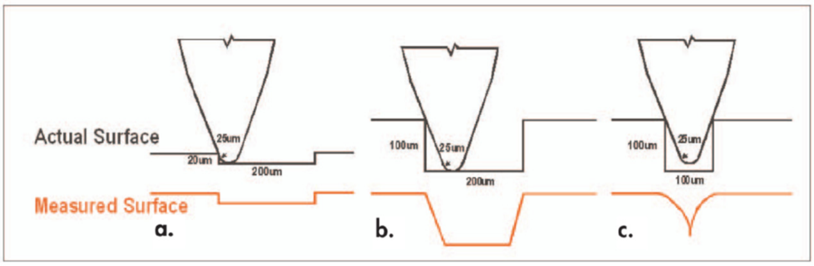

Figure 9. *Effect of the stylus geometry on the profile resolution. This 25-μm tip measures easily larger trenches (a), but cannot accurately measure the width (b) and height (c) as the aspect ratio of the trench increases.*[27]

The shape of the tip has a great impact on the resolution of the surface profile, as demonstrated in **Figure 9** referring to the case of a 25-µm stylus and a trench of increasing aspect ratio (height to width). In this thesis, the characterization of sub-micron lines and trenches was required. Thus, a sub-micron stylus of 0.7-µm radius was installed on the instrument to profile these very constrained areas (displayed in **Figure 10**).

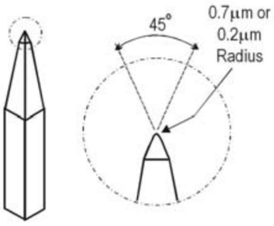

Figure 10. *Shape of the 0.7-µm stylus (diamond tip) installed on the DektakXT profiler for the thickness measurements.*[27]

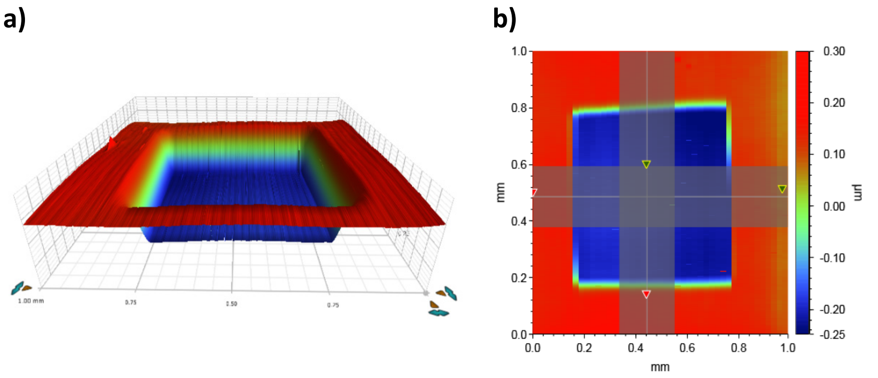

Figure 11. *a) 3D image of a SIMS crater performed on a 360-nm thick PS layer deposited on Si substrate, and b) averaged estimation of the crater depth in correspondence of the SIMS analysis area (200 x 200 µm²) concentric to the sputtered area (600 x 600 µm²), as indicated by the gray intersection region (cursor width: 200 µm).*

Figure 11 shows a typical 3D image obtained by stylus profilometry from a SIMS crater created on a 360-nm thick film of PS spin-coated onto a Si wafer. The determination of the crater depth is averaged over a 200 x 200 µm^2 area concentric to the crater edges, and corresponding roughly to the area from which the SIMS mass spectra are recorded. Stylus profilometry has also been used for the determination of the thickness of polymer layers by means of 2D and 3D scans of the sample surface after the incision of the film with a very sharp blade (refer to §4.3.2.2).[28] An example of 3D image of the scratch performed on a 220-nm PS film is illustrated in **Figure 12**.

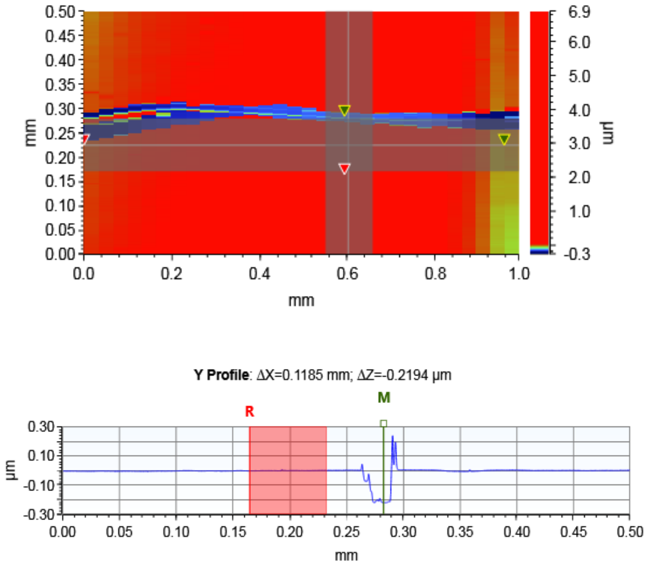

Figure 12. *3D map of an incision performed on a 220-nm thick PS layer deposited on Si substrate (on the top) and the related Y profile (on the bottom). The polymer surface appears in red color, whereas the silicon substrates is in blue.*

Ellipsometry

Ellipsometry is a technique based on the measurement of the relative phase change of polarized light after reflection from a thin film, in order to characterize its optical functions, such as the refractive index (n) and the absorption coefficient (k), and other properties like, for instance, the film thickness. Indeed, it is known to determine the thickness of single layers or multi-layered structures ranging from a few angstroms to several microns with an excellent accuracy, which is the interest of the study of Chapter 4. Additionally, as an optical technique, ellipsometry ensures a non-destructive and contactless analysis of the samples. Ellipsometry is also an indirect technique, i.e. the measured data need the application of a model analysis and a regressional data fitting procedure. This is based on the use of mathematical relations called dispersion formulae with specific fit parameters, to be converted in the optical constants of the samples, and to characterize the film thickness.

Figure 13 illustrates the schematic setup of an ellipsometric measurement.[29,30] Electromagnetic radiation is emitted by a light source, and linearly polarized by a polarizer. It can pass through an optional compensator (retarder, quarter wave plate; not shown in the schematic), before reaching the sample. After reflection, the radiation passes a compensator (not shown because optional) and a second polarizer, which is called analyzer, and then arrives at the detector. The light reflected by the sample has elliptical polarization (origin of the term “ellipsometry”). There are two different ellipsometer configurations, where the light is modulated either by a rotating analyzer (RAE) or by a rotating polarizer (RPE). Furthermore, ellipsometry is a specular optical technique (i.e. the angle of incidence and the angle of reflection are equal). The Fresnel theory is the most applied model for the interpretation of the ellipsometric data. Based on this model, the electric field of an incident linearly polarized electromagnetic radiation is decomposed in two orthogonal components, one normal to the incidence plane E_s (the "s" is contributed from the German "senkrecht", that means perpendicular), and the other one E_p parallel to it.

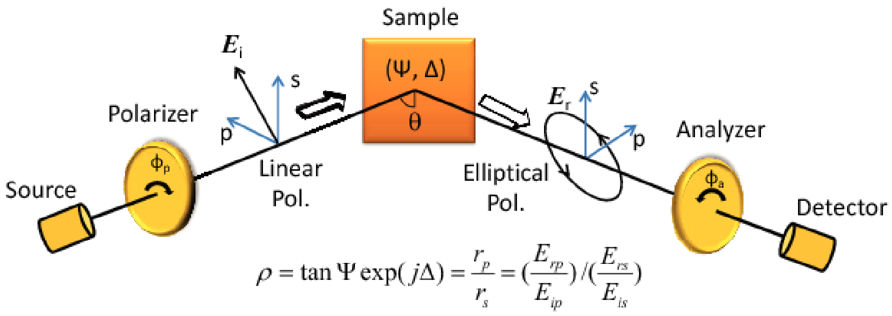

Figure 13. *Schematic overview of spectroscopic ellipsometry measurements, including the fundamental units of the instrumentation. A linearly polarized plane radiation is converted into an elliptically polarized radiation upon reflection from the sample.*[31]

Figure 13 also reports the fundamental equation of ellipsometry (**Equation (3)**),[29] that is:

$$\rho = \frac{r_p}{r_s} = \tan(\psi)e^{i\Delta} \tag{3}$$

Ellipsometry measures the complex reflectance ratio, ρ, of a system, which may be parametrized by the amplitude component ψ and the phase difference

Δ. The amplitudes of the "s" and "p" components of the beam, after reflection and normalized to their initial value, are denoted by r_s and r_p, respectively (cf. Figure 13). Thus, ellipsometry measures the complex reflectance ratio ρ, (a complex quantity), which is the ratio of r_p over r_s. Thus, tan(ψ) is the amplitude ratio upon reflection, and Δ is the phase shift (difference). Since ellipsometry is measuring the ratio (or difference) of two values (rather than the absolute value of either), it is a very accurate and reproducible technique.

The two independent parameters ψ and Δ do not possess a direct physical meaning (they are pseudo angles). However, they permit to determine optical properties of the sample (complex refractive index or dielectric function), as well as geometrical properties such as the film thickness. To this purpose, a model need to be built, which considers the optical constants and thickness parameters of the single layers of the sample including their sequence. Using an iterative procedure, the unknown optical constants and/or thickness parameters are varied. So, ψ and Δ values are calculated using the Fresnel equations. The calculated ψ and Δ values which match the experimental data best provide the optical constants and thickness of the specimen. The most commonly used dispersion functions (mathematical models that simulate the optical behaviors of materials) are: Cauchy[32] and Lorentz (Classical)[33] for transparent or weakly absorbing films; Amorphous, New Amorphous, and Tauc-Lorentz for semi-transparent materials (dielectrics, polymers, semiconductors absorbing in the VIS/FUV); and Drude for metals.[34] The Cauchy model is historically the first (1836) to deal with the dependence of the refraction index on the wavelength (λ) for transparent materials (**Equation (4)**)[30,32]:

$$\begin{cases} n(\lambda) = \mathrm{A} + \dfrac{B}{\lambda^2} + \dfrac{C}{\lambda^4} + \dots \\ k(\lambda) = 0 \end{cases} \tag{4}$$

Generally, the first two terms are sufficient, where the coefficient A represents the static refractive index for λ → ∞. A second formulation of the Cauchy model was developed for weakly absorbing materials. A non-zero extinction coefficient (k) is now given by an expression similar to the previous used for n(λ). For further details, refer to the technical notes Horiba.[32] Instead, for polymer materials such as PS and PMMA, the "New amorphous" model (formulated by Horiba)[35,36] is particularly well suited. In this case the absorption/extinction coefficient as a function of energy is given by **Equation (5)**:

$$k(\omega) = \begin{cases} \dfrac{f_j.(\omega-\omega_g)^2}{(\omega-\omega_j)^2+\Gamma_j^2}; & \omega > \omega_g \\ 0 \qquad ; & \omega \leq \omega_g \end{cases} \tag{5}$$

and the refractive index is expressed as follows (**Equation (6)**):

$$n(\omega) = n_\infty + \frac{B.(\omega-\omega_j)+C}{(\omega-\omega_j)^2+\Gamma_j^2} \tag{6}$$

where n_∞ represents n for ω → ∞ (its value is >1), and four parameters describe the absorption/extinction coefficient (f_j, Γ_j, ω_j, and ω_g). A detailed description of the formulation of the "New amorphous" model can be found in the technical notes provided by Horiba.[35]

In this thesis, two different typologies of ellipsometry were adopted, i.e. spectroscopic and single-wavelength ellipsometry. Spectroscopic or multi-wavelength ellipsometry (SE) employs a broad band light source, which covers a certain spectral range in the infrared, visible or ultraviolet spectral region. In this specific case, a spectroscopic ellipsometer Uvisel from Horiba-Jobin-Yvon at an incidence angle of ca. 70°, and operating in a wavelength range from 210 to 880 nm (Uvisel VIS spectral range), was employed for the thickness determination of polymer single-layers deposited on Si (see §4.3.2.2). The picture of the experimental apparatus is shown in **Figure 14**. Ellipsometric data were fitted using the DeltaPsi 2 software with a three-layer model: silicon (bulk), native silicon oxide (1.7-nm thickness), and a single photoresist film of variable thickness. The refractive index of this polymer film was generally modeled as a New Amorphous layer.

Figure 14. *Spectroscopic ellipsometer Uvisel from Horiba-Jobin-Yvon used in this thesis.*[37]

The tabulated optical constants of Si and SiO_2 were used. The measurements were repeated 3-5 times at different points on the sample surface to obtain an average thickness. A single-wavelength ellipsometer was used for the thickness characterization of the bilayered polymer structures on Si substrates. In this thesis, a Digisel rotating compensator ellipsometer from Jobin-Yvon/Sofie Instruments (not shown), working with a monochromatic light source emitting at 632.8 nm (He-Ne laser), was employed. The experimental procedure will be extensively explained in §4.3.2.2.

3.3. References

[1] Online help in the IONTOF software "SurfaceLab version 6.5", Hardware reference - Instrument Overview - Location of Instrument units.

[2] Bi Nanoprobe. https://www.iontof.com/bi-nanoprobe-bismuth-organic-inorganic-sims-applications.html

[3] F. Kollmer. Cluster primary ion bombardment of organic materials. *Applied Surface Science* **2004**, *231*, 153.

[4] Online help in the IONTOF software "SurfaceLab version 6.5", Hardware reference - Bi NanoProbe - Schematic overview.

[5] J. C. Vickerman, D. Briggs. ToF-SIMS: materials analysis by mass spectrometry. IM Publications and SurfaceSpectra, Chichester & Manchester, 2nd edition, **2013**, Chapter 10, 272.

[6] F. Kollmer, P. Hoerster, A. Duetting (Ion-Tof Technologies GmbH) *US8525125 B1*, **2013**.

[7] Online help in the IONTOF software "SurfaceLab version 6.2", Hardware reference - GCIB ion column - General description.

[8] J. C. Vickerman, D. Briggs. ToF-SIMS: materials analysis by mass spectrometry. IM Publications and SurfaceSpectra, Chichester & Manchester, 2nd edition, **2013**, Chapter 10, 274.

[9] Ion sources, ionization and desorption methods (Universität Basel). http://www.chemie.unibas.ch/~tulej/Mass%20Spectrometry/Mass_Spectr2_2011.pdf

[10] I. S. Gilmore, M. P. Seah. Electron flood gun damage in the analysis of polymers and organics in time-of-flight SIMS. *Applied Surface Science* **2002**, *187*, 89.

[11] I. S. Gilmore, M. P. Seah. Investigating the difficulty of eliminating flood gun damage in TOF-SIMS. *Applied Surface Science* **2003**, *203*, 600.

[12] A. G. Shard, R. Havelund, M. P. Seah, S. J. Spencer, I. S. Gilmore, N. Winograd, D. Mayo, T. Miyayama, E. Niehuis, D. Rading, R. Moellers. Argon cluster ion beams for organic depth profiling: Results from a VAMAS interlaboratory study. *Analytical Chemistry* **2012**, *84*, 7865.

[13] I. Retzko. Pulsplasmapolymerisation von Acetylen, Ethylen, 1,3-Butadien und Styrol. Ph.D. Thesis, Free University, Berlin, **2001**.

[14] U. Oran. Surface chemical characterization of plasma-chemically deposited polymer films by time of flight static secondary ion mass spectrometry. Ph.D. Thesis, Free University, Berlin, **2005**.

[15] Online help in the IONTOF software "SurfaceLab version 6.5", Hardware reference - Flood gun - Introduction.

[16] J. C. Vickerman, D. Briggs. ToF-SIMS: materials analysis by mass spectrometry. IM Publications and SurfaceSpectra, Chichester & Manchester, 2nd edition, **2013**, Chapter 9, 249.

[17] L. Kelner, S. P. Markey. Energy distribution of secondary organic ions. *International Journal of Mass Spectrometry and Ion Processes* **1984**, *59*, 157.

[18] A. Delcorte, X. Vanden Eynde, P. Bertrand, D. F. Reich. Influence of the primary ion beam parameters (nature, energy, and angle) on the kinetic energy distribution of molecular fragments sputtered from poly (ethylene terephthalate) by kiloelectron volt ions. *International Journal of Mass Spectrometry* **1999**, *189*, 133.

[19] Time-of-Flight (TOF) Analysis (University of Bristol).
http://www.chm.bris.ac.uk/ms/tof.xhtml

[20] J. C. Vickerman, D. Briggs. ToF-SIMS: Surface analysis by mass spectrometry. IM Publications and SurfaceSpectra Limited, Manchester, 1st edition, **2001**.

[21] Online help in the IONTOF software "SurfaceLab version 6.5", Hardware reference - Analyser - Operation - Overview.

[22] D. Rading, R. Moellers, H.-G. Cramer, E. Niehuis. Dual beam depth profiling of polymer materials: Comparison of C_{60} and Ar cluster ion beams for sputtering. *Surface and Interface Analysis* **2013**, *45*, 171.

[23] J. C. Vickerman, D. Briggs. ToF-SIMS: materials analysis by mass spectrometry. IM Publications and SurfaceSpectra, Chichester & Manchester, 2nd edition, **2013**, Chapter 23, 617, and references herein.

[24] SIMS XVIII international conference: Short course on SIMS depth-profiling, available on
http://www.simssociety.org/PPT/fredstevieXVIII/1_Depth_Profiling_083111.pdf

[25] S. Nair. Surface properties - Measurement techniques - Profilometer. http://www.slideshare.net/SandeepNair41/optical-profiler

[26] DektakXT Stylus Profiler. https://www.bruker.com/fileadmin/user_upload/8-PDF-Docs/SurfaceAnalysis/StylusProfilometry/Brochures/B516-RevB2-DektakXT_Stylus_Profiler-Brochure.pdf

[27] Dektak stylus capabilities: How to choose the correct stylus for any application https://www.bruker.com/fileadmin/user_upload/8-PDF-Docs/SurfaceAnalysis/StylusProfilometry/ApplicationNotes/AN526-Dektak_Stylus_Capabilities_How_to_Choose_the_Corre.pdf

[28] R. F. M. Lobo, M. A. Pereira-da-Silva, M. Raposo, R. M. Faria, O. N. Oliveira Jr, M. A. Pereira-da-Silva, R. M. Faria. In situ thickness measurements of ultra-thin multilayer polymer films by atomic force microscopy. *Nanotechnology* **1999**, *10*, 389.

[29] Ellipsometry. https://en.wikipedia.org/wiki/Ellipsometry

[30] G. Stracci, F. De Matteis Libello di Ellissometria e Spettrofotometria. http://docplayer.it/2311933-Libello-di-ellissometria-e-spettrofotometria-g-stracci-f-de-matteis.html

[31] M. Neshat, et al. Developments in THz range ellipsometry. http://inspirehep.net/record/1376195/plots

[32] Online Horiba technical notes: Cauchy and related Empirical Dispersion Formulae for Transparent Materials.

[33] Online Horiba technical notes: Classical Dispersion Model.

[34] http://www.horiba.com

[35] Online Horiba technical notes: New Amorphous Dispersion Formula.

[36] Online Horiba technical notes: Forouhi-Bloomer alias Amorphous Dispersion Formula.

[37] Spectroscopic ellipsometry. http://www.horiba.com/scientific/products/ellipsometers/spectroscopic-ellipsometers/uvisel/uvisel-spectroscopic-ellipsometer-covering-a-range-from-fuv-to-nir-640/

EXPERIMENTAL RESULTS

CHAPTER 4
Fundamental study on molecular depth-profiling of polymers by large argon clusters

4.1. General introduction

In the last few years the application of argon gas cluster ion beams (GCIB) in SIMS molecular depth-profiling of polymers (conventionally synthesized, plasma-deposited, plasma-treated, etc.) and other organic materials has rapidly increased worldwide. Indeed, massive argon cluster projectiles produce a “low damage” etching of organic/polymer systems compared to the previous sputter ion beams, allowing the preservation of structure-related (or molecular) information of the material. The versatility of GCIB in SIMS molecular depth-profiling induces a pressing need to predict the argon cluster sputter yield of organic and polymer systems for experimental planning and quantification of depth-profiles (conversion of the sputtering time in depth scale).

Recently, two empirical equations have been developed, independently by Seah[i] and Cumpson et al.[ii], to estimate sputter yields by fitting their few parameters to experimental data. These equations have been already applied successfully to data sets concerning some polymer materials (polystyrene, poly (methyl methacrylate), and polycarbonate), with high molecular weight and polydisperse. However, the first section of this chapter will show an effect of the polymerization degree on the sputtering efficiency of two model polymers, that should be taken into account in the studies of the sputter yields. The finding has been published in 2014, and these experimental data has been used by Seah (2015) to evaluate the effect of the molecular weight or the end-group density on the fit parameters of the “universal” sputtering equation. The sputtering yields and their dependence on the molecular weight have also been predicted by molecular dynamics simulations.[iii] The second section of the chapter is focused on the investigation of the effects of

---

[i] M. P. Seah. Universal equation for argon gas cluster sputtering yields. *The Journal of Physical Chemistry C* **2013**, *117*, 12622.

[ii] P. J. Cumpson, J. F. Portoles, A. J. Barlow, N. Sano. Accurate argon cluster-ion sputter yields: Measured yields and effect of the sputter threshold in practical depth-profiling by X-ray photoelectron spectroscopy and secondary ion mass spectrometry. *Journal of Applied Physics* **2013**, *114*, 124313.

[iii] A. Delcorte, M. Debongnie. Macromolecular sample sputtering by large Ar and CH_4 clusters: Elucidating chain size and projectile effects with molecular dynamics. *The Journal of Physical Chemistry C* **2015**, *119*, 25868.

the thickness of ultrathin model polymer layers and the nature of the substrate (hard versus soft) on the efficiency of the sputtering process. The thickness dependence of the sputter yields will provide important insights about the physics underlying this phenomenon, as well as useful recommendations to properly compare sputter yield data from different organic/polymer systems.

4.2. Argon cluster sputtering of polymers: Effects of cluster size and molecular weight

(Ar Cluster Sputtering of Polymers: Effects of Cluster Size and Molecular Weights. Surface and Interface Analysis 2014, 46 (S1), 79-82; DOI: 10.1002/sia.5424 and 10.1002/sia.5668)

4.2.1. Abstract

This fundamental contribution on time-of-flight secondary ion mass spectrometry (ToF-SIMS) polymer depth-profiling by massive argon clusters is focused on the investigation of the influence of the Ar cluster size and the molecular weight of the investigated polymers on the efficiency of the sputtering process. For this purpose, 100-nm thin films of poly (methyl methacrylate) (PMMA) and polystyrene (PS), with a range of molecular weights (10^3 – 1.5×10^5 amu) spin-coated onto Si wafers, are sputtered by 10 keV Ar_n^+ cluster ions with selected sizes (1500, 3000, 5000 atoms/cluster) employing Bi_5^+ as analysis source. The experiments show that the sputtering yield volume (nm^3/primary ion), Y, decreases with the increase of the molecular weight, M_w, for a selected cluster size and, at constant molecular weight, Y decreases with the increasing cluster size.

The experimental results are in good agreement with molecular dynamics (MD) simulations and previous studies for high molecular weight PS. Furthermore, the trend of Y versus M_w seems to be related to the variation of the glass transition temperature (T_g) of the investigated polymers.

4.2.2. Introduction

An important innovation in SIMS depth-profiling of organic materials and, in particular, polymers concerns the recent introduction of gas cluster ion beams (GCIBs) to perform the sputtering process. Nowadays, the most widespread superclusters are those based on argon and constituted of hundreds to thousands of atoms. In molecular depth-profiling, Ar cluster ions offer more promising results compared to smaller polyatomic ion beams.[1] Cluster beams developed and commercialized in the last decade, such as SF_5 and C_{60}, are not adequate for the molecular depth-profiling of certain classes of organic materials, because of severe chemical damage induced by the ionic bombardment,[2] which prevents the retention of distinctive fragments of the investigated systems. Emblematic cases are polystyrene (PS) and polycarbonate (PC). In order to improve the depth-profiling of these polymers with C_{60}^{n+} ion guns, a nitric oxide gas dosing combined with the sample cooling can be used to limit the cross-linking processes which occur upon sputtering.[3] However, this makes the experiment more complex and hazardous (NO is highly poisonous). In contrast, those polymers can be readily profiled by means of GCIBs, as demonstrated by Ninomiya et al.[4] in 2009, so that Ar clusters constitute a more universal probe for molecular depth-profiling than the predecessors. A key factor of the success of GCIBs is that each atom of the massive cluster has an energy of the order of only a few eV, comparable to the dissociation energy of the polymer chemical bonds. This leads to a reduction of the thickness of the beam-induced altered layer and of the bond breaking and degradation induced in the surface with, at the same time, sufficient sputtering yields to wipe out that damage upon repeated bombardment.[5] The combination of these aspects ensures the retention of molecular information of the initial system through the depth-profiling experiment. Furthermore, with large Ar clusters, one can select both the energy and the number of atoms in the projectile, allowing us to modulate several experimental parameters and to carefully test their influence on the sputtering yields, the degree of fragmentation or the depth resolution of the profiles. In this context a study conducted by Moritani et al.[6] suggests the possibility of breaking specific bonds of a PS target by properly adjusting the energy per atom of the gas cluster ion by simple selection of the cluster size.

Recently, Seah published an analysis on Ar gas cluster sputtering yields of both inorganic and organic materials as a function of the beam energy (E) and the cluster size (n).[7] The analysis of polymer systems, such as PS, PMMA and PC, is based on the yield data and concerns mainly high molecular weights and high polydispersity. The article determines a simple empirical universal equation for the sputtering yields, with three fitting parameters whose meaning is qualitatively discussed in the paper. However, the influence of the material properties on the sputtering induced by large gas cluster ions is not fully understood yet, especially in the case of complex organic materials. The aim of the present contribution consists in the investigation of the influence of the molecular weight of two classical model polymers, PS and PMMA, and the Ar cluster size on the sputtering efficiency.

4.2.3. Materials and methods

4.2.3.1. Samples

PS and PMMA standards for gel permeation chromatography (GPC) with a range of molecular weights (10^3 – 1.5×10^5 amu) were purchased from Sigma-Aldrich Inc. and Scientific Polymer Products, Inc. PS 286k and polydisperse PS were provided by Polymer Source, Inc. and Polyscience, Inc., respectively. Molecular weight (M_w), polydispersity (M_w/M_n) and source of all used polymers are specified in **Table 1**.

Polymer	M_w (amu)[a]	M_w/M_n[b]	Source
Polystyrene (PS)	1 110	1.12	SPP Inc.
	1 920	1.08	SA Inc.
	4 330	1.04	SA Inc.
	10 000	n.d.[c]	SA Inc.
	61 800	1.07	SPP Inc.
	139 000	1.03	SA Inc.
	286 000	1.06	PS Inc.
	125 000 – 250 000	Polydisperse	P Inc.
Poly (methyl methacrylate) (PMMA)	2 180	1.10	SA Inc.
	4 200	1.06	SA Inc.
	10 900	1.05	SA Inc.
	68 200	1.13	SPP Inc.
	150 000	n.d.	SA Inc.

[a]Molecular weight determined by GPC; [b]M_w/M_n, polysdispersity; [c]n.d., not determined.

Table 1. *Description of the employed polymers.*

Solutions of each polymer in toluene (Sigma-Aldrich, ≥ 99,71% purity) were prepared and spin-coated onto clean Si wafer of 1 x 1 cm^2 at 5000 rpm with acceleration 20000 rpm/s for 60 s. The wafers were sonicated in isopropanol prior to the coating and then dried under N_2 flux. Calibration curves of the thickness as a function of the solution concentration were performed in order to obtain ~100-nm thick films. The polymer layer thickness was estimated by ellipsometry and then verified by AFM measurements.

4.2.3.2. ToF-SIMS instrument

Molecular depth-profiling was performed using an ION-TOF TOF.SIMS 5 (Münster, Germany) instrument equipped with both Bi-LMIG and Ar-GCIB primary ion sources mounted at 45° to the surface normal. The secondary ions were collected by a time-of-flight analyzer perpendicular to the sample surface. The profiles, acquired only in positive polarity, were obtained in dual ion beam mode. 10 keV Ar_n^+ ions (0.3 nA) with selected cluster sizes in a range of 1250-7000 atoms/ion (with the full width at half maximum of 1400 to 2360 atoms/ion, respectively) were employed to sputter a 600 x 600 μm^2 area, and 30 keV Bi_5^+ ions (0.05 pA) for collecting the spectra from 200 x 200 μm^2 area concentric to the sputtered surface. Since the measurements showed excellent reproducibility, only two profiles per sample were acquired.

4.2.4. Results

The depth-profiles are characterized by a high stability of the characteristic fragment ion signals (for example: $C_6H_5^+$, $C_7H_7^+$, $C_8H_9^+$, $C_9H_7^+$ for PS and $C_2H_3O_2^+$, $C_3H_7O^+$, $C_4H_5O^+$, $C_5H_9O^+$ for PMMA) down to the silicon interface (not shown), indicating minimal chemical damage, as was already reported in the literature.[4] In order to study the effect of the molecular weight (M_w) and the cluster size (n) on the sputtering efficiency, the sputtering yield volumes in nm^3/primary ion (Y) were calculated. First, the fluence needed to reach the polymer/Si interface was determined (50% of the maximum intensity of the substrate signal – Si^+, m/z = 28). Then, the measured layer thickness was divided by this fluence.

In **Figure 1**, the sputtering yield volume is shown as a function of the molecular weight for PS (Figure 1.a) and PMMA (Figure 1.b). The evolutions obtained for three different Ar cluster ions (nominal mean cluster size of 1500, 3000 and 5000 atoms/ion, respectively)[iv] with constant initial energy of 10 keV are reported. For both polymers, Y decreases with increasing M_w for a given cluster size, showing two regions in the curves: below 60 000 amu, Y drops rapidly, then it becomes constant. In the case of

---

[iv] For the sake of clarity, the nominal Ar cluster sizes of 1500, 3000 and 5000 atoms/ion are given in the text. The measured cluster sizes of 1300, 1698, 2778, 5000 and 6549 are used to perform the scaling of Y and E by n in Figure 2. For the PS 286k the data were acquired at a later stage and so have slightly different n values. Consequently, Figure 2 may be converted into the Figure 1, since they derive from the same data set.

PS, the steady state is confirmed by additional measurements on PS 286k. The resulting Y values are very close to those found for PS 139k.

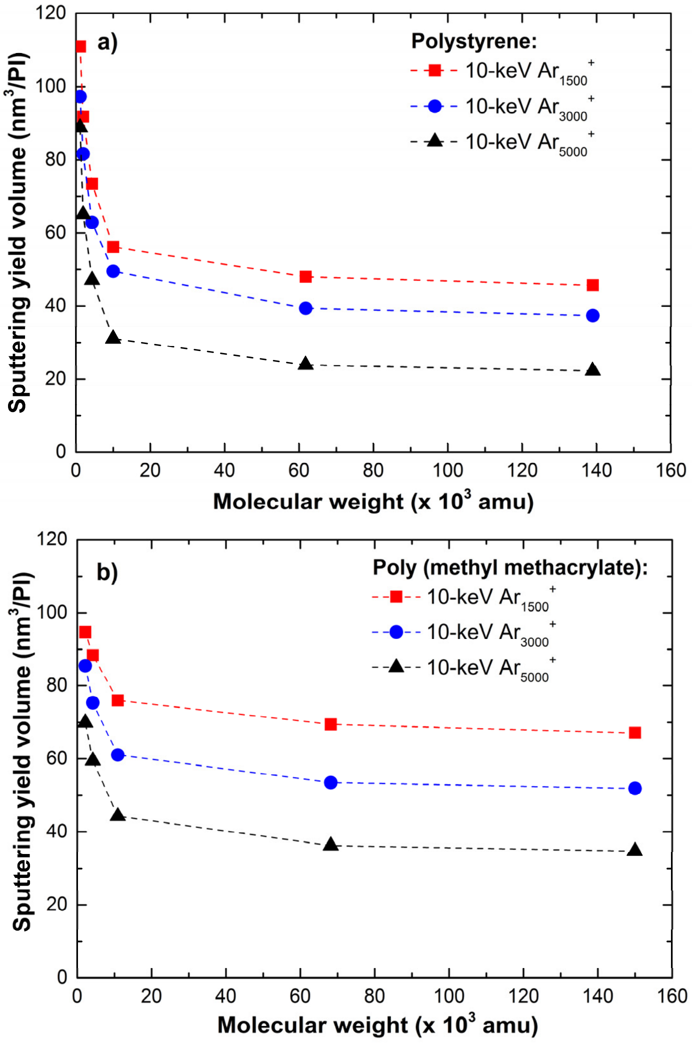

Figure 1. *Sputtering yield volume versus molecular weight of PS (a) and PMMA (b), obtained for three different 10-keV Ar cluster ions (nominal mean cluster size of 1500 – 3000 – 5000 atoms/ion, respectively).*

Figure 1 also shows that, at constant polymer molecular weight and constant projectile energy, Y decreases with increasing cluster size, i.e. when the energy per atom in the cluster decreases. This effect is better shown in **Figure 2**, which reports the sputtering yield volume per cluster atom, Y/n, as a function of the energy per atom, E/n, for PS (Figure 2.a) and PMMA (Figure 2.b). For both polymers it is observed that Y/n increases with increasing energy per atom. The increase is linear up to 7 eV per atom.

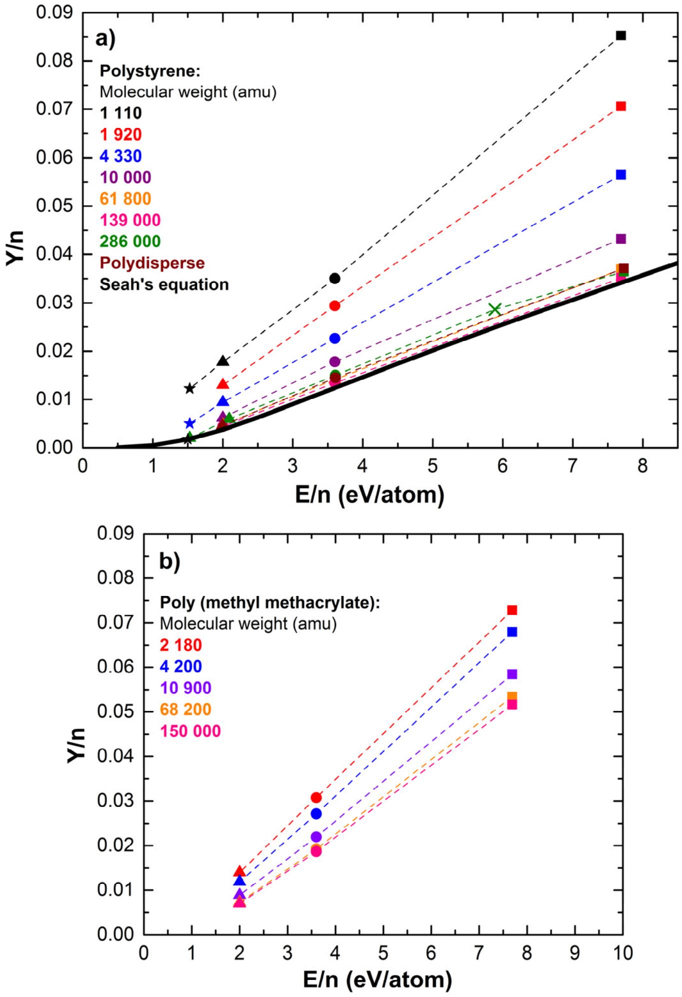

Figure 2. *Sputtering yield volume per cluster atom, Y/n, versus energy per atom, E/n, for PS (a) and PMMA (b) under 10-keV* Ar_n^+ *bombardment with cluster size in the range 1250-7000 atoms/ion.*[v]

Moreover, in the range of low M_w, an increase of the molecular weight of the polymer causes a reduction of Y/n at a selected E/n. The curves of Y/n for

---

[v] Measured Ar cluster sizes of 1300 (squares), 1698 (crosses), 2778 (circles), 5000 (triangles), and 6549 (stars) atoms/ion, respectively.

PS 61.8k, PS 139k, PS 286k and polydisperse PS are overlapped, confirming that the effect of the molecular weight on the sputtering becomes negligible beyond 60 000 amu.

4.2.5. Discussion

The trend of the sputtering yield volume as a function of the polymer molecular weight is in good agreement with the results obtained by molecular dynamics simulations on polyethylene samples bombarded with C_{60} projectiles.[8] In terms of physical properties of the polymers, it can also be related to the variation of the glass transition temperature (T_g) of the material as a function of M_w. T_g corresponds to the start of the translational motion of polymer chain segments and it is known to be essentially independent of the M_w, except for the region of low degrees of polymerization, where T_g increases with increasing M_w. Differential scanning calorimetry measurements[9] demonstrate that the T_g of PS is constant above M_w = 46 800, which corresponds roughly to the transition towards the plateau region of the sputtering yield volume in Figure 1.a (analogous considerations can be done for PMMA, Figure 1.b).[10] The anti-correlation between Y and T_g is illustrated in **Figure 3** for the case of Ar_{5000}^+ bombardment.

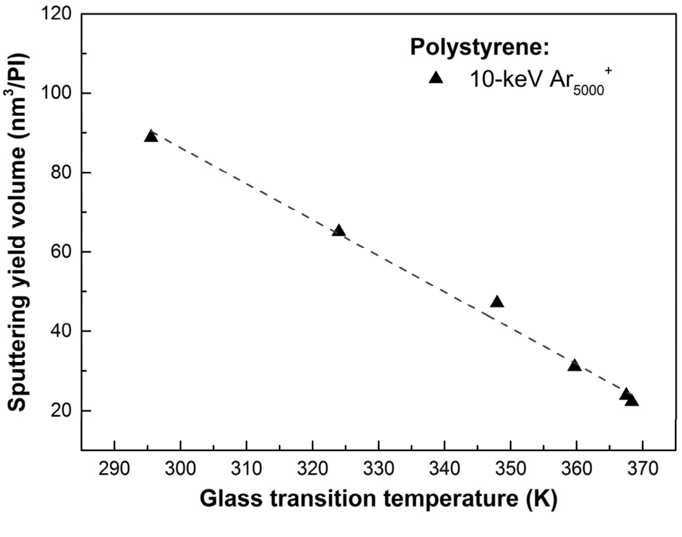

Figure 3. *Sputtering yield volume of PS under 10-keV* Ar_{5000}^+ *bombardment versus glass transition temperature.*

This relationship suggests that the physical parameters governing chain mobility in polymers also influence the soft sputtering by large argon clusters. However, additional theoretical work is required in order to better understand the underlying physics.

The comparison between PMMA and PS (Figure 1) indicates that the sputtering yield volumes are higher for the acrylic polymer and decrease more significantly with increasing molecular weight in the case of PS. These trends might be explained by the different radiochemical behavior of those materials.[1,11,12] Upon irradiation, PMMA tends to undergo chain-scission processes that favor the removal of beam-induced chemical damage. In contrast, PS undergoes prevalently cross-linking under ion bombardment, which disfavors the etching process and, consequently, lowers the sputtering yields.

The increase of Y/n as a function of E/n (Figure 2) is in agreement with the results of Rading et al. [13] for the higher molecular weights (>60 000 amu). This makes sense because their measurements were conducted on bulk samples of high M_w PS, PC and PMMA, bombarded by Ar_n^+ projectiles in the range of 2-10 eV/atom. In that study, a sputter threshold of ~1.4 eV/atom was also retrieved from the linear fit of Y versus E/n, obtained under Ar_{2000} and Ar_{5000} sputtering of PS. The results indicate that the threshold is independent of the cluster size and characteristic of the investigated material. The present contribution indicates that, if there is a sputter threshold (hypothesis of a linear fit), it varies with the molecular weight of the investigated polymer. The threshold would then increase with increasing M_w, as suggested by the linear regression of the experimental data. It is also possible to compare the yield data previously described with Seah's equation, which assumes a non-linear behavior at low E/n and the absence of threshold.[7] The equation for PS is based on the sputtering yields provided by Rading et al.[13] The energy range of the primary ions employed in that study is $2500 \leq E \leq 20000$ eV and the cluster sizes n = 500, 2000 and 5000, with incidence angle of 45°. For PMMA, the sputtering yields are taken from Ichiki's PhD thesis[14] and they refer to experiments conducted at normal incidence and non-size-selected Ar clusters. Since the applied experimental conditions for PMMA are different from this contribution, our comparison applies only to PS. It was indeed shown that there exists an angular dependence of the sputtering yield.[15] For instance, in the case of 5-10 keV Ar_{2000} bombardment of PS, the maximum yield was observed for an incidence angle of 45°.[13]

Finally, the agreement with Rading's measurements and Seah's model equation does not allow us to decide about the existence or absence of threshold in the case of our samples. To resolve this issue, additional measurements at lower E/n would be needed.

4.2.6. Conclusion

This fundamental contribution demonstrates that the sputtering yield volume is strongly dependent on the polymer molecular weight and the argon cluster size. Based on the relationship between T_g and M_w, we can speculate that Y is also related to the mobility of the oligomer chains, such as T_g. Nevertheless, in order to establish a better understanding of the involved phenomena, additional theoretical work should be undertaken.

4.2.7. References

[1] C. M. Mahoney. Cluster secondary ion mass spectrometry of polymers and related materials. *Mass Spectrom. Rev.* **2009**, *29*, 247.

[2] R. Möllers, N. Tuccitto, V. Torrisi, E. Niehuis, A. Licciardello. Chemical effects in C_{60} irradiation of polymers. *Appl. Surf. Sci.* **2006**, *252*, 6509.

[3] R. Havelund, A. Licciardello, J. Bailey, N. Tuccitto, D. Sapuppo, I. S. Gilmore, J. S. Sharp, J. L. S. Lee, T. Mouhib, A. Delcorte. Improving secondary ion mass spectrometry $C_{60}^{(n+)}$ sputter depth profiling of challenging polymers with nitric oxide gas dosing. *Anal. Chem.* **2013**, *85*, 5064.

[4] S. Ninomiya, K. Ichiki, H. Yamada, Y. Nakata, T. Seki, T. Aoki, J. Matsuo. Precise and fast secondary ion mass spectrometry depth profiling of polymer materials with large Ar cluster ion beams. *Rapid Commun. Mass Spectrom.* **2009**, *23*, 1601.

[5] B. Czerwinski, Z. Postawa, B. J. Garrison, A. Delcorte. Molecular dynamics study of polystyrene bond-breaking and crosslinking under C_{60} and Ar_n cluster bombardment. *Nucl. Instruments Methods Phys. Res. Sect. B Beam Interact. with Mater. Atoms* **2013**, *303*, 22.

[6] K. Moritani, G. Mukai, M. Hashinokuchi, K. Mochiji. Site-specific fragmentation of polystyrene molecule using size-selected ar gas cluster ion beam. *Appl. Phys. Express* **2009**, *2*, 046001.

[7] M. P. Seah. Universal equation for argon gas cluster sputtering yields. *J. Phys. Chem. C* **2013**, *117*, 12622.

[8] A. Delcorte, B. J. Garrison. Sputtering polymers with buckminsterfullerene projectiles: A coarse-grain molecular dynamics study. *J. Phys. Chem. C* **2007**, *111*, 15312.

[9] P. Claudy, J. M. Létoffé, Y. Camberlain, J. P. Pascault. Glass transition of polystyrene versus molecular weight. *Polym. Bull.* **1983**, *9*, 208.

[10] L. Andreozzi, C. Autiero, M. Faetti, M. Giordano, F. Zulli. Dynamics, fragility, and glass transition of low-molecular-weight linear homopolymers. *Philos. Mag.* **2008**, *88*, 4151.

[11] A. Chapiro, Radiation Chemistry of Polymeric Systems, John Wiley and Sons, New York & London, **1962**, 712.

[12] L. Calcagno. Ion-chain interactions in polymers. *Nucl. Instruments Methods Phys. Res. Sect. B* **1995**, *105*, 63.

[13] D. Rading, R. Moellers, H.-G. Cramer, E. Niehuis. Dual beam depth profiling of polymer materials: Comparison of C_{60} and Ar cluster ion beams for sputtering. *Surf. Interface Anal.* **2013**, *45*, 171.

[14] K. Ichiki. Study on size effect of cluster ion beam irradiation. Ph.D. Thesis, Kyoto University, **2012**.

[15] B. Czerwinski, L. Rzeznik, R. Paruch, B. J. Garrison, Z. Postawa. Effect of impact angle and projectile size on sputtering efficiency of solid benzene investigated by molecular dynamics simulations. *Nucl. Instruments Methods Phys. Res. Sect. B* **2011**, *269*, 1578.

4.3. Argon cluster sputtering of polymers: Influence of the thickness of nanoscale thin films

4.3.1. Abstract

This fundamental contribution on SIMS polymer depth-profiling by large argon clusters investigates the dependence of the sputter yield (Y) on the thickness (d) of ultrathin films as a function of the substrate nature, i.e. hard vs soft. For this purpose, thin films of two model polymers, namely polystyrene (PS) and poly (methyl methacrylate) (PMMA) with low molecular weight (~4 000 amu), are spin-coated onto hard substrates of silicon and, then, bombarded by 10-keV Ar_{3000}^+ ions. The investigated thickness range is ~15-230 nm. The results show a decrease of the sputtering yield volume Y (nm^3/primary ion) of ~20% with increasing thickness for both systems. More specifically, Y(d) presents an initial steep decay, that gradually attenuates till reaching a plateau slightly below 100 nm. PS films deposited onto a soft substrate, i.e. 143-nm thick PMMA layer, are also studied. In the latter case, Y does not vary significantly with the increase of thickness. Additionally, the influence of the polymer molecular weight (M_w) on Y(d) for PS thin films on Si is explored. The experimental observations are in good agreement with molecular dynamics computer simulations on organic ultrathin films. The thickness dependence of Y can be ascribed to the backreflection of the projectile energy deposited in the polymer film, caused by dense substrates like silicon in ultrathin overlayers, that can contribute to the sputtering process.

4.3.2. Introduction

For a long time, SIMS was limited to the surface analysis of polymers, due to the loss of distinctive structure-related information during the erosion of the sample with monoatomic projectiles. In the late 1990s, the advent of cluster-SIMS[1] paved the way for the molecular depth-profiling of polymer materials, and more generally of organics, thanks to the utilization of cluster ions like SF_5^+ and C_{60}^+ for sputtering. However, it was not until the development of massive Ar cluster ion beams (i.e. 5-10 keV $Ar_{500\text{-}5000}^+$) as sputter sources that molecular depth-profiling of polymers could be performed universally, including even aromatic polymers (e.g. polystyrene), where the more traditional fullerene ion beams failed.[2] In order to explain the greater success of massive Ar cluster ion sputtering of organic/polymer surfaces in cluster-SIMS, an extensive body of theoretical studies using MD simulations was conducted.[3,4,5] Simulations pointed out the minimal molecular degradation and fragmentation induced by the massive cluster impact (closer to the concept of desorption), compared to that of smaller polyatomic projectiles (like C_{60}^{+} ions).[6]

Several theoretical and experimental studies were devoted to the investigation of the effects of the Ar cluster energy and nuclearity, as well as the incidence angle, on the energy deposition and fragmentation of organic solids.[7,8] Additionally, the energy deposition pathways and the efficiency of ejection in organic solids were computationally investigated as a function of the overlayer thickness, first for the more popular fullerene projectiles,[9] and then for the large Ar cluster impact.[10,11] However, to our best knowledge, the effect of the thickness of ultrathin polymer layers (i.e. in the nanoscale) on the sputtering efficiency upon massive Ar cluster bombardment has not been experimentally investigated yet. Recently, experiments highlighted the influence of the molecular weight of two model polymers, namely PS and PMMA, on the sputtering yields,[12] which was successively clarified by MD simulations.[13] In this fundamental contribution, the same two polymers (i.e. PS and PMMA) were chosen, and the influence of their molecular weights was taken into account in the conception of the model systems to investigate.

In the present study, thin layers of (low M_w) PS and PMMA of different thickness, spin-coated onto two different substrates (silicon and PMMA), were bombarded by a 10-keV Ar_{3000}^{+} ion beam in order to look at the thickness dependence of the sputter yield. The sputtering efficiency is found to be strongly dependent on the overlayer thickness, only in the case of the silicon substrate. A simple phenomenological model is proposed for the description of the thickness dependence of the sputtering efficiency. MD simulations conducted with similar samples and ion bombardment conditions predict a significant increase of the sputtering yield for ultrathin layers on rigid substrates, induced by energy confinment in the polymer, and support our phenological model.

4.3.3. Materials and methods

4.3.3.1. Samples

Polystyrene and poly (methyl methacrylate) standards for gel permeation chromatography (GPC) with relatively low molecular weight (M_w) of ~4 000 amu, and high molecular weight of ~60 000 and 150 000 amu for PS and PMMA, respectively, were purchased from Sigma-Aldrich Inc. and Scientific Polymer Products, Inc.

Polymer	M_w (amu)[1]	M_w/M_n[2]	Source	Polymer name
Polystyrene	4 330	1.04	Sigma-Aldrich Inc.	PS 4k
	61 800	1.07	Scientific Polymer Products, Inc.	PS 60k
Poly(methyl methacrylate)	4 200	1.06	Sigma-Aldrich Inc.	PMMA 4k
	150 000	n.d.[3]	Sigma-Aldrich Inc.	PMMA 150k

[1] Molecular weight determined by GPC; [2] M_w/M_n, polydispersity; [3] n. d., not determined.

Table 1. *Description of the employed polymers.*

An overview of the polymer materials employed for the sample preparation is reported in **Table 1**.

Polymer ultrathin films were deposited onto 1 x 1 cm^2 silicon substrates covered by a native oxide layer, preventively cleaned by sonication in isopropanol (VWR Chemicals, 99.9% purity) and dried under nitrogen flux. PS 4k, PS 60k and PMMA 4k solutions were prepared in toluene (Sigma-Aldrich, purity ≥99.71%) with a concentration ranging from 7 to 72 g/L for PS and PMMA with low M_w, and from 6 to 54 g/L for PS 60k. This low pressure vapor solvent has been noticed to provide very smooth morphologies for the three resulting polymer layers by the spin coating technique,[14,15,16] an important requirement for the estimation of the sputter efficiency of ultrathin films. The solutions were then filtered using 0.2-µm Teflon filters to remove any non-dissolved particles and dust before their deposition on the Si supports. The solutions were spin-coated onto the silicon wafers at 5000 rpm with an acceleration of 20000 rpm/s for 60 s, in order to obtain polymer single-layers with thickness comprised between ~15 nm and ~230 nm. The quality of the PS 4k film series in terms of morphology and roughness as a function of the thickness was verified by AFM measurements.

The polymer films on Si represent 3 model systems of polymer single-layers of type I, PS 4k and PS 60k, and type II, PMMA 4k, respectively. In the particular case of PS, the additional influence of M_w (i.e. 4 000 versus 60 000 amu) on the thickness dependence of the sputtering efficiency is investigated. Silicon is a hard, relatively hydrophilic substrate, since no treatment was done to remove the outermost native SiO_x layer of the semiconductor. In order to study the effect of the substrate nature on Y(d), i.e. hard vs soft, a fourth model system was conceived. There, a soft substrate is simulated by a relatively thick polymer layer spin-coated onto Si to ensure a very smooth interface, which is not the case with commercial polymer sheets. Some known constraints exist in the polymer bilayer preparation as SIMS model systems, which are listed here: 1) the bottom layer should have minimal solubility in the solvent used to deposit the top layer, 2) high quality of both top film surface and polymer/polymer interface is required, and last but not least, 3) in the present study, a wide thickness range of the top layer is demanded. The work conducted by Ennis et al. provides an ideal system for this investigation: direct spin casting of PS thin films onto PMMA.[16] Indeed, it shows very smooth surfaces, with roughness of the uppermost PS layer comparable to that obtained with the correspondent single-layers spun-cast from toluene, and sharp interfaces (see Figure 4). Dynamic-SIMS reveals an interfacial width below the depth resolution limit of ~10 nm. The roughness of the PMMA layer seems to remain at a very low values <1 nm also after the deposition of the upper layer. Furthermore, the established protocol permits to play in windows of PS thickness of ~5-500 nm and M_w of ~3-15000 amu, but it also requires PMMA with M_w > 3000 amu. Thus, it was decided to spin-coat the same PS 4k of the single-layers onto PMMA 150k (high M_w to avoid its dissolution in the selective solvent of the PS). A unique solution of PMMA 150k was prepared in toluene, filtered and spin-coated onto several clean Si wafers at room temperature. The samples were left to dry for 24 hours. Then, filtered solutions of PS 4k in 1-chloropentane (Aldrich Chemistry, 99% purity) of increasing concentrations were deposited onto the PMMA 150k layers. None of the polymers was annealed after deposition. **Table 2** summarizes the 4 model systems used in this investigation, where the polymer names in italic indicate the outermost layers whose thickness is varied.

4.3.3.2. Ellipsometry

A spectroscopic ellipsometer (SE) Uvisel from Horiba-Jobin-Yvon was used to measure the thickness of the PS and PMMA single-layers (systems A-B-C in Table 2), in the wavelength range 300-800 nm with intervals of 10 nm at an incidence angle of 70°. The measurements were carried out at least three times at different points of the sample to obtain an average thickness. The data acquisition and consecutive modeling were performed with the DeltaPsi2 software. The systems A-B-C were modeled by a 3-layer structure with a silicon substrate covered by a dielectric layer, with the optical constants of SiO_2 and fixed thickness of 1.70 nm, and on top the PMMA or PS layer. The dispersion formula used for the polymer layer is called “New Amorphous” (refer to §3.2), and it is derived from Forouhi-Bloomer formulation.[17,18]

Model system	Sample	Polymer film thickness[1]
A) *PS 4k* / Si 	A1	17.5 ± 0.0 nm
	A2	36.4 ± 0.4 nm
	A3	60.9 ± 0.3 nm
	A4	87.8 ± 0.1 nm
	A5	194.0 ± 0.2 nm
B) *PMMA 4k* / Si 	B1	15.7 ± 0.3 nm
	B2	27.9 ± 1.1 nm
	B3	37.6 ± 0.1 nm
	B4	56.3 ± 0.2 nm
	B5	89.7 ± 0.1 nm
	B6	199.3 ± 2.4 nm
C) *PS 60k* / Si 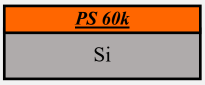	C1	16.1 ± 0.4 nm
	C2	34.4 ± 0.1 nm
	C3	72.8 ± 0.5 nm
	C4	130.9 ± 0.3 nm
	C5	230.2 ± 0.8 nm
D) *PS 4k* / PMMA 150k / Si 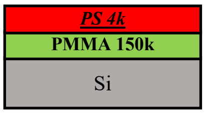		• PS 4k layer:[2]
	D1	27.5 ± 0.4 nm
	D2	67.3 ± 4.0 nm
	D3	92.1 ± 1.8 nm
	D4	128.0 ± 5.1 nm
	D5	156.0 ± 1.6 nm
	D6	235.0 ± 1.3 nm
		• PMMA 150k layer:[2]
	D0	143.3 ± 1.2 nm (constant)

[1] Determined by spectroscopic ellipsometry

[2] Determined by single-wavelength ellipsometry

Table 2. *Description of the four investigated model systems, sample names and related thickness values.*

The "New Amorphous" model works particularly well for amorphous polymers like PS and PMMA and, more generally, for amorphous materials exhibiting an absorption in the visible and/or far ultraviolet (100-200 nm) range. The difference between the given model and the experimental data, indicated by the mean square error value (MSE), were in most of the cases below 1, showing an acceptable quality of the fitting. The results of the SE regression analysis of the polymer layers were also compared with those obtained from other models, i.e. Cauchy[19,20] and Classical (Lorentz). The comparison leads to no significant variations of the thickness values when changing the dispersion formula. A further verification of the quality of the data modeling consisted in the comparison of the post-calculated n values at constant wavelength with those reported in the literature.[21, 22, 23] Additionally, the ellipsometry measurements were compared to the thickness estimations from AFM images of scratches performed on the PS 4k single-layers (system A).[24] As reported in **Figure 1**, the measured step for sample A1 is 17.5 nm, in good agreement with the SE value of 17.5 ± 0.0 nm, while for sample A5 it is 198 nm (vs 194.0 ± 0.2 nm in SE).

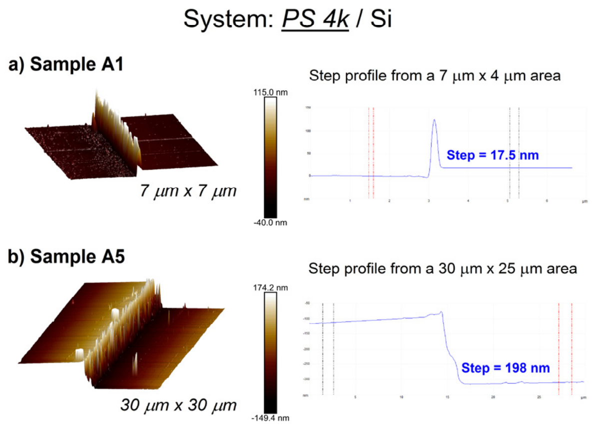

Figure 1. *Tridimensional AFM images of a single edge of the incisions performed on the samples A1 and A5 of the PS 4k single-layer system (left side) and step profiles obtained from pre-selected areas of the AFM images for an averaged estimation of the polymer film thickness (right side).*

In the case of the polymer bilayer (system D), because of the very similar optical properties of PS 4k and PMMA 150k, the thickness was determined more accurately by a Digisel rotating compensator ellipsometer from Jobin-Yvon/Sofie Instruments (single-wavelength ellipsometer working at 632.8 nm), imposing the n of the two materials. Firstly, the PMMA 150k single-layer of the D-system series (sample D0) was measured. Then, its thickness was assumed to remain unvaried after spin-coating of the upper PS layer, so that the topmost polymer layer was characterized. This procedure is validated by prior studies demonstrating that there is no significant reduction in the PMMA thickness or roughening after the deposition of the PS solution in 1-chloropentane.[16] Moreover, in order to validate this data treatment in ellipsometry, including the selection of refractive indices for PMMA and PS, sample D2 was additionally analyzed by X-ray reflectivity (XRR). The total thickness found by fitting was 210.0 nm, very close to the ellipsometry value of 143.3 nm + 67.3 nm = 210.6 nm. The results of the thickness measurements are summarized in Table 2.

4.3.3.3. ToF-SIMS molecular depth-profiling

The molecular depth-profiles, acquired in positive ion polarity, were obtained in non-interlaced dual ion beam mode. A 10 keV Ar_{3000}^+ cluster ion beam (0.3 nA, 0.1 nA and 0.05 nA) was employed to sputter a 600 x 600 μm^2 area. The argon cluster size distributions used to profile the different model systems are shown in **Figure 2**. A pulsed beam of 30 keV Bi_5^+ ions (0.06 pA) was used to collect the mass spectra from a 200 x 200 μm^2 area, concentric to the sputtered surface. A 20 eV electron flood gun was employed for charge compensation.

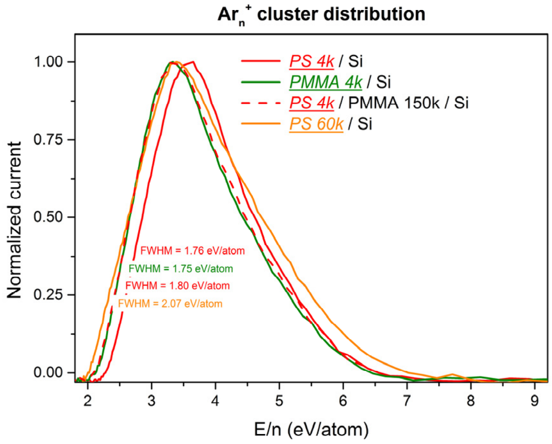

Figure 2. *10 keV Ar_n^+ (n ~3000 atoms) cluster ion distributions used for the SIMS depth-profiling of the Si-supported PS 4k, PMMA 4k and PS 60k single-layers, and the PS 4k / PMMA 150k bilayer. The average energy per constituent atom is ~3.5 eV. The full width at half maximum (FWHM) for all the cluster distributions is <2000 atoms.*

The four model systems described in §4.3.2.1 were analyzed with three different sputter currents of 0.3, 0.1 and 0.05 nA, depending on the thickness of the polymer (single- or bilayer) film deposited on the Si substrate. Especially for the thinnest films, the sputter current had to be lowered in order to record a reasonable number of scans along the polymer depth, so that an accurate determination of the polymer/Si interface was made possible. For the PS 4k/ PMMA 150k bilayer, all the SIMS measurements were acquired at the higher current, that is 0.3 nA. Indeed, in these erosion conditions it was feasible to profile in reasonable times thick layer systems as the one under investigation where, in addition, one of the polymer layer possess high M_w and relatively low sputter rate. Since the overall SIMS measurements showed high reproducibility, generally only two profiles per sputter current were acquired. The different sputter conditions employed in this study for the 4 model systems are summarized in **Table 3**.

Sample	**10 keV Ar_{3000}^+ beam current (nA)**[1]		
	0.3	**0.1**	**0.05**
System A: PS 4k / Si			
A1	x	x	x
A2	x	x	x
A3	x		
A4	x		
A5	x		
System B: PMMA 4k / Si			
B1	x		x
B2	x		x
B3	x		x[2]
B4	x		
B5	x		
B6	x		
System C: PS 60k / Si			
C1		x	
C2	x		
C3	x		
C4	x		
C5	x		
System D: PS 4k / PMMA 150 k / Si			
D1	x		
D2	x		
D3	x		
D4	x		
D5	x		
D6	x		

[1] Two measurements per sample and sputter current

[2] Only one measurement (for confirmation)

***Table 3**. Sputter conditions employed for the four different model systems analyzed by SIMS.*

No significant effect of the Ar cluster current is observed on the sputter yield volume. This concept is better seen in the depth-profiles of the thinnest PS film (A1), acquired in the three different erosion conditions reported in **Figure 3**. The respective ratios of analysis fluence (30 keV Bi_5^+ beam) to sputtering fluence (10 keV Ar_{3000}^+ source) are indicated next to the profiles. According to the literature, the reported Y values neglect the contribution of the analysis beam.[25] Thus, along this work, all the Y values obtained for a given system and related to different sputter currents will be merged.

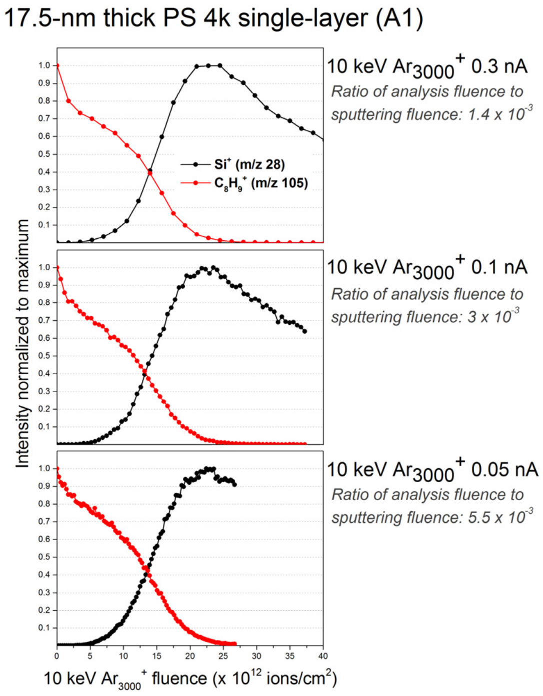

Figure 3. *SIMS molecular depth-profiles of the 17.5-nm thick PS 4k film on silicon acquired with three different 10 keV* Ar_{3000}^+ *currents: 0.3 nA, 0.1 nA and 0.05 nA. The polymer layer is represented by the characteristic fragment ion* $C_8H_9^+$*, and the substrate by the* Si^+ *ion. For each sputter condition, the ratio of the total ion fluences cumulated over the entire profile for the 30 keV* Bi_5^+ *beam and the 10 keV* Ar_{3000}^+ *beam is calculated. Note that there is no effect of the sputter current on the determination of the polymer/Si interface.*

For single-layers on Si (samples A-C), the sputter yield volume Y (nm^3/PI) was calculated as in §4.2.4. In the case of the PS/PMMA bilayer on Si (sample D), an analogue procedure was used for the polymer/polymer interface determination, taking into account characteristic ions of the “soft substrate” (PMMA 150k) that derive solely from the fragmentation of the polyacrylate, like for instance the ion $C_2H_3O_2^+$ at m/z 59. The Y determination for the single- and bilayer model systems is illustrated in **Figure 4**.

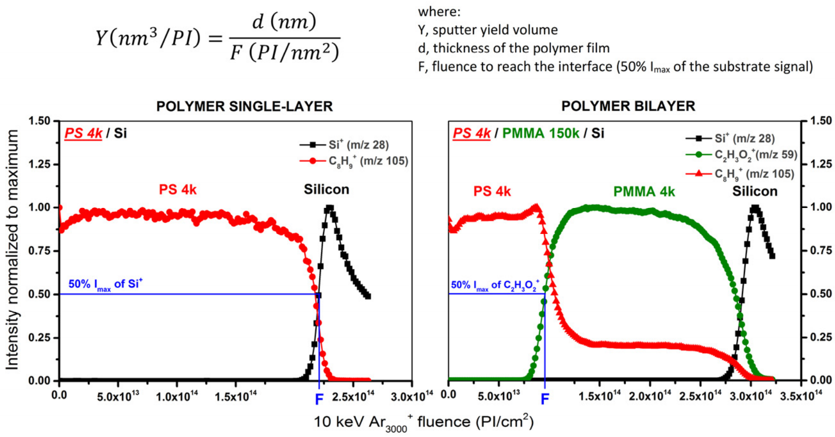

$$Y(nm^3/PI) = \frac{d\ (nm)}{F\ (PI/nm^2)}$$

where:
Y, sputter yield volume
d, thickness of the polymer film
F, fluence to reach the interface (50% I_{max} of the substrate signal)

Figure 4. *Description of the sputter yield volume (Y) calculation from thickness meaurements (by ellipsometry) and SIMS molecular depth-profiling in the case of single- and bilayers of polymers.*

4.3.4. Results

The depth-profiling experiments conducted on all the model systems with thickness of several tens of nm show a high stability of the polymer structure-related fragments (such as e.g. $C_2H_3O_2^+$, $C_3H_7O^+$, $C_4H_5O^+$, $C_5H_9O_2^+$ (protonated repeat unit), $C_6H_{11}O_2^+$ in the case of the PMMA, and $C_6H_5^+$, $C_7H_7^+$, $C_8H_9^+$ (protonated repeat unit), $C_9H_7^+$, $C_{13}H_9^+$, $C_{15}H_{13}^+$ in the case of the PS) down to the Si interface. This observation indicates the retention of the molecular information in the depth-profiling of type I and II polymers, a characteristic feature of large Ar cluster ion sputtering, as already mentioned in §4.2.2. Furthermore, even the thinnest polymer films cover the Si supports uniformly, as demonstrated by the absence of the substrate signals at the surface of the specimens in the depth-profiles (an example is given in Figure 3).

4.3.4.1. Effect of the layer thickness on the sputter yield

As was already mentioned in §4.3.2.1, AFM measurements were performed on the PS 4k single-layer series to investigate their morphology and roughness as a function of the thickness. Very smooth morphologies are observed in the overall thickness range (**Figure 5**). The average surface roughness (R_a) values were acquired from scans of 10 x 10 µm^2, 3 x 3 µm^2 and 1 x 1 µm^2 of two different areas of each polymer surface. The 3 x 3 µm^2 AFM images of the PS single-layers, for instance, show typical R_a values around 0.3 nm (close to the roughness of the silicon wafer, R_a ~0.2 nm),[26] independently from the given film thickness. These results are in good agreement with the investigation of Ennis et al. on PS-59 (that stands for PS with M_w of 59 000 amu) films spun-coated from toluene, where the scanning force microscopy gave root-mean-square (RMS) roughness values of ~0.6 nm.[16]

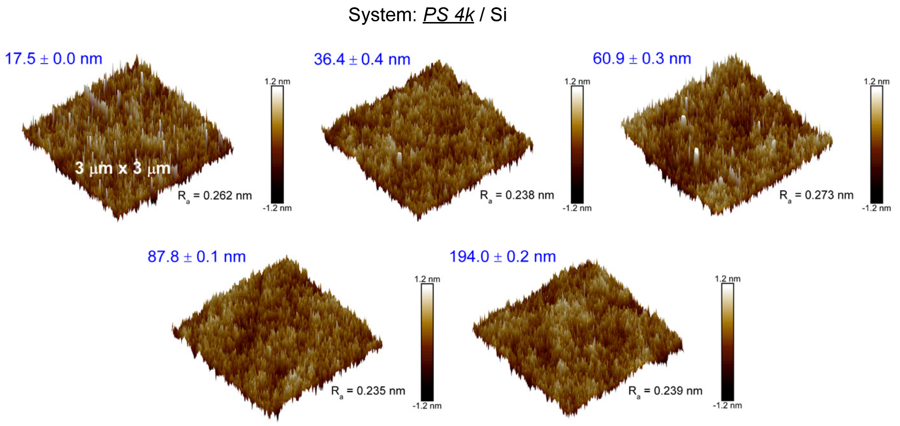

Figure 5. *Tridimensional AFM images (3 x 3 µm^2) and related average surface roughness (R_a) versus the thickness of Si-supported PS 4k ultrathin films determined by spectroscopic ellipsometry.*

Figure 6 shows the variation of the sputter yield volume Y for the model system **“*__PS 4k__* / Si”**, where the thickness of the polystyrene layer is varied from ~17 nm to 194 nm (see the black symbols related to the left y-scale). The graph of Figure 6 reports the thickness d on the left y-axis and Y on the right y-axis, both as a common function of the sputter fluence at the polymer/substrate interface (F in x-scale). A linear fit of d(F) has been performed imposing a zero intercept and passing by the last point representing a bulk-like PS layer. An adjusted R-square value of 0.9983 was found, indicating the quality of the linear regression. The equation d = b*F, reported in the graph of Figure 6, represents the ideal situation of linearity, where the correlation coefficient b = 67.2 nm^3/PI constitutes the sputter yield volume of the bulk material (Y_{bulk}). The related linear fits of all the investigated systems are shown in §4.3.6 (**Figure S2**). However, the experimental d(F) data deviates from linearity below ~90 nm, which explains the asymptotic trend of Y(F) described by the following analytical function y = a-b*c^x (in the present case: Y = 65.4-(-36.6)*0.115^F).

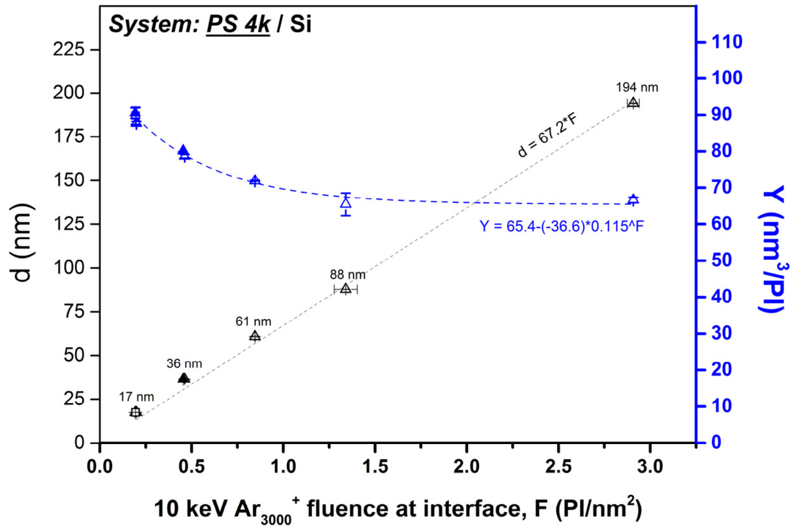

Figure 6. *Thickness (d) and sputter yield volume (Y) of the PS 4k single-layers as a function of the sputter fluence needed to reach the polymer/silicon interface. The data points indicated by open triangles, open squares and solid triangles (black for d and blue for Y) refer to the different 10 keV* Ar_{3000}^+ *ion currents of 0.3 nA, 0.1 nA and 0.05 nA, respectively. The fitted curves of d and Y as a function of F (fluence) are also reported.*

F represents the "sputter fluence" variable and the asymptote a = 65.4 nm^3/PI corresponds to the Y value of the bulk material (very close to that obtained by linear regression). In qualitative terms, Y decreases with increasing d till reaching a plateau around 90 nm. The sputter yield volumes (for 0.3 nA) vary from 88 nm^3/PI at 17 nm to 67 nm^3/PI at 194 nm (value close to the "bulk" material), that corresponds to an overall ΔY(d) variation of ~23%. This points out a dependence of Y on the thickness in the nanoscale range (from a few nm to tens of nm). However, the quantification of ΔY(d) depends significantly on the specific technique employed for the determination of d, as demonstrated by AFM (not shown). This justifies the choice of reporting Y (as well as d) as a function of the fluence. The plot of Y as a function of d can be found in §4.3.6 (**Figure S1**).

Figure 7 shows the case of the model system **"*PMMA 4k* / Si"**, where the thickness of the polymer layer is varied from 16 nm to 199 nm. As was the case for PS 4k, the loss of linearity between d and F leads to an effect of the thickness on Y, that is noticeable below ~90 nm. The trend of the sputter yield volume is once again asymptotic, going from 103 nm^3/PI at 16 nm to 80 nm^3/PI at 199 nm (see the blue open triangles), which corresponds to a

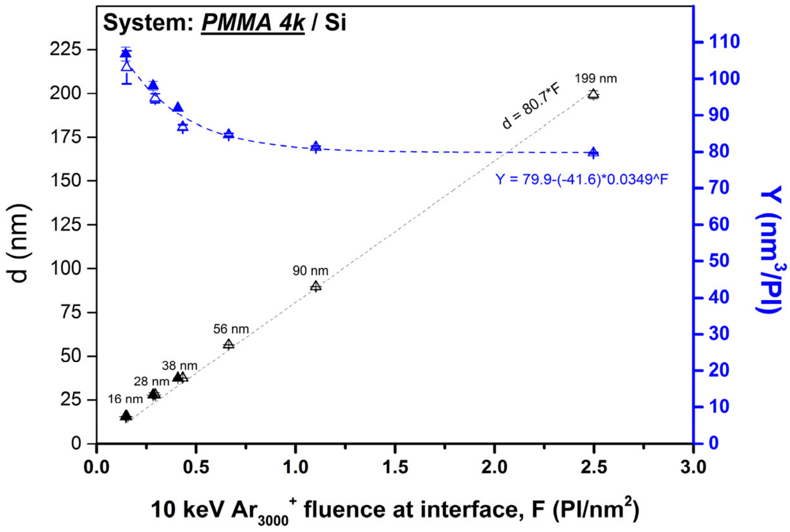

Figure 7. *Thickness (d) and sputter yield volume (Y) of the PMMA 4k single-layers as a function of the sputter fluence needed to reach the polymer/silicon interface. The data points indicated by open triangles and solid triangles (black for d and blue for Y) refer to the different 10 keV* Ar_{3000}^{+} *ion currents of 0.3 nA and 0.05 nA, respectively. The fitted curves of d and Y as a function of F (fluence) are also reported.*

variation of ~22% based on spectroscopic ellipsometry estimation. The trend of Y as a function of the sputter fluence follows the equation: Y = 79.9-(-41.6)*0.0349^F, where the Y_{bulk} value is 79.9 nm^3/PI. Clearly, Y of PMMA 4k single-layers is higher than Y of PS 4k (see Figure 6 and 7). For example, ~100-nm thick PMMA layers possess Y values close to 80 nm^3/PI, while PS layers have Y around 65 nm^3/PI, a factor of ~1.2. This is explained by the different degradation behaviour of the two polymers upon ionic bombardment,[27] that favors the sputtering of the polyacrylate compared to that of the polystyrenes. A similar difference is observed for high M_w PS and PMMA, as reported by Seah.[7]

4.3.4.2. Effect of the substrate nature on the thickness dependence of Y

In **Figure 8**, the model system **"*PS 4k* / PMMA 150k / Si"** is considered, where the 143-nm thick PMMA 150k layer constitutes a soft substrate and only the thickness of the topmost PS 4k layer is varied from 28 nm to 235 nm.

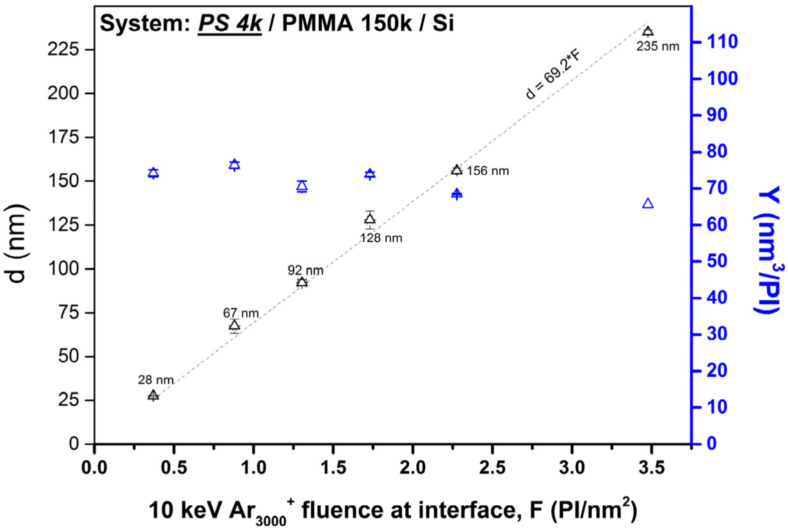

Figure 8. *Thickness (d) and sputter yield volume (Y) of the uppermost PS 4k films in the bilayer model system (C) as a function of the sputter fluence needed to reach the polymer/polymer interface. The data points indicated by open triangles (black for d and blue for Y) refer to a sputter beam current of 0.3 nA. The fitted curve of d as a function of F (fluence) is reported.*

The linear regression on the data set d(F) of the uppermost PS 4k layer in the bilayer system points out an identical slope (within the experimental error) to that found for PS 4k single-layers spin-coated directly on the Si substrates, as observed in Figure S2 reported in §4.3.6. In this specific case, however, the sputter yield volume oscillates around an average value of ~73 nm^3/PI (excluding the last point represented by a single measure), without any peculiar trend. Thus, SIMS reveals no Y dependence on the thickness of polymer films deposited onto polymer-based substrates.

4.3.4.3. Effect of the polymer molecular weight on the thickness dependence of Y

The last case of study is represented by the polymer system "***PS 60k*** / **Si"** depicted in **Figure 9**, whose thickness goes from 16 nm to 230 nm. Here, the influence of the M_w of the polystyrene on the thickness dependence of Y is investigated. The study conducted in §4.2 on the effect of the M_w on the sputtering efficiency highlighted that Y depends on M_w only for low polymerization degrees, while Y(M_w) is constant for M_w above ~50 000 amu (estimated by comparison with differential scanning calorimetry measurements).

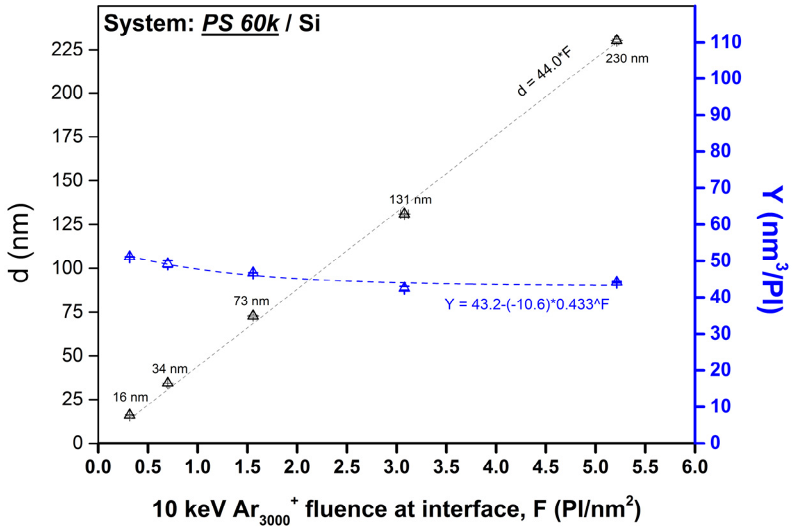

Figure 9. *Thickness (d) and sputter yield volume (Y) of the PS 60k single-layers as a function of the sputter fluence needed to reach the polymer/silicon interface. All the measurements were performed with 10 keV* Ar_{3000}^{+} *at 0.3 nA, with the exception of the 1st sample (0.1 nA). The fitted curves of d and Y as a function of F (fluence) are reported.*

Higher fluences were required to erode layers of PS 60k than layers of PS 4k of comparable thicknesses corresponding to lower sputter rates for the high M_w polymer. Figure 9 shows that the variation of Y as a function of the fluence, in the given d range 16-230 nm, is around 14% for PS 60k. It is therefore notably reduced when compared to the PS 4k films, but still present. The experimental data can be fitted by the equation Y = 43.2-(-10.6)*0.433^F. The Y value in the bulk material is consequently estimated to be close to 43 nm^3/PI. This finding is confirmed with an additional sample of 366 nm (not shown). However, the decay of Y appears to be slower along the observed fluence range, so that higher fluences/thicknesses are needed to reach the Y_{bulk} value.

In conclusion of this section, **Figure 10** summarizes the fitted curves Y(d) of the two investigated model polymers, PS and PMMA, deposited on the two different supports, i.e. hard (Si) and soft (PMMA 150k). The influence of the M_w can be also derived from the comparison between PS 4k and PS 60k. Hence, this last figure illustrates the behaviors of all the proposed model systems, and will be used as a basis for the discussion of the underlying physics. The corresponding summary of the fitted curves Y(F) is reported in **Figure S3** (§4.3.6).

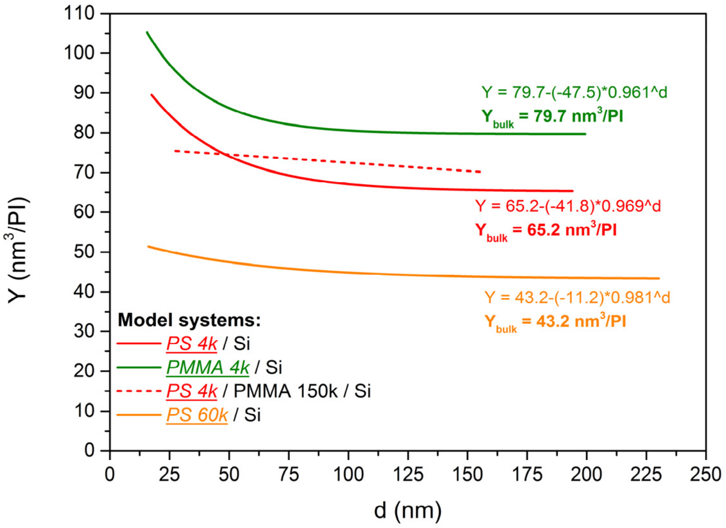

Figure 10. *Fitted curves (analytical function: y = a-b*c^x) of the sputter yield volume as a function of the film thickness for the Si-supported PS 4k, PMMA 4k and PS 60k single-layers, and the Y trend (dotted red line) of topmost layer of the PS 4k / PMMA 150k bilayer.*

4.3.5. Discussion

Deviations from the bulk physical properties when a polymer sample is confined up to the point that the surface to volume ratio and the interface become crucial, known as nanoconfinement effect, have been widely observed, like e.g. for glass transition temperature (T_g), polymer chain diffusion, chain conformation, and crystallization.[28] Keddie et al. (1994) were the first to provide a direct evidence of nanoconfinement effects for PS ultrathin films on SiO_2/Si by reporting a reduction of T_g of 25 K for a 10-nm thick film compared to the bulk.[29] The onset of the deviation of the bulk T_g was seen at ~40 nm. This phenomenon was explained by the presence of a liquid-like layer at the free surface of the system of high cooperative segmental mobility and, consequently, reduced T_g.[30] This was confirmed by the experiments of Sharp and Forrest (2003),[31] who capped the PS films with 5-nm thick gold layers, leading to the disappearance of the bulk T_g reduction within the first 8 nm of the polymer film.

At first sight, the effect of the “free surface” could explain also the observed enhancement of the sputter yield volume (Y) for the lowest thicknesses of nanoscale PS 4k films on untreated Si (cf. Figure 10). However, experiments conducted on PMMA, P2VP (poly (2-vinylpyridine)) and PVC (polyvinyl chloride), all deposited on unmodified Si or glass supports, showed an opposite behavior of T_g compared to PS, i.e. T_g increases when d decreases.[32] This last observation is now ascribed to the different interfacial interactions. Indeed, the methyl methacrylate units are attracted to the native Si oxide substrate, forming H-bonds. Conversely, in the case of PS, only weak Van der Waals interactions are created with the native Si oxide substrate.[16,33] These enthalpic considerations are validated by the fact that switching the PMMA substrate to gold or hydrophobic glass, the T_g behaves like in the case of PS. This also means that for PMMA ultrathin films, the attractive polymer-substrate interactions overcome the effect of the “free surface”.[34] However, if the interfacial interactions of the two investigated polymers are a relevant parameter in the nanoconfinement effect of Y, one should expect an opposite trend of the Y(d) curves for PS and PMMA in Figure 10, but it is not the case. The interfacial interactions as key parameter in the Y dependence on d could be definitely discarded by using hydrophobically treated silicon for the deposition of both polymers. Preliminary studies have already been conducted on PS 4k and PMMA 4k single-layers deposited onto H-terminated silicon. They indicate that Y decreases with increasing d in the same extent for both systems, independently of the change in the polymer-substrate attractive interactions (notably reduced in the case of PMMA). These preliminary results would rather suggest a mechanistic nature of the nanoconfinement effect on Y, as already indicated by molecular dynamics (MD) computer simulations on other types of organic systems.

In this respect, MD simulations have been carried out by Rzeznik and co-workers (2008) to gain microscopic insights into the sputtering of polystyrene tetramer (PS4) monolayers on Ag induced by large Ar cluster projectiles.[10] The ion bombardment of the organic overlayer was performed with clusters composed of hundreds to 29 000 Ar atoms having kinetic energy per atom in the range 0.1-40 eV/atom. Simulations have shown a distinct physics of ejection by these large and slow clusters compared to the popular SIMS clusters, such as C_{60}, Au_3 and SF_5. The organic molecules are expulsed not in consequence of a direct interaction with individual substrate atoms, which is the case for atomic and small cluster bombardment, but by a collective motion of the recovering substrate. At the light of this novel ejection physics with large Ar clusters, Rzeznik et al. have conducted simulations (2009) to elucidate the sputtering of a denser, thicker and well organized system represented by Langmuir-Blodgett multilayers of bariated molecules of arachidic acid.[11] Among other investigations, in this work, the sputtering yield has been analyzed as a function of the thickness of the deposited multilayer. The system was composed of 1, 2, 4 and 6 monolayers. The sputtering was performed by means of a 15 keV Ar_{872} cluster (~17 eV/atom) and at a normal incidence angle. The sputtering yield goes through a maximum, then decreases, and finally becomes constant as the LB layer becomes thicker. A similar behavior has been evidenced in cluster depth-profiling of cholesterol films sputtered with 40 keV C_{60}^{+}, in which the erosion rate increases as the organic-substrate interface is approached.[35] This behavior is explained by a competition between signal enhancement due to the increasing number of molecules contained in the organic overlayer, and the signal decrease due to lowering of the amount of the primary energy being back-reflected into the organic layer by the organic/metal interface.[11] The sputtering yield is independent of the thickness when the latter is much larger than the penetration depth of the projectile.

Model for the thickness dependence of the sputter yield

Based on the insights provided by the simulation studies about the sputtering process of organic overlayers with large Ar clusters,[10,11] a basic physical model is here proposed to explain the Y-confinement behavior. In this model, the polymer film (single-layer system) is considered as composed by two layers, so the name "2-layer model": one located at the interface with the hard substrate (e.g. silicon) that undergoes the Y-enhancement effect due to the Ar_n^+ sputtering, and on top a second layer with a bulk Y. Accordingly, there is a critical thickness in the range of the first nanometers of the overlayer, where Y assumes the highest value due to a maximal contribution to the sputtering of the primary energy being back-reflected into the polymer layer by the polymer/Si interface.[36 ,7] The correspondent Y value is indicated as $Y_{interface}$, and the critical thickness as $d_{interface}$. Then, with increasing thickness, the sputter yield gradually tends to its bulk value because of the lowering of the interface effect. This is observed to happen for PS 4k and PMMA 4k single-layers below ~90 nm (see red and green solid lines of Figure 10). In the end, for both systems, a final bulk regime for Y(d) is identified at thickness >90 nm ($Y = Y_{bulk}$). In the model this gradual transition is represented by the following expression:

$$Y_{tot} = \frac{d_{interface}}{d_{interface} + d_{bulk}} Y_{interface} + \frac{d_{bulk}}{d_{interface} + d_{bulk}} Y_{bulk} \tag{1}$$

that becomes:

$$Y_{tot} = \frac{d_{interface}}{d_{tot}} Y_{interface} + \frac{d_{tot} - d_{interface}}{d_{tot}} Y_{bulk} \tag{2}$$

where Y_{tot}, d_{tot} and Y_{bulk} are determined experimentally, whereas $d_{interface}$ and the related $Y_{interface}$ need to be estimated by fitting. **Figure 11.a** depicts **Equation (2)** for the PS 4k single-layer, by using the characteristic parameters of the given system (Y_{bulk} = 65.4 nm^3/PI for d = 194 nm showed in Figure 6). Based on the 2-layer model, $d_{interface}$ and $Y_{interface}$ are 3 nm and 200 nm^3/PI, respectively. As it can be observed, the model is oversimplified to describe accurately the experimental data set. However, the refined description of the gradual transition of Y(d) from $Y_{interface}$ (200 nm^3/PI) to Y_{bulk} (65.4 nm^3/P) should lead to a more accurate model.

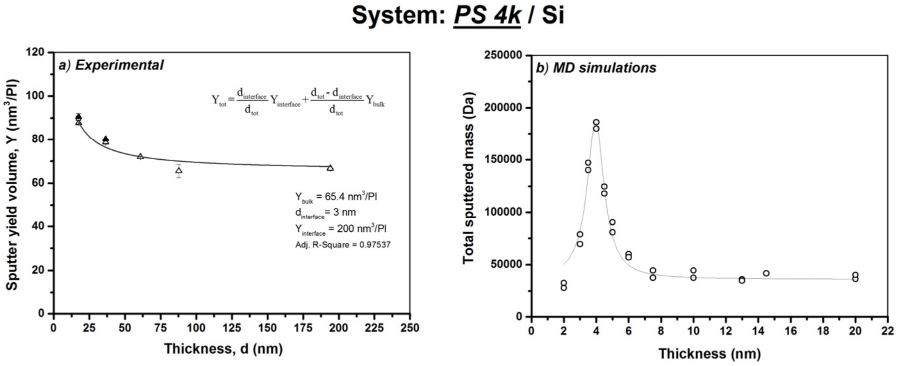

__Figure 11__. a) 2-layer model applied to the experimental data set for the "PS 4k / Si" system (gray solid line), and b) MD simulations conducted on an amorphous film of polyethylene-like oligomers of increasing thickness (from 2 to 20 nm) onto a hard substrate.

MD simulations were performed by Professor A. Delcorte, in order to validate the hypotheses of the phenomenological model previously proposed. For this purpose, an amorphous molecular sample made of 1.4 kDa polyethylene-like molecules was modelled using a coarse-grained representation of CH_2 and CH_3 residues, as described elsewhere[13]. This model gave excellent results for the quantitative modelling of Ar cluster sputtering of organic materials. In these new simulations, the top layer of the organic sample, with a total thickness d, was left free to move, mimicking the oligomer layer. In contrast, the bottom layer of the sample was made "rigid" by constraining the atoms to their initial positions. The thickness of the rigid layer was adjusted to obtain a free film thickness d ranging between 2 and 15 nm (the total thickness of the model sample). For these samples, damping zones were used for the four lateral sides of the box (1.5-nm thickness), using a Langevin algorithm with a friction coefficient, in order to absorb the pressure waves traveling laterally, but not at the bottom. This arrangement models an infinite film of thickness d on an infinitely hard substrate. Another set of measurements was made by also using a damping zone at the bottom (Langevin algorithm with a friction coefficient), in order to absorb the pressure waves and in that case, mimic a semi-infinite, bulk sample. Two different impact points were calculated for each film thickness.

Figure 11.b shows the total sputtered mass of polymer as a function of thickness d. As a reference point for the bulk value, the results obtained for the sample with a bottom damping zone were arbitrarily placed at a film thickness of 20 nm (larger than the thickness of the model system). The other data points correspond to the first set of sample described above, with only a rigid bottom layer below a free film of thickness d. The results show that the sputtered mass remains constant down to a film thickness of 7 nm. Under that thickness, the sputtered mass increases very steeply, up to a maximum value at 4 nm, then decreases again. The final decrease at small d can be explained by the limited amount of material left to be sputtered. The maximum, due to the back-scattering of the projectile atoms (and energy) by the substrate, corresponds to a sputtered mass that is ~4 times larger than the bulk value. Though the analytical model presented above uses a crude representation of the curve obtained in the MD simulations, with only two steps of sputter yield (one for the ultrathin film regime and one for the bulk), the values of thickness and yield extracted for the layer with enhanced sputtering are in qualitative agreement with the MD results ($d_{\mathrm{interface}} = 3$ nm and $Y_{\mathrm{interface}} = 3 * Y_{\mathrm{bulk}}$, see Figure 11.a). These simulation results therefore support the interpretation and the simple model of sputtering including a layer with enhanced sputtering near the substrate, resulting from the confinement of the Ar cluster energy for ultrathin organic films on hard substrates.

The proposed model is confirmed by the study of the bilayer system "*PS 4k* / PMMA 150k / Si", where the energy deposited by the projectile in the uppermost PS layer is not confined anymore by a dense substrate like Si, but it is now dispersed in the underlying soft PMMA layer. As a consequence, the nanoconfinement effect on the sputter yield volume disappears, as indicated by the red dotted line in Figure 10. Moreover, the comparison of the extrapolated ideal dependence of the sputter fluence as a function of d (obtained by linear regression) shows that the cases of PS 4k deposited onto Si and PMMA 150k are substantially identical (see Figures 6 and 8, or Figure S2). Indeed, for PS 4k on Si the fitted Y_{bulk} value is 67.2 nm^3/PI, while for PS4k on PMMA 150 k is 69.2 nm^3/PI.

As further validation of the hypothesis done, the PS 60k single-layer system also presents a Y-confinement behavior (see orange solid line in Figure 10). Here, the influence of the higher M_w is reflected in smaller variations of Y vs d. This may be explained by the fact that at higher M_w, long portion of macromolecules remain still entangled to the polymer surface after each Ar cluster bombardment event, conversely to low M_w polymers, where the material volume energized in the ion impact is wiped out more effectively because there is no need to break covalent bonds.[12,37] Additional factors may intervene in the Y-nanoconfinement of PS 60k compared to PS 4k, such as a larger extent of entanglements of the polymer chains and lower interfacial (air/polymer) free volume.[38] In fact, they could dramatically mitigate the observed Y(d) enhancement of PS 4k single-layers in the case of PS 60k. In this respect, decreasing evolution of Y as a function of the polymer M_w has been established in §4.2.5. M_w has been demonstrated to have an impact also on the T_g(d) depression for silica-supported PS and PMMA films, that is more pronounced for oligomers than for the long chain analogues.[39] Same conclusions are claimed by Xia and co-workers (2015) in the investigation of free-standing PMMA films at low and high M_w.[38]

4.3.6. Conclusion

This study demonstrates a noticeable nanoconfinement behavior of the sputter yield with massive Ar clusters of model polymer films deposited onto a hard substrate (in this case silicon). To our best knowledge, it is the first time that a similar behavior is experimentally shown for polymer-based materials. Indeed, previous investigations were carried out with different organic systems and cluster projectiles or by MD simulations. The thickness dependence of Y for PS 4k ultrathin layers on Si substrate has been confirmed by two independent measurements of the film thickness, i.e. ellipsometry versus atomic force microscopy. The quantification of the phenomenon has been based on the ellipsometric determination of the thickness ranging from ~15 nm to ~230 nm. Y shows a steep decay in the region below 90 nm for both PS 4k and PMMA 4k single-layers, then it levels off. The absence of the Y-confinement for ultrathin polymer layers of PS 4k on a soft substrate leads to hypothesize a mechanistic nature of the observed phenomenon involving the reflection of the Ar cluster energy at the interface with the hard silicon substrate and its confinement in the polymer layer. A physical "2-layer" model was developed to describe the thickness dependence of Y, where the maximal sputter yield is located at a critical thickness of a few nm, depending on the energized volume by the primary ion impact (1st constant layer). Then, the gradual increase of d, by means of a 2nd hypothetical layer of increasing thickness, mitigates the interface effect till the complete annulation around 90 nm, where a bulk value of Y is reached. MD results obtained on ultrathin layers of PE-like oligomers onto a hard substrate are in qualitative agreement with this model, supporting the interpretation of the Y-nanoconfinement on mechanistic bases. Finally, an effect of the polymer M_w on the Y-nanoconfinement is highlighted in the case of PS. Indeed, an increase of M_w leads to a decrease of the Y-confinement, due presumably to the larger extent of entanglements and lower end-chain density. Further investigation could be undertaken both in experiments and theoretical work. Based on these results, it is recommended to work with polymer thin films deposited onto hard matter substrates such as silicon wafers either with a thickness above 100 nm, or at least by keeping the thickness constant, especially for the estimation of sputter yields.

4.3.7. Supporting information

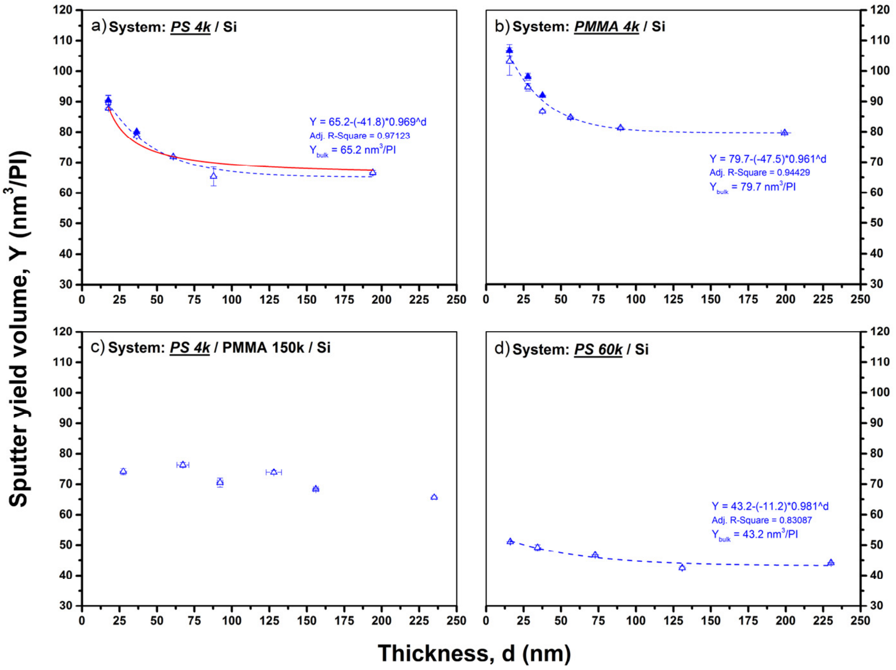

Figure S1. *Sputter yield volume versus thickness of the Si-supported thin films of PS 4k (a), PMMA 4k (b), PS 60k (d), and Y of the uppermost PS 4k layer of the polymer bilayer system (c). Asymptotic fits are reported exclusively to describe the trend of the experimental data.*

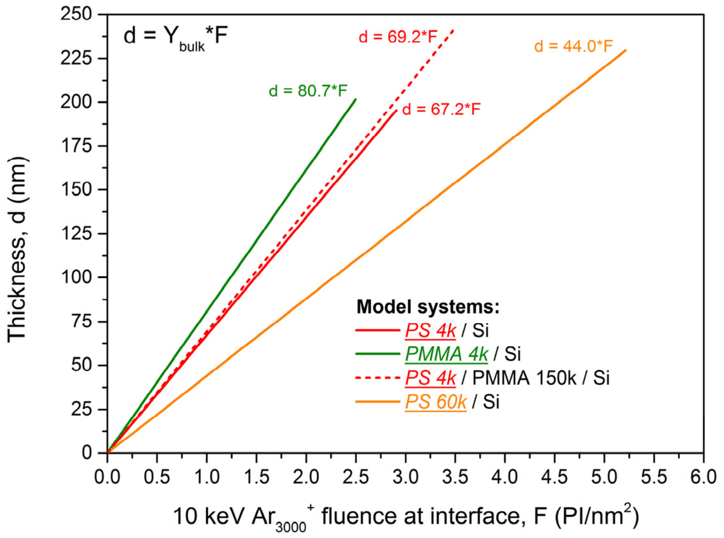

Figure S2. *Ideal linearity between thickness of the investigated ultrathin films and sputter fluence needed to reach the polymer/Si or polymer/polymer interface. Higher is the slope of the curve, whose physical meaning is* Y_{bulk}*, easier is to erode the material.*

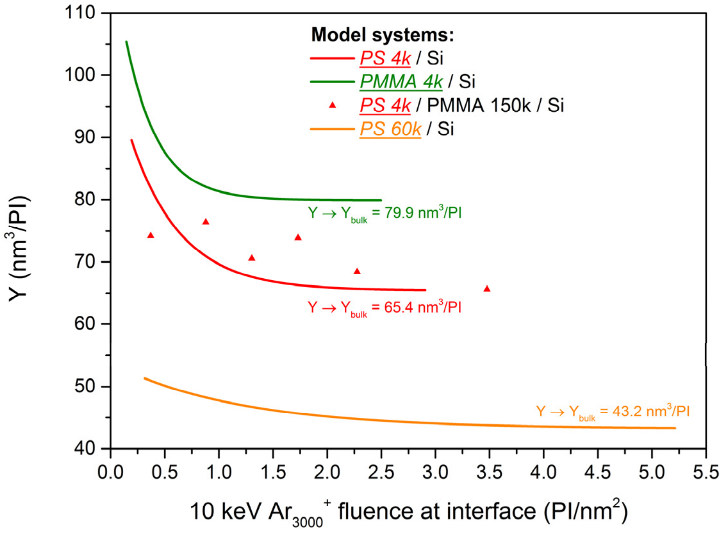

Figure S3. *Fitted curves (analytical function: y = a-b*c^x) of the sputter yield volume (Y) versus the sputter fluence of the Si-supported thin films of PS 4k, PMMA 4k and PS 60k. Y of the uppermost PS 4k layer of the polymer bilayer system is also depicted by red solid triangles. The Y values of the bulk material are estimated from asymptotic fits of the experimental data.*

4.3.8. References

[1] C. M. Mahoney. Cluster secondary ion mass spectrometry of polymers and related materials. *Mass Spectrom. Rev.* **2009**, *29*, 247, and references herein.

[2] S. Ninomiya, K. Ichiki, H. Yamada, Y. Nakata, T. Seki, T. Aoki, J. Matsuo. Precise and fast secondary ion mass spectrometry depth profiling of polymer materials with large Ar cluster ion beams. *Rapid Commun. Mass Spectrom.* **2009**, *23*, 1601

[3] B. J. Garrison, Z. Postawa. Computational view of surface based organic mass spectrometry. *Mass Spectrometry Reviews* **2008**, *27*, 289.

[4] A. Delcorte, O. A. Restrepo, B. Czerwinski, Cluster SIMS of organic materials: Theoretical Insights, Chapter 2 in Cluster Secondary Ion Mass Spectrometry: Principles and Applications, First Edition, John Wiley & Sons, New Jersey, **2013**.

[5] A. Delcorte, V. Cristaudo, V. Lebec, B. Czerwinski Sputtering of polymers by keV clusters: Microscopic views of the molecular dynamics. *International Journal of Mass Spectrometry* **2014**, *370*, 29.

[6] B. Czerwinski, Z. Postawa, B. J. Garrison, A. Delcorte. Molecular dynamics study of polystyrene bond-breaking and crosslinking under C_{60} and Ar_n cluster bombardment. *Nucl. Instruments Methods Phys. Res. Sect. B Beam Interact. with Mater. Atoms* **2013**, *303*, 22.

[7] M. P. Seah. Universal equation for argon gas cluster sputtering yields. *The Journal of Physical Chemistry C* **2013**, *117*, 12622, and references herein.

[8] B. Czerwinski, L. Rzeznik, R. Paruch, B. J. Garrison, Z. Postawa. Effect of impact angle and projectile size on sputtering efficiency of solid benzene investigated by molecular dynamics simulations. *Nucl. Instruments Methods Phys. Res. Sect. B* **2011**, *269*, 1578.

[9] R. Paruch, L. Rzeznik, B. Czerwinski, B. J. Garrison, N. Winograd, Z. Postawa. Molecular dynamics simulations of sputtering of Langmuir-Blodgett multilayers by keV C_{60} projectiles. *The Journal of Physical Chemistry. C, Nanomaterials and Interfaces* **2009**, *113*, 5641.

[10] L. Rzeznik, B. Czerwinski, B. J. Garrison, N. Winograd, Z. Postawa. Microscopic insight into the sputtering of thin polystyrene films on Ag {111} induced by large and slow Ar clusters. *The Journal of Physical Chemistry C* **2008**, *112*, 521.

[11] L. Rzeznik, R. Paruch, B. Czerwinski, B., B. J. Garrison, Z. Postawa. Sputtering of thin films of bariated molecules of arachidic acid by large noble gas clusters. *Vacuum* **2009**, *83*, S155.

[12] V. Cristaudo, C. Poleunis, B. Czerwinski, A. Delcorte. Ar cluster sputtering of polymers: Effects of cluster size and molecular weights. *Surface and Interface Analysis* **2014**, *46*, 79.

[13] A. Delcorte, M. Debongnie. Macromolecular sample sputtering by large Ar and CH_4 clusters: Elucidating chain size and projectile effects with molecular dynamics. *The Journal of Physical Chemistry C* **2015**, *119*, 25868.

[14] C. B. Walsh, E. I. Franses. Ultrathin PMMA films spin-coated from toluene solutions. *Thin Solid Films* **2003**, *429*, 71.

[15] E. Mohajerani, F. Farajollahi, R. Mahzoon, S. Baghery. Morphological and thickness analysis for PMMA spin coated films. *Journal of Optoelectronics and Advanced Materials* **2007**, *9*, 3901.

[16] D. Ennis, H. Betz, H. Ade. Direct spincasting of polystyrene thin films onto poly (methyl methacrylate). *Journal of Polymer Science Part B: Polymer Physics* **2006**, *44*, 3234.

[17] Online Horiba technical notes: Forouhi-Bloomer alias Amorphous Dispersion Formula

[18] Online Horiba technical notes: New Amorphous Dispersion Formula

[19] J. N. Hilfiker, R. A. Synowicki, C. L. Bungay, R. Carpio. Spectroscopic ellipsometry for polymer thin films. *Solid State Technology* **1998**, *41*, 101.

[20] H. M. El-Nasser, O. D. Ali, Effect of molecular weight and UV illumination on optical constants of PMMA thin films. *Iranian Polymer Journal* **2010**, *19*, 57.

[21] Website: refractiveindex.info

[22] G. Beadie, M. Brindza, R. A. Flynn, A. Rosenberg, J. S. Shirk. Refractive index measurements of poly(methyl methacrylate) (PMMA) from 0.4-1.6 μm, *Applied Optics* **2015***, 54*, F139.

[23] N. Sultanova, S. Kasarova, I. Nikolov. Dispersion properties of optical polymers, *Acta Physica Polonica A* **2009**, *116*, 585. (fit of the experimental data with the Sellmeier dispersion formula: refractiveindex.info)

[24] R. F. M. Lobo, M. A. Pereira-da-Silva, M. Raposo, R. M. Faria, O. N. Oliveira Jr, M. A. Pereira-da-Silva, R. M. Faria. In situ thickness measurements of ultra-thin multilayer polymer films by atomic force microscopy. *Nanotechnology* **1999**, *10*, 389.

[25] A. G. Shard, R. Havelund, M. P. Seah, S. J. Spencer, I. S. Gilmore, N. Winograd, D. Mayo, T. Miyayama, E. Niehuis, D. Rading, R. Moellers. Argon

cluster ion beams for organic depth profiling: Results from a VAMAS interlaboratory study. *Analytical Chemistry* **2012**, *84*, 7865.

[26] T. Ohmi, M. Miyashita, M. Itano, T. Imaoka, I. Kawanabe. Dependence of thin-oxide films quality on surface microroughness. *IEEE Transactions on Electron Devices* **1992**, *39*, 537.

[27] A. Chapiro, Radiation Chemistry of Polymeric Systems, John Wiley and Sons, New York & London, **1962**, 712.

[28] R. D. Priestley. Effects of nanoscale confinement and interfaces on the structural relaxation of amorphous polymers monitored at the molecular scale by fluorescence and dielectric spectroscopy. Ph.D. Thesis, Northwestern University, **2008**.

[29] J. L. Keddie, R. A. L. Jones, R. Cory. Size-dependent depression of the glass transition temperature in polymer films. *Europhysics Letters* **1994**, *27*, 59.

[30] S. Kim, S. A. Hewlett, C. B. Roth, J. M. Torkelson. Confinement effects on glass transition temperature, transition breadth, and expansivity: comparison of ellipsometry and fluorescence measurements on polystyrene films. *The European Physical Journal E* **2009**, *30*, 83.

[31] J. S. Sharp, J. A. Forrest. Free surfaces cause reductions in the glass transition temperature of thin polystyrene films. *Physical Review Letters* **2003**, *91*, 235701.

[32] P. Rittigstein. The glass transition and physical aging behavior of polymer nanocomposites studied via fluorescence. Ph.D. Thesis, Northwestern University, **2008**.

[33] S. Tardio, M.-L. Abel, R. H. Carr, J. Watts. Polystyrene-silicon bonding through π electrons: A combined XPS and DFT study. *Surface and Interface Analysis* **2015**, DOI 10.1002/sia.5879.

[34] J. L. Keddie, R. A. L. Jones, R. Cory. Interface and surface effects on the glass-transition temperature in thin polymer films. *Faraday Discussions* **1994**, *98*, 219.

[35] J. Kozole, A. Wucher, N. Winograd. Energy deposition during molecular depth profiling experiments with cluster ion beams. *Analytical Chemistry* **2008**, *80*, 5293.

[36] N. Matsunami, Y. Yamamura, Y. Itikawa, N. Itoh, Y. Kazumata, S. Miyagawa, K. Morita, R. Shimizu, H. Tawara. Energy dependence of the ion-induced sputtering yields of monatomic solids. *Atomic Data and Nuclear Data Tables* **1984**, *31*, 1.

[37] A. Delcorte, O. A. Restrepo, K. Hamraoui, B. Czerwinski. Cluster impacts in organics: microscopic models and universal sputtering curves. *Surface and Interface Analysis* **2014**, *46*, 46.

[38] W. Xia, D. D. Hsu, S. Keten. Molecular weight effects on the glass transition and confinement behavior of polymer thin films. *Macromolecular Rapid Communications* **2015**, *36*, 1422.

[39] J. Chen, L. Li, D. Zhou, J. Xu, G. Xue. Effect of molecular chain architecture on dynamics of polymer thin films measured by the ac-chip calorimeter. *Macromolecules* **2014**, *47*, 3497.

CHAPTER 5
SIMS characterization of polyethylene surfaces modified by atmospheric Ar-D_2O post-discharges

5.1. General introduction

This chapter concerns the injection of H_2O into atmospheric plasmas, as an alternative route to the use of O_2 as reactive gas, to achieve the oxidative functionalization of polyolefins. Plasma diagnostics have been conducted by S. Collette et al. at ULB to better understand the specific chemical mechanisms occurring in presence of H_2O. However, the physical and chemical interactions between the H_2O injected into an atmospheric post-discharge and the polymer substrate need to be clarified. This investigation is particularly challenging with "open air" plasmas, because of the inevitable intervention of the atmospheric O_2 and H_2O (moisture), that contribute to the polymer oxidation. To help tracing the water reactivity, an original protocol combining deuterated water (D_2O) and secondary ion mass spectrometry (SIMS) is proposed here.[i]

The first section of the chapter deals with the investigation of the hydrogen-deuterium exchange in polyethylene films treated by an atmospheric Ar-D_2O post-discharge. The quantification of the deuteration at the polymer surface as a function of the torch-to-sample distance is performed via the elaboration of a mathematical parameter R_D (deuteration ratio). Thanks to this methodology, the optimization of the plasma treatment parameters becomes feasible. Furthermore, to our best knowledge, the first example of ultra-shallow molecular depth-profiling of polymers by Ar noble gas clusters is reported, showing the detailed variation of the deuteration process in the topmost surface layers (first few nanometers).

The second section of the chapter reports the application of a combined approach based on SIMS and principal component analysis (PCA), both on the specimen surface and along the depth, to thoroughly investigate the plasma-induced modifications in the polymer material in terms of oxidation, H-D exchange, N-uptake, and chemical damage. This study proves unequivocally the influence of two selected parameters of the plasma treatment, namely the treatment time and the torch-to-sample distance, on the

---

[i] The plasma treatment of the polymer films was carried out by S. Collette at CHANI (Chimie Analytique et Chimie des Interfaces, ULB). The SIMS characterization of the samples was performed in the SUCH (Surface characterization) platform at UCL.

oxidative functionalization along the top ten nanometers of the polyethylene. In addition to the use of Ar clusters for molecular depth-profiling, a novelty of our methodology consists in the application of PCA not only to the surface analysis results, but also to the depth-profiles themselves.

5.2. Investigation of H-D exchange in polyethylene treated by atmospheric Ar-D_2O post-discharge

(Surface Analysis and Ultra-Shallow Molecular Depth-Profiling of Polyethylene Treated by an Atmospheric Ar-D_2O Post-Discharge. Plasma Processes and Polymers 2015, 12(9), 919-925; DOI: 10.1002/ppap.201400248)

5.2.1. Abstract

In an original approach to trace water reactivity upon surface treatment by ambient "open air" plasma, the H-D exchange processes induced in polyethylene by an Ar-D_2O post-discharge are investigated using time-of-flight secondary ion mass spectrometry, both at the surface and along the sample depth. The surface characterization points out the strong influence of the sample-torch distance. The most important chemical modifications, excluding polymer overheating, occur at 5 mm of distance, with 25% of deuterated monomer units at the surface. For the first time, ultra-shallow molecular depth-profiling by Ar noble gas clusters shows the detailed variation of the deuteration of the polymer repeat unit in the topmost surface layer. Our results indicate that the fraction of deuterated monomer units is reduced by a factor >2 over a depth of ~3 nm.

5.2.2. Introduction

Numerous industrial applications of polymer-based materials require the modification of their surface physicochemical properties like, for instance, adhesion and biocompatibility. The use of atmospheric plasmas for surface modification of polymers has expanded tremendously since the last decade.[1-3] In addition to the many advantages offered by the more conventional low pressure plasma techniques, atmospheric plasmas allow us to avoid the constraints of the vacuum, thereby achieving surface treatments at lower costs and with the possibility of an industrial implementation in continuous production lines. Furthermore, by working in the post-discharge region of the plasma, instead of the discharge itself, milder surface treatment conditions can be applied and the structural and chemical modifications of the polymer can be confined in a shallower region of the surface (only a few tens of nanometers).[4]

In order to upgrade these surface plasma treatments to industrial scale, the chemical and physical properties of the polymers treated in atmospheric post-discharges need to be better understood. However, this investigation is made complex by the interaction between the post-discharge and the environment. Oxygen, nitrogen and water are always present in the atmosphere, intervening inevitably in the plasma-induced processes. Many studies about the surface characterization of plasma-modified or plasma-deposited polymers have been published, and the reader can refer to a few review papers.[5,6] Some studies have been carried out to investigate the effect of the oxygen in the plasma.[1,7,8] A recent example is given by the study of Dufour et al. on the compositional modification of the (sub)surface of high density polyethylene (HDPE) exposed to atmospheric He or He-O_2 post-discharges generated by a radiofrequency (RF) plasma torch, as a function of the plasma parameters (treatment time and gap between the specimen surface and the plasma source).[9] Their study aimed to identify the oxygen-containing functional groups responsible for the observed wettability changes and to investigate the ageing process of the material. Angle-resolved X-ray photoelectron spectroscopy (AR-XPS) was used to study the chemical composition and the chemical bonds (O-containing functionalities) of the HDPE subsurface, down to 9 nm in depth. Another study about the diffusion of oxygen into a low density polyethylene (LDPE) film, treated in atmospheric Ar and Ar-O_2 post-discharges, was conducted by Abou Rich et al. applying a combination of AR-XPS and ToF-SIMS depth-profiling with a low energy Cs^+ sputter ion source.[4] These measurements showed that oxygen could diffuse down to 20-40 nm in the polymer film depth, depending on the plasma conditions.

Another branch of research focuses on the effect of the water present at the interface between an atmospheric plasma torch and a polymer substrate. Often, the presence of water vapor in a plasma can be considered as problematic as water is known to destabilize the plasma.[10-12] However, water vapor can be deliberately mixed into the plasma to achieve a milder treatment or to generate radicals of interest. As the post-discharge of an atmospheric plasma torch can interact with the water molecules contained in the ambient air, OH radicals can easily be produced. For instance, Duluard et al. observed the production of OH radicals in the post-discharge of an RF plasma torch only supplied in Ar as carrier gas (30 L min^{-1}).[8]

The presence of water vapor in the plasma induces the grafting of -OH groups onto polymer surfaces, representing a promising functionalization route for industrial and medical applications.[13] However, tracing of the water reactivity in the polymer modification remains challenging. Whereas the induced oxidation can be satisfactorily monitored both at the surface and along the depth of the polymers,[4, 9] hydrogen uptake or exchange as a result of the interaction with the plasma water is much more difficult to assess. In order to investigate the reactions involving hydrogen, and thereby obtain a comprehensive view of the surface modification by water plasmas, one must be able not only to detect hydrogen (out of reach of XPS) but also to separate the hydrogen contributions from the water vapors (plasma or natural atmospheric water) and from the polymer itself.

In this contribution, we propose an original approach to gain insights into the reactions involving hydrogen, using a combination of deuterated water in the plasma and state-of-the-art SIMS analysis. For this purpose, D_2O vapor was injected in the post-discharge of an atmospheric argon plasma torch. LDPE was selected for the plasma treatment because it is widely used in multiple applications and already well studied in the literature.[4,7,14]

ToF-SIMS was chosen for the surface and in-depth analysis because it is the only surface technique possessing sufficient sensitivity and selectivity to the hydrogen isotopes as elements and in molecular fragments.[15-17] This capability has been already exploited in surface studies of deuterated or H-D exchanged polymer surfaces, where the group of Friedrich and Unger modified PE and deuterated PE using low pressure NH_3 and ND_3 plasma,[18,19] but not upon molecular depth-profiling. Here, capitalizing on the advent of Ar cluster ion beams for sample sputtering, the modifications of the polymer molecular structure will also be followed along the sample depth.[20,21] Better than their predecessors SF_5 and C_{60} for sensitive material depth-profiling,[21] large Ar clusters (hundreds to thousands of atoms) exhibit excellent depth resolution and retention of the molecular ion signals even after very large bombardment doses, corresponding to micrometers of erosion.[22] An additional advantage offered by these ion beams is the possibility to vary the cluster size as well as the energy, in order to optimize the level of damage,[23,24] the depth resolution[25-27] and the speed of profiling. By choosing the right conditions, it is now possible to obtain ultra-shallow organic depth-profiles on polymers.[28]

In the article following sections, a protocol for the quantification of the deuteration at the surface is first established by defining a deuteration ratio based on the SIMS intensities of the monomeric fragments of LDPE. Based on that parameter, the torch-surface distance is optimized. In the second part of the results, the evolution of the deuteration in a shallow region of the sample subsurface is followed using molecular depth-profiling, demonstrating the usefulness of Ar cluster beams for that purpose.

5.2.3. Experimental section

5.2.3.1. Materials and surface treatments by atmospheric plasma

The low density polyethylene (LDPE) used in the present work was provided by Goodfellow. It is a 50 μm-thick film and additive free. The absence of additives in the polymer film was checked, both on the surface and along the depth, by performing static and dynamic SIMS, since this technique possesses an excellent surface sensitivity <1 p.p.m. (which is not accessible to XPS), adequate for their detection. Finally, the absence of any surface contamination was verified by acquiring mass spectra of the pristine LDPE in both polarities and comparing them with the LDPE fragmentation pattern reported in the SIMS libraries.

The LDPE film was treated by an atmospheric RF plasma torch (Atomflo^{TM} 250D) from SurfX Technologies LLC.[4,29] The torch consists in 2 parallel 126-holes circular electrodes. The source was connected to an RF power generator operating at 27.12 MHz. The gas flow is oriented perpendicular to the 2 electrodes and consists in an argon gas supply with flow rate of 30 L min^{-1} for all the experiments. The power was fixed at 80 W. In the post-discharge region of the argon plasma torch, deuterated water (D_2O) (minimum deuteration degree of 99.9%, MagniSolv™ Merck KGaA, Darmstadt, Germany) vapors were injected by means of a bubbler and with a flow rate of 6 L min^{-1}of argon passing through the D_2O at the room temperature. In order to investigate the efficacy of the deuteration process as a function of the gap between the LDPE film and the plasma source, the experiments were performed during 5 minutes of treatment at three different distances - 5, 7 and 10 mm - which correspond to the distance between the grid of the plasma torch and the substrate as shown on the schematic representation of **Figure 1**. Smaller distances were excluded because they induced overheating of the polymer surface. Finally, the polymer film was treated also by only Ar and Ar-H_2O post-discharges (with the same flow rate of 6 L min^{-1} for Ar and H_2O from the bubbler than D_2O) at 5 min/5 mm for comparison.

The plasma-modified samples were kept in atmospheric conditions for two weeks, until their SIMS analyses. Indeed, recent studies on the air ageing

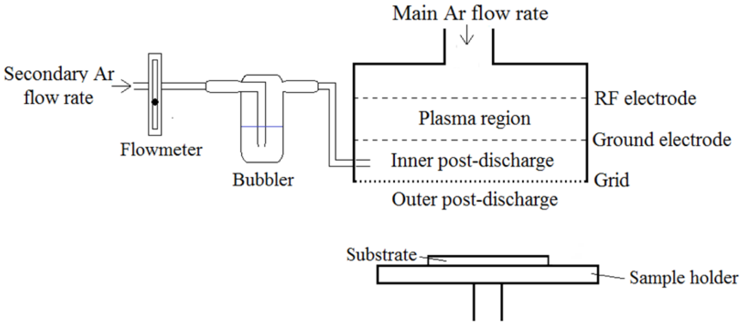

Figure 1. *Schematic of the atmospheric RF plasma torch (Atomflo^{TM} 250D) used for the surface treatment of LDPE films.*

of LDPE treated by atmospheric post-discharges suggest that this time would be sufficient for the equilibration of the plasma-treated specimens.[9,29-31]

5.2.3.2. ToF-SIMS surface analysis and molecular depth-profiling

Secondary ion mass spectra and molecular depth-profiling experiments were performed using an ION-TOF TOF.SIMS 5 (Münster, Germany) instrument equipped with both Bi-LMIG (liquid metal ion gun) and Ar-GCIB (gas cluster ion beam) primary ion sources mounted at 45° to the surface normal. The secondary ions were collected by a time-of-flight analyzer perpendicular to the sample surface.

ToF-SIMS spectra were obtained using a 30 keV Bi_5^+ beam (0.06 pA) on a 200 x 200 μm^2 sample area from 60 s acquisition. The total dose density was less than 6 x 10^{10} ions cm^{-2}, which ensured the static bombardment conditions. Three measurements per polarity were acquired from each sample. The intensity values in each spectrum were normalized to the respective total secondary ion yields and the three normalized spectra of each sample were averaged.

The molecular depth-profiles, acquired in both polarities, were obtained in dual ion beam mode. 10 keV Ar_{5000}^+ ions (0.1 nA; full width at half maximum of the mass distribution of the Ar cluster ions is 1940 atoms/ion), corresponding to an energy of around 2 eV per constituent atom, were employed to sputter a 600 x 600 μm^2 area, and 30 keV Bi_5^+ ions (0.06 pA) for collecting the spectra from a 200 x 200 μm^2 area concentric to the sputtered surface. Since the measurements showed excellent reproducibility, only two profiles per polarity and per sample were acquired. A non-interlaced mode was used and an electron flood gun was employed for charge compensation.

The total fluence for the 30 keV Bi_5^+ beam was of the order of magnitude of 10^{11} ions cm^{-2}, while the fluence accumulated during the whole profile for the 10 keV Ar_{5000}^+ source was 10^{14} ions cm^{-2}. The ratio between the reported doses excludes a significant contribution of the analysis beam in the sputtering process.[26,28]

The aforementioned sputtering protocol corresponds to an extremely mild erosion of the sample and leads to very small crater depth for long measurement times. Therefore, the resulting craters could not be measured and another procedure was devised to estimate the sputtering yields and infer the total etching depths of the profiles. For this purpose, a crater was etched in a sample of pristine LDPE using faster erosion conditions, but the same cluster size, incidence angle and energy, which are the determining parameters for the sputtering. The erosion was performed by 10 keV Ar_{5000}^+, with a current of 0.4 nA and a bombarded area of 400 x 400 μm^2 (i.e. an order of magnitude faster than the initial depth-profiling conditions), up to a total fluence of 4 x 10^{16} ions cm^{-2} (~7 hours bombardment). The final crater depth was measured by a DektakXT profilometer (Bruker) and its value was 840 nm. The calculated sputter yield (1.9 x 10^{-21} cm^3/primary ion) was used for the depth calibration of the LDPE profiles.

5.2.4. Results and discussion

The positive mass spectra of the plasma-deuterated LDPE exhibit a mass resolution that is sufficiently high for discriminating $^2H^+$ (signified from now on as D^+) from H_2^+, showing an m/z difference of 0.002 with the employed acquisition parameters. In order to identify each fragment ion of the deuterated polymer mass spectra, a detailed comparison with the pristine material and the LDPE surfaces modified by Ar and Ar-H_2O post-discharges was conducted. The mass resolution (m/Δm) for the entire set of acquired SIMS spectra was about 5000 at m/z 29 ($C_2H_5^+$) in positive polarity and about 5500 at m/z 49 (C_4H^-) in negative polarity. Specimens treated under Ar and Ar-H_2O post-discharges display a very similar fragmentation pattern, mainly characterized by oxygen- and nitrogen-containing peaks. Their origin, oxidation and nitrogen uptake either from the plasma treatment or the air, and the additional effects of sample ageing, are well known in atmospheric pressure plasma treatments.[9] Using deuterated water in the post-discharge, the mass spectra become more complicated because of the additional process of H-D exchange. This isotopic substitution provides important information about the hydrogenation. Following H-D exchange, the positive mass spectra indicate the presence of mixed ions, such as $C_xH_yD_z^+$ and $C_xH_yD_z(N/O)_m^+$. For those fragment ions, the assignment of the exact number of hydrogen isotopes incorporated in the monomer structure is challenging. Indeed, the different contributions cannot always be separated because the mass resolution becomes insufficient with increasing mass. Two tables (**Table S1 and S2**) are provided in supporting information, which list the most intense peaks in the range $0 \leq m/z \leq 70$ of the pristine and plasma-treated LDPE mass spectra, and their most reasonable attributions, for both polarities (taking into account the uncertainty on the H isotope content). Other tables of characteristic fragments of deuterated polyethylene and related to an ammonia plasma treatment at low pressure can be found in the work of Min et al.[18]

The objective of the present work is to study the deuteration of the LDPE surface and sub-surface regions. To assess the extent of the deuteration, it is recommended to focus on molecular fragment ions. The reason is twofold. First, the molecular ions provide richer information than the atomic ions H^+ and D^+ and, second, in the conditions of depth-profiling, they are more trustable. Indeed, monatomic species like H or D can be easily kicked into the depth of the sample by the impinging projectiles, giving rise to artifacts upon repeated bombardment and analysis sequences. Therefore, the ions selected for the analysis were the protonated PE repeat unit, $C_2H_5^+$ ($m/z = 29.039$), and its progressive deuteration reaction products, $C_2DH_4^+$ ($m/z = 30.044$), $C_2D_2H_3^+$ ($m/z = 31.052$), $C_2D_3H_2^+$ ($m/z = 32.058$), $C_2D_4H^+$ ($m/z = 33.065$) and $C_2D_5^+$ ($m/z = 34.071$).[ii] It is important to note that all these fragment ions, differing only by their H isotopic ratio, should possess the same ionization probability.

Once these methodological precautions and protocols are established, the influence of the sample-torch gap on the H-D exchange at the surface can be investigated. **Figure 2** shows the results of the ToF-SIMS analysis of the deuterated LDPE for three different torch-surface distances, 5, 7 and 10 mm.

[ii] The choice of the $C_2H_{5-x}D_x^+$ ($0 \leq x \leq 5$) ion series represents the best compromise between the degrading mass resolution with increasing m/z, which is necessary to discriminate each hydrocarbon ion ($C_2H_{5-x}D_x^+$) from the nearest N-containing ion, as can be seen in **Figure S1**, and the complexity of the fragment (at least 2 carbon atoms). On the other hand, the probability of total deuteration (complete replacement of H with D) of a given fragment ion decreases with increasing the ion size (i.e. the number of C and H atoms).

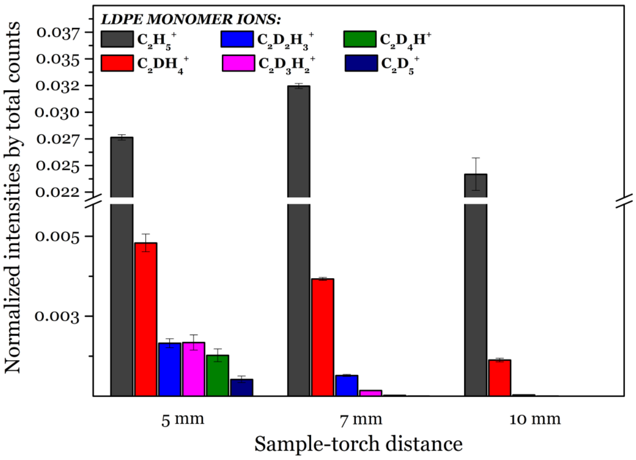

Figure 2. *Surface analysis of the LDPE samples treated by Ar-D$_2$O post-discharge for 5 min. Effect of the torch-sample distance on the deuteration.*

In order to obtain a synthetic view of the sample deuteration, it is useful to introduce an H-D exchange indicator or "deuteration ratio", R_D, which is defined as follows:

$$R_D = \sum_{x=1}^{5} C_2H_{5-x}D_x^+ \Big/ \sum_{x=0}^{5} C_2H_{5-x}D_x^+$$

where the notation $C_2H_{5-x}D_x^+$ ($0 \leq x \leq 5$) represents the SIMS counts of a given ion fragment related to the structure of the protonated repeat unit of the polyethylene ($C_2H_5^+$).

Our results show that 5 mm gap gives a R_D of ~25 %, which decreases strongly with the sample-torch distance, down to a value of ~5% for a gap of 10 mm. For the 5 mm distance, the statistics of mono-substitution of the hydrogen atoms contained in the monomer structure is 12.6%. The fully deuterated monomer intensity represents 1.3% of the total.

The second objective of this work is to study the deuteration along the sample depth. The sample functionalized in the optimized conditions, with a torch-surface distance of 5 mm was depth-profiled in the dual-beam mode, as described in the experimental section. The results are reported in **Figure 3**. The evolution of the monomer unit ions $C_2D_xH_{5-x}^+$ ($0 \leq x \leq 5$), previously studied by static SIMS conditions on the specimen surface, is now followed along the depth. The intensity of each signal is normalized by its maximum value to point out the different trends of the fragments, the absolute intensity of $C_2H_5^+$ being much higher than the others (almost two orders of magnitude

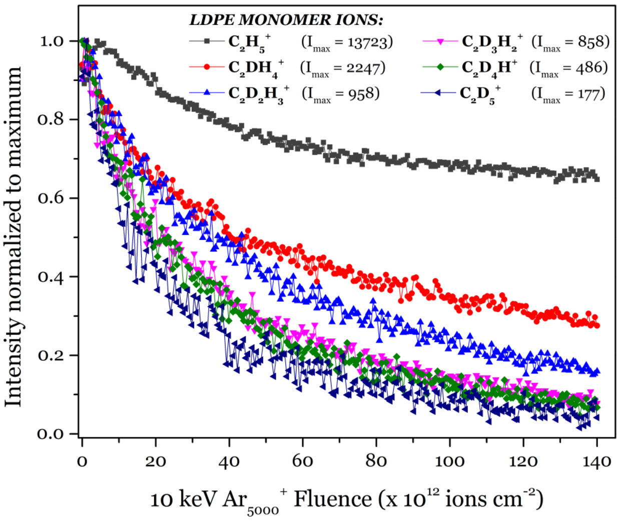

Figure 3. *Depth-profile of the LDPE film treated for 5 min at 5 mm. Intensity of the* $C_2D_xH_{5-x}^+$ *fragments* ($0 \leq x \leq 5$) *as a function of the Ar cluster fluence (total value of* 1.4 x 10^{14} *ions* cm^{-2}*).*

compared to $C_2D_5^+$). There is a very strong decrease of the deuterated species with the sample depth. However, there is also a smaller decrease of the $C_2H_5^+$ intensity (30%), which might be the result of diverse causes such as, for instance, the presence of smaller chains on the surface, more branching of the molecules and/or oxidation.[4,9,32] The first hypothesis cannot be ruled out because the samples were not washed after the plasma treatment in order to avoid swelling of the polymer. The order of the curves follows the order of deuteration, $C_2D_5^+$ presenting the steepest decrease. At the end of the profile, the less deuterated species are still present with significant intensities, but the fully deuterated repeat unit intensity is close to zero. A longer acquisition time confirms the stabilization of the $C_2H_5^+$ intensity and the continuous decay of the $C_2D_xH_{5-x}^+$ ($2 \leq x \leq 5$) intensities down to zero, as shown in **Figure S2**. Only the $C_2DH_4^+$ intensity does not level off due to the interference of the $^{13}CCH_5^+$ peak. This ^{13}C-contribution to the mono-substituted monomer unit ion corresponds to an overestimation of the deuteration ratio R_D of ~3%. The conversion of the fluence (ions cm^{-2}) reported in the x-axis of the profile to depth (nm) was performed according to the procedure defined in the experimental section. The entire profiles shown in Figure 3 correspond to a depth of only ~3 nm. Even though this value might bear a non-negligible error because of the indirect measurement of the sputter yield on a pristine sample, we expect it to be well below a factor of two, which means that in any case the probed depth is the extreme surface. It is comparable to the depth resolution usually announced for organic materials in cluster SIMS. The implications of this finding will be discussed in more detail at the end of this section. Finally, signal broadening might derive from the nanoscopic roughness, which is the roughness commensurate with the scale of the volume sampled by the projectile bombardment, amongst other factors. Considering some broadening induced by the local roughness (not known) and by the actual volume of the material sputtered by each analysis projectile, the observed signal should provide an upper limit to the estimate of the profile width of the investigated deuterated molecular fragments. In terms of "decay length", defined as the depth interval in which the profile signal decays to 1/e (36.8%) of its original intensity and applicable to those depth-profiles without steps, the real profile could be characterized by smaller decay lengths of the considered ion fragments.

Because of the decrease of the non-substituted fragment ($C_2H_5^+$) intensity shown in Figure 3, a normalization procedure is required for quantification of the deuteration along the depth, in order to eliminate all the factors responsible of this initial decay (previously mentioned in the text). For this purpose, we consider once again the deuteration ratio R_D, in which the intensities of the deuterated repeat unit species are intrinsically normalized by the sum of all the peak intensities of the monomer unit. **Figure 4** shows the evolution of R_D as a function of the primary ion fluence, going from ~25%, that is the value obtained at the surface (Figure 2), to less than 10%, over the top 3 nm.

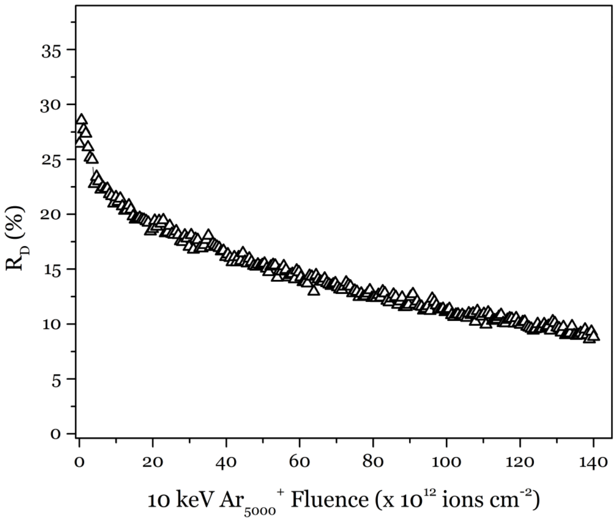

Figure 4. *Evolution of the deuteration ratio R_D as a function of the Ar cluster fluence upon depth-profiling of the LDPE sample treated for 5 min at 5 mm.*

The erosion depth deduced from the sputtering experiments places the evolutions observed in Figure 3 and 4 in the category of "ultra-shallow" depth-profiling. In the dual-beam depth-profiling procedure, the 30 keV Bi_5^+ clusters (45° incidence) used for analysis are expected to implant to a depth that is superior to the ~3 nm thickness sputtered by the Ar clusters. The experimental study of Muramoto et al. indicates implantation depths in the range 9-14 nm for 25 keV Bi_3^+ and 50 keV Bi_5^{+2}, using a similar experimental setup.[33] Our previous theoretical study suggests an implantation depth of ~7 nm for 10 keV Bi_5 at normal incidence.[34] Though the sputter rates of Ar clusters in our experiment are very low, a reasonable ratio of analysis versus sputtering ion fluence (6×10^{-3}) has been maintained, so that detrimental effects of the analysis beam can be excluded (damage, matrix effect). Following these considerations, the proposed picture is that of a surface with "isolated" Bi atoms/clusters essentially implanted below the depth-profiled area. In order to confirm this hypothesis, the signal of Bi^+ reemitted from the bombarded surface was followed in the exact same conditions as those of Figure 3 and 4, but over a longer bombardment time (**Figure 5**). Though the small fraction of implanted bismuth makes the signal quite weak, it clearly reaches saturation for an Ar cluster fluence that is larger than the full profiles of Figure 3 and 4 (5.99×10^{14} ions cm^{-2}). This result is consistent with our hypothesis.

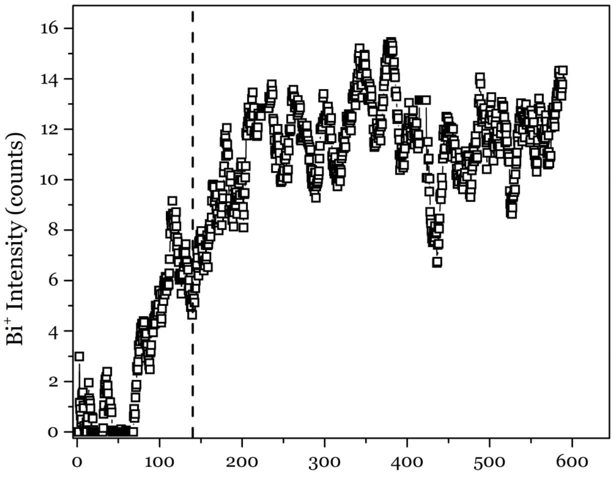

Figure 5. *Evolution of the Bi^+ signal intensity as a function of the Ar cluster fluence upon depth-profiling of the LDPE sample treated for 5 min at 5 mm. The vertical dashed line indicates the total sputtering fluence used for the depth-profiles of Figure 3 and 4.*

The small amount of implanted Bi warrants the reliability of the obtained profiles, despite the fact that they are obtained in the pre-equilibrium phase of the depth-profiling experiment.

Finally, the SIMS literature of the surface characterization of plasma-modified polymers provides indications of an isotopic effect for hydrogen isotopes in the plasma processes, that yields the hydrogenation more efficient when compared with the deuteration.[18] This phenomenon is ascribed to the lower diameters of protons and H atoms, giving higher mean-free paths in the plasma and higher diffusion coefficients in the samples when compared to deuterons and D atoms. Thus, this isotopic effect requires to take the proper precautions in transferring the knowledge acquired using D_2O-plasma to possible H_2O-related processes. However, to our knowledge, there are not insights in the literature about an influence of the isotopic effect along the sample depth. In order to elucidate this point, it was also performed LDPE treatment by atmospheric Ar-H_2O post-discharge, as described in the experimental section. By comparing the depth-profiles, no significant difference is observed in the evolution of the hydrogenated species of the sample exposed to Ar-H_2O post-discharge and the corresponding deuterated species of the polyethylene treated with Ar-D_2O post-discharge (such as for instance CHO^+ and CDO^+). This is shown in the **Figure S3** of the Supporting Information, reporting the depth-profiles of CHO^+/CDO^+ and CH_3O^+/CD_3O^+ species for the LDPE treated by atmospheric Ar-H_2O and Ar-D_2O post-discharges. Apparently, the different diffusion coefficients of the species D/D^+ and H/H^+ are not the dominant factor to explain the profiles. The diverse diffusive behavior expected for D/D^+ compared with H/H^+ remains likely in the experimental error of the measurements.

5.2.5. Conclusion

Hydrogen-deuterium exchange reactions caused by an Ar-D_2O post-discharge in LDPE were successfully and easily evidenced at the sample surface and along the depth using ToF-SIMS. Thanks to the elaboration of a mathematical parameter (R_D), it is possible to quantify the surface deuteration changes induced by the variation of the experimental parameters, such as the sample-torch distance (25% of deuterated monomer units for a distance of 5 mm). Single H-D substitution is the most probable mechanism explaining the observed fragments. For the first time, ultra-shallow molecular depth-profiling of an organic sample by Ar noble gas clusters is reported. It shows that the H-D substitution is an extreme surface process. Indeed, the deuteration ratio (R_D)

is reduced by a factor >2 over a depth of ~3 nm. Based on the methodological developments established in this article, future works will address the effects of the post-discharge parameters and post-treatment ageing on the distribution of deuterated and oxidized species in the (sub)surface of the polymer.

5.2.6. Supporting Information

Table S1. *List of the positive secondary fragment ions of the SIMS spectra in the mass range $0 \leq m/z \leq 70$ for:* ***Pristine LDPE****; LDPE treated by Ar post-discharge (****Ar/LDPE****); LDPE treated by Ar-H_2O post-discharge (****Ar-H_2O/LDPE****); and LDPE treated by Ar-D_2O post-discharge (****Ar-D_2O/LDPE****). The plasma treatments were performed for 5 min at 5 mm of distance from the torch.*

Mass (m/z)	**Pristine LDPE**	**Ar/LDPE**	**Ar-H_2O/LDPE**	**Ar-D_2O/LDPE**
1	H^+	H^+	H^+	H^+
2	-	-	-	D^+
	H_2^+	H_2^+	H_2^+	H_2^+
3	H_3^+	H_3^+	H_3^+	DH^+, H_3^+
12	C^+	C^+	C^+	C^+
13	CH^+	CH^+	CH^+	CH^+
14	CH_2^+	CH_2^+	CH_2^+	CD^+, CH_2^+
15	CH_3^+	CH_3^+	CH_3^+	CDH^+, CH_3^+
16	$^{13}CH_3^+$	$^{13}CH_3^+$	$^{13}CH_3^+$	$^{13}CH_3^+$, CD_2^+, CDH_2^+
17	-	NH_3^+	NH_3^+	NH_3^+
	-	-	-	CD_2H^+
18	-	NH_4^+	NH_4^+	NH_4^+
	-	-	-	CD_3^+
19	-	H_3O^+	H_3O^+	H_3O^+
	-	-	-	ND_2H^+, NDH_3^+
20	-	-	-	DH_2O^+
	-	-	-	ND_3^+, $ND_2H_2^+$
21	-	-	-	D_2HO^+
	-	-	-	ND_3H^+
22	-	-	-	D_3O^+
25	C_2H^+	C_2H^+	C_2H^+	C_2H^+
26	$C_2H_2^+$	$C_2H_2^+$	$C_2H_2^+$	C_2D^+, $C_2H_2^+$
27	$C_2H_3^+$	$C_2H_3^+$	$C_2H_3^+$	C_2DH^+, $C_2H_3^+$
28	-	CH_2N^+	CH_2N^+	CDN^+, CH_2N^+
	$C_2H_4^+$	$C_2H_4^+$	$C_2H_4^+$	$C_2D_2^+$, $C_2DH_2^+$, $C_2H_4^+$
29	-	CHO^+	CHO^+	CHO^+
	-	-	-	$CDHN^+$
	$C_2H_5^+$	$C_2H_5^+$	$C_2H_5^+$	$C_2D_2H^+$, $C_2H_5^+$
30	-	CH_2O^+	CH_2O^+	CDO^+, CH_2O^+
	-	CH_4N^+	CH_4N^+	CD_2N^+, CH_4N^+
	$^{13}CCH_5^+$	$^{13}CCH_5^+$	$^{13}CCH_5^+$	$C_2D_3^+$, $^{13}CCH_5^+$, $C_2DH_4^+$
31	CH_3O^+	CH_3O^+	CH_3O^+	$CDHO^+$, CH_3O^+
	-	$^{13}CH_4N^+$,	$^{13}CH_4N^+$,	$^{13}CH_4N^+$, CD_2HN^+, CDH_3N^+,
	-	CH_5N^+	CH_5N^+	CH_5N^+
		-	-	$C_2D_2H_3^+$
32	-	$^{13}CH_3O^+$	$^{13}CH_3O^+$	$^{13}CH_3O^+$, CD_2O^+, CDH_2O^+
	-	CH_6N^+	CH_6N^+	$CD_2H_2N^+$, CH_6N^+
	-	-	-	$C_2D_3H_2^+$
33	-	-	-	CD_2HO^+
	-	-	-	CD_3HN^+
	-	-	-	$C_2D_4H^+$

→→→

34	-	-	-	CD_3O^+
	-	-	-	CD_4N^+, $CD_2H_4N^+$
	-	-	-	$C_2D_5^+$
35	-	-	-	$CD_3H_3N^+$
36	-	-	-	$CD_4H_2N^+$
37	C_3H^+	C_3H^+	C_3H^+	C_3H^+
	-	-	-	CD_5HN^+
38	$C_3H_2^+$	$C_3H_2^+$	$C_3H_2^+$	C_3D^+, $C_3H_2^+$
39	$C_3H_3^+$	$C_3H_3^+$	$C_3H_3^+$	C_3DH^+, $C_3H_3^+$
40	$C_3H_4^+$	$C_3H_4^+$	$C_3H_4^+$	$C_3D_2^+$, $C_3DH_2^+$, $C_3H_4^+$
41	$C_3H_5^+$	$C_3H_5^+$	$C_3H_5^+$	$C_3D_2H^+$, $C_3DH_3^+$, $C_3H_5^+$
42	-	$C_2H_2O^+$	$C_2H_2O^+$	C_2DO^+, $C_2H_2O^+$
	-	$C_2H_4N^+$	$C_2H_4N^+$	-
	$C_3H_6^+$	$C_3H_6^+$	$C_3H_6^+$	$C_3D_3^+$, $C_3D_2H_2^+$, $C_3DH_4^+$, $C_3H_6^+$
43	$C_2H_3O^+$	$C_2H_3O^+$	$C_2H_3O^+$	C_2DHO^+, $C_2H_3O^+$
	$C_3H_7^+$	$C_3H_7^+$	$C_3H_7^+$	$C_3D_3H^+$, $C_3D_2H_3^+$, $C_3DH_5^+$, $C_3H_7^+$
44	-	CH_2NO^+	CH_2NO^+	$CDNO^+$,CH_2NO^+
	$C_2H_4O^+$	$C_2H_4O^+$	$C_2H_4O^+$	$C_2D_2O^+$, $C_2DH_2O^+$, $C_2H_4O^+$
	-	$C_2H_6N^+$	$C_2H_6N^+$	$C_2D_3N^+$, $C_2D_2H_2N^+$, $C_2DH_4N^+$, $C_2H_6N^+$
	-	-	-	$C_3D_4^+$, $C_3D_3H_2^+$, $C_3D_2H_4^+$, $C_3DH_6^+$
45	-	CHO_2^+	CHO_2^+	CHO_2^+
	$C_2H_5O^+$	$C_2H_5O^+$	$C_2H_5O^+$	$C_2D_2HO^+$, $C_2DH_3O^+$, $C_2H_5O^+$
	-	$CH_5N_2^+$	$CH_5N_2^+$	-
	-	-	-	$C_2D_3HN^+$, $C_2D_2H_3N^+$, $C_2DH_5N^+$
	-	-	-	$C_3D_4H^+$, $C_3D_3H_3^+$, $C_3D_2H_5^+$
46	-	$CH_2O_2^+$	$CH_2O_2^+$	CDO_2^+, $CH_2O_2^+$
	-	-	-	$C_2D_3O^+$, $C_2D_2H_2O^+$, $C_2DH_4O^+$
	-	-	-	$CD_3N_2^+$, $CD_2H_2N_2^+$, $CDH_4N_2^+$
	-	-	-	$C_3D_5^+$, $C_3D_4H_2^+$, $C_3D_3H_4^+$
47	-	$CH_3O_2^+$	$CH_3O_2^+$	$CDHO_2^+$, $CH_3O_2^+$
	-	-	-	$C_2D_3HO^+$, $C_2D_2H_3O^+$
	-	-	-	$CD_3HN_2^+$, $CD_2H_3N_2^+$, $CDH_5N_2^+$
	-	-	-	$C_2D_4HN^+$, $C_2D_3H_3N^+$, $C_2D_2H_5N^+$, $C_2DH_7N^+$
	-	-	-	$C_3D_5H^+$, $C_3D_4H_3^+$
48	-	-	-	$CD_2O_2^+$, $CDH_2O_2^+$
	-	-	-	$C_2D_4O^+$, $C_2D_3H_2O^+$
	-	-	-	$C_2D_5N^+$, $C_2D_4H_2N^+$, $C_2D_3H_4N^+$, $C_2D_2H_6N^+$
49	C_4H^+	C_4H^+	C_4H^+	C_4H^+
	-	-	-	$CD_2HO_2^+$
	-	-	-	$C_2D_4HO^+$
	-	-	-	$C_2D_5HN^+$, $C_2D_4H_3N^+$, $C_2D_3H_5N^+$
50	$C_4H_2^+$	$C_4H_2^+$	$C_4H_2^+$	C_4D^+, $C_4H_2^+$
	-	-	-	$C_2D_5O^+$
	-	-	-	$C_2D_6N^+$, $C_2D_5H_2N^+$, $C_2D_4H_4N^+$
51	$C_4H_3^+$	$C_4H_3^+$	$C_4H_3^+$	C_4DH^+, $C_4H_3^+$
	-	-	-	$C_2D_6HN^+$, $C_2D_5H_3N^+$
52	$C_4H_4^+$	$C_4H_4^+$	$C_4H_4^+$	$C_4D_2^+$, $C_4DH_2^+$, $C_4H_4^+$
	-	-	-	$C_2D_7N^+$, $C_2D_6H_2N^+$
53	-	C_3HO^+	C_3HO^+	C_3HO^+
	$C_4H_5^+$	$C_4H_5^+$	$C_4H_5^+$	$C_4D_2H^+$, $C_4DH_3^+$, $C_4H_5^+$
54	-	$C_3H_2O^+$	$C_3H_2O^+$	C_3DO^+, $C_3H_2O^+$
	$C_4H_6^+$	$C_4H_6^+$	$C_4H_6^+$	$C_4D_3^+$, $C_4D_2H_2^+$, $C_4DH_4^+$, $C_4H_6^+$

→→→

55	- $C_4H_7^+$	$C_3H_3O^+$ $C_4H_7^+$	$C_3H_3O^+$ $C_4H_7^+$	C_3DHO^+, $C_3H_3O^+$ $C_4D_3H^+$, $C_4D_2H_3^+$, $C_4DH_5^+$, $C_4H_7^+$
56	- $C_4H_8^+$	$C_3H_4O^+$ $C_4H_8^+$	$C_3H_4O^+$ $C_4H_8^+$	$C_3D_2O^+$, $C_3DH_2O^+$, $C_3H_4O^+$ $C_4D_4^+$, $C_4D_3H_2^+$, $C_4D_2H_4^+$, $C_4DH_6^+$, $C_4H_8^+$
57	$C_3H_5O^+$ $C_4H_9^+$	$C_3H_5O^+$ $C_4H_9^+$	$C_3H_5O^+$ $C_4H_9^+$	$C_3D_2HO^+$, $C_3DH_3O^+$, $C_3H_5O^+$ $C_4D_4H^+$, $C_4D_3H_3^+$, $C_4D_2H_5^+$, $C_4DH_7^+$, $C_4H_9^+$
58	- - -	$C_2H_2O_2^+$ $C_3H_6O^+$ $C_3H_8N^+$	$C_2H_2O_2^+$ $C_3H_6O^+$ $C_3H_8N^+$	$C_2DO_2^+$, $C_2H_2O_2^+$ $C_3D_3O^+$, $C_3D_2H_2O^+$, $C_3DH_4O^+$, $C_3H_6O^+$ $C_3D_4N^+ \rightarrow C_3H_8N^+$/ $C_4D_5^+ \rightarrow C_4DH_8^+$
59	- $C_3H_7O^+$ - -	$C_2H_3O_2^+$ $C_3H_7O^+$ $C_2H_7N_2^+$ -	$C_2H_3O_2^+$ $C_3H_7O^+$ $C_2H_7N_2^+$ -	$C_2DHO_2^+$, $C_2H_3O_2^+$ $C_3D_3HO^+$, $C_3D_2H_3O^+$, $C_3DH_5O^+$, $C_3H_7O^+$ - $C_4D_5H^+$, $C_4D_4H_3^+$, $C_4D_3H_5^+$, $C_4D_2H_7^+$
60	- - - -	$C_2H_4O_2^+$ - $C_3H_{10}N^+$ -	$C_2H_4O_2^+$ - $C_3H_{10}N^+$ -	$C_2D_2O_2^+$, $C_2DH_2O_2^+$, $C_2H_4O_2^+$ $C_3D_4O^+$, $C_3D_3H_2O^+$, $C_3D_2H_4O^+$, $C_3DH_6O^+$ $C_3D_5N^+ \rightarrow C_3H_{10}N^+$ $C_4D_6^+$, $C_4D_5H_2^+$, $C_4D_3H_6^+$
61	C_5H^+ - - - -	C_5H^+ $C_2H_5O_2^+$ - - -	C_5H^+ $C_2H_5O_2^+$ - - -	C_5H^+ $C_2D_2HO_2^+$, $C_2DH_3O_2^+$, $C_2H_5O_2^+$ $C_3D_4HO^+$, $C_3D_3H_3O^+$, $C_3D_2H_5O^+$ $C_2D_4HN_2^+ \rightarrow C_2H_9N_2^+$ $C_4D_6H^+$, $C_4D_5H_3^+$, $C_4D_4H_5^+$
62	$C_5H_2^+$ - - - -	$C_5H_2^+$ - - - -	$C_5H_2^+$ - - - -	C_5D^+, $C_5H_2^+$ $C_2D_3O_2^+$, $C_2D_2H_2O_2^+$, $C_2DH_4O_2^+$ $C_3D_5O^+$, $C_3D_4H_2O^+$, $C_3D_3H_4O^+$ $C_2D_5N_2^+ \rightarrow C_2DH_8N_2^+$ $C_4D_7^+$, $C_4D_6H_2^+$, $C_4D_5H_4^+$
63	$C_5H_3^+$ - - -	$C_5H_3^+$ - - -	$C_5H_3^+$ - - -	C_5DH^+, $C_5H_3^+$ $C_3D_5HO^+$, $C_3D_4H_3O^+$ $C_2D_5HN_2^+ \rightarrow C_2D_2H_7N_2^+$ $C_3D_6HN^+ \rightarrow C_3D_3H_7N^+$
64	$C_5H_4^+$ - -	$C_5H_4^+$ - -	$C_5H_4^+$ - -	$C_5D_2^+$, $C_5DH_2^+$, $C_5H_4^+$ $C_3D_6O^+$, $C_3D_5H_2O^+$ $C_3D_7N^+ \rightarrow C_3D_4H_6N^+$
65	$C_5H_5^+$ - -	$C_5H_5^+$ - -	$C_5H_5^+$ - -	$C_5D_2H^+$, $C_5DH_3^+$, $C_5H_5^+$ $C_3D_6HO^+$ $C_3D_7HN^+$, $C_3D_6H_3N^+$, $C_3D_5H_5N^+$
66	- $C_5H_6^+$ - -	$C_4H_2O^+$ $C_5H_6^+$ - -	$C_4H_2O^+$ $C_5H_6^+$ - -	C_4DO^+, $C_4H_2O^+$ $C_5D_3^+$, $C_5D_2H_2^+$, $C_5DH_4^+$, $C_5H_6^+$ $C_3D_7O^+$ $C_3D_8N^+$, $C_3D_7H_2N^+$, $C_3D_6H_4N^+$
67	$C_4H_3O^+$ $C_5H_7^+$ -	$C_4H_3O^+$ $C_5H_7^+$ -	$C_4H_3O^+$ $C_5H_7^+$ -	C_4DHO^+, $C_4H_3O^+$ $C_5D_3H^+$, $C_5D_2H_3^+$, $C_5DH_5^+$, $C_5H_7^+$ $C_3D_8HN^+$, $C_3D_7H_3N^+$
68	- $C_5H_8^+$ -	$C_4H_4O^+$ $C_5H_8^+$ -	$C_4H_4O^+$ $C_5H_8^+$ -	$C_4D_2O^+$, $C_4DH_2O^+$, $C_4H_4O^+$ $C_5D_4^+$, $C_5D_3H_2^+$, $C_5D_2H_4^+$, $C_5DH_6^+$, $C_5H_8^+$ $C_3D_9N^+$, $C_3D_8H_2N^+$
69	- - $C_5H_9^+$	$C_3HO_2^+$ $C_4H_5O^+$ $C_5H_9^+$	$C_3HO_2^+$ $C_4H_5O^+$ $C_5H_9^+$	$C_3HO_2^+$ $C_4D_2HO^+$, $C_4DH_3O^+$, $C_4H_5O^+$ $C_5D_4H^+ \rightarrow C_5H_9^+$
70	- - $C_5H_{10}^+$	- $C_4H_6O^+$ $C_5H_{10}^+$	- $C_4H_6O^+$ $C_5H_{10}^+$	$C_3DO_2^+$ $C_4D_3O^+$, $C_4D_2H_2O^+$, $C_4DH_4O^+$, $C_4H_6O^+$ $C_5D_5^+ \rightarrow C_5H_{10}^+$

Table S2. *List of the negative secondary fragment ions of the SIMS spectra in the mass range 0 ≤ m/z ≤ 70 for:* ***Pristine LDPE****; LDPE treated by Ar post-discharge (****Ar/LDPE****); LDPE treated by Ar-H_2O post-discharge (****Ar-H_2O/LDPE****); and LDPE treated by Ar-D_2O post-discharge (****Ar-D_2O/LDPE****). The plasma treatments were performed for 5 min at 5 mm of distance from the torch.*

Mass (m/z)	Pristine LDPE	Ar/LDPE	Ar-H₂O/LDPE	Ar-D₂O/LDPE
1	H^-	H^-	H^-	H^-
2	H_2^-	H_2^-	H_2^-	D^-
12	C^-	C^-	C^-	C^-
13	CH^-	CH^-	CH^-	CH^-
14	CH_2^-	CH_2^-	CH_2^-	CD^-, CH_2^-
15	- CH_3^-	NH^- CH_3^-	NH^- CH_3^-	NH^- CDH^-, CH_3^-
16	O^- - -	O^- NH_2^- -	O^- NH_2^- -	O^- ND^-, NH_2^- CD_2^-, CDH_2^-
17	OH^- -	OH^- -	OH^- -	OH^- CD_2H^-
18	-	-	-	OD^- CD_3^-
19	-	H_3O^-	H_3O^-	H_3O^-
20	-	-	-	D_2O^-
21	-	-	-	D_2HO^-
22	-	-	-	D_3O^-
24	C_2^-	C_2^-	C_2^-	C_2^-
25	C_2H^-	C_2H^-	C_2H^-	C_2H^-
26	CN^- $^{13}CCH^-$, $C_2H_2^-$	CN^- $^{13}CCH^-$, $C_2H_2^-$	CN^- $^{13}CCH^-$, $C_2H_2^-$	CN^- $^{13}CCH^-$, C_2D^-, $C_2H_2^-$
27	$^{13}CN^-$, CHN^- - $C_2H_3^-$	$^{13}CN^-$, CHN^- - $C_2H_3^-$	$^{13}CN^-$, CHN^- - $C_2H_3^-$	$^{13}CN^-$, CHN^- $^{13}CCD^-$ C_2DH^-, $C_2H_3^-$
28	- $^{13}CCH_3^-$	CH_2N^- $^{13}CCH_3^-$	CH_2N^- $^{13}CCH_3^-$	CDN^-, CH_2N^- $C_2D_2^-$, $C_2DH_2^-$
29	- - -	CHO^- - -	CHO^- - -	CHO^- $CDHN^-$ $C_2D_2H^-$
30	- - -	- - -	- - -	CDO^- CD_2N^- $C_2D_3^-$
31	- -	CH_3O^- -	CH_3O^- -	CH_3O^- $^{13}CCD_3^-$
32	- -	O_2^- -	O_2^- -	O_2^- CDH_2O^-
33	- -	HO_2^- -	HO_2^- -	HO_2^- CD_2HO^-
34	$H_2O_2^-$ -	$H_2O_2^-$ -	$H_2O_2^-$ -	DO_2^-, $H_2O_2^-$ CD_3O^-
36	C_3^-	C_3^-	C_3^-	C_3^-
37	C_3H^-	C_3H^-	C_3H^-	C_3H^-
38	- $C_3H_2^-$	C_2N^- $C_3H_2^-$	C_2N^- $C_3H_2^-$	C_2N^- C_3D^-, $C_3H_2^-$
39	- $C_3H_3^-$	C_2HN^- $C_3H_3^-$	C_2HN^- $C_3H_3^-$	C_2HN^- C_3DH^-, $C_3H_3^-$
40	C_2O^- $C_2H_2N^-$ $^{13}CC_2H_3^-$	C_2O^- $C_2H_2N^-$ $^{13}CC_2H_3^-$	C_2O^- $C_2H_2N^-$ $^{13}CC_2H_3^-$	C_2O^- C_2DN^-, $C_2H_2N^-$ $^{13}CC_2H_3^-$, $C_3D_2^-$, $C_3DH_2^-$

→→→

41	C_2HO^-	C_2HO^-	C_2HO^-	C_2HO^-
	-	-	-	C_2DHN^-
	$C_3H_5^-$	$C_3H_5^-$	$C_3H_5^-$	$C_3D_2H^-$, $C_3H_5^-$
42	CNO^-	CNO^-	CNO^-	CNO^-
	-	-	-	C_2DO^-
	-	-	-	$C_3D_3^-$, $C_3DH_4^-$
43	$^{13}CNO^-$	$^{13}CNO^-$	$^{13}CNO^-$	$^{13}CNO^-$
	$C_2H_3O^-$	$C_2H_3O^-$	$C_2H_3O^-$	$C_2H_3O^-$
44	CO_2^-	CO_2^-	CO_2^-	CO_2^-
	-	CH_2NO^-	CH_2NO^-	$CDNO^-$, CH_2NO^-
	-	-	-	$C_2DH_2O^-$
	-	-	-	$C_3D_4^-$, $C_3D_3H_2^-$
45	CHO_2^-	CHO_2^-	CHO_2^-	CHO_2^-
	-	$C_2H_5O^-$	$C_2H_5O^-$	$C_2D_2HO^-$, $C_2H_5O^-$, $C_3D_4H^-$
	-	-	-	$C_3D_4H^-$
46	-	-	-	CDO_2^-
	-	-	-	$C_2D_3O^-$, $C_2DH_4O^-$
	-	-	-	$C_3D_5^-$
47	-	$CH_3O_2^-$	$CH_3O_2^-$	$CH_3O_2^-$
	-	-	-	$C_2D_2H_3O^-$
48	C_4^-	C_4^-	C_4^-	C_4^-
49	C_4H^-	C_4H^-	C_4H^-	C_4H^-
50	-	C_3N^-	C_3N^-	C_3N^-
	$C_4H_2^-$	$C_4H_2^-$	$C_4H_2^-$	C_4D^-, $C_4H_2^-$
51	$C_4H_3^-$	$C_4H_3^-$	$C_4H_3^-$	C_4DH^-, $C_4H_3^-$
52	C_3O^-	C_3O^-	C_3O^-	C_3O^-
	-	$C_3H_2N^-$	$C_3H_2N^-$	-
	$C_4H_4^-$	$C_4H_4^-$	$C_4H_4^-$	$C_4D_2^-$, $C_4DH_2^-$, $C_4H_4^-$
53	C_3HO^-	C_3HO^-	C_3HO^-	C_3HO^-
	$C_4H_5^-$	$C_4H_5^-$	$C_4H_5^-$	$C_4D_2H^-$, $C_4DH_3^-$, $C_4H_5^-$
54	$C_3H_2O^-$	$C_3H_2O^-$	$C_3H_2O^-$	C_3DO^-, $C_3H_2O^-$
	-	$C_3H_4N^-$	$C_3H_4N^-$	$C_3D_2N^-$, $C_3H_4N^-$
	-	-	-	$C_4D_3^-$, $C_4D_2H_2^-$, $C_4DH_4^-$
55	$C_3H_3O^-$	$C_3H_3O^-$	$C_3H_3O^-$	C_3DHO^-, $C_3H_3O^-$
	-	-	-	$C_4D_3H^-$, $C_4D_2H_3^-$
56	$C_3H_4O^-$	$C_3H_4O^-$	$C_3H_4O^-$	$C_3D_2O^-$, $C_3DH_2O^-$, $C_3H_4O^-$
	-	-	-	$C_4D_4^-$, $C_4D_3H_2^-$
57	-	$C_2HO_2^-$	$C_2HO_2^-$	$C_2HO_2^-$
	$C_3H_5O^-$	$C_3H_5O^-$	$C_3H_5O^-$	$C_3D_2HO^-$, $C_3DH_3O^-$, $C_3H_5O^-$
	-	-	-	$C_4D_4H^-$
58	$C_2H_2O_2^-$	$C_2H_2O_2^-$	$C_2H_2O_2^-$	$C_2DO_2^-$, $C_2H_2O_2^-$
	-	$C_2H_4NO^-$	$C_2H_4NO^-$	-
	-	-	-	$C_3D_3O^-$, $C_3D_2H_2O^-$, $C_3DH_4O^-$
	-	-	-	$C_4D_5^-$
59	$C_2H_3O_2^-$	$C_2H_3O_2^-$	$C_2H_3O_2^-$	$C_2DHO_2^-$, $C_2H_3O_2^-$
	-	-	-	$C_3D_3HO^-$, $C_3D_2H_3O^-$
60	-	CO_3^-	CO_3^-	CO_3^-
	C_5^-	C_5^-	C_5^-	C_5^-
	-	$C_2H_4O_2^-$	$C_2H_4O_2^-$	$C_2D_2O_2^-$, $C_2DH_2O_2^-$, $C_2H_4O_2^-$
		-	-	$C_3D_4O^-$, $C_3D_3H_2O^-$
61	-	CHO_3^-	CHO_3^-	CHO_3^-
	C_5H^-	C_5H^-	C_5H^-	C_5H^-
	-	-	-	$C_2D_2HO_2^-$, $C_2DH_3O_2^-$
	-	-	-	$C_3D_4HO^-$

→→→

62	-	-	-	CDO_3^-
	$C_5H_2^-$	$C_5H_2^-$	$C_5H_2^-$	C_5D^-, $C_5H_2^-$
	-	-	-	$C_2D_3O_2^-$, $C_2D_2H_2O_2^-$
	-	-	-	$C_3D_5O^-$
63	$C_5H_3^-$	$C_5H_3^-$	$C_5H_3^-$	C_5DH^-, $C_5H_3^-$
64	C_4O^-	C_4O^-	C_4O^-	C_4O^-
	-	$C_4H_2N^-$	$C_4H_2N^-$	C_4DN^-, $C_4H_2N^-$
	$C_5H_4^-$	$C_5H_4^-$	$C_5H_4^-$	$C_5D_2^-$, $C_5DH_2^-$, $C_5H_4^-$
65	C_4HO^-	C_4HO^-	C_4HO^-	C_4HO^-
	$C_5H_5^-$	$C_5H_5^-$	$C_5H_5^-$	$C_5D_2H^-$, $C_5DH_3^-$, $C_5H_5^-$
66	C_3NO^-	C_3NO^-	C_3NO^-	C_3NO^-
	$C_4H_2O^-$	$C_4H_2O^-$	$C_4H_2O^-$	C_4DO^-, $C_4H_2O^-$
	$C_5H_6^-$	$C_5H_6^-$	$C_5H_6^-$	$C_5D_3^-$, $C_5D_2H_2^-$, $C_5DH_4^-$, $C_5H_6^-$
67	$C_4H_3O^-$	$C_4H_3O^-$	$C_4H_3O^-$	C_4DHO^-, $C_4H_3O^-$
	$C_5H_7^-$	$C_5H_7^-$	$C_5H_7^-$	$C_5D_3H^-$, $C_5D_2H_3^-$, $C_5DH_5^-$, $C_5H_7^-$
68	-	$C_3O_2^-$	$C_3O_2^-$	$C_3O_2^-$
	$C_4H_4O^-$	$C_4H_4O^-$	$C_4H_4O^-$	$C_4D_2O^-$, $C_4DH_2O^-$, $C_4H_4O^-$
	-	-	-	$C_5D_4^-$, $C_5D_3H_2^-$, $C_5D_2H_4^-$, $C_5DH_6^-$
69	$C_3HO_2^-$	$C_3HO_2^-$	$C_3HO_2^-$	$C_3HO_2^-$
	$C_4H_5O^-$	$C_4H_5O^-$	$C_4H_5O^-$	$C_4D_2HO^-$, $C_4DH_3O^-$, $C_4H_5O^-$
	-	-	-	$C_5D_4H^-$, $C_5D_3H_3^-$, $C_5D_2H_5^-$
70	-	$C_3H_2O_2^-$	$C_3H_2O_2^-$	$C_3DO_2^-$, $C_3H_2O_2^-$
	$C_4H_6O^-$	$C_4H_6O^-$	$C_4H_6O^-$	$C_4D_3O^-$, $C_4D_2H_2O^-$, $C_4DH_4O^-$, $C_4H_6O^-$
	-	-	-	$C_5D_5^-$, $C_5D_4H_2^-$, $C_5D_3H_4^-$

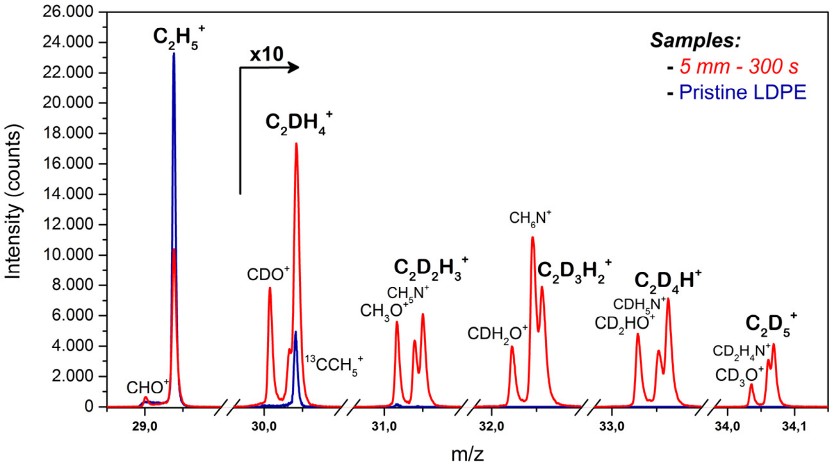

Figure S1. *Portion of the ToF-SIMS positive ion mass spectrum for the 5 mm – 300 s sample and the pristine LDPE (reference), showing the entire series of the* $C_2H_{5-x}D_x^+$ *($0 \leq x \leq 5$) fragments ions (indicated in bold). The* $C_2H_5^+$ *ion (m/z 29) corresponds to the protonated repeat unit of the polyethylene. The mass resolution (m/Δm) at m/z 29 (i.e.* $C_2H_5^+$*) is around 5000.*

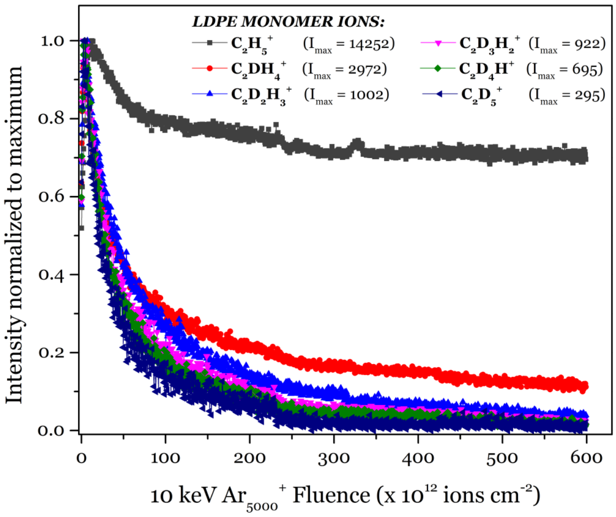

Figure S2. *ToF-SIMS depth-profile of the LDPE film treated by an atmospheric Ar-D_2O post-discharge for 5 min at 5 mm. Intensity of the $C_2D_xH_{5-x}^+$ fragments ($0 \leq x \leq 5$) as a function of the Ar cluster fluence (total value of 5.99 x 10^{14} ions cm^{-2}).*

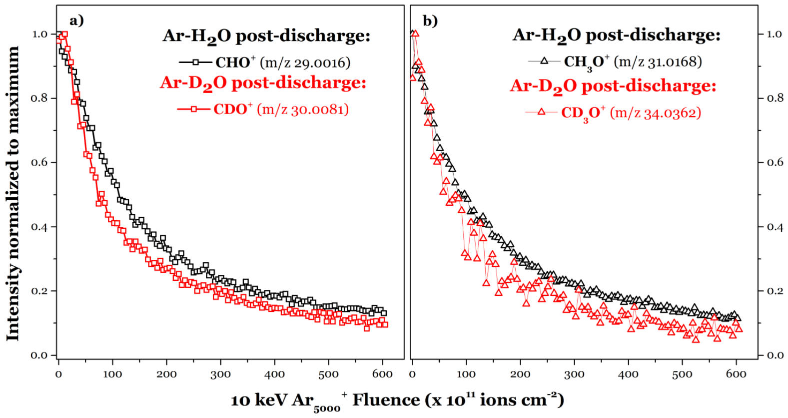

Figure S3. *ToF-SIMS depth-profiles of the LDPE film treated by atmospheric Ar-H_2O and Ar-D_2O post-discharges for 5 min at 5 mm. a) Comparison of the fragment ions CHO^+ and CDO^+. b) Comparison of the fragment ions CH_3O^+ and CD_3O^+.*

5.2.7. References

[1] D. Pappas, A. Bujanda, J. Orlicki, R. Jensen. Chemical and morphological modification of polymers under a helium-oxygen dielectric barrier discharge. *Surface and Coatings Technology* **2008**, *203*, 830.

[2] C. Liu, J. Wu, L. Ren, J. Tong, J. Li, N. Cui, B. Brown, B. Meenan. Comparative study on the effect of RF and DBD plasma treatment on PTFE surface modification. *Materials Chemistry and Physics* **2004**, *85*, 340.

[3] B. Tompkins, J. Dennison, E. Fisher. H_2O plasma modification of track-etched polymer membranes for increased wettability and improved performance. *Journal of Membrane Science* **2013**, *428*, 576.

[4] A. S. Abou Rich, P. Leroy, T. Dufour, N. Wehbe, L. Houssiau, F. Reniers. In-depth diffusion of oxygen into LDPE exposed to an Ar-O_2 atmospheric post-discharge: A complementary approach between AR-XPS and ToF-SIMS techniques. *Surface and Interface Analysis* **2014**, *46*, 164.

[5] N. Vandencasteele, F. Reniers. Plasma-modified polymer surfaces: Characterization using XPS. *Journal of Electron Spectroscopy and Related Phenomena* **2010**, *178*, 394.

[6] S. Swaraj, U. Oran, A. Lippitz, J. F. Friedrich, W. E. S. Unger. Surface analysis of plasma-deposited polymer films, 6. *Plasma Processes and Polymers* **2005**, *2*, 572.

[7] M. Ataeefard, S. Moradian, M. Mirabedini, M. Ebrahimi, S. Asiaban. Surface properties of low density polyethylene upon low-temperature plasma treatment with various gases. *Plasma Chemistry and Plasma Processing* **2008**, *28*, 377.

[8] C. Duluard, T. Dufour, J. Hubert, F. Reniers. Influence of ambient air on the flowing afterglow of an atmospheric pressure Ar/O_2 radiofrequency plasma. *Journal of Applied Physics* **2013**, *113*, 093303.

[9] T. Dufour, J. Minnebo, S. Abou Rich, E. C. Neyts, A. Bogaerts, F. Reniers. Understanding polyethylene surface functionalization by an atmospheric He/O_2 plasma through combined experiments and simulations. *Journal of Physics D: Applied Physics* **2014**, *47*, 224007.

[10] N. Srivastava, C. Wang. Effects of water addition on OH radical generation and plasma properties in an atmospheric argon microwave plasma jet. *Journal of Applied Physics* **2011**, *110*, 053304.

[11] L. Magne, S. Pasquiers, K. Gadonna, P. Jeanney, N. Blin-Simiand, F. Jorand, C. Postel. OH kinetic in high-pressure plasmas of atmospheric gases containing C_2H_6 studied by absolute measurement of the radical density in a pulsed homogeneous discharge. *Journal of Physics D: Applied Physics* **2009**, *42*, 165203.

[12] I. Koo, W. Lee. Hydrogen isotope exchange reactions in an atmospheric pressure discharge utilizing water as carrier gas. *Plasma Chemistry and Plasma Processing* **2004**, *24*, 537.

[13] G. Fridman, G. Friedman, A. Gutsol, A. B. Shekhter, V. N. Vasilets, A. Fridman. Applied Plasma Medicine. *Plasma Processes and Polymers* **2008**, *5*, 503.

[14] M. L. Steen, A. C. Jordan, E. R. Fisher. Hydrophilic modification of polymeric membranes by low temperature H_2O plasma treatment. *Journal of Membrane Science* **2002**, *204*, 341.

[15] D. Briggs, M. P. Seah. Practical Surface Analysis, Volume 2 – Ion and Neutral Spectroscopy, Wiley, Chichester, 2nd edition, **1992**, 395.

[16] J. Lub, F. C. B. M. van Vroonhoven, D. van Leyen, A. Benninghoven. The time of flight static secondary negative ion mass spectra of poly (methylmethacrylate), poly (ethylmethacrylate), and poly (methylmethacrylate-co-ethylmethacrylate). Ion structures and quantification. *Journal of Polymer Science, Part B: Polymer Physics* **1989**, *27*, 2071.

[17] R. H. G. Brinkhuis, W. J. van Ooij. Identification of positive secondary ions in static sims spectra of poly(methylmethacrylate) using the deuterated polymer. *Surface and Interface Analysis* **1988**, *11*, 214.

[18] H. Min, S. Wettmarshausen, J. F. Friedrich, W. E. S. Unger. A ToF-SIMS study of the deuterium-hydrogen exchange induced by ammonia plasma treatment of polyolefins. *Journal of Analytical Atomic Spectrometry* **2011**, *26*, 1157, and references therein.

[19] S. Wettmarshausen, H. Min, W. Unger, C. Jaeger, G. Hidde, J. Friedrich. Significance of hydrogen-deuterium exchange at polyolefin surfaces on exposure to ammonia low-pressure plasma. *Plasma Chemistry and Plasma Processing* **2011**, *31*, 551.

[20] J. Hubert, C. Poleunis, A. Delcorte, P. Laha, J. Bossert, S. Lambeets, A. Ozkan, P. Bertrand, H. Terryn, F. Reniers. Plasma polymerization of C_4Cl_6 and $C_2H_2Cl_4$ at atmospheric pressure. *Polymer* **2013**, *54*, 4085.

[21] C. M. Mahoney. Cluster secondary ion mass spectrometry of polymers and related materials. *Mass Spectrom. Rev.* **2009**, *29*, 247.

[22] S. Ninomiya, K. Ichiki, H. Yamada, Y. Nakata, T. Seki, T. Aoki, J. Matsuo. Precise and fast secondary ion mass spectrometry depth profiling of polymer materials with large Ar cluster ion beams. *Rapid Commun. Mass Spectrom.* **2009**, *23*, 1601.

[23] K. Moritani, G. Mukai, M. Hashinokuchi, K. Mochiji. Site-specific fragmentation of polystyrene molecule using size-selected Ar gas cluster ion beam. *Appl. Phys. Express* **2009**, *2*, 046001.

[24] S. Ninomiya, K. Ichiki, Y. Nakata, T. Seki, T. Aoki, J. Matsuo. The emission process of secondary ions from solids bombarded with large gas cluster ions. *Nuclear Instruments and Methods in Physics Research, Section B: Beam Interactions with Materials and Atoms* **2007**, *256*, 528.

[25] J. L. S. Lee, S. Ninomiya, J. Matsuo, I. S. Gilmore, M. P. Seah, A. G. Shard. Organic depth profiling of a nanostructured delta layer reference material using large argon cluster ions. *Analytical Chemistry* **2010**, *82*, 98.

[26] A. G. Shard, R. Havelund, M. P. Seah, S. J. Spencer, I. S. Gilmore, N. Winograd, D. Mayo, T. Miyayama, E. Niehuis, D. Rading, R. Moellers. Argon cluster ion beams for organic depth profiling: results from a VAMAS interlaboratory study. *Analytical Chemistry* **2012**, *84*, 7865.

[27] E. Niehuis, R. Möllers, D. Rading, H.-G. Cramer, R. Kersting. Analysis of organic multilayers and 3D structures using Ar cluster ions. *Surface and Interface Analysis* **2013**, *45*, 158.

[28] J. C. Vickerman, D. Briggs. ToF-SIMS: materials analysis by mass spectrometry. IM Publications and SurfaceSpectra, Chichester & Manchester, 2nd edition, **2013**, 656.

[29] S. A. Rich, T. Dufour, P. Leroy, L. Nittler, J. J. Pireaux, F. Reniers. Low-density polyethylene films treated by an atmospheric Ar-O_2 post-discharge: functionalization, etching, degradation and partial recovery of the native wettability state. *Journal of Physics D: Applied Physics* **2014**, *47*, 065203.

[30] Y. De Puydt, D. Léonard, P. Bertrand. *Metallized Plastics 3: Fundamental and Applied Aspects.* A static SIMS study of the chemical modifications induced by plasma and flame treatments at the surface of polyolefins. K. L. Mittal, Plenum Press, New York, **1992**, 225.

[31] F. Garbassi, M. Morra, E. Occhiello, L. Barino, R. Scordamaglia. Dynamics of macromolecules: A challenge for surface analysis. *Surface and Interface Analysis* **1989**, *14*, 585.

[32] T. Dufour, J. Hubert, P. Viville, C. Duluard, S. Desbief, R. Lazzaroni, F. Reniers. PTFE surface etching in the post-discharge of a scanning RF plasma torch: Evidence of ejected fluorinated species. *Plasma Processes and Polymers* **2012**, *9*, 820.

[33] S. Muramoto, J. Brison, D. G. Castner. Castner. Exploring the surface sensitivity of ToF-secondary ion mass spectrometry by measuring the implantation and sampling depths of Bi_n and C_{60} ions in organic films. *Analytical Chemistry* **2011**, *84*, 365.

[34] A. Delcorte, C. Leblanc, C. Poleunis, K. Hamraoui. Computer simulations of the sputtering of metallic, organic, and metal-organic surfaces with Bi_n and C_{60} projectiles. *Journal of Physical Chemistry C* **2013**, *117*, 2740.

5.3. Study of oxidative functionalization of polyethylene treated by Ar-D_2O post-discharge

(Molecular surface analysis and depth-profiling of polyethylene modified by an atmospheric Ar-D_2O post-discharge, Plasma Processes and Polymers 2016, 13(11), 1106-1119, DOI: 10.1002/ppap.201600061)

5.3.1. Abstract

The injection of water vapor into ambient "open air" plasmas for the treatment of polymers represents a promising functionalization route for industrial and medical applications. The present study reports a scientist-independent methodology, based on the ToF-SIMS (time-of-flight secondary ion mass spectrometry) technique coupled with PCA/Wavelet-PCA (principal component analysis), to probe the (sub)surface chemical/structural modifications induced by an atmospheric Ar-D_2O post-discharge on low density polyethylene (LDPE) films as a function of two external plasma parameters, namely sample-torch distance and treatment time. The SIMS characterization identifies two different families of samples (type I and II) as a function of time and distance. The highest reactivity of the D_2O vapors with the LDPE films is achieved for times of few tens of seconds at a distance of 5 mm from the plasma source.

5.3.2. Introduction

Surface functionalization of polymers is needed to impart selective and tuneable properties of adhesion, printability, sealability, biocompatibility, etc., preserving the required physical and chemical bulk properties of those particular materials. Among all the available physical and chemical methods to perform surface modification of polymers, the atmospheric pressure cold plasma technologies are expanding enormously because they are suitable to be upgraded to the industrial scale (there is no need of expensive vacuum systems so they can be implemented in a continuous production line).[1-2] Furthermore, milder conditions of treatment are offered by the atmospheric plasmas because they are working in the post-discharge mode. Indeed, most of the highly energetic particles of the plasma, such as electrons and ions, are neutralized before reaching the polymer substrate. So the plasma-polymer interactions mainly occur by means of excited species and radicals and they remain confined in the outermost atomic layers of the polymer.[3] A typical example of surface modification concerns the polyolefins and, more specifically polyethylene, employed in a multitude of applications from the everyday life, such as food packaging and medicine, to the highly technological ones in the automotive and electronics fields. Generally, polyolefins show poor adhesion properties, which constitutes an impediment for further deposition of a layer of interest to create multilayered structures (e.g. in the case of food packaging). A known route to improve the adhesion of the polyolefins consists in the so-called oxidative functionalization, usually obtained by the use of O_2 as reactive gas, that induces the grafting of O-containing functional groups. The literature reports a series of recent works carried out with atmospheric Ar-O_2 or He-O_2 post-discharges for improving the hydrophilicity of LDPE or HDPE (high density polyethylene).[3,4,5] This result is obtained by the grafting of three polar functionalities – C–O, C=O and O–C=O – whose densities on the polymer surface decrease with increasing the treatment time. This suggests that an erosion process, competitive to the functionalization, occurs in flowing post-discharges.[4] Furthermore, higher hydrophilicity values are obtained for sample-torch gaps <15 mm, while at distances >20 mm from the plasma source the effectiveness of the polymer treatment drops dramatically. A study conducted in 2015 investigates the chemical surface composition and the surface morphology, evidenced by X-ray photoelectron spectroscopy (XPS), water contact angle (WCA) and atomic force microscopy (AFM), as a function of the torch-to-substrate distance, treatment time and O_2 flow rate, for LDPE modified by two atmospheric torches with different configurations (linear and showerhead, the latter being the one used in this work). Finally, the species which are responsible for the chemical surface functionalization, the surface roughening, and etching were identified.[6]

Oxidative functionalization of polyolefins can also be achieved by using H_2O as reactive gas, which is gradually replacing O_2 since it permits milder treatments.[7-8] The injection of water in plasmas finds several fields of application, such as material science,[8] biocompatibility,[9] and medicine[10]. The presence of water traces in a plasma is considered as problematic because it induces electrical instabilities of the discharge.[11] However, water vapor can be deliberately introduced into an atmospheric post-discharge to generate large densities of OH and O radicals, that could be homogeneously grafted onto polymer surfaces. In this branch of research, recent and complementary studies, such as the simulations conducted by Atanasova et al.,[12] the experimental contributions of Duluard et al.[13] and the plasma diagnostics of Collette et al.,[14] all based on the same plasma device as the one used in this work, elucidate the chemical mechanisms occurring in presence of water. Specifically, the production of O, H, and OH radicals as well as H_2O_2 has been evidenced as responsible of the LDPE surface modifications induced by an Ar/H_2O post-discharge. However, the physical and chemical interactions between the H_2O injected into the post-discharge and the polymer surfaces need to be clarified.

In the plasma literature, a popular procedure for the surface characterization of plasma-modified polymers is reported, that combines XPS (information about elements and chemical bonds), WCA (wettability of the surface related to the new grafted functionalities) and AFM (morphology).[5-6] In this context, ToF-SIMS is an excellent complement, indispensable to elucidate the structural and chemical modifications of plasma-treated polymers, not only at the surface (via the mass spectra), but also along the depth (via the molecular depth-profiles).[15] The latter was recently possible using large argon gas cluster ion beams (GCIB) for sputtering. In these beams, each Ar_n^+ ion projectile is constituted by hundreds to thousands of atoms (n) and possesses an energy of few keV. Thanks to the development of this new technology, the profilability of specific polymers, such as polyolefins, unachievable with previous sputter beams has become feasible.[16] Indeed, polyolefins are known to undergo chemical damage upon bombardment with traditional monoatomic beams and also with relatively small polyatomic projectiles (SF_5^+ and C_{60}^+), preventing the collection of molecular information during the erosion of the sample. One of the main benefits offered by the GCIB consists in the possibility to vary the energy and/or the cluster size, permitting to tune the etching rate of the specimen under bombardment until ensuring extremely mild erosion conditions.[17-18] On the other hand, depths of a few microns are commonly attainable, while preserving the molecular information of the polymer-based material, which is out of reach of AR-XPS (angle-resolved X-ray photoelectron spectroscopy) or XPS combined with monatomic Ar^+ ion sputtering.

The ability of SIMS to probe the chemical structure of plasma-modified LDPE, both at the surface and along the top tens of nanometers, has been already evidenced in a previous work conducted in our research team.[19] In that investigation, H_2O was replaced by D_2O in order to discriminate the H contributions coming from the polymer itself and the atmospheric moisture from the water deliberately mixed to the plasmagen gas. This approach exploited the high sensitivity and selectivity of the SIMS technique for the detection of H isotopes contained in molecular ion fragments present in the outermost layer of the specimen, a capability that is out of reach of XPS).[20,21,22,23,24] The H-D exchange in the surface region was thoroughly studied. It was found that the most important modifications of the LDPE take place for a torch-sample distance of 5 mm, with 25% of deuterated repeat units at the surface. The deuteration degree decreased of a factor >2 over a depth of around 3-6 nm.

In such studies, however, a problem of data treatment arises from the huge amount of information collected in a single ToF-SIMS experiment, especially when one attempts to compare different experimental plasma conditions. A regular mass spectrum acquired at high mass resolution contains thousands of peaks. To find out the general intensity trends of the diverse molecular ion categories present in these huge datasets constitutes an endless task for the scientist. The issue of extraction and interpretation of the most important molecular fragments is even more complicated for depth-profiles. Indeed, each point of the profile (ranging from tens to hundreds) corresponds to a mass spectrum, which in turn contains thousands of peaks. In the SIMS literature, in order to solve this issue, statistical methods such as principal component analysis (PCA) are used to process the mass spectra.[25,26] This procedure has been recently validated for the surface characterization of plasma-polymers.[27,28,29,30] In addition to this well documented protocol, in this article, a procedure recently introduced for feature extraction from ToF-SIMS depth-profiles by Wavelet-PCA is applied.[31] The method is based on the application of wavelet transform directly to a raw dataset for their compression and noise removal. The data obtained in this way are then examined by PCA. Finally, the depth-profiles are reconstructed from the scores values of the most important principal components and the "pseudo-spectra" are calculated after the inverse-wavelet transform applied to the loadings values. In such a way, a reliable discrimination of the most statistically important peaks is obtained, based on the study of PCA loadings without any subjective interpretation of the original data.

In this paper, SIMS surface analysis combined with PCA has been performed to investigate in a systematic way all the characteristic features of LDPE specimens treated by an atmospheric Ar-D_2O post-discharge, in terms of H-D exchange, oxygen/nitrogen-uptake, unsaturation, branching and cross-linking. First, these modifications concerning the uppermost polymer layer have been probed as a function of two external plasma parameters: treatment time (30, 60 and 300 seconds) and sample-torch distance (3, 5, 7 and 10 mm); while the amount of D_2O in the feeding flux was kept constant. Then, the ultra-shallow modifications of the LDPE films induced by the Ar-D_2O post-discharge[19] have been studied by means of molecular depth-profiling with large argon ion cluster beams coupled with Wavelet-PCA, demonstrating their dependence on the varied external plasma parameters along the third dimension. The SIMS results have been corroborated with XPS measurements previously performed on LDPEs treated by an Ar-H_2O post-discharge in the same experimental conditions in order to quantify oxidation. Finally, the novel SIMS-PCA combined approach, proposed in the present contribution for a more extended characterization of plasma-treated polymers, provides important insights that can be used to better control the polymer functionalization, simultaneously in the surface and along the depth for the desired applications of the investigated material.

5.3.3. Experimental section

5.3.3.1. Materials and surface treatments by atmospheric plasma

The LDPE film used for the plasma treatment was purchased from Goodfellow. The polymer manufacturer claims a film thickness of 50 μm and an additive free material.[19] No washing procedure was performed prior to surface treatment, in order to avoid contamination evidenced from preliminary SIMS analyses (since this technique possesses an excellent surface sensitivity <1 p.p.m.). Finally, the samples were prepared by fixing 1 x 1 cm^2 polymer films onto glass substrates, in order to ensure the flatness of the specimens during the exposure to the post-discharge.

The LDPE film was treated by an atmospheric radiofrequency (RF) plasma torch (AtomfloTM 250D) from SurfX Technologies LLC.[3,4] The schematic representation of the experimental device, called "showerhead plasma torch" because of its configuration, is shown elsewhere.[14,19] The torch consists in two parallel circular electrodes perforated by 126 holes, each one with a critical diameter of 0.6 mm. The manufacturer suggests to supply the plasma source with argon for a proper use. The Ar plasma is formed by applying a RF power of 80 W at 27.12 MHz to the top electrode, whereas the bottom electrode is grounded. The main Ar flow is oriented perpendicularly to the 2 electrodes and its flow rate is 30 L/min for all the experiments. In order to homogenize the flowing inner post-discharge, a 126-holes circular metallic mesh is located parallel and downstream the two electrodes. The output area of this plasma torch is evaluated to 35.6 mm^2.[6] A secondary Ar flow is sent to a bubbler via a volumetric flowmeter from Aalborg with a flow rate of 6 L/min. The bubbler contains H_2O or D_2O (minimum deuteration degree of 99.9%, MagniSolv™ Merck KGaA, Darmstadt, Germany) at room temperature for the XPS and the SIMS experiments, respectively. The corresponding H_2O or D_2O flow rate entering in the inner post-discharge region is 2 mL/s. Finally, the reactive mixture Ar-H_2O or Ar-D_2O flows down from the torch to modify the polymer surface, located in the outer post-discharge.

In order to investigate the reactivity of the H_2O/D_2O vapors injected into the post-discharge and the LDPE surface, two external plasma parameters have been varied, specifically the sample-torch gap (the distance between the LDPE surface and the bottom metallic mesh of the plasma source) from 3 to 10 mm, and the duration of the treatment, ranging from 30 to 300 seconds. Distances below 3 mm were not considered because of the overheating of the polymer surface (the gap must be >3 mm to have a $T < 70$ °C). The influence of the power on the LDPE functionalization is not clear when performed with the experimental plasma device chosen for this investigation, as confirmed by the work carried out by Leroy et al.[32] Thus, the injected power has been fixed at 80 W for all the experiments. **Table 1** reports the experimental conditions in which each polymer film has been treated and the corresponding sample names.

Sample	**External plasma parameters**		**Sample name**
	Distance (1)	Time (2)	
1	3 mm	30 s	*3 mm - 30 s*
2		60 s	*3 mm - 60 s*
3		300 s	*3 mm - 300 s*
4	5 mm	30 s	*5 mm - 30 s*
5		60 s	*5 mm - 60 s*
6		300 s	*5 mm - 300 s*
7	7 mm	30 s	*7 mm - 30 s*
8		60 s	*7 mm - 60 s*
9		300 s	*7 mm - 300 s*
10	10 mm	30 s	*10 mm - 30 s*
11		60 s	*10 mm - 60 s*
12		300 s	*10 mm - 300 s*
13	None	None	Pristine LDPE

(1) Distance: gap between the torch and the LDPE film
(2) Time: duration of the surface treatment

Table 1. *Experimental plasma conditions applied for the treatment of the LDPE films and the corresponding sample names.*

The plasma-modified samples were kept in Petri dishes and analyzed by SIMS in the shortest possible time (a few hours later), in order to minimize the loss of grafted O-containing functionalities exposed to the surface due to the hydrophobic recovery. Indeed, according to recent studies on the air ageing of LDPE treated by atmospheric post-discharges[32,33] the most significant hydrophobic recovery happens in the first 2-3 days after the plasma treatment. However, the LDPE samples conserved for a few months never go back to their native hydrophobic state.[4,5,34,35]

5.3.3.2. ToF-SIMS surface spectra acquisition and data treatment

Secondary ion mass spectrometry of the sample surface and molecular depth-profiling experiments were performed using an ION-TOF TOF.SIMS 5 (Münster, Germany) instrument equipped with both Bi-LMIG (liquid metal ion gun) and Ar-GCIB (gas cluster ion beam) primary ion sources mounted at 45° to the surface normal. The secondary ions were collected by a reflectron-type time of flight analyzer perpendicular to the sample surface.

ToF-SIMS spectra, acquired in positive and negative polarities, were obtained by scanning a pulsed 30 keV Bi_5^+ beam (0.06 pA) on a 200 x 200 μm^2 sample area, with an acquisition time of 120 s. The total ion dose was 1.17×10^{11} ions/cm^2, which ensured static bombardment conditions. Three measurements per polarity were performed for each sample. The calibration peaks were chosen according to the chemical and structural nature of the material. In particular, CH_3^+, $C_2H_5^+$, $C_5H_{11}^+$ and $C_6H_{11}^+$ fragments were considered the best to calibrate the positive ion mass spectra. On the other hand, the CH^-, C_2^-, C_3H^- and C_4H^- fragments were selected for the calibration of the negative ion mass spectra.

Principal component analysis of the positive and negative ion mass spectra was conducted using the Spectragui code developed by NESAC/BIO (http://www.nb.uw.edu/). It runs on the calculation software MATLAB® 2013 (developed by MathWorks®). The explanation of the PCA method applied to the ToF-SIMS data is reported elsewhere.[25] In order to perform the multivariate analysis on the positive and negative ion mass spectra, a manual selection and integration of the peaks was made for the mass range $0 \leq m/z \leq 200$, which represents the "fingerprint" region of the polymer spectrum, rich in information concerning the chemical structure of the investigated plasma-treated LDPE.[36] This is confirmed by the significant percentage of the total intensity of the spectrum that corresponds to this mass interval (i.e. 70% for the positive spectrum of LDPE treated at 5 mm for 60 s). The resulting peak lists count respectively ~550 and ~500 mass contributions for the PCA conducted on the positive and negative spectra of the overall set of samples. Data pre-treatments were conducted before PCA, consisting in normalizing by the total counts of the spectrum (number of detected secondary ions) and mean centering. The total intensity of the mass spectra varies significantly as a function of the plasma conditions used for the treatment. This justifies the performed normalization procedure, that allows us to eliminate the variance produced by a systematic error due to the variation of the secondary ion formation efficiency, which depends on matrix effect, surface topography, charging effects and instrumental factors. Finally, the mean centering procedure ensures that the observed differences in samples were due to variations around the means and not to the variance of the means.

5.3.3.3. ToF-SIMS molecular depth-profiles acquisition and data treatment

The molecular depth-profiles, acquired in both ion polarities, were obtained in dual ion beam mode that is, alternating sputtering and analysis periods with two different ion beams. 10 keV Ar_{3000}^+ ions (0.5 nA) were employed to sputter a 600 x 600 µm^2 area (= sputtering beam). The argon cluster size distribution was close to Gaussian, with a full width at half maximum (FWHM) < 2000 atoms. The average energy per constituent atom was ~3 eV. A second pulsed beam of 30 keV Bi_5^+ ions (0.06 pA) was used to collect the mass spectra from a 200 x 200 µm^2 area, concentric to the sputtered surface (= analysis beam). As it was observed in a previous work,[19] the measurements showed excellent reproducibility, so only two profiles per polarity and per sample were acquired. A non-interlaced mode was used and an electron flood gun was employed for charge compensation. The total ion dose cumulated over an entire profile for the 30 keV Bi_5^+ beam was of the order of 10^{11} ions/cm^2, while for the 10 keV Ar_{3000}^+ source it was kept around 10^{14} ions/cm^2. The ratio between the analysis and sputter doses excludes a significant contribution of the Bi_5^+ beam in the etching process of the specimen.[37,17] The aforementioned sputtering protocol corresponds to an extremely mild erosion of the sample. The estimated sputter yield volume of 1.3 x 10^{-20} cm^3/primary ion was used for the depth calibration of the acquired polyethylene profiles.

A detailed description of the Wavelet-PCA performed on the acquired ToF-SIMS depth-profiles was reported elsewhere.[31] Briefly, the mass spectrum related to each single scan was extracted from the whole profile rawdata and then compressed. The wavelet compression was performed by using "coif5" mother function at the 4th compression level by means of PyWavelet Python-based library (http://www.pybytes.com/pywavelets/). PCA analysis of the wavelet coefficients matrix obtained from ToF-SIMS spectra was performed using Scikit-learn, a machine-learning Python-based library (http://scikit-learn.org/). The PCA dataset matrix was created using the approximation coefficients of wavelet compression that represent the variables. The depth scans, acquired during the ToF-SIMS depth-profiling, represent the objects of matrix. Before multivariate analysis, the dataset was mean-centered and normalized to the total intensity of each in-depth scan, so that the variations in intensity of the spectrum related to any instrumental phenomena (variations of the primary beam, surface charging, etc.) do not affect the result of the Wavelet-PCA study. The scores plots were obtained reporting each of the principal components versus the in-depth scans. The loadings plots were obtained reporting each of the principal components versus the mass-to-charge (m/z) ratio obtained by the inverse discrete wavelet transformation.

5.3.3.3. XPS analysis

XPS measurements were performed by means of a Physical Electronics PHI-5600 instrument with a Mg Kα X-ray source (1253.6 eV) operating at 200 W and with a base pressure of 1×10^{-9} mbar in the analysis chamber. Wide spectra were acquired between 0 to 1000 eV at 93.90 eV pass-energy, in order to determine the chemical elements present on the LDPE surface. Narrow-region photoelectron spectra were used for the chemical study of the C 1s, O 1s peaks (at 93.90 eV pass-energy). The elemental composition was calculated after removal of a Shirley background line and using the sensitivity coefficients: $S_C = 0.205$, $S_O = 0.63$. The detection angle was normal to the surface. The XPS analyses were done immediately after the surface treatment.

5.3.4. Results and discussion

For the sake of clarity, the following section of this paper is divided in two parts. The first sub-section concerns the surface analysis, in which the effects of the two external plasma parameters on the surface treatment, namely the “sample-torch distance” and the “treatment time”, are elucidated. The surface analysis section is followed by the in-depth characterization, where by means of the application of the Wavelet-PCA, general behaviors of molecular ion fragments are highlighted and correlated to processes taking place during the LDPE (sub)surface modification induced by the atmospheric Ar-D_2O post-discharges.

5.3.4.1. Surface analysis

LDPE films have been treated by an atmospheric Ar-H_2O post-discharge in previous experiments carried out by this research team. The effects on the surface functionalization of the polymer of three different sample-torch distances - namely 5, 7, and 10 mm - and several times of treatment, ranging from 30 s to 300 s, have been mainly investigated by XPS. The XPS determination of the oxygen content in the plasma-exposed LDPEs as a function of the time (x axis) and gap (different curves) is displayed in **Figure 1**. Concerning the oxidative functionalization induced by the exposure to the reactive water vapors, two different behaviors as a function of time depending on the torch-sample distance are found out. Indeed, when increasing the treatment time, the O content decreases almost linearly at 5 and 7 mm, while it increases at 10 mm (at least up to 300 s). These two different behaviors (as a function of time) will be referred to as type I and II, respectively.

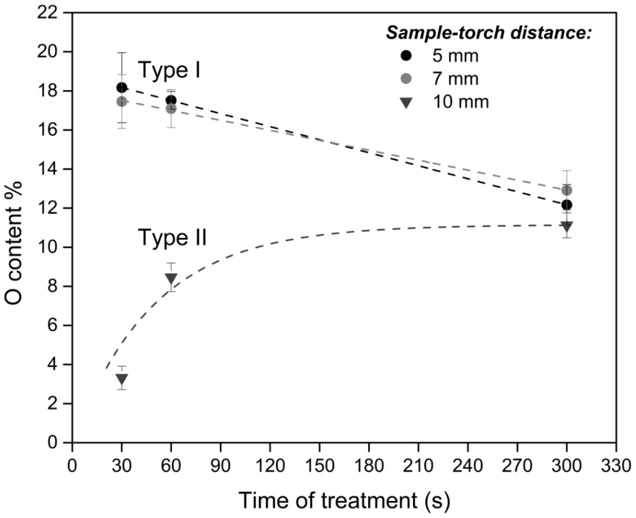

Figure 1. *O content % (determined by XPS) as a function of the time of treatment for LDPE films modified by an Ar-*H_2O *post-discharge at the three different sample-torch distances of 5, 7, 10 mm.*

In SIMS, the effect of the surface treatment was first assessed by overlapping the positive ion mass spectra. After the plasma treatment, one observes the emergence of a large number of new peaks, estimated around 400 in the range 0-200 amu. First, the H-D exchange (also named deuteration) generates a new pattern of fragmentation reproducing that of the pristine LDPE, but shifted in the m/z scale because of the double mass of the deuterons compared to that of the protons. However, the mass resolution achieved in these ToF-SIMS spectra (about 5000 for $C_2H_5^+$ at m/z 29), is insufficient for an accurate determination of the isotopic ratio of a given fragment ion.[19] This issue is illustrated in **Figure 2** with the peak at m/z 30.043, whose possible identifications are $C_2DH_4^+$, $C_2D_2H_2^+$, and $C_2D_3^+$ because of the uncertainty on the H isotope content. The most probable structure for the ion is considered the one containing the lowest number of deuterium atoms.[23] Second, the intensities of the characteristic molecular fragment ions of the pristine polymer, such as $C_2H_5^+$, $C_3H_5^+$, $C_3H_7^+$, $C_4H_7^+$ and $C_4H_9^+$, decrease in the treated PEs. Third, the previous variation is accompanied by the appearance of a series of O-containing molecular ion fragments. The overall set of new peaks observed in the mass spectra can be ascribed to the interaction of the polyethylene surface with reactive species coming from the post-discharge and the environment (mainly O_2, N_2 and H_2O), since the torch operates in open air. These active species determine concomitant processes of oxidation, nitrogen-uptake and H-D exchange, resulting in mixed ions with general chemical formulas $C_xH_yD_z^+$ and $C_xH_yD_z(N/O)_m^+$, as illustrated in Figure 2. In addition, energetic particles created in the plasma medium provoke the chemical damage of the treated polymer, in terms of main chain scissions, branching, unsaturation, and cross-linking.

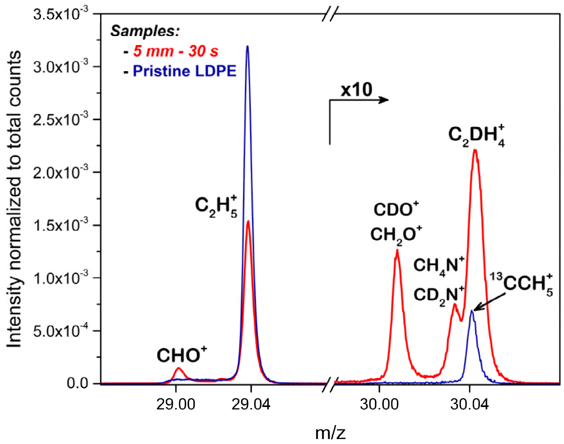

Figure 2. *Portion of the ToF-SIMS positive ion mass spectrum for the 5 mm – 30 s sample and the pristine LDPE (reference), where the* $C_2H_5^+$ *ion (m/z 29) corresponds to the protonated repeat unit of the polyethylene. Note the appearance of new mixed ion species with general chemical formulas* $C_xH_yD_z^+$ *and* $C_xH_yD_z(N/O)^+$.

Because of the complexity of the fragmentation pattern, a more systematic comparison of the effect of the external plasma parameters on the surface modification requires the use of multivariate analysis.

The first PCA was applied to the overall set of treated and pristine LDPEs to globally investigate the effect of the plasma treatment. **Figure 3** displays the PC2 versus PC1 scores plot obtained in this analysis, which shows the relationships (spreading or clustering) among the investigated samples.

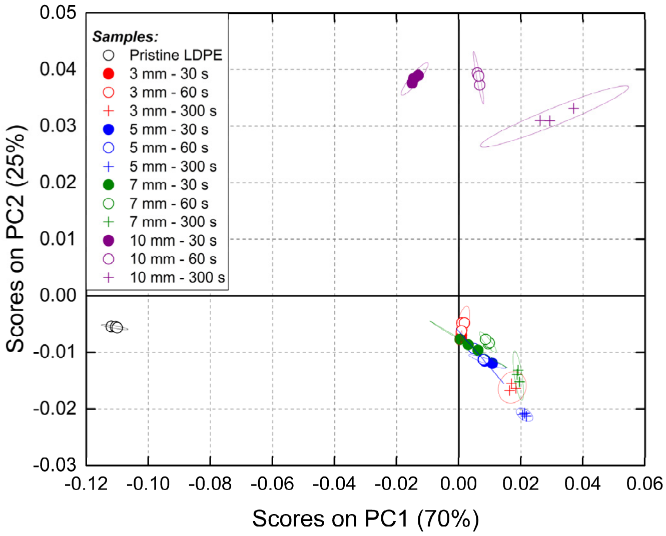

Figure 3. *PC2 versus PC1 scores plot obtained from the PCA applied to the ToF-SIMS positive ion mass spectra of the pristine and all the plasma-treated LDPEs (sample-torch distance: 3, 5, 7, 10 mm; time of treatment: 30, 60, 300 s; three spectra per sample).*

In the graph, each sample (or plasma condition) is represented by a different symbol, where the color is indicative of the distance from the torch and the shape of the exposure time to the post-discharge. Moreover, each specimen is represented by three positive ion mass spectra (same symbol). The ellipses represent a confidence limit of 95% for each plasma experiment. Together PC1 and PC2 capture 95% of the total variance within the set of samples. PC1 separates the reference (pristine film) and the film treated at 10 mm for 30 s (negative scores) from all the other samples (positive scores). On the other hand, PC2 discriminates the samples treated at 10 mm (positive scores) from all the others, including the reference (negative scores). In the PCA, the information displayed by the PC2 versus PC1 scores plot needs to be combined with that contained in the loadings plot, which provides the contribution of every single SIMS peak to the given PC and identifies the fragments responsible for the differences observed within the data set. The samples with positive scores exhibit higher relative SIMS intensities for the peaks attributed to positive loadings and vice versa. The same consideration is valid for the negative scores and loadings. For the sake of clarity, the tables reporting the loadings of the first two PCs are shown separately.

Table 2 reports all the molecular ion fragments with the relative exact masses and absolute loading values > 0.015 for the PC1. The loadings are listed in decreasing order of absolute value or importance.

PC1 (70%) loading > 0 (Treated LDPEs)			PC1 (70%) loading < 0 (Pristine LDPE / *10 mm – 30 s*)		
Loading	**Mass**	**Peak**	**Loading**	**Mass**	**Peak**
0.137	43.018	$C_2H_3O^+$	-0.583	43.055	$\mathbf{C_3H_7^+}$
0.056	55.016	$C_3H_3O^+$	-0.468	55.054	$C_4H_7^+$
0.053	45.030	$C_2H_5O^+$	-0.416	57.070	$\mathbf{C_4H_9^+}$
0.043	44.023	$C_2H_4O^+$	-0.349	41.038	$C_3H_5^+$
0.035	46.036	$\mathit{C_2DH_4O^+}$	-0.180	69.070	$C_5H_9^+$
0.031	18.034	NH_4^+	-0.143	29.039	$\mathbf{C_2H_5^+}$
0.027	91.049	$C_7H_7^+$	-0.135	71.085	$\mathbf{C_5H_{11}^+}$
0.025	57.031	$C_3H_5O^+$	-0.108	67.053	$C_5H_7^+$
0.024	105.063	$C_8H_9^+$	-0.089	83.085	$C_6H_{11}^+$
0.022	40.028	$C_3H_4^+$	-0.068	85.100	$\mathbf{C_6H_{13}^+}$
0.020	56.022	$C_3H_4O^+$	-0.046	56.058	$C_4H_8^+$
0.020	51.020	$C_4H_3^+$	-0.039	97.099	$C_7H_{13}^+$
0.019	32.047	CH_6N^+	-0.036	54.043	$C_4H_6^+$
0.018	58.036	$C_3H_6O^+$	-0.029	70.073	$C_5H_{10}^+$
0.018	93.065	$C_7H_9^+$	-0.025	68.058	$C_5H_8^+$
0.017	46.049	$\mathit{CDH_4N_2^+}$	-0.021	81.068	$C_6H_9^+$
0.016	28.029	$C_2H_4^+$	-0.017	53.036	$C_4H_5^+$
0.016	31.017	CH_3O^+			
0.016	30.043	$\mathit{C_2DH_4^+}$			
0.016	119.078	$C_9H_{11}^+$			
0.016	128.050	$C_{10}H_8^+$			
0.016	115.044	$C_9H_7^+$			
0.015	133.094	$C_{10}H_{13}^+$			
0.015	107.080	$C_8H_{11}^+$			

Legend

Saturated hydrocarbon ions: $\mathbf{C_xH_y^+}$
O-containing ions: $C_xH_yO_z^+$
N-containing ions: $C_xH_yN_z^+$
D-containing ions: $\mathit{C_xH_yD_z(O/N)_m^+}$

Table 2. *List of the most influential PC1 loadings, and corresponding molecular ion fragments, extracted from the PCA obtained on the ToF-SIMS positive ion mass spectra of the pristine and all the plasma-treated LDPEs (sample-torch distance: 3, 5, 7, 10 mm; time of treatment: 30, 60, 300 s). A threshold value for the loadings of* ±*0.015 has been fixed.*

The two main columns correspond to the PC1 loadings > 0, representative of all the treated samples (scores > 0), and PC1 loadings < 0, characteristic of the reference and the *10 mm – 30 s* sample (scores < 0). The identification of the molecular ion fragments indicated by the PCA is based on the tables (Table S1 and S2) provided in supporting information of our previous work.[19] They list the peaks in the range 0 ≤ m/z ≤ 70 of the pristine and plasma-treated LDPE mass spectra, and their most reasonable attributions, for both polarities (taking into account the uncertainty on the H isotope content). In this paper, the deuterated contributions to the characteristic LDPE peaks are not specified for a clearer description of the results. However, the ion is shown in italic when the deuterated contribution is dominant. An example is the peak at m/z 30.043, which in the case of the LDPE treated by plasma, and mainly at the shortest distances, is due to the spectral sum of two fragments: $^{13}CCH_5^+$ and $C_2DH_4^+$. The latter contribution arises from the H-D mono-substitution of the $C_2H_5^+$ ion and constitutes the main contribution in the plasma surface treatment by the Ar-D_2O reactive mixture at 3, 5, and 7 mm from the torch. First, the highest values of positive loadings are associated to ion species with low m/z containing oxygen atoms (in red), as well as deuterium, clearly evidenced in the $C_2DH_4O^+$ ion (in red and italic type), deriving probably from the grafting of OD radicals. Second, the column of the loadings < 0 shows the characteristic fragmentation pattern of pristine LDPE. The fragment ions associated to the highest values of loadings represent the most intense peaks observed in the positive PE mass spectrum. Most of the saturated hydrocarbons (bold), representative of the pristine structure, appear in the negative loadings. For the plasma treated samples (positive loadings), an increased C/H ratio is found for $C_xH_y^+$ ions, in addition to aromatic fragments, such as i.e. $C_7H_7^+$ (m/z 91.049), $C_8H_9^+$ (m/z 105.063) and $C_{10}H_8^+$ (m/z 128.050). These ions constitute plausible recombination products upon bombardment by energetic particles present in the post-discharge (Ar^+ and Ar^M, discussed later in this paper). The increase of the aromaticity degree of the investigated polymer, combined with the decrease of the H content ascribable to the processes of unsaturation, branching and cross-linking (impossible to discern based on the C/H content), lead to a picture of a material that has undergone chemical damage. A calculation of the C/H ratio to determine the extent of the H loss would be misleading, because of the uncertainty on the isotopic content (D/H) in the aforementioned ion fragments.[30] Finally, the presence of nitrogen on the polymer surface exposed to the post-discharge is documented by the ions NH_4^+ and CH_6N^+ (in green), totally absent in the native polymer and due to the atmospheric N_2.[14]

In summary, PC1 confirms the chemical/structural modifications of the polyethylene induced by its exposure to the Ar-D_2O post-discharge. It consists fundamentally in the grafting of O/N-containing functionalities and H-D exchange (involving the breakage of C-H bonds and the subsequent replacement of H by D), combined with the accumulation of chemical damage (mainly related to the formation of new C-C bonds). Moreover, an indication about the influence of the distance from the plasma source can be already inferred from the PC1 analysis: *10 mm - 30 s* is separated from the remaining experimental plasma conditions (being more similar to the reference). Next, we turn to the interpretation of PC2.

PC2 divides the films treated at 10 mm (scores > 0) from all the others (scores < 0), including the reference. It is worth noticing that the pristine

LDPE locates close to zero values of the loadings, thus it has a minimal weight in the separation of the samples along this principal component. **Table 3** reports the most important PC2 loadings.

PC2 (25%) loading > 0 (10 mm)			PC2 (25%) loading < 0 (3 - 7 mm / Pristine LDPE)		
Loading	**Mass**	**Peak**	**Loading**	**Mass**	**Peak**
0.660	43.018	$C_2H_3O^+$	-0.111	43.055	$\mathbf{C_3H_7^+}$
0.442	55.016	$C_3H_3O^+$	-0.105	46.036	$C_2DH_4O^+$
0.279	57.031	$C_3H_5O^+$	-0.072	18.034	NH_4^+
0.240	55.054	$C_4H_7^+$	-0.070	57.070	$\mathbf{C_4H_9^+}$
0.160	41.038	$C_3H_5^+$	-0.062	32.047	CH_6N^+
0.145	29.039	$\mathbf{C_2H_5^+}$	-0.061	91.049	$C_7H_7^+$
0.125	39.022	$C_3H_3^+$	-0.055	42.043	$C_3H_6^+$
0.116	71.048	$C_4H_7O^+$	-0.053	44.057	$C_3DH_6^+$
0.102	27.023	$C_2H_3^+$	-0.048	105.063	$C_8H_9^+$
0.094	67.053	$C_5H_7^+$	-0.045	46.049	$CDH_4N_2^+$
0.086	83.045	$C_5H_7O^+$	-0.045	40.028	$C_3H_4^+$
0.082	69.031	$C_4H_5O^+$	-0.038	45.063	$C_3D_2H_5^+$
0.078	85.025	$C_4H_5O_2^+$	-0.034	46.067	$C_3D_3H_4^+$
0.065	31.017	CH_3O^+	-0.033	30.043	$C_2DH_4^+$
0.050	81.029	$C_5H_5O^+$	-0.032	92.054	$C_7H_8^+$
0.047	97.061	$C_6H_9O^+$	-0.031	93.065	$C_7H_9^+$
0.045	71.009	$C_3H_3O_2^+$	-0.031	133.094	$C_{10}H_{13}^+$
0.040	53.036	$C_4H_5^+$	-0.029	117.060	$C_9H_9^+$
0.040	111.039	$C_6H_7O_2^+$	-0.028	119.078	$C_9H_{11}^+$
0.039	99.039	$C_5H_7O_2^+$	-0.028	78.041	$C_6H_6^+$
0.037	85.060	$C_5H_9O^+$	-0.028	45.030	$C_2H_5O^+$
0.037	68.995	$C_3HO_2^+$	-0.026	35.068	CD_4HN^+
0.034	95.044	$C_6H_7O^+$	-0.025	58.072	$C_4DH_8^+$
0.034	29.002	CHO^+	-0.025	128.050	$C_{10}H_8^+$
0.031	59.047	$C_3H_7O^+$	-0.024	31.040	CH_5N^+
0.029	97.023	$C_5H_5O_2^+$	-0.024	131.075	$C_{10}H_{11}^+$
0.026	42.008	$C_2H_2O^+$	-0.023	129.056	$C_{10}H_9^+$
0.021	70.036	$C_4H_6O^+$	-0.023	32.057	$C_2D_3H_2^+$
			-0.022	62.078	$C_2DH_8N_2^+$
			-0.022	56.058	$C_4H_8^+$
			-0.021	30.008	CH_2O^+
			-0.021	44.023	$C_2H_4O^+$
			-0.020	28.029	$C_2H_4^+$
			-0.020	107.080	$C_8H_{11}^+$
			-0.020	121.095	$C_9H_{13}^+$

Legend

Saturated hydrocarbon ions: $\mathbf{C_xH_y^+}$
O-containing ions: $C_xH_yO_z^+$
N-containing ions: $C_xH_yN_z^+$
D-containing ions: $C_xH_yD_z(O/N)_m^+$

Table 3. *List of the most influential PC2 loadings, and corresponding molecular ion fragments, extracted from the PCA obtained on the ToF-SIMS positive ion mass spectra of the pristine and all the plasma-treated LDPEs (sample-torch distance: 3, 5, 7, 10 mm; time of treatment: 30, 60, 300 s). A threshold value for the loadings of* ±*0.02 has been fixed.*

Table 3 clearly shows the highest abundance of molecular ions containing 1 or 2 oxygen atoms characterizing the samples treated at 10 mm (loadings > 0), in comparison with those at lower distances (loadings < 0). Among the oxidized species indicated by the PCA as characteristic of the 10 mm specimens, $C_2H_3O^+$, $C_3H_3O^+$, and $C_3H_5O^+$ exhibit the highest loading values. These are typical ions, together with CH_3O^+, $C_2H_5O^+$ and $C_3H_7O^+$, that are found after the air ageing process of the native LDPE. Furthermore, as already shown in PC1 for the *10 mm – 30 s* specimen, the samples treated at 10 mm possess a hydrocarbon pattern more similar to that of the untreated PE because of the presence of $C_xH_y^+$ ions near saturation ($C_4H_7^+$, $C_3H_5^+$, $C_2H_5^+$), and less damaged (absence of aromatic fragments, but still some unsaturated fragments are evidenced: see $C_3H_3^+$ and $C_2H_3^+$). In particular, H-D exchange seems to be absent. In contrast, all the other plasma experimental conditions lead to plausible grafting of OD radicals onto the polymer chain (see the second highest negative loading: $C_2DH_4O^+$), incorporation of nitrogen, appearance of a certain aromaticity degree (see $C_7H_7^+$), deuteration (see $C_3DH_6^+$) that can reach the total H-D substitution of small fragment typical of the PE such as $C_2H_5^+$ and $C_3H_7^+$ (like in the case of *5 mm - 60 s*).

Returning to the mass spectra, the effect of the distance on the surface functionalization can be exemplified, for a given treatment time, by the behavior of selected O-based molecular ion fragments. It is worthy to notice that this observation cannot be done by XPS, which is not sensitive to H/D and only detects the global trend of the oxidation.

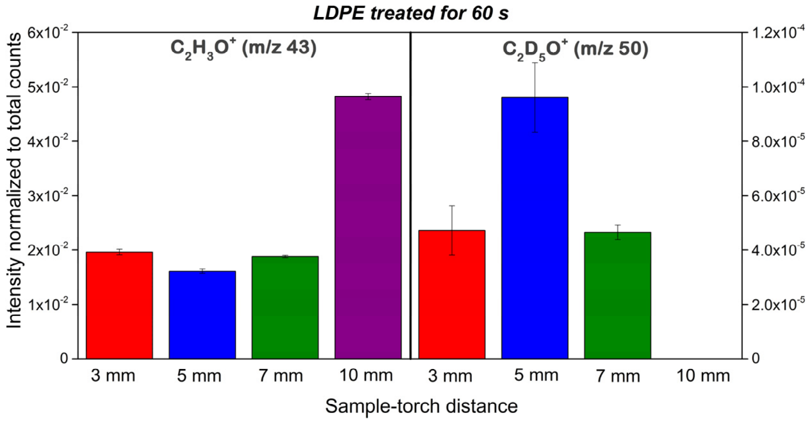

Figure 4. *Relative intensities of the ions $C_2H_3O^+$ and $C_2D_5O^+$ as a function of the sample-torch distance for the LDPE films exposed for 60 s to the Ar-D_2O post-discharge.*

Figure 4 reports the relative intensity of $C_2H_3O^+$ and $C_2D_5O^+$ as a function of the sample-torch distance for a treatment time fixed at 60 s. The $C_2H_3O^+$ ion, constituting the loading with the highest value > 0, distinguishes the 10 mm distance and it is mainly hydrogenated. On the other hand, $C_2D_5O^+$ possesses a loading value < 0 (it does not appear in Table 3 because of the selected loadings threshold) and it is fully deuterated. These two ions exemplify the different trend observed as a function of the distance for H/O-containing fragments (see $C_2H_3O^+$) and D/O-containing molecular ions (see $C_2D_5O^+$). In the first case, the relative ion intensity increases with increasing the distance, going from 3-7 mm to 10 mm. The latter shows a maximum at 5 mm and follows the reactivity of the D_2O vapors with the polyethylene substrate.

In order to clarify the effect of the treatment time for the two series of treated samples identified by the first PCA and by the XPS data (type I and II), a second PCA was conducted only with the specimens of type I – namely 3, 5, and 7 mm.

The scores plot for the first two PCs and the PC1 loadings list are reported in **Figure 5** and **Table 4**, respectively. PC1 separates the samples treated at 300 s from all the others (30 s and 60 s for a distance of 3, 5, and 7 mm) and captures 79% of the overall variance. PC2 is not studied because it does not provide a clear division among the samples.

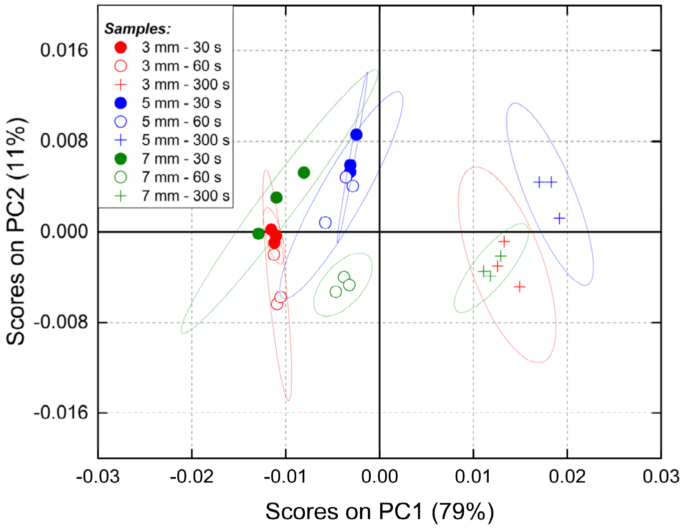

Figure 5. *PC2 versus PC1 scores plot for the PCA performed with the ToF-SIMS positive ion mass spectra of the LDPE samples treated at 3, 5, and 7 mm at the three different times of 30, 60, and 300 s (three spectra per sample).*

PC1 (79%) loading > 0 (300 s)			PC1 (79%) loading < 0 (30 s and 60 s)					
Loading	**Mass**	**Peak**	**Loading**	**Mass**	**Peak**	**Loading**	**Mass**	**Peak**
0.131	91.049	$C_7H_7^+$	-0.405	41.038	$C_3H_5^+$	-0.045	83.085	$C_6H_{11}^+$
0.104	46.049	*$CDH_4N_2^+$*	-0.392	43.055	**$C_3H_7^+$**	-0.045	53.036	$C_4H_5^+$
0.092	105.063	$C_8H_9^+$	-0.329	55.054	$C_4H_7^+$	-0.043	67.053	$C_5H_7^+$
0.088	81.068	$C_6H_9^+$	-0.295	29.039	**$C_2H_5^+$**	-0.040	58.036	$C_3H_6O^+$
0.071	93.065	$C_7H_9^+$	-0.249	57.070	**$C_4H_9^+$**	-0.039	30.043	*$C_2DH_4^+$*
0.069	62.078	*$C_2DH_8N_2^+$*	-0.233	43.018	$C_2H_3O^+$	-0.036	71.048	$C_4H_7O^+$
0.056	95.082	$C_7H_{11}^+$	-0.227	18.034	NH_4^+	-0.036	68.058	$C_5H_8^+$
0.052	133.094	$C_{10}H_{13}^+$	-0.193	27.023	$C_2H_3^+$	-0.035	31.017	CH_3O^+
0.052	119.078	$C_9H_{11}^+$	-0.176	39.022	$C_3H_3^+$	-0.033	52.027	$C_4H_4^+$
0.049	137.129	$C_{10}H_{17}^+$	-0.152	45.030	$C_2H_5O^+$	-0.032	44.995	CHO_2^+
0.049	107.080	$C_8H_{11}^+$	-0.116	44.023	$C_2H_4O^+$	-0.031	68.995	$C_3HO_2^+$
0.048	109.098	$C_8H_{13}^+$	-0.115	71.085	**$C_5H_{11}^+$**	-0.030	30.008	CH_2O^+
0.044	128.050	$C_{10}H_8^+$	-0.106	57.031	$C_3H_5O^+$	-0.026	51.020	$C_4H_3^+$
0.043	115.044	$C_9H_7^+$	-0.096	42.043	$C_3H_6^+$	-0.026	44.057	*$C_3DH_6^+$*
0.043	121.095	$C_9H_{13}^+$	-0.093	46.036	*$C_2DH_4O^+$*	-0.025	70.001	$C_3H_2O_2^+$
0.040	123.113	$C_9H_{15}^+$	-0.091	55.016	$C_3H_3O^+$			
0.038	117.060	$C_9H_9^+$	-0.083	28.029	$C_2H_4^+$			
0.037	131.075	$C_{10}H_{11}^+$	-0.083	40.028	$C_3H_4^+$			
0.037	77.033	$C_6H_5^+$	-0.071	54.043	$C_4H_6^+$			
0.033	79.049	$C_6H_7^+$	-0.068	56.058	$C_4H_8^+$			
0.030	129.056	$C_{10}H_9^+$	-0.056	69.070	$C_5H_9^+$			
0.030	173.122	$C_{13}H_{17}^+$	-0.056	85.100	**$C_6H_{13}^+$**			
0.028	135.112	$C_{10}H_{15}^+$	-0.055	56.022	$C_3H_4O^+$			
0.027	141.056	$C_{11}H_9^+$	-0.050	29.002	CHO^+			

Legend

Saturated hydrocarbon ions: **$C_xH_y^+$**
O-containing ions: $C_xH_yO_z^+$
N-containing ions: $C_xH_yN_z^+$
D-containing ions: *$C_xH_yD_z(O/N)_m^+$*

Table 4. *List of the most influential PC1 loadings, and corresponding molecular ion fragments, extracted from the PCA applied to the ToF-SIMS positive ion mass spectra of the plasma-treated LDPEs (sample-torch distance of 3, 5, 7 mm; time of treatment: 30, 60, 300 s). A threshold value for the loadings of ±0.025 has been fixed.*

Loadings > 0 are chemically representative of the LDPE films exposed to the Ar-D_2O post-discharge for 300 s, while loadings < 0 characterize the films treated for the shorter times of 30 s and 60 s. The samples modified for 300 s by the plasma torch do not exhibit O-containing fragments, but mainly aromatic and unsaturated hydrocarbon species. Aromatic fragments, such as $C_7H_7^+$ at m/z 91.049 (highest loading > 0) and $C_8H_9^+$ at m/z 105.063, have been observed in the first PCA, discussed at the beginning of this section, and they are considered as indicators of the damaged polyethylene. Molecular ion fragments with a higher C/H ratio can be considered as signs of branching/cross-linking of the LDPE under plasma exposure. However, the relative intensities of the aromatic and unsaturated hydrocarbon species for the 300 s treatment (thus, associated to loadings > 0, like $C_{10}H_{17}^+$ at m/z 137.129) decrease with increasing distance from the plasma source (going from 3 to 10 mm, confirmed by the rawdata). The times of 30 s and 60 s correspond to a minor degree of aromaticity in the samples. Furthermore, the sample-torch gap does not seem to have an influence on the formation of aromatics for these low-time treatments (loadings < 0).

Loadings < 0 indicate the presence of some of the native LDPE characteristic peaks (close or completely saturated). These peaks are shown by samples treated for 30 s and 60 s. However, such characteristic fragments reacted at the interface with the Ar-D_2O post-discharge to generate predominantly oxidized and deuterated species. This is a further confirmation of the conclusions deduced from the previous PCA model.

The PCA has been applied also to the ToF-SIMS spectra in negative polarity, extracting a similar information concerning the oxidative functionalization achieved by the atmospheric Ar plasma torch and confirming the conclusions drawn from the PCA of the positive polarity. The related PC2 versus PC1 scores plot and PC1 loadings table are reported in supporting information (**Figure S1** and **Table S1**, respectively).

In conclusion, the overall picture that emerges from the SIMS surface analysis is as follows:

a) Time-dependence of the ion intensities varying with the torch-sample distance, with the discrimination of two different trends for 3-7 mm and 10 mm (type I and type II, as illustrated in Figure 1). This is evidenced by the first PCA (figure 3). At 10 mm the treated films show an oxidation mainly linked to the presence of H/O-containing functionalities. However, at 3-7 mm the samples are more deuterated and oxidized by the D_2O vapors. This could be explained by the fact that at 10 mm the polymer substrate is too far from the torch to interact principally with the dissociation products of D_2O generated by the following reaction in the outer post-discharge: $Ar^M + D_2O \rightarrow Ar + OD^{\cdot} + D^{\cdot}$, where the concentration of Ar^M (the metastable Ar species) decays with increasing the distance from the torch because of their consumption via reaction with Ar atoms.[12] Hence, the functionalization is mainly due to O-based chemical species from the air, such as O_2 molecules, O_3 and O radicals originated from the atmospheric oxygen, (no O_2^+ intervenes because of the absence of Penning dissociation of O_2 by the too-low energetic metastable Ar species in the post-discharge).[14] This concept is exemplified by figure 4, where two different trends are depicted for H/O-based fragments (i.e. $C_2H_3O^+$), related to the functionalization by O_2 and H_2O of the air (and all their plasma-induced species), and D/O-based fragments (such as $C_2D_5O^+$), related to the functionalization by means of the D_2O vapors. Consequently, the diverse functionalization occurring at 3-7 mm and 10 mm may be explained by the limited lifetime of the reactive species present in the flowing post-discharge. This hypothesis is corroborated by the absence of H-D exchange at 10 mm distance, since D radicals are not anymore produced in the post-discharge from the dissociation of D_2O.

Additionally, the samples treated at 3-7 mm show also higher degree of aromaticity due to chemical damage during the exposure to the plasma torch. This chemical damage can be ascribed to Ar^+ and Ar^M arising from the plasma medium.[12,14] Moreover, the VUV radiations emitted by the plasma have a negligible effect in ambient air because of the oxygen absorption.[38] Finally, the observed N-uptake can be explained by the grafting of N_2 molecules from the atmosphere.[14]

b) Opposite effect of time for the type I and II samples. Indeed, the second PCA (figure 5) conducted on 3-7 mm samples indicates an increase of aromaticity and unsaturation going from 30 s – 60 s to 300 s, accompanied by a reduction of the density of the O-based functionalities on the polymer surface. This observation may be explained by the competition between the grafting of O-containing functional groups and etching process, as already reported in the literature.[6,39] For times > 60 s the etching starts to prevail on the grafting, verifying its responsibility in the promotion of branching and/or cross-linking of the polyethylene. Instead, the effect of time is reversed at 10 mm, as shown by the separation of the *10 mm - 30 s* sample from all the other films treated at the same distance in PC1 of the 1st PCA (figure 3). This can be explained by an erosion depowered at higher distances (>7 mm), that promotes the accumulation of the functionalization in the surface rather than its removal, at least for times up to 300 s.

5.3.4.2.Molecular depth-profiling

In this section, the Wavelet-PCA will be applied to the two most representative samples of type I and II (at constant treatment time): "*5 mm - 60 s*" and "*10 mm - 60 s*". Finally, some remarks concerning the application of this statistical method to the depth-profile of the pristine LDPE will be given.

It is worth noticing the retention of the initial mass resolution of the spectra after application of the Wavelet-PCA, that is normally lost by the mass-binning methods of peaks selection.[25,31] This constitutes a fundamental requirement when working with $C_xH_yD_z(O)_m^+$ mixed ions, whose intensities are generally very low compared to the typical peaks of the polymer under study and the best mass resolution achieved with the selected experimental setup is not excellent for their recognition.

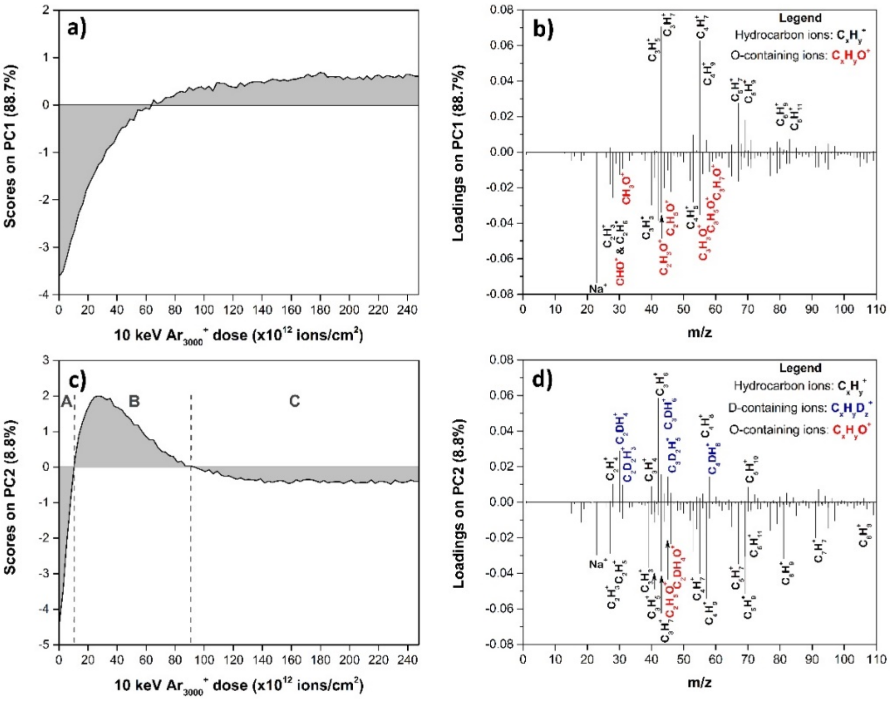

Figure 6. *Wavelet-PCA applied to the LDPE film treated at 5 mm for 60 s. Scores plots of the first two PCs as a function of the sputtering dose (a, c). Loadings plots of the first two PCs as a function of the mass (b, d).*

Figure 6 a,c reports the scores plots of the first two PCs as a function of the dose of 10 keV Ar_{3000}^+ ions used for the sputtering process of the *5 mm - 60 s* sample, and **Figure 6 b,d** the corresponding loadings plots as a function of m/z ratio. The first two components explain 97.5% of the total variance. The PC1 scores plot permits a clear discrimination between two portions of the depth-profile, indicating an interface around the dose value of ~6 x 10^{13} ions/cm^2 (~8 nm). It turns out from the corresponding loadings plot that the main peaks responsible for the differences between the two discriminated portions of the depth-profile are the molecular fragments of the treated part of the sample (scores and loadings < 0) and those related to the inner region of the polymer (scores and loadings > 0). In particular, the loadings with highest values < 0 are associated to O-containing fragments, such as $C_2H_3O^+$ at m/z

43 and $C_3H_3O^+$ at m/z 55, whereas the loadings > 0 are related to typical hydrocarbon ions of the native PE, such as $C_3H_7^+$ and $C_4H_7^+$ at m/z 43 and 55, respectively. Furthermore, small unsaturated $C_xH_y^+$ ions appear among the fragments with loadings < 0. Therefore, PC1 discriminates the oxidized part of the sample, somewhat damaged, from the inner region, which is not affected by the plasma treatment.

The PC2 discriminates two additional regions inside the uppermost modified layer of the LDPE, determining a structure of the type A-B-C going from the surface to the bulk of the polymer. The inspection of the loadings plot shows that the outer region of the treated LDPE layer (region A with loadings < 0) is mostly characterized by the presence of typical fragments related to the O-containing functionalities with(out) D. This is the case, for instance, of the ions $C_2H_5O^+$ and $C_2DH_4O^+$. Additionally, unsaturated small $C_xH_y^+$ ions ($C_2H_3^+$, $C_3H_3^+$) and aromatic ions ($C_7H_7^+$, $C_8H_9^+$) characterize the outermost layer A of the treated LDPE. Finally, characteristic PE peaks show loading values < 0, since they describe the chemical composition of the inner region of the polymer not modified by the Ar-D_2O post-discharge (layer C). Instead, loadings > 0 characterize chemically the inner part of the plasma-treated PE layer (signified as layer B). They are related to deuterated hydrocarbons with low content of D (1-3 atoms). For typical PE ions, like $C_2H_4^+$, $C_3H_6^+$ and $C_4H_8^+$, a deuterated contribution in the layer B cannot be excluded.

Figure 7 displays the scores plot (left hand side) and the loadings plot (right hand side) of the first principal component obtained from the Wavelet-PCA of the LDPE treated at 10 mm for 60 s.

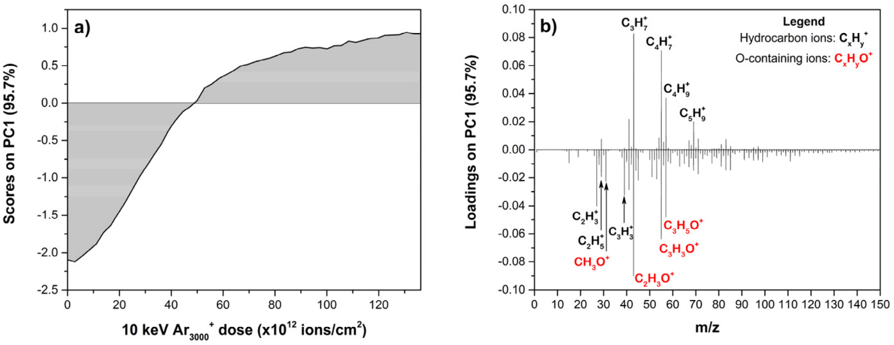

Figure 7. *Wavelet-PCA applied to the LDPE film treated at 10 mm for 60 s: a) Scores plot of the first principal component as a function of the sputtering dose. b) Loadings plot of the first principal component as a function of the mass.*

Remarkably, in this case the only PC1 explains almost 96% of the overall data variance, in contrast with the previous case where two PCs were necessary for the interpretation of the plasma-induced modification in the investigated material. The PC1 scores plot reveals the presence of an interface located at a sputtering dose of ~5 x 10^{13} ions/cm^2 (slightly less than *5 mm - 60 s*). Moreover, no additional sub-regions in the plasma-treated layer of the LDPE are identified. The most important peaks obtained from the study of the loadings show that the uppermost region of the sample is mainly oxidized and damaged (see, for example, $C_2H_3O^+$ and $C_2H_3^+$). Then, the effect of the plasma treatment tends to disappear in a gradual transition with the native material, mainly characterized by the peaks $C_3H_7^+$, $C_4H_7^+$, $C_4H_9^+$ and $C_5H_9^+$ (positive loadings and scores). Thus, for the experimental conditions *10 mm - 60 s*, a structure A-C can be proposed, where the intermediate B layer, located in the treated fraction of the surface material and representing the H-D exchange in the polymer structure, is missing. Finally, the absence of mixed ions $C_xH_yD_zO^+$ is indicated by the study of the PC1 loadings as a further confirmation of the absence of reactivity between D_2O and LDPE at *10 mm - 60 s*.

For verification purposes, the same data processing protocol was applied to the ToF-SIMS depth-profiles of the untreated LDPE. First, O-containing peaks are not observed in the mass spectra. Moreover, the Wavelet-PCA results do not indicate a clear presence of chemical/structural difference along the depth, suggesting that the pristine LDPE used as reference is very homogeneous and suitable for this kind of investigation (**Figure S2** reported in supporting information).

Finally, in order to illustrate the interpretation of the results extracted using the Wavelet-PCA, **Figure 8** shows the depth-profiles of the ion fragments representing the most influential loadings for each PC of the sample *5 mm - 60 s*: $C_3H_7^+$, $C_3D_2H_5^+$ and $C_2H_3O^+$. In this way, a conventional ToF-SIMS depth-profile is reconstructed, where the three regions A-B-C identified in the PC2 of the first Wavelet-PCA are easily visualized. First, the trend of $C_2H_3O^+$ shows an oxidation that decreases from the surface, until disappearing at 14 x 10^{13} ions/cm^2 (around 18 nm). Second, $C_3D_2H_5^+$ shows an H-D exchange shifted towards the depth compared to $C_2H_3O^+$, which may be explained by the different diffusion coefficient of O and D. Finally, these evolutions are accompanied by the initial drop and successive recovery of the $C_3H_7^+$ intensity, that is characteristic of the investigated untreated polymer. This variation may be explained by several factors, such as the production of smaller fragment ions, branching and cross-linking provoked by the plasma-

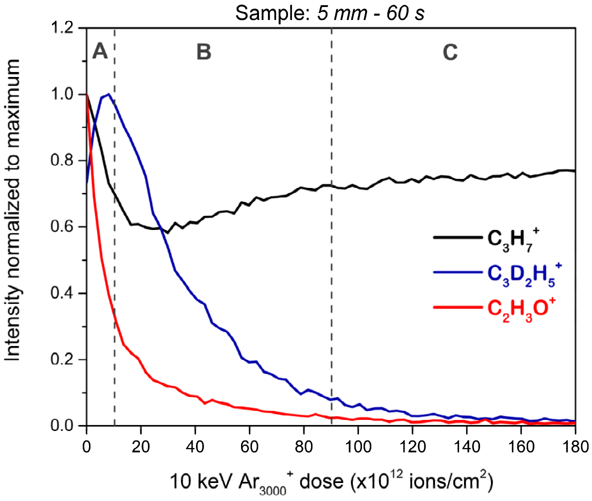

Figure 8. *ToF-SIMS molecular depth-profile of the LDPE film modified by an Ar-D_2O post-discharge at 5 mm of distance from the plasma torch and during 60 s of treatment.*

induced etching process, as well as matrix effects due to the inclusion of oxygen.[3,5]

The corresponding ToF-SIMS depth-profile of the sample *10 mm - 60 s* can be found in the supporting information (**Figure S3**).

5.3.5. Conclusion

The influence of the external plasma parameters “sample-torch distance” (3, 5, 7 and 10 mm) and “treatment time” (30, 60 and 300 s) on the oxidative functionalization of LDPE (sub)surfaces by an atmospheric Ar-D_2O post-discharge was elucidated thanks to the application of a recent scientist-independent ToF-SIMS/(Wavelet-)PCA combined protocol, both at the surface and along the first tens of nanometers. Two different oxidation trends for the treated LDPEs were found out as a function of time depending of the distance from the torch: type I for 3-7 mm, where the functionalization decreases with increasing time, and type II for 10 mm, where the oxidation behaves inversely. Whereas XPS provides only the quantification of the oxidative process for the two types of samples, ToF-SIMS provides a more complete picture of the plasma-induced modifications of the polymer by tracing the reactivity of the water vapor, injected into the post-discharge, with the polymer surface. Indeed, ToF-SIMS could follow the gradual decrease of the oxidation efficiency related to the D_2O vapor with increasing the distance from the torch. The LDPE functionalization at distances >7 mm is fundamentally due to the intervention of the atmospheric O_2 and H_2O. The effect of time has been particularly highlighted for the type I samples, as consisting in the accumulation of chemical damage and loss of O-based functionalities with increasing the duration of the plasma treatment. This observation is explainable with the competition mechanism functionalization-etching already reported in the literature. Finally, the ToF-SIMS/Wavelet-PCA approach probed the in-depth LDPE modifications, indicating a gradual transition of a functionalized and damaged polymer at the surface to a native material along the first ten of nm. In light of the results of this study, showing the presence of type I and II samples, it would be worthy a further investigation of the transition from one to the other typology of functionalization in order to better understand the chemistry underlying this process. The approach proposed in this paper could be applied to a large variety of atmospheric plasma treatments of polymer-based materials in order to better understand the chemical/physical interactions of the post-discharge at the interface with a polymer substrate. Based on this protocol, future work will be addressed to the study of the post-treatment ageing process in the sub-surface region of LDPE films functionalized by an atmospheric Ar-D_2O post-discharge.

5.3.6 Supporting information

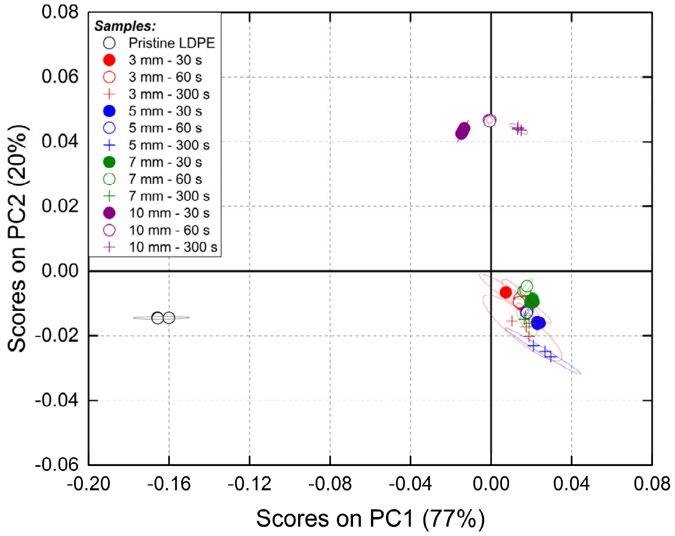

Figure S1. *PC2 versus PC1 scores plot obtained from the PCA applied to the ToF-SIMS negative ion mass spectra of the pristine and all the plasma-treated LDPEs (sample-torch distance: 3, 5, 7, 10 mm; time of treatment: 30, 60, 300 s; three spectra per sample).*

PC1 (77%) loading > 0 (Treated LDPEs)			PC1 (77%) loading < 0 (Pristine LDPE / *10 mm - 30 s*)		
Loading	**Mass**	**Peak**	**Loading**	**Mass**	**Peak**
0.155	42.010	$C_2DO^-/C_2H_2O^-$	-0.880	25.009	C_2H^-
0.127	41.005	C_2HO^-	-0.298	49.009	C_4H^-
0.113	17.004	OH^-	-0.099	38.016	$C_3H_2^-$
0.075	26.015	$C_2D^-/C_2H_2^-$	-0.096	13.008	CH^-
0.074	15.996	O^-	-0.071	51.023	$C_4H_3^-$
0.055	2.015	D^-/H_2^-	-0.060	37.008	C_3H^-
0.051	74.001	$C_2H_2O_3^-$	-0.058	73.008	C_6H^-
0.050	41.999	CNO^-	-0.048	62.015	$C_5H_2^-$
0.041	44.999	CHO_2^-	-0.042	39.024	$C_3H_3^-$
0.039	46.006	$CDO_2^-/CH_2O_2^-$	-0.034	63.023	$C_5H_3^-$
0.038	61.028	$C_2H_5O_2^-$			
0.036	26.004	CN^-	***Legend***		
0.035	45.034	$C_2H_5O^-$			
0.035	60.022	$C_2H_4O_2^-$	O-containing ions: $C_xH_yO_z^+$		

Table S1. *List of the most influential PC1 loadings, and corresponding molecular ion fragments, extracted from the PCA obtained on the ToF-SIMS negative ion mass spectra of the pristine and all the plasma-treated LDPEs (sample-torch distance: 3, 5, 7, 10 mm; time of treatment: 30, 60, 300 s). A threshold value for the loadings of* ±*0.03 has been fixed.*

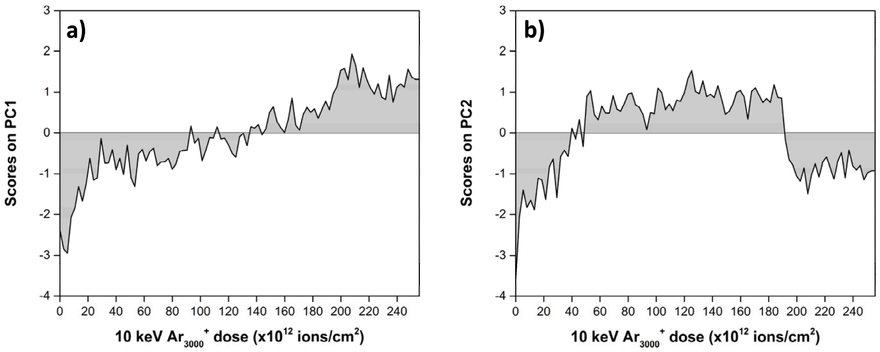

Figure S2. *Wavelet-PCA applied to the pristine LDPE film. Scores plot of the first two principal components as a function of the sputtering dose. The first PC explains 35.4% and the second PC explains 25.1%.*

The Wavelet-PCA applied to the pristine LDPE films shows no significant evidence of compositional changes along the depth. The variations of the first two PCs, shown in **Figure S2**, can be interpreted in terms of noise or variations that are insignificant from the chemical point of view. It is worth to note that, since the initial dataset is normalized to the total ion counts of each scan, the variations in intensity of the spectrum related to any instrumental phenomena (variations of the primary beam, surface charging, etc.) do not affect the result of the Wavelet-PCA study.

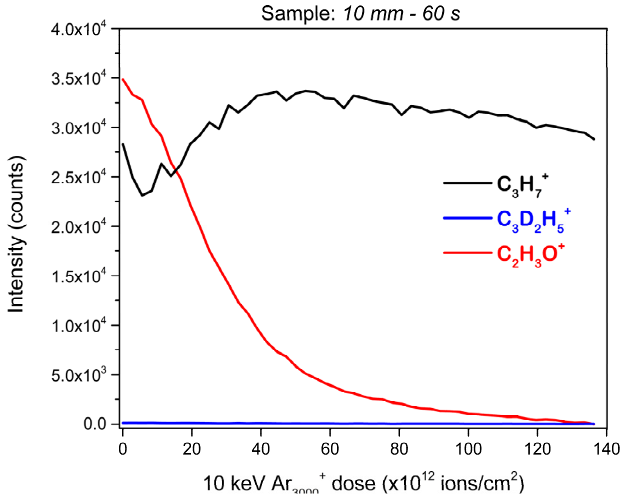

Figure S3. *ToF-SIMS molecular depth-profile of the LDPE film modified by an Ar-*D_2O *post-discharge at 10 mm of distance from the plasma torch and during 60 s of treatment. Note that the intensity of the deuterated species* $C_3D_2H_5^+$ *remains at the level of the noise.*

5.3.7. References

[1] N. Vandencasteele, F. Reniers. Plasma-modified polymer surfaces: Characterization using XPS. *Journal of Electron Spectroscopy and Related Phenomena* **2010**, *178*, 394.

[2] S. K. Pankaj, C. Bueno-Ferrer, N. N. Misra, V. Milosavljević, C. P. O'Donnell, P. Bourke, K. M. Keener, P. J. Cullen. Applications of cold plasma technology in food packaging. *Trends in Food Science & Technology* **2014**, *35*, 5.

[3] S. Abou Rich, P. Leroy, T. Dufour, N. Wehbe, L. Houssiau, F. Reniers. In-depth diffusion of oxygen into LDPE exposed to an Ar-O_2 atmospheric post-discharge: A complementary approach between AR-XPS and ToF-SIMS techniques. *Surface and Interface Analysis* **2014**, *46*, 164.

[4] S. A. Rich, T. Dufour, P. Leroy, L. Nittler, J. J. Pireaux, F. Reniers. Low-density polyethylene films treated by an atmospheric Ar-O_2 post-discharge: functionalization, etching, degradation and partial recovery of the native wettability state. *Journal of Physics D: Applied Physics* **2014**, *47*, 065203.

[5] T. Dufour, J. Minnebo, S. A. Rich, E. C. Neyts, A. Bogaerts, F. Reniers. Understanding polyethylene surface functionalization by an atmospheric He/O_2 plasma through combined experiments and simulations. *Journal of Physics D: Applied Physics* **2014**, *47*, 224007.

[6] S. Abou Rich, T. Dufour, P. Leroy, F. Reniers, L. Nittler, J. J. Pireaux. LDPE surface modifications induced by atmospheric plasma torches with linear and showerhead configurations. *Plasma Processes and Polymers* **2015**, *12*, 771.

[7] L. Liu, D. Xie, M. Wu, X. Yang, Z. Xu, W. Wang, X. Bai, E. Wang. Controlled oxidative functionalization of monolayer graphene by water-vapor plasma etching. *Carbon* **2012**, *50*, 3039.

[8] V. Rybkin, E. Kuvaldina, A. Grinevich, A. Choukourov, H. Iwai, H. Biederman. A compartive study of poly(propylene) surface oxydation in DC low-pressure oxygen and water vapor discharges and in flowing afterglow of water vapor discharge. *Plasma Process and Polymers* **2008**, *5*, 778.

[9] K. S. Siow, L. Britcher, S. Kumar, H. J. Griesser. Plasma methods for the generation of chemically reactive surfaces for biomolecule immobilization and cell colonization - A review. *Plasma Processes and Polymers* **2006**, *3*, 392.

[10] X. Zhang, M. Li, R. Zhou, K. Feng, S. Yang. Ablation of liver cancer cells in vitro by a plasma needle. *Applied Physics Letters* **2008**, *93*, 021502.

[11] I. Koo, W. Lee. Hydrogen isotope exchange reactions in an atmospheric pressure discharge utilizing water as carrier gas. *Plasma Chemistry and Plasma Processing* **2004**, *24*, 537.

[12] M. Atanasova, E. Carbone, D. Mihailova, E. Benova, G. Degrez, J. J. van der Mullen. Modelling of an RF plasma shower. *Journal of Physics D: Applied Physics* **2012**, *45*, 145202.

[13] C. Y. Duluard, T. Dufour, J. Hubert, F. Reniers. Influence of ambient air on the flowing afterglow of an atmospheric pressure Ar/O_2 radiofrequency plasma. *Journal of Applied Physics* **2013**, *113*, 093303.

[14] S. Collette, T. Dufour, F. Reniers. Reactivity of water vapor in an atmospheric argon flowing post-discharge plasma torch. *Plasma Sources Science and Technology* **2016**, *25*, 025014.

[15] A. Delcorte, V. Cristaudo, M. Zarshenas, D. Merche, F. Reniers, P. Bertrand. Chemical analysis of plasma-treated organic surfaces and plasma polymers by secondary ion mass spectrometry. *Plasma Processes and Polymers* **2015**, *12*, 905.

[16] C. M. Mahoney. Cluster secondary ion mass spectrometry of polymers and related materials. *Mass Spectrom. Rev.* **2009**, *29*, 247.

[17] J. C. Vickerman, D. Briggs. ToF-SIMS: materials analysis by mass spectrometry. IM Publications and SurfaceSpectra, Chichester & Manchester, 2nd edition, **2013**, 656.

[18] M. P. Seah. Universal equation for argon gas cluster sputtering yields. *J. Phys. Chem. C* **2013**, 117, 12622.

[19] V. Cristaudo, S. Collette, C. Poleunis, F. Reniers, A. Delcorte. Surface analysis and ultra-shallow molecular depth-profiling of polyethylene treated by an atmospheric Ar-D_2O post-discharge. *Plasma Processes and Polymers* **2015**, *12*, 919.

[20] R. H. G. Brinkhuis, W. J. van Ooij. Identification of positive secondary ions in static sims spectra of poly(methylmethacrylate) using the deuterated polymer. *Surface and Interface Analysis* **1988**, *11*, 214.

[21] J. Lub, F. C. B. M. van Vroonhoven, D. van Leyen, A. Benninghoven. The time of flight static secondary negative ion mass spectra of poly (methylmethacrylate), poly (ethylmethacrylate), and poly (methylmethacrylate-co-ethylmethacrylate). Ion structures and quantification. *Journal of Polymer Science, Part B: Polymer Physics* **1989**, *27*, 2071.

[22] D. Briggs, M. P. Seah. Practical Surface Analysis, Volume 2 – Ion and Neutral Spectroscopy, Wiley, Chichester, 2nd edition, **1992**, 395.

[23] H. Min, S. Wettmarshausen, J. F. Friedrich, W. E. S. Unger. A ToF-SIMS study of the deuterium-hydrogen exchange induced by ammonia plasma treatment of polyolefins. *Journal of Analytical Atomic Spectrometry* **2011**, *26*, 1157, and references therein.

[24] S. Wettmarshausen, H. Min, W. Unger, C. Jaeger, G. Hidde, J. Friedrich. Significance of hydrogen-deuterium exchange at polyolefin surfaces on exposure to ammonia low-pressure plasma. *Plasma Chemistry and Plasma Processing* **2011**, *31*, 551.

[25] D. J. Graham, D. G. Castner. Multivariate analysis of ToF-SIMS data from multicomponent systems: The why, when, and how. *Biointerphases* **2012**, *7*, 49.

[26] X. Ren, L. T. Weng, K. M. Ng, C. M. Chan. Effects of Ar- and Ar/O_2-plasma-treated amorphous and crystalline polymer surfaces revealed by ToF-SIMS and principal component analysis. *Surface and Interface Analysis* **2013**, *45*, 1158.

[27] L. Denis, D. Cossement, T. Godfroid, F. Renaux, C. Bittencourt, R. Snyders, M. Hecq. Synthesis of allylamine plasma polymer films: Correlation between plasma diagnostic and film characteristics. *Plasma Processes and Polymers* **2009**, *6*, 199.

[28] L. Denis, D. Thiry, D. Cossement, P. Gerbaux, F. Brusciotti, I. Van De Keere, V. Goossens, H. Terryn, M. Hecq, R. Snyders. Towards the understanding of plasma polymer film behaviour in ethanol: A multi-technique investigation. *Progress in Organic Coatings* **2011**, *70*, 134.

[29] L. Denis, F. Renaux, D. Cossement, C. Bittencourt, N. Tuccitto, A. Licciardello, M. Hecq, R. Snyders. Physico-chemical characterization of methyl isobutyrate-based plasma polymer films. *Plasma Processes and Polymers* **2011**, *8*, 127.

[30] D. Cossement, F. Renaux, D. Thiry, S. Ligot, R. Francq, R. Snyders. Chemical and microstructural characterizations of plasma polymer films by time-of-flight secondary ion mass spectrometry and principal component analysis. *Applied Surface Science* **2015**, *355*, 842.

[31] N. Tuccitto, G. Zappalà, S. Vitale, A. Torrisi, A. Licciardello. A wavelet - PCA method saves high mass resolution information in data treatment of SIMS molecular depth profiles. *Surface and Interface Analysis* **2016**, *48*, 317.

[32] P. Leroy, S. A. Rich, F. Reniers. Ageing of LDPE surfaces modified by low temperature plasma torch, 20th International Symposium on Plasma Chemistry (ISPC 20), Philadelphia, USA, **2011**.

[33] G. Borcia, C. A. Anderson, N. M. D. Brown. The surface oxidation of selected polymers using an atmospheric pressure air dielectric barrier discharge. Part I. *Applied Surface Science* **2004**, *221*, 203.

[34] Y. De Puydt, D. Léonard, P. Bertrand. *Metallized Plastics 3: Fundamental and Applied Aspects.* A static SIMS study of the chemical modifications induced by plasma and flame treatments at the surface of polyolefins. K. L. Mittal, Plenum Press, New York, **1992**, 225.

[35] F. Garbassi, M. Morra, E. Occhiello, L. Barino, R. Scordamaglia. Dynamics of macromolecules: A challenge for surface analysis. *Surface and Interface Analysis* **1989**, *14*, 585.

[36] U. Oran, S. Swaraj, J. F. Friedrich, W. E. S. Unger. Surface analysis of plasma-deposited polymer films by Time of Flight Static Secondary Ion Mass Spectrometry (ToF-SSIMS) before and after exposure to ambient air. *Surface and Coatings Technology* **2005**, *200*, 463.

[37] A. G. Shard, R. Havelund, M. P. Seah, S. J. Spencer, I. S. Gilmore, N. Winograd, D. Mayo, T. Miyayama, E. Niehuis, D. Rading, R. Moellers. Argon cluster ion beams for organic depth profiling: Results from a VAMAS interlaboratory study. *Analytical Chemistry* **2012**, *84*, 7865.

[38] T. Dufour, J. Hubert, N. Vandencasteele, P. Viville, R. Lazzaroni, F. Reniers. Competitive and synergistic effects between excimer VUV radiation and O radicals on the etching mechanisms of polyethylene and fluoropolymer surfaces treated by an atmospheric He-O_2 post-discharge. *Journal of Physics D: Applied Physics* **2013**, *46*, 315203.

[39] J. Hubert, T. Dufour, N. Vandencasteele, S. Desbief, R. Lazzaroni, F. Reniers. Etching processes operating on a PTFE surface exposed to He and He-O_2 atmospheric post-discharges. *Langmuir* **2012**, *28*, 9466.

CHAPTER 6

Ex-situ characterization of plasma-polymerized polystyrene (pp-PS) films deposited at (sub)-atmospheric pressure

6.1. Introduction

This chapter focuses on the investigation of the chemical structure of plasma deposited films from the styrene monomer in (sub)-atmospheric pressure or near atmospheric pressure. More specifically, the influence of the effective power injected into the plasma medium on the chemistry of coatings (plasma-polymerized polystyrene or pp-PS), after exposure to ambient air, is mainly studied by means of SIMS molecular depth-profiling with massive Ar cluster ion sputtering. The plasma deposition was carried out by Dr. D. Merche at ULB, in the research laboratory on plasmas headed by Professor F. Reniers. Then, the ex-situ characterization of the polymer films was performed at UCL, and mostly in the SUCH (SUrface CHaracterization) platform.

A considerable amount of research has been conducted on the plasma polymerization of the styrene monomer at low pressure, but to our best knowledge only a few works have addressed the use of atmospheric pressure devices. Hence, the elucidation of the chemical structure of pp-PS obtained near atmospheric pressure is desired by the scientific community.

Conversely to the static-SIMS characterization of plasma-polymer surfaces reported in the literature, the present study investigates the inner layers of the material because they are more representative of the actual chemical structure during the film growth. Indeed, some surface-related phenomena, such as adventitious organic contamination or post-oxidation in air, can be safely disregarded. This investigation also includes complementary, surface-sensitive and bulk techniques, i.e. X-ray photoelectron spectroscopy (XPS) and Fourier-transform infrared spectroscopy (FT-IR), respectively.

In the bulk characterization of the pp-PS films by SIMS, a classical approach of data analysis is first attempted, in order to gain insights about the unsaturation, branching and cross-linking contents. To this purpose, two commercial references, i.e. linear and cross-linked polystyrene, have been chosen. However, some limitations arise because of the oxygen incorporation occurring during the plasma polymerization, that alters the secondary ion emission probabilities. Additionally, one is dealing with a polymer showing new structural features, not ascribable to the conventionally polymerized counterparts for which the SIMS traditional structural indicators have been defined. Hence, a more systematic (or statistical) study of the secondary ion mass spectra, that is principal component analysis (PCA), is proposed to extract more reliable information about the pp-PS structure. Furthermore, considerations about the methyl-substitution, already mentioned in the literature in the case of plasma-polymerized styrene (PPS),[1] 2-vinylpyridine (PP2VP)[2] and vinylferrocene (PPVF),[3] are provided, thanks to the comparison of the pp-PS with other alkyl-substituted derivatives of polystyrene. In the end, the integration of the information derived from XPS (surface-related), IR and SIMS/PCA (bulk-related) leads to a clearer picture of the chemical structure of the investigated plasma-polymer, as well as the dependence on the power injected into the plasma medium.

6.2. Experimental

6.2.1. Materials

The liquid styrene monomer used for the plasma polymerization was provided by Fluka (99.5% purity, 0.005% of 4-*tert*-butylcathecol as stabilizer). The styrene was employed without any further purification. Argon was chosen as carrier gas and plasmagen gas. An argon cylinder was purchased from Air Liquide (99.999% purity). The plasma-polymerized styrene was deposited onto silicon substrates of 1 cm x 4-5 cm size, cleaned by sonication in isopropanol (VWR Chemicals, HiPerSolv CHROMANOFORM for HPLC, 99.9% purity) and dried under nitrogen flux. The plasma-polymer film on Si was successively cut into 1 x 1 cm^2 pieces to be characterized by different analytical techniques, such as XPS, FT-IR, and SIMS. This methodology was found to be the best in order to avoid the edge effects, and to obtain more homogeneous films in terms of chemical structure and thickness. Linear and cross-linked PS, used as reference samples, were purchased from Goodfellow.[4] Both references were provided by Dr. Merche, who used them for her investigation on pp-PS published in 2009.[5] The linear PS is called by the manufacturer “amorphous PS”, name maintained by Dr. Merche in her Ph.D. thesis,[6] and publication. The two reference materials are polymer sheets with ~1 mm thickness. The linear PS looks transparent and very smooth, while the second polymer is white, very rough and breakable without any specific tools. The manufacturer did not provide any information about the synthesis of these two materials.

Additional commercial references were employed in this study, namely poly (α-methyl styrene) (PAMS), poly (4-methyl styrene) (P4MS), and poly (4-vinylphenol) (PVP). Briefly, they represent three derivatives of the polystyrene, with or without presence of oxygen (PAMS and P4MS vs PVP), and with a methyl group either on the main chain (case of PAMS) or as substituent on the phenyl ring (case of P4MS, where the -CH_3 occupies the position 4 or -para). The specific choice of these polymers as additional references will be discussed in the SIMS section of this chapter (§.6.6.3.5). The poly (α-methyl styrene) was purchased from Scientific Polymer Product, and it is a polydisperse polymer. Both poly (4-methyl styrene) and poly (4-vinylphenol), also named poly (4-hydroxy styrene), were purchased from Sigma-Aldrich. Their average M_w determined by GPC (by the polymer supplier) are ~72 000 and ~25 000, respectively.

PAMS, P4MS and PVP thin films on Si substrates were prepared exclusively for SIMS characterization. First, PAMS and P4MS powders were dissolved in toluene (Sigma-Aldrich, purity ≥99.71%), whereas PVP was dissolved in isopropanol (VWR Chemicals, 99.9% purity). The polymer solutions were filtered using 0.2-µm Teflon filters to remove any non-dissolved particles and dust before their deposition on the Si supports. The silicon wafers used for the preparation of these samples were cleaned with the same procedure employed for the pp-PS substrates. Then, the solutions were spin-coated onto the silicon. The spin-coating parameters (speed, acceleration, and time) and the concentration of the polymer solutions were varied in order to optimize the film quality in terms of morphology and roughness. Thus, the polymer films were deposited at 5000 rpm with acceleration 20000 rpm/s for 60 s. The solution concentrations were ~0.1 g/L for PAMS and P4MS, and ~0.05 g/L for PVP.

6.2.2. Dielectric barrier discharge equipment and sample preparation

For this study, plasmas were produced in a ULB homemade reactor of the dielectric barrier discharge (DBD) type, that works at sub-atmospheric pressure. The schematic of the DBD device and picture of the reactor are reported in **Figure 1** and **Figure 2**.

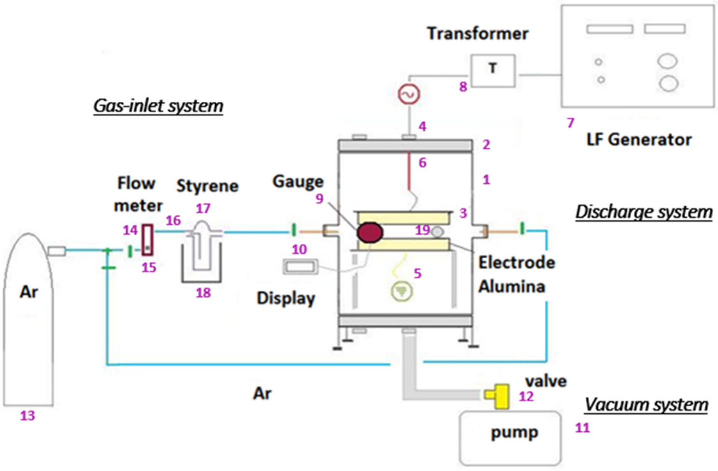

1.	Cylindrical gas reactor
2.	UHV stainless-steel flanges
3.	Cu electrode covered by Al_2O_3
4.	Current feedthrough
5.	Ground wire
6.	High voltage
7.	LF generator
8.	Transformer
9.	Pressure gauge
10.	Display (pressure indicator)
11.	Combinatory primary pump system
12.	Dosing valve
13.	Ar cylinder
14.	Leaking valve
15.	Volumetric flowmeter
16.	Flexible PFA tube
17.	Bubbler
18.	Thermostated bath
19.	Ar/styrene mixture inlet

Figure 1. *Schematic of the dielectric barrier discharge (DBD) device used in this study, including the gas-inlet system, the discharge system, and the vacuum system.*

The reactor consists in a glass cylinder made of pyrex from PierreGlass, 7 mm of thickness, 200 mm of height, and 100.5 mm radius with six entries (KF DN 25) located at half-height for the gas inlets and the pressure gauge. It is connected to two UHV stainless-steel flanges (SA Georis), and the insulation is ensured by two Viton O-rings. Each UHV stainless-steel flange presents two feedthroughs KF DN 16, for the passage of current (on the top), and the pumping system (on the bottom).

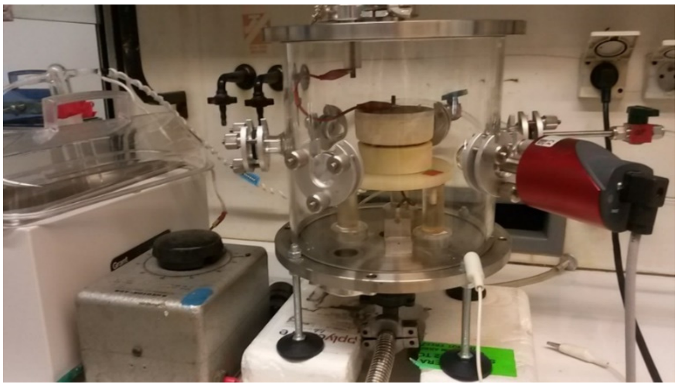

Figure 2. *Picture of the dielectric barrier discharge (DBD) reactor.*

The remaining unused are closed with OD flanges. Two copper electrodes, covered with aluminum oxide (alumina, 99.7% purity), with 8 cm diameter and 3 mm thick are provided by Ceratech. The interelectrode distance is 3-4 mm. The alumina-covered electrode lays on a PVC support. The alumina represents an ideal dielectric material for the DBD in the tension and frequency ranges used in this work. In addition to the excellent dielectric properties shown in a large range of frequency (accumulation of ions and electrons to reduce the discharge current and to avoid the arc formation), the alumina presents also good mechanical, chemical, and physical properties. High voltage is applied to the top electrode, whereas the bottom electrode is grounded. The DBD device is equipped with two different gas inputs: 1) mixture of carrier gas and styrene (monomer to polymerize), and 2) only carrier gas, that in this case is employed to put the chamber at atmospheric pressure (it can also be used for surface pre-treatment or modification). The liquid styrene monomer is kept at 313 K (40 °C) in a bubbler immersed in a thermostated bath. The monomer vapors are carried into the discharge by an Ar flux via a volumetric flowmeter from Aalborg with a flow rate of 4 L/min. The gases are driven to the plasma chamber using PFA (perfluoroalkoxy copolymer) and stainless-steel lines (Swagelok®). The lines are heated by thermal bands from the bubbler to the chamber in order to minimize the monomer condensation.

After the introduction of the silicon substrate (1 cm x 4-5 cm) for the plasma deposition (see **Figure 3**), on the bottom electrode and perpendicularly to the Ar/styrene inlet, the chamber is pumped down to a pressure of 1-5 mbar ($1x10^2$-$5x10^2$ Pa) by a primary pump, "Chemvac combination pump system 6 Dp-101". It consists in a chemical diaphragm pump (PTFE) resistant to corrosive gases, combined with an Ilmvac rotatory pump. Then, the chamber is refilled by the gas mixture (Ar/styrene) to the working pressure of 200 mbar (2 x 10^4 Pa, that is 1/5 of the atmospheric pressure) measured by a gauge CMR 361. The use of a slightly reduced pressure is justified by the need to increase the interelectrode distance sufficiently to be able to place the sample, and to minimize the breakdown voltage. The cylindrical chamber is pumped continuously during the plasma polymerization (dynamic flux) in order to minimize the air contamination of the growing polymer film.

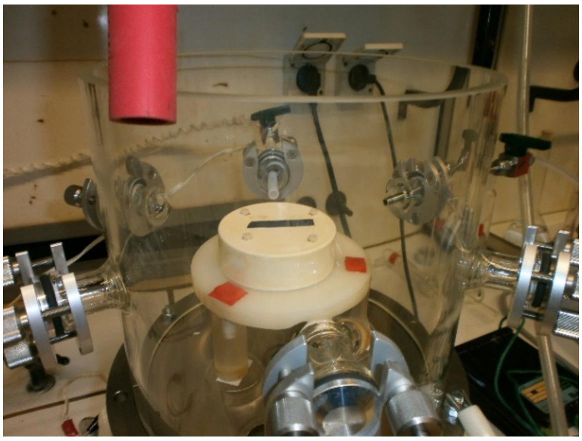

Figure 3. *Positioning of the silicon substrate (1 cm x 4-5 cm) on the bottom electrode, and perpendicularly to the Ar/styrene inlet for the growth of the plasma-deposited film.*

A dosing valve Balzers-Pfeiffer Vacuum EVN 116 is located between the pump and the chamber in order to reduce the pumping rate during the film deposition. The low frequency (LF) plasma is ignited using a AFS (G10 S-V) generator, coupled with a transformer that permits to vary the frequency from 6 to 30 kHz and to amplify the sinusoidal signal of the a.c. voltage. The frequency is fixed at 18160 Hz. Plasma-polymer films are prepared varying the power from 10 W to 80 W. The deposition time is kept constant at 5 minutes. After the film deposition, the sample is left in the reactor under (sub)-atmospheric pressure during 5 additional minutes, in order to minimize the post-polymerization oxidation due to the surviving radicals trapped inside the polymer structure. Then, the plasma chamber is brought to atmospheric pressure. Therefore, the samples are collected to be analyzed by SIMS within the first few hours from their polymerization. The samples investigated in this study, as well as the reference polymer materials, are described in **Table 1**.

Investigated samples	**Power (W)**	**Sample name**
Plasma-polymerized polystyrene (pp-PS)	10 20 30 40 50 60 70 80	pp-PS/10W pp-PS/20W pp-PS/30W pp-PS/40W pp-PS/50W pp-PS/60W pp-PS/70W pp-PS/80W
Reference samples	**Long name**	**Sample name**
Polystyrenes (PS)	Amorphous PS* Cross-linked PS	Linear PS Cross-linked PS
PS derivatives	poly (α-methyl styrene) poly (4-methyl styrene) poly (4-vinylphenol)	PAMS P4MS PVP

* Commercial name (Goodfellow).

***Table 1.** List of the investigated samples.*

6.2.3. Estimation of plasma power

As mentioned in the introduction of the chapter, this study is focused on the investigation of the chemical structure of pp-PS films deposited by DBD as a function of the plasma power. To this purpose, the generator power is varied from 10 to 80 W. However, the power delivered by the LF generator could differ from the power that is actually injected into the plasma, because of dissipation and reflection phenomena. The percentage of power loss is not constant and varies with many parameters, such as the excitation frequency,[7] the gas pressure,[8,9,10] the gas mixture,[11] the electrode gap,[12] the reactor design[13] and the matching network topology. Depending on these parameters, the power absorbed by the plasma can vary between 40 and 80% of the applied power. Therefore, in this investigation, an accurate determination of the actual power dissipated into the plasma discharge is needed.

The literature reports four different approaches for the estimation of the plasma power in DBD reactors and atmospheric pressure systems, namely the analytical, electrical, Lissajous figure, and comparative methods. An overview of the different available approaches for the power estimation, together with their main properties, is proposed by M. Hołub.[14]

In this work, the Lissajous curve approach was applied for the determination of the discharge power. The method is based on the following assumptions:

$$P_{el} = f\,.\,E_{el} \tag{1}$$

$$E_{el} = \oint U(t)\,\frac{dQ}{dt}\,dt = C_{meas}\oint U(t)\;dU_{meas} \tag{2}$$

that permits to obtain the value of power (P_{el}) when an additional measurement capacitor (with capacitance C_{meas}), is connected in series with the reactor, as shown in **Figure 4**. f represents the frequency of the alternating feeding voltage $U(t)$, E_{el} the electric energy consumed per voltage cycle, and Q is the transferred charge.

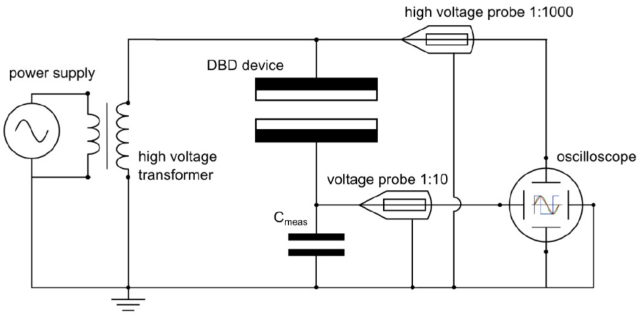

Figure 4. Electrical circuit for the power measurements, where a measurement capacitor C_{meas}, is connected in series with the DBD reactor. The circuit includes additional elements to the matching network power supply/high voltage transformer/plasma reactor*, such as an oscilloscope, a high voltage probe 1:1000, and a voltage probe 1:10.*

From the so-called Lissajous curve, that is a Q-U oscillographic presentation (reported in **Figure 5**), the minimum external voltage U_{min} at which the ignition occurs can be calculated. Furthermore, E_{el} can be estimated by **Equation (3)** (derived from **Equation (2)**)[15] and the related P_{el} (refer to **Equation (1)**) can be determined:

$$E_{el} = C_{meas}\oint U(t)\;dU_{meas} = 2\,(U_{max}\,.\,Q_0 - Q_{max}\,.\,U_0) \\ = AREA\ of\ (Q-U)\ diagram \tag{3}$$

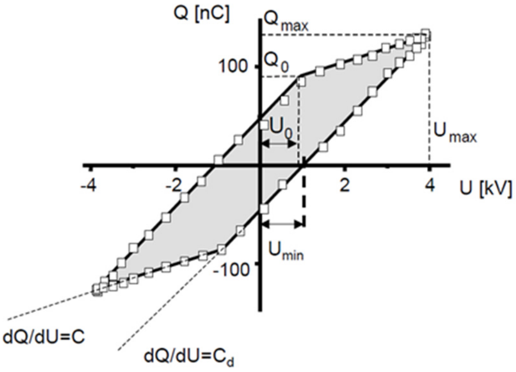

Figure 5. *Exemplary Lissajous curve, an Q-U oscillographic presentation (figure from Wagner et al.).*[15]

Lissajous figure also permits to determine the main reactor parameters (C, C_d, C_g from **Equation (4)**), since a DBD reactor can be thought as the serial connection of two capacitances (compare with **Figure 6**): the gap capacitance C_g, and dielectric capacitance C_d.[15] Then, the total capacitance C is given by the expression:

$$C = \frac{C_d \cdot C_g}{C_d + C_g} \tag{4}$$

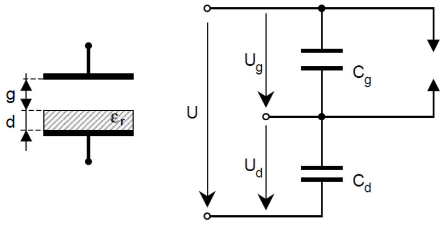

(a) (b)

Figure 6. *One-sided barrier discharge (DBD) configuration (a), and the equivalent circuit (b). Figure from Wagner et al.*[15]

In this study, the electrical circuit shown in Figure 4 was obtained by connecting in series the DBD reactor used for the pp-PS deposition (described in §6.2.2), via its grounded electrode, with a measurement capacitor. The capacitance of this probe (C_{meas}) was chosen to do not be intrusive. In order to ensure this condition, C_{meas} needs to be sufficiently large so that the voltage difference between the DBD electrodes is almost equal to the voltage applied to the powered electrode. For these power measurements, a 33 nF capacitor was used. So, the voltage drop across the capacitor is small enough to be measured. In addition, a digital phosphor oscilloscope (Tektronix DPO 3032) of two channels was employed for the power consumption measurements. The oscilloscope channel 1 was connected by a HV probe 1:1000 (Tektronix P6015A) to the powered electrode of the DBD, while channel 2 was connected to the capacitance probe C_{meas}, as depicted in Figure 4.

The measurements were led for 8 different power levels, going from 10 W to 80 W. All the measurements were performed for a frequency (*f*) of 18.16 kHz. The discharge was switched off each time before increasing the generator power level, in order to cool the DBD electrodes down. Two different discharges were investigated, only Ar and Ar/styrene (4 L/min). For both plasmas, the measurements were performed at initial time (t_0) and after 1 min (t_1). In the specific case of the Ar/styrene mixture, additional measurements were done during a time lapse of 5 min (each minute after t_0: t_1, t_2, t_3, t_4, t_5), in order to investigate the power evolution during the deposition time of the pp-PS films.

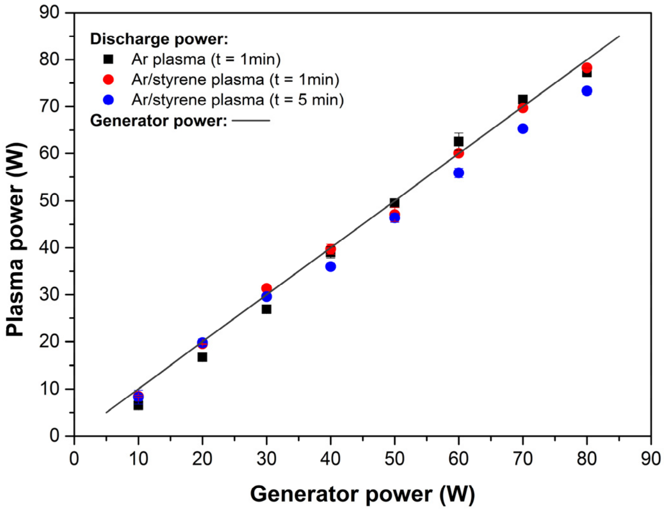

Figure 7. *Power measured for the Ar and Ar/styrene discharges as a function of the power supplied by the generator. For the latter discharge, two different time evolutions have been investigated, i.e. during 1 min (t = 1 min) and 5 min (t = 5 min). The grey solid curve represents the generator power.*

The measurement data created by the oscilloscope were analyzed by the program CalcPlasmaPower_v7. The results of the power measurement/calculations are summarized in **Figure 7**, where the average power values (over 1 min and 5 min) of the two discharges are reported, as well as the ideal curve representing the generator power. It can be observed that every single discharge follows, to some extent, the generator curve. Furthermore, a slight drift of the discharge power for the process mixture Ar/styrene can be found after longer deposition times (red vs blue solid circles). However, the 8 different power levels are still identified. For the sake of conciseness, the 8 levels of the injected power into the Ar/styrene discharge (average over 5 min) will be indicated by the nominal values reported in **Table 2**.

Ar/styrene plasma

Measured* $P_{discharge}$ (W)	Nominal $P_{discharge}$ (W)
8.27	10
19.77	20
29.58	30
35.97	40
46.38	50
55.87	60
65.27	70
73.34	80

*Average values over the deposition time (5 min)

Table 2. *Average power values of the Ar/styrene discharge measured during 5 min of the pp-PS film deposition ($P_{discharge}$), and related nominal power values that will be used in the text to easily identify the 8 different power levels.*

6.3. XPS characterization of pp-PS films

6.3.1. Experimental

XPS measurements were performed by means of a Kratos Axis Ultra spectrometer (Kratos Analytical, Manchester, UK) equipped with a monochromatized aluminium X-ray source (powered at 10 mA and 15 kV). The pressure in the analysis chamber was about 10^{-6} Pa. The angle between the normal to the sample surface and the direction of photoelectrons collection was about 0°. The X-ray bombarded area was approximately 2000 µm x 800 µm. The analyses were performed in the hybrid lens mode (a combination of magnetic and electrostatic lenses) with the slot aperture. The resulting analysed area was 700 µm x 300 µm. The pass energy was set at

160 eV for the survey scan and 40 eV for narrow scans. In the latter conditions, the full width at half maximum (FWHM) of the Ag $3d_{5/2}$ peak of a standard silver sample was about 0.9 eV. The samples were fixed on a standard stainless steel multi-specimen holder by using a piece of double sided insulating tape. Charge compensation was achieved by using the Kratos Axis device. It consists of an electron source mounted co-axially to the electrostatic lens column and a charge balance plate used to reflect electrons back towards the sample. The magnetic field of the immersion lens placed below the sample acts as a guide path for the low energy electrons returning to the sample. The electron source was operated at 0.16 A filament current and a bias of -1.1 eV. The charge balance plate was set at -4.2 V.

The following sequence of spectra was recorded: survey spectrum, C 1s, O 1s, Si 2p, and C 1s again to check for charge stability as a function of time and the absence of degradation of the sample during the analyses. The $\underline{\mathbf{C}}_{\mathrm{aliph}}$-(C,H) component of the C1s peak of carbon has been fixed at 284.8 eV to set the binding energy scale. Spectra were decomposed with the CasaXPS program (Casa Software Ltd., UK) with a Gaussian/Lorentzian (70/30) product function and after subtraction of a linear baseline. Molar fractions (%) were calculated using peak areas normalized on the basis of acquisition parameters after a linear background subtraction, experimental sensitivity factors (C = 0.278, O = 0.780 and Si = 0.328, based on those of Wagner)[16] and transmission factors provided by the manufacturer.

The XPS analyses were conducted immediately after the SIMS depth-profiling experiments (same samples), that took place within a few hours after the plasma deposition by DBD.

6.3.2. Results and discussion

Table 3 reports the surface elemental composition determined by XPS of the two reference samples provided by Goodfellow, i.e. linear and cross-linked PS, and the plasma-polymerized polystyrene (pp-PS) films on Si wafers in the power range 10 W – 80 W. It consists essentially in carbon (>90%), oxygen (up to ~9% for the pp-PS films), and in some cases traces of silicon (0.3-0.4%). The binding energy scale was calibrated on the $\underline{\mathbf{C}}_{\mathrm{aliph}}$-(C,H) component of the main C 1s peak (284.8 eV) both for conventional PS and pp-PS, as already mentioned in the experimental section about the XPS analyses. Furthermore, the position of the $\underline{\mathbf{C}}_{\mathrm{arom}}$-(C,H) component was fixed at 284.55 eV, that is 0.25 eV lower than $\underline{\mathbf{C}}_{\mathrm{aliph}}$-(C,H), following the procedure proposed by Beamson and Briggs.[17]

XPS peak	**O 1s**	**C 1s**						**Si 2p**	**O1s/ $\underline{C}$-O**
Assignment	-	Shake-up	O=$\underline{C}$-O	$\underline{C}$=O, O-$\underline{C}$-O	$\underline{C}$-O	$\underline{C}$-(C,H)	C_{total}	-	
Position (eV)	532.2	291.2	288.8	287.8	286.3	284.7	-	101.7	
Sample									
Linear PS	0.7	6.6	0.0	0.0	1.5	91.2	99.3	-	0.5
Cross-linked PS	4.6	2.4	0.1	0.3	2.9	87	92.6	2.8	0.6*
pp-PS/10W	7.2	4.8	0.3	2.5	8.5	76.7	92.8	-	0.8
pp-PS/20W	8.7	4.6	0.6	3.0	8.8	73.9	91.0	0.3	1.0
pp-PS/30W	7.7	4.1	0.7	3.2	9.1	75.2	92.3	-	0.8
pp-PS/40W	8.1	4.3	0.6	3.2	9.3	74.6	91.9	-	0.9
pp-PS/50W	8.4	4.1	0.3	2.0	9.1	76.2	91.6	-	0.9
pp-PS/60W	8.5	3.7	1.0	3.3	10.6	72.4	91.1	0.4	0.8
pp-PS/70W	9.2	3.6	0.8	4.0	11.1	70.8	90.4	0.4	0.8
pp-PS/80W	9.0	3.9	0.8	3.4	10.2	72.3	90.6	0.4	0.9

*PDMS contribution subtracted (2.8%) to O 1s peak

Table 3. *Elemental composition (determined by XPS) and content (in %) of the functional groups derived from the decomposition of the C1s peak for the PS reference samples, linear and cross-linked, and the pp-PS films synthesized by DBD in the power range 10 W - 80 W. The last column lists the ratios of the O 1s peak to the* $\underline{\mathbf{C}}$*-O component of the C 1s peak (at 286.3 eV).*

This difference in the binding energies is due to the relaxation-energy difference between the aromatic (photoelectron vacancy screened by Π electrons) and the aliphatic component (photoelectron vacancy screened by σ electrons, less polarizable). However, in Table 3 the sum of both components of the C 1s peak, $\underline{\mathbf{C}}_{aliph}$-(C,H) and $\underline{\mathbf{C}}_{arom}$-(C,H), is reported in the column indicated as $\underline{\mathbf{C}}$-(C,H). The aromatic component is accompanied by the so-called "π-π* shake-up satellite" or simply "shake-up" peak at ~291.2 eV, that is due to π-π* transitions of the aromatic rings of PS and unsaturated side chains. The decomposition of the C 1s peak in its oxidized components was performed by fixing the following binding energies, allowing to reliably compare the different samples (see Figure S1): 288.8 eV for COOR/COOH (indicated in the table as O=$\underline{\mathbf{C}}$-O), 287.8 eV for RR'C=O ($\underline{\mathbf{C}}$=O, O-$\underline{\mathbf{C}}$-O), and 286.3 eV for C-OR/C-OH ($\underline{\mathbf{C}}$-O). The positions of the remaining photoelectron peaks reported in Table 3 are averaged values, since they were not fixed.

The gray zone of Table 3 concerns the reference samples, linear PS and cross-linked PS. The PS structure of the first listed sample, i.e. linear PS, is confirmed by its elemental composition. It consists of 99.3% of carbon and only 0.7% of oxygen, explainable by surface contamination. However, the percentage of the shake-up satellite is close to the one reported in the XPS library for the polystyrene (~10% of CC_{arom}).[17] The XPS characterization of the linear PS confirms that, in terms of purity, the chosen material is a good reference for this study.

The second reference material for this investigation is the cross-linked PS, whose cross-linking procedure was not clarified by the manufacturer. The XPS analysis points out a higher content of oxygen (4.6%), and the presence of organic silicon (2.8%). One can notice a decrease of the shake-up satellite of ~3 times with respect to the previous reference PS (linear). The presence of oxygen is partly linked to surface contamination of poly (dimethylsiloxane) (PDMS), that will be confirmed in the in-depth SIMS characterization (refer to the SIMS section, §6.6.1). The remaining oxygen is mostly involved in **C̲**-O chemical bonds of ether/alcohol nature.

Table 3 depicts also the chemical composition of the pp-PS films obtained by increasing the power injected in the plasma medium from 10 to 80 W. These samples differ fundamentally from the PS references for the much higher content of O ranging from ~7% to ~9%. Presence of surface contamination could be derived from the detection of the Si 2p peak, which does not come from the substrate because uniformly covered by the plasma film. The O-uptake of the plasma-polymers could take place during the plasma polymerization and/or to be due to post-polymerization oxidation in the air since radical species remain trapped in the film after plasma deposition (very high concentration of 10^{17}-10^{20} spins/cm^3 based on the literature[18]). Additionally, a method reported in the literature to express the degree of aromaticity consists in the representation of the shake-up satellite as percentage from the area of the main C 1s peak. The values obtained in this way for the pp-PS films prepared for this study are in the same range of those obtained in the work of Merche et al. (for instance at 10 W 5.2% vs 4.76% of the sample pp-PS/DBD/Ar on PTFE (10')).[5] However, the presence of adventitious organic contamination could alter this parameter by the $\underline{\mathbf{C}}_{\mathrm{aliph}}$-(C,H) component.

In order to better elucidate the nature of the O-uptake in the plasma-polymers, as well as in the two reference samples, the **C̲**-O component of the main C 1s peak is plotted versus the O 1s peak in **Figure 8**. A correlation is found for the pp-PS films deposited by DBD and the linear PS. However, it was said that the surface of the cross-linked PS is mostly contaminated by PDMS, as it will be determined by SSIMS in §6.6.1. Thus, if the PDMS contribution to the O 1s peak is subtracted (2.8% of Si 2p, cf. Table 3), one can observe that the cross-linked PS aligns with the other samples (see "cross-linked (corrected)" in Figure 8). So, it is found that the O-uptake in all these polymer structures occurs mainly via C-O simple bonds. However, the ratio O 1s to **C̲**-O is different in the case of the cross-linked PS, as shown in the last column of Table 3. Indeed, for the pp-PS films the O 1s/C-O ratio is close to 1, suggesting the preponderant presence of alcoholic functionalities (C-OH), independently of the power applied during the plasma deposition. On the contrary, for the cross-linked PS this ratio is almost 0.5, pointing out that each O atom is bonded to two C atoms (C-O-C or ether groups). Additionally, the O content of the pp-PS increases slightly with power (refer also to Table 3). This variation is significant considering that repeated measurements on selected samples (four XPS spectra per each sample) of the plasma-deposited film series highlighted a high homogeneity of the pp-PS surfaces (standard deviation of ±0.2% for 10 W and ±0.1% for 40 W). This increase in oxidation going from 10 W to 80 W is accompanied by a decrease of the shake-up satellite (~1%) and the aromatic component of the C 1s peak.

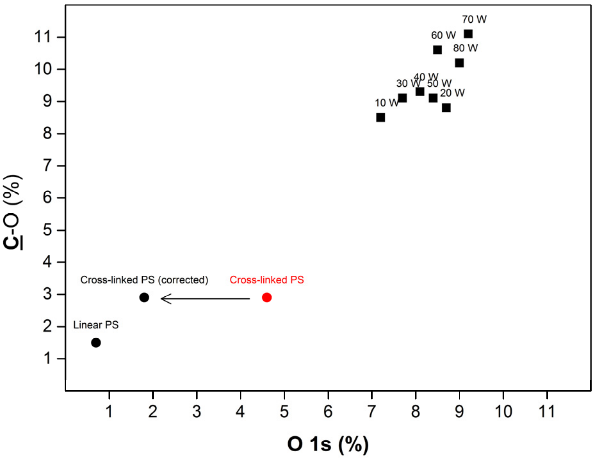

Figure 8. *Correlation between the O 1s peak and the **C**-O component of the main C 1s peak for the two commercial references, linear and cross-linked PS (solid circles), and all the plasma-deposited films (solid squares). For the cross-linked PS, the contribution to the O 1s coming from the PDMS contaminant (2.8%) has been subtracted, obtaining the shift of the sample towards the black solid circle (indicated as "corrected" cross-linked PS).*

This fact is better shown by the anti-correlation between the **C**-O component and the shake-up satellite, depicted in **Figure 9**. The splitting of the cross-linked PS from the other specimens is explained by the two different typologies of oxidation already mentioned. With increasing the power of the plasma polymerization, the C-O functionalities increase to the detriment of the aromaticity (shake-up). This could suggest an oxidative functionalization of the phenyl rings with subsequent disruption of the aromaticity, as described by Potter et al.[18] But, other factors could be evoked, such as the concomitant fragmentation of the styrene monomer in the plasma medium, leading to the loss of aromatic rings, and the O-grafting to the aliphatic moieties of the polymer in growth.

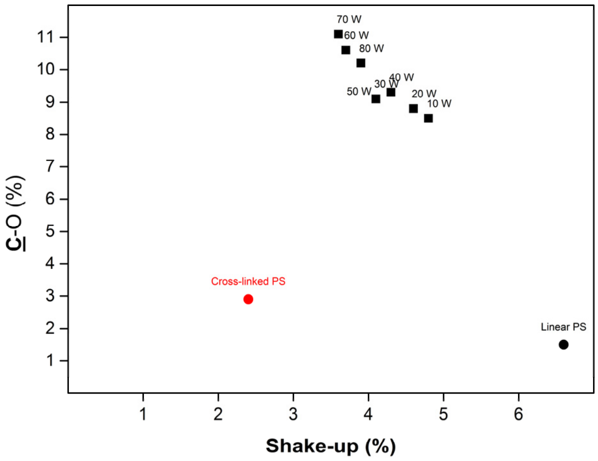

Figure 9. *Anti-correlation between the shake-up satellite and the* ***C̲****-O component of the main C 1s peak for the reference linear PS (solid circles), and the pp-PS films deposited at different plasma powers (solid squares). The cross-linked PS remains apart from the overall sample set.*

In conclusion, in the cross-linked PS, the increase of the C-O and aliphatic components of the C 1s peak, as well as the related decrease of the aromatic component and the shake-up peak lead to the hypothesis that the cross-linking of the polystyrene was well performed by addition of divinylbenzene (DVB), but also some PEG-like (polyethylene glycol) moieties are present in the polymer structure. The origin of the O-uptake in this sample remains unknown.

Although XPS elucidates the chemical composition of the pp-PS films, and their chemical bonds (in this case, C-C and C-O), IR spectroscopy is well suited to bring information about the C-H_x bonds. The next section will concern the IR characterization of the plasma-polymers synthesized in the DBD at increasing power, as well as the two commercial reference PS.

6.4. FT-IR characterization of pp-PS films

6.4.1. Experimental

FT-IR analysis of the pp-PS films deposited onto Si supports in the power range 10-80 W (see Table 1 in §6.2.2) were recorded on a Nicolet spectrometer (Nexus 870), equipped with Continuum microscope, in transmission mode. FT-IR spectra were obtained with 32 scans at a resolution of 8 cm^{-1} over a spectral range from 4000 to 500 cm^{-1}. The samples pp-PS/10W and pp-PS/20W were too thin for the IR analysis. On the contrary, as they were too thick, IR spectra of the two commercial reference samples, linear and cross-linked PS, were performed with the same apparatus in ATR (attenuated total reflectance) mode, using a silicon crystal in mono-reflection. A total of 128 scans were taken with a resolution of 8 cm^{-1} over a spectral range from 4000 to 650 cm^{-1}. Baselines were corrected manually.

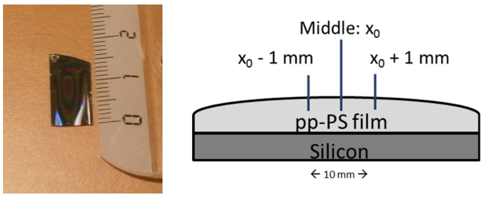

	Thickness (µm)		
Position	*x_0 – 1 mm*	*x_0*	*x_0 + 1 mm*
Sample			
pp-PS/10W	0.16	0.13	0.10
pp-PS/20W	0.45	0.57	0.35
pp-PS/30W	0.59	1.77	0.78
pp-PS/40W	1.25	1.6	0.93
pp-PS/50W	1.21	4.14	0.9
pp-PS/60W	3.35	6.03	1.08
pp-PS/70W	0.9	8.18	0.89
pp-PS/80W	1.71	4.71	0.73

Figure 10. *Picture of a pp-PS film on Si accompanied by the sketch of its cross-section along the x direction. The x-size of all the samples is 10 mm. In addition, the position of the thickness determination by profilometry is indicated on the sketch (it is only an estimation). The thickness values for the films investigated by FT-IR are reported in the table. pp-PS/80W does not seem to follow the increase of thickness as a function of the power. This could be related to the position of the cut of the original 1 x 5* cm^2 *sample in smaller pieces destined to the different characterization techniques.*

The thickness of the investigated plasma-deposited polymer films varies highly along the x and y directions. This peculiarity of the pp-PS films is illustrated in **Figure 10**. Additionally, the chemical structure of these plasma-deposits varies with the plasma power. In that respect, the XPS analyses presented in the previous section pointed out a decrease of the aromaticity and an increase of the oxidation with increasing the power. The combination of these two factors led to the impossibility of normalizing the IR spectra in order to compare them in quantitative terms. Indeed, there is no vibrational band in the pp-PS IR spectrum that could be set as internal reference for the comparison of films of different thicknesses. Thus, qualitative information was essentially extracted from the IR analyses.

6.4.2. Results and discussion

First, the IR-ATR spectra of the two commercial reference samples, depicted in **Figure 11**, are analyzed. The linear PS shows the main finger-printing IR bands of the polystyrene, as indicated on the spectrum (Figure 11.a) and in **Table 4**. For the sake of clarity, the related wavenumbers are reported on the IR spectrum of the second reference PS (Figure 11.b).

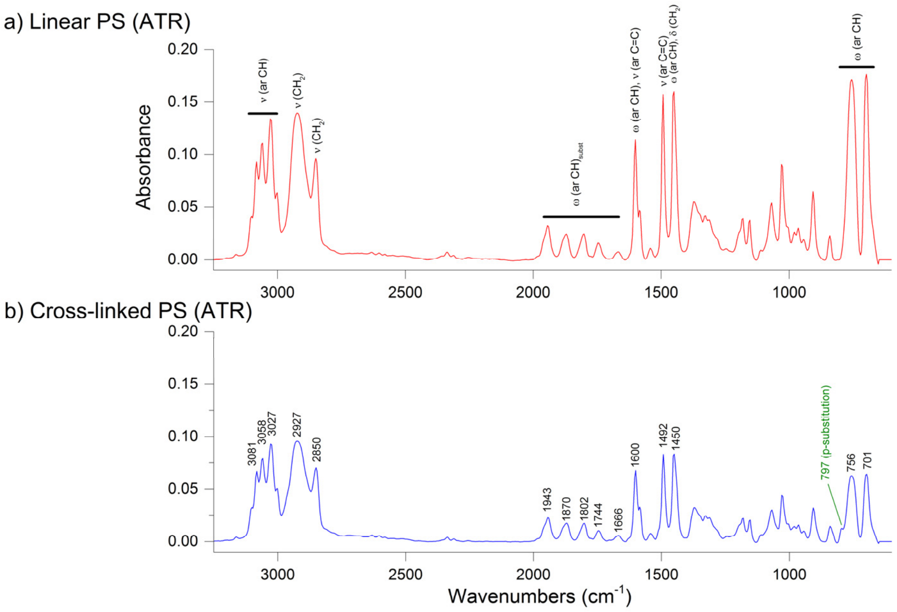

Figure 11. *FT-IR spectra acquired in ATR mode of the two commercial reference samples (provided by Goodfellow): a) linear PS, and b) cross-linked PS. The wavenumbers of the main vibrational bands and their assignments are reported.*

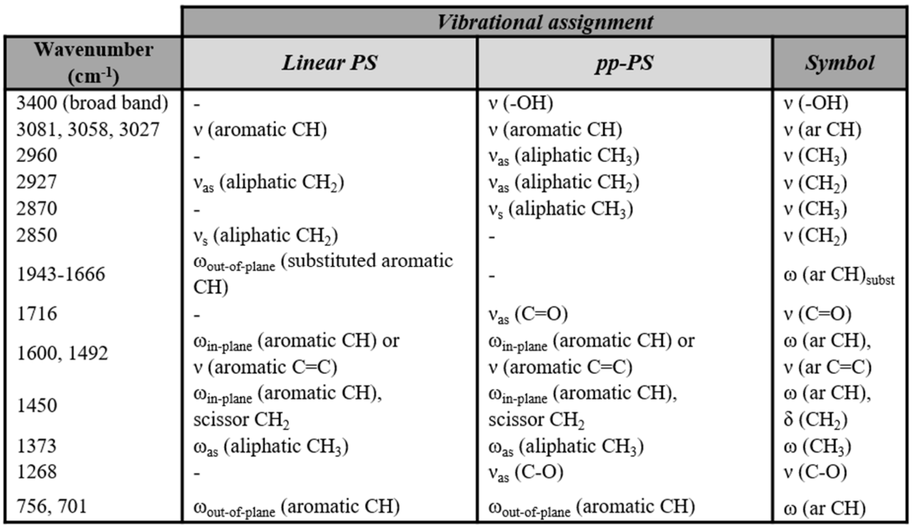

	Vibrational assignment		
Wavenumber (cm^{-1})	*Linear PS*	*pp-PS*	*Symbol*
3400 (broad band)	-	ν (-OH)	ν (-OH)
3081, 3058, 3027	ν (aromatic CH)	ν (aromatic CH)	ν (ar CH)
2960	-	ν_{as} (aliphatic CH_3)	ν (CH_3)
2927	ν_{as} (aliphatic CH_2)	ν_{as} (aliphatic CH_2)	ν (CH_2)
2870	-	ν_s (aliphatic CH_3)	ν (CH_3)
2850	ν_s (aliphatic CH_2)	-	ν (CH_2)
1943-1666	$\omega_{out\text{-}of\text{-}plane}$ (substituted aromatic CH)	-	ω (ar CH)$_{subst}$
1716	-	ν_{as} (C=O)	ν (C=O)
1600, 1492	$\omega_{in\text{-}plane}$ (aromatic CH) or ν (aromatic C=C)	$\omega_{in\text{-}plane}$ (aromatic CH) or ν (aromatic C=C)	ω (ar CH), ν (ar C=C)
1450	$\omega_{in\text{-}plane}$ (aromatic CH), scissor CH_2	$\omega_{in\text{-}plane}$ (aromatic CH), scissor CH_2	ω (ar CH), δ (CH_2)
1373	ω_{as} (aliphatic CH_3)	ω_{as} (aliphatic CH_3)	ω (CH_3)
1268	-	ν_{as} (C-O)	ν (C-O)
756, 701	$\omega_{out\text{-}of\text{-}plane}$ (aromatic CH)	$\omega_{out\text{-}of\text{-}plane}$ (aromatic CH)	ω (ar CH)

Table 4. *IR assignments of the main characteristic bands of the reference sample, linear PS, and the pp-PS films.*[5]

Both bands of the mono-substituted aromatic ring at 756 cm^{-1} and 701 cm^{-1} are unequivocally identified, in addition to the so-called "five aromatic finger" bands between 1943 and 1666 cm^{-1}. They are assigned to the out-of-plane bending deformation of the mono-substituted aromatic ring. Thus, these overtones tend to disappear in PS derivatives like P4MS, chosen as additional reference for the SIMS analysis. The related IR spectrum of the P4MS is illustrated in **Figure S4** (§6.9 of supporting information). Furthermore, the bands at 1492 and 1450 cm^{-1} appear in the IR spectrum, due to the vibration of the aromatic C=C and the in-plane phenyl-ring bending mode (also the scissoring of the CH_2), respectively. Going towards higher wavenumbers, specifically at 3027 and 2927 cm^{-1}, the aromatic CH and aliphatic CH_2 stretchings are found. These particular IR features of the PS have been compared with those identified for polystyrenes (different source and sample preparation) used as references in other works on pp-PS films, such as those conducted by Retzko et al.,[19] and Chen et al.[20] This comparison confirms, once again, after the XPS analysis, the adequacy of the linear PS as reference for this study. The polymer is also lacking oxidation, as demonstrated by the absence of the typical IR bands associated to O-based functional groups, such as e.g. the C=O asymmetrical vibration at 1716 cm^{-1} or the C-O asymmetrical vibration at 1268 cm^{-1}. Concerning the second reference, the cross-linked PS, the relative FT-IR spectrum looks extremely similar to the previous one. Indeed, the unique difference concerns the appearance of a small vibrational band at 797 cm^{-1} (highlighted in green in Figure 11.b). This wavenumber shift of the band assigned to the out-of-plane bending of the aromatic ring could be attributed to a poly-substitution that takes place during the cross-linking of the polymer, when using 1-2% of DVB. In particular, this could indicate the para-substitution of the aryl groups in the polystyrene structure, as already known in the IR literature for aromatic compounds.[21,22] However, insights about the presence of PEG-like aliphatic moieties in the PS network, as hypothesized in XPS, are hard to extract. In fact, vibrational bands related to CH_2-O- should clearly appear around 1200 cm^{-1}. Generally, no presence of oxidation is pointed out by IR analysis, conversely to the XPS results on the cross-linked PS presented in the previous section and in Merche's thesis.[6]

Figure 12 depicts the IR spectrum of the styrene monomer (from NIST library), in order to look at the main differences between the monomer and the resulting polymer before studying the pp-PS films deposited by DBD. The styrene monomer lacks only the aliphatic saturated CH vibrational bands. As a consequence, styrene and PS infrared spectra share absorption peaks related to the aromatic CH, as well as the aliphatic unsaturated CH. The latter can occur at the same wavenumber range of aromatic CH or C=C (3010-3100 cm^{-1}, 1620-1680 cm^{-1}, and 675-1000 cm^{-1}).[5] Thus, a noticeable difference consists in the absence of the aliphatic saturated CH stretchings between 2850 and 2927 cm^{-1}, in addition to the vinyl (-CH=CH_2) stretchings at 1640 cm^{-1}, with respect to the spectrum recorded for the linear PS. These differences are clearer in the IR spectrum of the styrene monomer (in transmittance) reported in **Figure S5**.[23]

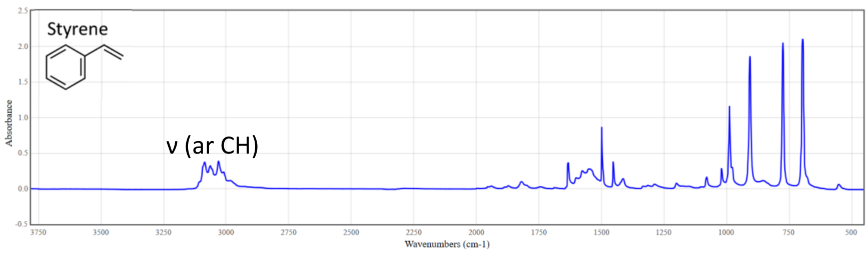

Figure 12. *IR spectrum of the styrene monomer taken from NIST Chemistry WebBook.*[24]

In **Figure 13**, the pp-PS films synthesized at different plasma powers are shown. For the sake of clarity, only two pp-PS deposits are reported (Figure 13.a): pp-PS/30W, that represents the plasma-polymer deposited at the lowest power analyzed successfully by IR, and pp-PS/80W, which constitutes the hardest power condition in this investigation. These two infrared spectra are compared qualitatively with the one of the linear PS depicted by a red solid line in the same figure (Figure 13.b). It is worthy to notice that the spectral range for the linear PS is shorter, thus no information can be derived from 650 to 500 cm^{-1}.

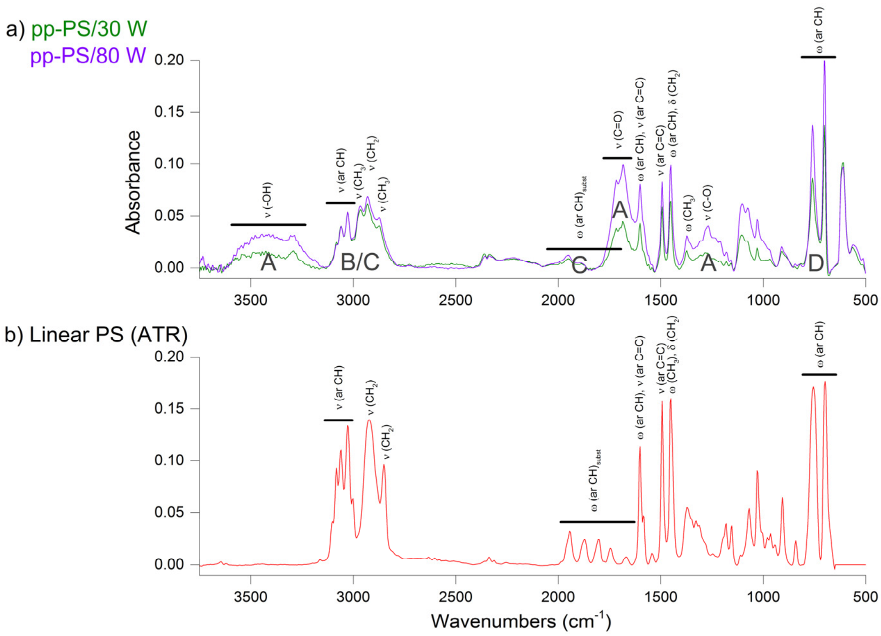

Figure 13. *a) FT-IR spectra acquired in transmission mode of two pp-PS films obtained at 30 W and 80 W, respectively. b) IR-ATR spectrum of the commercial reference, linear PS. The main vibrational bands are identified.*

The comparison of the pp-PS films (Figure 13.a) with the styrene monomer (Figure 12) points out that the plasma-polymer is well synthesized. Indeed, one can observe the appearance of the aliphatic saturated CH stretchings between 2850 and 2927 cm^{-1}, which are absent in the case of the monomer. Furthermore, one can observe the absence of the absorption bands characteristic of the vinyl group, such as the two strong bands at ~1000 and ~900 cm^{-1} (**Table S1**, and Figure 12). However, the presence of traces of the free monomer cannot be ruled out, since the plasma-polymer films release a strong odor of styrene even after several days from their synthesis.

At a first glance, the main finger-printing IR bands of the polystyrene are present in the IR spectra of the pp-PS films. This constitutes a further proof of that plasma polymerization of the styrene monomer took place. However, some remarkable differences between the pp-PS and the conventionally polymerized PS exist.[5] They are discussed following the order of appearance proposed in Table 4:

A. The pp-PS appears oxidized at all the plasma powers, as already shown by the XPS results. This can be stated because of the presence of absorption peaks associated to O-based functionalities, such as the C=O and C-O stretching bands at 1716 and 1268 cm^{-1}, respectively. Also a broad band around 3400 cm^{-1}, associated to -OH stretching, is present in the whole plasma-polymer series. However, based on the correlation table of §6.9 (Table S1), it is more likely that this band derives from the presence of H_2O in the plasma films which are involved in H-bonds. Moreover, the bulk oxidation demonstrated by IR characterization seems to be caused substantially by an O-uptake occurring in the plasma reactor, rather than by post-polymerization reaction of the remaining radical sites trapped in the polymer film with the atmospheric O_2. This hypothesis will be confirmed by SIMS depth-profiling.

B. Concerning the spectral range of the aliphatic saturated CH stretchings from 2960 to 2850 cm^{-1}, two new peaks appear in the pp-PS films with respect to the linear PS due to ν_{as} (aliphatic CH_3) and ν_s (aliphatic CH_3), and respectively at 2960 and 2870 cm^{-1}.[5] This represents an insight about the strong presence of methyl groups, totally unexpected for the conventional PS, where the $-CH_3$ constitutes solely chain ends of long linear macromolecules. Also in the case of polystyrene at low M_w, like the one reported in **Figure S2**, this infrared feature is totally missing. A plausible explanation of the $-CH_3$ presence in the pp-PS films, also observed for PS synthesized at lower pressures,[19,20,25,26] is represented by the methyl-substitution or $-CH_3$ grafting (often indicated in the literature as branching)[5]. It is likely that $CH_3\cdot$ radicals are formed in the plasma-induced fragmentation of the monomer, and then they recombine with radical sites on the aliphatic chains. Prohaska et al. hypothesized more specifically a structure for the pp-PS films similar to poly (α-methyl styrene) or poly (β-methyl styrene), with a certain degree of cross-linking (compare with the 3100-2850 cm^{-1} region of the IR spectrum of PAMS in **Figure S3**). Additionally, in the literature of pp-PS films synthesized in very similar plasma conditions,[5] the decrease of the ν_{as} (aliphatic CH_2) at 2927 cm^{-1}, as well as the disappearance of the ν_s (aliphatic CH_2) at 2850 cm^{-1} is reported.[5] This could be ascribed to several factors, such as unsaturation, H abstraction, cross-linking, grafting of oxygen or -CH_3 on the aliphatic moieties of the polymer chain.[5] Nevertheless, in the present study, any observation about those two vibrational bands would need to be verified by a peak decomposition procedure, which was not performed. Anyway, in the specific case of unsaturation, the alkene absorption peaks appear in the same wavenumber range as the aromatic ones (as previously mentioned). This makes the discrimination of unsaturation from aromaticity problematic.

C. Another peculiarity of the pp-PS deposits concerns the intensity decrease of the vibrational bands of the aromatic CH above 3000 cm^{-1} compared to those of the aliphatic CH below 3000 cm^{-1}, accompanied by the decrease of the “five aromatic finger” bands between 1943 and 1666 cm^{-1}. They represent CH bending deformation of mono-substituted aromatic rings. This can be partly ascribed to the baseline correction. However, this observation can be related to the partial destruction of the phenyl groups of the precursor in the plasma, in addition to a partial substitution of the aromatic rings as a consequence of cross-linking, for instance.

D. Prevalence of mono-substitution of the aryl groups as indicated by the $\omega_{out\text{-}of\text{-}plane}$ (aromatic CH) at 756 and 701 cm^{-1}. Indeed, the IR spectral region comprised between 1000 and 700 cm^{-1} provides insights about the substitution of aromatic compounds (refer to Table S1, section of the mononuclear aromatics). So, for instance, the para-substitution of the P4MS determines the presence of $\omega_{out\text{-}of\text{-}plane}$ (aromatic CH) at 816 cm^{-1} (see Figure S4). However, the possibility of partial poly-substitution in the pp-PS deposits cannot be ruled out. Retzko et al. observed a band occurs at 584 cm^{-1}, which could be interpreted as a ring deformation vibration of a poly-substituted aromatic ring based on reference.[19] This band is not present in the pp-PS films prepared in this work. Only a band at 613 cm^{-1} occurs in this case of study, that is interpreted as CH_3 vibration by Li et al.[26] However, this absorption band is not reported in the literature for the ethylbenzene,[27] thus not identified in Table 4.

To some extent, an internal comparison of the pp-PS series was attempted. According to the work carried out by Prohaska et al.,[25] the ratio of the peak heights of the ν (aromatic CH) at 3027 cm^{-1} to the $ν_{as}$ (aliphatic CH_2) at 2927 cm^{-1} (2930 cm^{-1} in their study) (A3027/A2927) could be used as an indicator of the bulk aromaticity. Here, the following A3027/A2927 values of 0.957, 0.961, 0.875 and 0.779 can be found for the linear PS, cross-linked PS, pp-PS/30W and pp-PS/80W. Therefore, the bulk aromaticity indicator of the two reference samples is very similar, while it decreases progressively with increasing the plasma power. This could suggest that increasing the plasma power, more phenyl rings of the monomer are destroyed to form a cross-linked structure, which is more difficult to dissolve (e.g. in acetone or methanol). Prohaska et al. proposed another ratio in order to compare the pp-PS films, that is the ratio of the $ν_{as}$ (aliphatic CH_3) at 2960 cm^{-1} to the $ν_{as}$ (aliphatic CH_2) at 2927 cm^{-1}, more simply indicated as A2960/A2927. In this case, the methyl group substitution of the polymer chains is expressed by the ratio A2960/A2927. In this investigation, A2960/A2927 values go from 0.91 to 0.88 with increasing the injected power from 30 W to 80 W. This trend could be difficult to interpret without a proper peak decomposition procedure. Indeed, A2960 is expected to increase from the SIMS results, but apparently A2927 increases also in the way to result in an overall diminution of the ratio. However, the trend of A2927 in the investigated plasma-polymer series cannot be known by normalization, because of the thickness uncertainty plus the lack of an internal reference in their IR spectrum.

Finally, in order to get insights about the polymerization degree of the pp-PS films deposited by DBD, it was decided to carry out GPC analysis. Moreover, the plasma-synthesized films are not oily and sticky in contrast with the deposits obtained at high pressures or low power levels,[20,28] suggesting that they are cross-linked. A picture of a pp-PS film on silicon was provided in Figure 10.

6.5. GPC analysis of pp-PS films

Gel permeation chromatography (GPC) was kindly conducted by the research team of Professors J.-F. Gohy and C.-A. Fustin at UCL. Only two pp-PS films deposited at different plasma powers were selected for the GPC characterization, i.e. pp-PS/30W and pp-PS/60W. Each polymer film on Si substrate was immersed in toluene (Sigma-Aldrich, purity ≥99.71%) for 16 hours, and heated at 40 °C to favor the dissolution. Then, the silicon substrate was removed from the solvent, even if the wafer was still covered by a polymer deposit. The solution was concentrated, then dried. A new solution was prepared in dimethylformamide (DMF) with a concentration of 1-2 mg/mL. The solution was filtered prior the GPC analysis with a 0.2-µm Teflon filter, in order to remove any dust particles.

Molecular weights (M_w) of the polymers were measured on an Agilent gel permeation chromatography system equipped with an Agilent 1100/1200 pump (35 °C; eluent: DMF; flow rate of 1 mL/min), an Agilent differential refractometer and two PSS GRAM columns (beads 10 µ; porosity of column 1: 1000 Å; porosity of column 2: 100 Å). The calibration was performed using polystyrene standards.

The chromatogram of the solution obtained from the pp-PS film deposited at 30 W is illustrated in **Figure 14**.

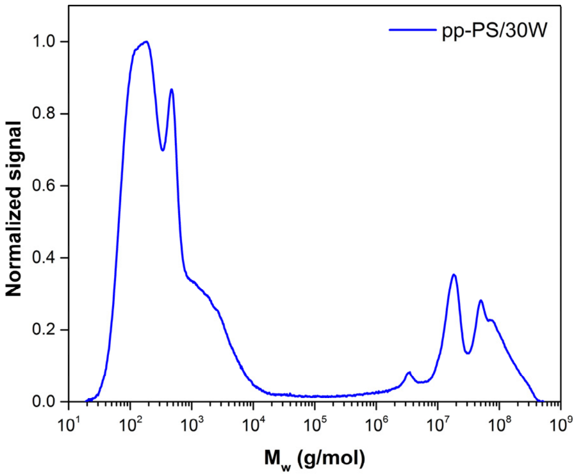

Figure 14. *GPC chromatogram of the solution obtained from the pp-PS film deposited at 30 W. Two main weight distributions can be distinguished at molecular weight below 1 x* 10^3 *g/mol, and above 1 x* 10^6 *g/mol.*

Two main weight distributions can be distinguished. The first molecular weight distribution below 1 x 10^3 g/mol is essentially constituted of oligomers ranging from 2 to 10 repeating units of PS, and traces of monomer. Whereas, the second main weight distribution above 1 x 10^6 g/mol is composed of long polymer chains (up to ~10000 repeating units), linear or cross-linked. However, only qualitative information about the polymerization degree can be extracted from this GPC analysis, and the reason is two-fold: 1) the solubility of the sample is likely very limited, so that the relative chromatogram is not fully representative of the polymer structure under investigation, and 2) the pp-PS structure is not well known and it can be only assimilated to the one of the conventionally polymerized PS. On the other hand, the GPC analysis demonstrates the presence of oligomers in the pp-PS/30W specimen.

The higher population of oligomers compared to that of long polymer chains (cf. Figure 14) can be explained by the fact that smaller chains can be more easily desorbed from the polymer matrix. In addition, it can be presumed that the weight distribution above 1 x 10^6 g/mol does not represent the actual polymer network, that instead remains on the support after prolonged immersion in the solvent, as shown in **Figure 15**.

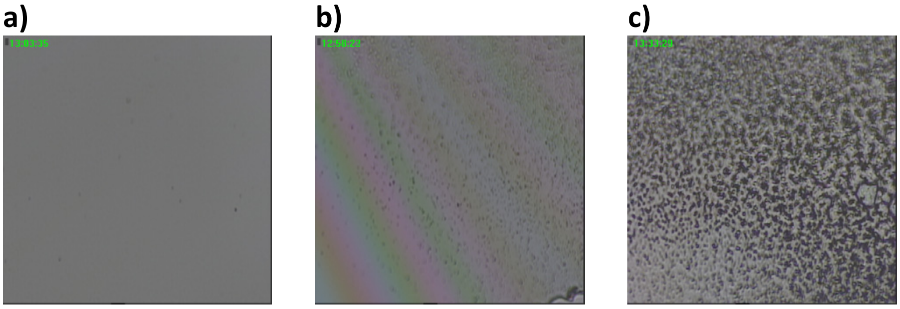

Figure 15. *Pictures of the surface areas (height x width: 790 µm x 865 µm) of the sample pp-PS/60W selected for SIMS depth-profiling, before immersion in toluene (a), and after partial dissolution and/or abstraction of the plasma-deposited film (b, c). Pictures b and c also show the development of a differential degree of porosity on the surface of the plasma film.*

Here, one can observe the remaining polymer deposit on the Si substrate after partial dissolution and/or abstraction in toluene for 16 hours, which shows the appearance of a certain degree of porosity. SIMS depth-profiling was carried out on areas of different topography of this polymer deposit. The mass spectra reconstructed from the inner layers of the same polymer film, before and after immersion in the solvent, were almost identical. SSIMS of the oligomers contained in the toluene solution after deposition onto clean Si substrates was tried too. However, this analysis is very sensitive to minimal levels of organic surface contamination of the support used, thus the results are not reliable. In the case of the pp-PS film synthesized at 60 W, the related chromatogram (not shown) looks very similar to the one reported in Figure 14, except a smaller (apparent) fraction of the polymer chains with $M_w > 1 \times 10^6$ g/mol. However, further comparisons of the two plasma films analyzed in this section are not possible, since the relative percentage of dissolved polymer is unknown and probably very limited.

In conclusion, the GPC characterization of the two investigated pp-PS films demonstrates that the styrene monomer is well polymerized in the plasma at (sub)-atmospheric pressure. Indeed, GPC indicates the formation of a partially cross-linked polymer network (insoluble in the standard conditions applied for the dissolution of high M_w polystyrenes, cf. §4.2.3), in which an undetermined percentage of oligomers remains trapped.

6.6. SIMS characterization of pp-PS films

6.6.1. Introduction to bulk-like mass spectra

The main strong point of the present SIMS characterization of plasma-polymerized polystyrene coatings consists in the replacement of the more classical SSIMS spectra[29] with what will be called "bulk-like" mass spectra of the investigated polymers. The bulk-like SIMS spectra are made possible thanks to the recent development of gas cluster ion beams (GCIB) as sputter sources for organic/polymer materials. Indeed, the resulting depth-profiling measurements show the evolution of the chemical structure of the plasma-synthesized polymer along the third dimension. This permits to identify the steady state region of the characteristic structure-related fragments, where most of the phenomena occurring near the surface, like for instance air contamination,[30] post-polymerization oxidation[31,32] or segregation of low molecular weight chains,[30] can be safely disregarded. As a matter of fact, a ToF-SIMS depth-profile consists in a 3D matrix, where each voxel represents a full mass spectrum. This data matrix can be computer processed to give, for example, the cumulative mass spectrum of a certain depth region (or volume) of interest. In this study, it is the sub-surface region of the plasma-deposited films, in which the chemical structure appears to be constant. Because the thickness of these pp-PS deposits is well above the scale where nanoconfinement phenomena are observed, one can assimilate this SIMS-reconstructed region to the bulk material. Hence, the expression "bulk-like" to designate the related mass spectra. As a consequence, this novel approach allows the SIMS, typically known as a surface-sensitive technique, to be compared to some bulk techniques, such as the IR spectroscopy discussed previously (§6.4).

In this work, the depth-profiles were performed by sputtering the samples with 10 keV Ar_{3000}^+ projectiles. The reconstructed bulk-like mass spectra, obtained using 30 keV Bi_5^+ ions, are expected to be more representative of the film chemistry during the growth process in the plasma than those acquired from the surface. In that respect, a striking example is given by the commercial reference cross-linked PS, whose positive ion mass spectra of the surface and the inner layers (simply indicated as bulk) are reported in **Figure 16**. It can be observed that, at the specimen surface, the specific fragmentation pattern of polystyrene[33] (cf. the bulk mass spectrum) is covered by an ill-identified organic contamination, as suggested by the low mass aliphatic saturated ion peaks (e.g. $C_2H_5^+$ at m/z 29, $C_3H_7^+$ at m/z 43, and $C_4H_9^+$ at m/z 57), in addition to the presence of PDMS. The latter surface contamination is indicated by a series of specific ion fragments, such as $[Si(CH_3)_3]^+$ at m/z 73, $[Si_2O(CH_3)_5]^+$ at m/z 147, $[Si_3O_3(CH_3)_5]^+$ at m/z 207, and so on.[34] The main characteristic fragments of PDMS are labelled on the surface mass spectrum of the cross-linked PS in Figure 16. When eroding with large Ar clusters, the characteristic PS fragmentation starts to emerge. So, for instance, the PDMS ion $[Si_3O_3(CH_3)_5]^+$ at m/z 207.032 does not interfere anymore with the characteristic ion $C_{16}H_{15}^+$ of the polystyrene at m/z 207.117. This sample exemplifies a case of surface contamination. Nevertheless, more complex situations are envisaged in the outermost layers of plasma-synthesized polymers. In this context, an important achievement of the retrospective analysis of the acquired ToF-SIMS rawdata consists in the discrimination of the O-uptake occurring when the specimen is extracted from the plasma chamber. This permits to focus exclusively on the oxidation of the growing film. In addition, the organic contamination of the surface, inevitably present because SIMS characterization is performed ex-situ, can be definitively disregarded.

For the sake of simplicity, from now on the terminology "bulk-like" used to describe the reconstructed mass spectra from a specific depth region of the investigated polymer films will be omitted.[i] Indeed, all the SIMS data presented in this chapter derive from the same protocol of retrospective analysis of the SIMS rawdata obtained by depth-profiling. However, the distinction between surface and bulk-like mass spectra needs to be kept in mind when one desires to compare the SIMS results of this chapter with those reported up to now in the literature (only relating to the uppermost layer of the specimen).

---

[i] The superscript (*) will be added to the term "mass spectrum" (= mass spectrum*) only in this chapter, to remind that one is dealing with bulk-like mass spectra, and not SSIMS spectra.

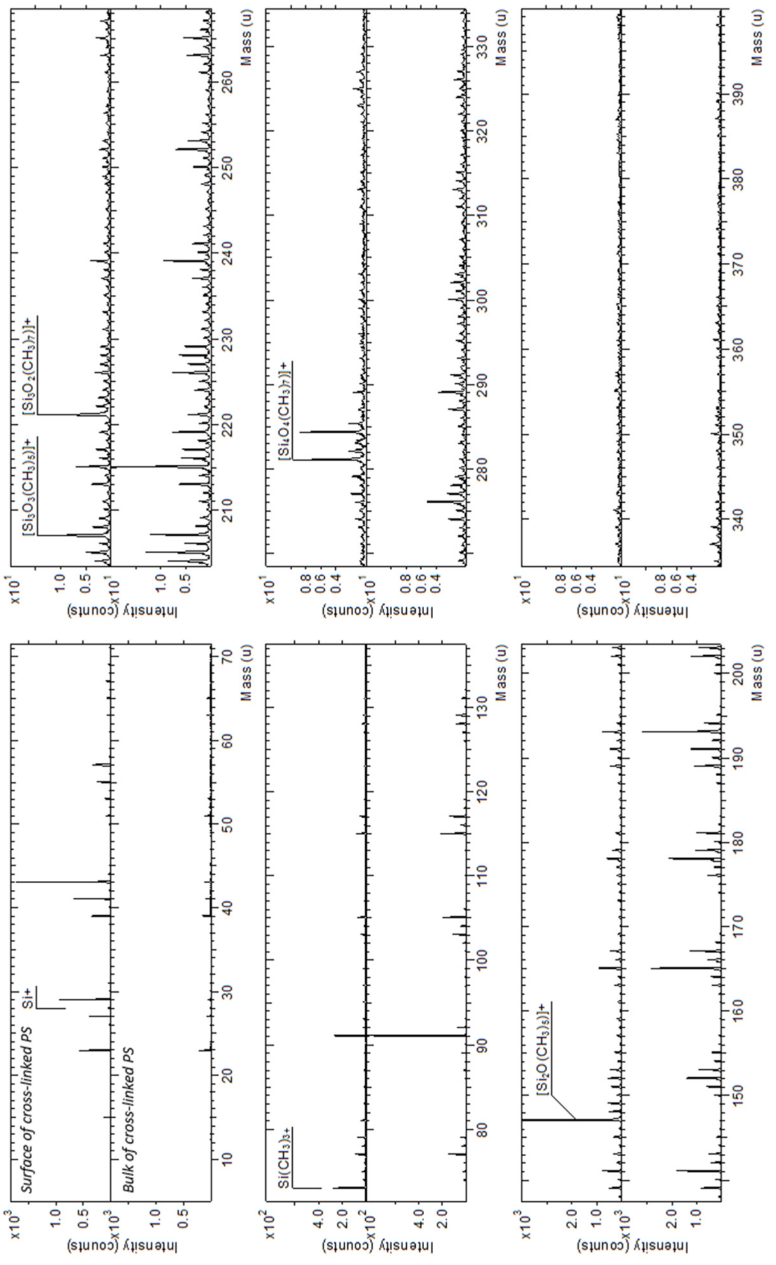

Figure 16. *SIMS positive ion mass spectra of the surface and the bulk (after a 10 keV* Ar_{3000}^+ *sputter fluence of 8.9 x* 10^{14} *ions/cm*^{2}*) of the commercial cross-linked PS. Note the surface contamination due to poly (dimethyl siloxane) (PDMS), whose most characteristic ions are labelled.*

6.6.2. Experimental

SIMS molecular depth-profiling experiments were performed using an ION-TOF TOF.SIMS 5 (Münster, Germany) instrument equipped with both Bi(Mn) Nanoprobe-LMIG (liquid metal ion gun) and Ar-GCIB (gas cluster ion beam) primary ion sources mounted at 45° to the surface normal. The secondary ions were collected by a reflectron-type time of flight analyzer perpendicular to the sample surface. The plasma-polymer samples were analyzed ex-situ by SIMS a few hours later their preparation. The polymer thin films deposited on silicon were insulated from the ground.

The molecular depth-profiles were acquired only in positive ion polarity, due to the poor hydrogen-related information provided by the negative ion polarity combined to the fact that insights about oxidation can be extracted from the positive ion mode. Moreover, the depth-profiling was performed in non-interlaced dual ion beam mode. 10 keV Ar_{3000}^+ ions were employed to sputter a 600 x 600 μm^2 area. The sputter current used for all the experiments was 2 nA (for the conventionally polymerized PS and the pp-PS), with the exception of the plasma films prepared at 10 W and 20 W. In the latter case, the sputter current had to be lowered to 0.3 nA, because of the small film thickness compared to the other plasma samples. A second pulsed beam of 30 keV Bi_5^+ ions (0.06 pA) was used to collect the mass spectra from a 200 x 200 μm^2 area, concentric to the sputtered surface. The cycle time was set at 200 µs. The measurements showed excellent reproducibility, so three profiles per sample were acquired in order to run PCA. A 20 eV electron flood gun was employed for charge compensation. For the non-interlaced mode, the timing of the different sequences of analysis, sputtering, and electron flooding were 3.28 s, 3.28 s, and 8.44 s, respectively (cf. §3.1.6). For the thickest plasma-deposited films (i.e. from 30 to 80 W), the total ion fluence cumulated over an entire profile for the 30 keV Bi_5^+ beam was of the order of 10^{12} ions/cm^2, while for the 10 keV Ar_{3000}^+ source it was kept around 5 x 10^{14} ions/cm^2. The ratio between the analysis and sputter fluences excludes a significant contribution of the Bi_5^+ beam in the etching process of the specimen.[35,36] In the above-mentioned sputter conditions, a crater depth of ~250 nm and ~190 nm were measured by a stylus profilometer in 3D-imaging mode for the pp-PS/40W and pp-PS/80W specimens, respectively. The mass resolution at m/z 29 ($C_2H_5^+$) was around 5000, which is good enough to resolve the hydrocarbon from the O-containing peaks at the low mass region.

The "bulk-like" mass spectra were obtained by means of a computer reconstruction of the SIMS rawdata over a sputter fluence of ~4 x 10^{13} ions/cm^2, ~3 x 10^{14} ions/cm^2, ~7 x 10^{14} ions/cm^2 for the pp-PS films polymerized at 10-20 W and 30-80 W, and the two commercial PS (linear and cross-linked), respectively. These depth-regions of the profiles show high stability of the most characteristic fragments of the PS (like for instance $C_7H_7^+$, $C_8H_9^+$, and $C_9H_9^+$), and some O-based molecular ions observed in the pp-PS deposits (such as CH_3O^+, and $C_2H_3O^+$). An example is given by the molecular depth-profile of the cross-linked PS illustrated in **Figure 17**, where thanks to the retrospective SIMS analysis the surface contamination due to PDMS can be disregarded.

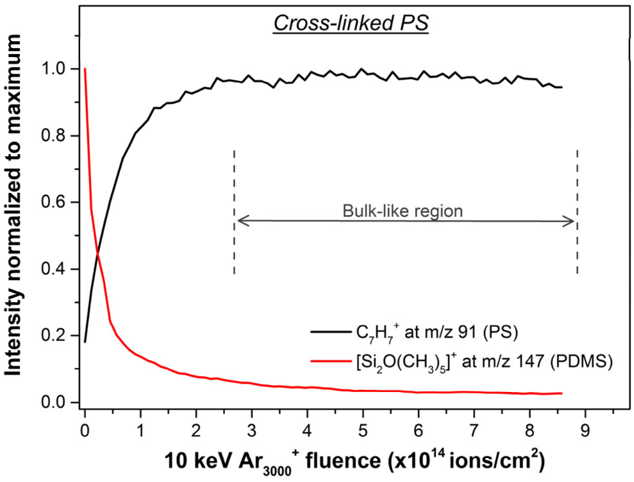

Figure 17. *Molecular depth-profiling of the cross-linked PS acquired in positive ion mode showing the "bulk-like" region, where the surface contamination (due to PDMS) can be disregarded.*

6.6.3. Results

6.6.3.1. Classical data treatment

In order to characterize the pp-PS films by ToF-SIMS, the linear PS (provided by Goodfellow, see Table 1 in §6.2.2) has been chosen as reference, because of its well-known chemical structure. Indeed, XPS and IR analyses have been carried out on such polymer, obtaining the results expected for a conventional polystyrene. On the contrary, the second reference sample, named cross-linked PS, also provided by Goodfellow, showed a relatively high oxidation of the surface by XPS (4.6%, cf. Table 3).

Figure 18 provides an overview of the positive ion mass spectra* of the sample set used for this SIMS study, i.e. the conventionally polymerized PS, linear (reference) and cross-linked, and the plasma-deposited PS, pp-PS/10W and pp-PS/80W. The two pp-PS samples shown in the figure represent the lowest and highest applied plasma powers. The m/z range from 0 to 250 amu is known as the "fingerprint region" of the mass spectrum, where the fragmentations of the PS repeat unit -(C_8H_8)- (repeat unit M_w = 104.1 g/mol) and the bigger moieties -$(C_8H_8)_n$- (with n = 2, 3, …) are combined. This m/z region represents a large fraction of the total intensity of the mass spectrum. So, a large amount of chemical information about the polymer can be extracted and, particularly, in terms of aromaticity, branching and cross-linking.

The linear PS, used as proper reference for this study (cf. Figure 18.a), shows all the characteristic secondary ions of the polystyrene reported in the literature. The most intense ion fragments per each $C_xH_y^+$ (x = 2, 3, 4, 5, …, and y = 1, …, 2x+1) series are at m/z 27, 39, 51, 63, 77, 91, 105, 115, 128, 141, 152, 165, 178, and 193. They are in good agreement with the SSIMS spectrum of PS illustrated in **Figure 19**, that reports also the related ion structures.[37] The slight differences in the fragmentation pattern of Figure 19 are mainly ascribed to the different analysis beam employed, that is a 4.5 keV Xe^+ ion source.[38] These characteristic secondary ions are very likely produced by re-arrangement reactions of species sputtered from the PS surface. However, the resulting ions are still PS structure-related fragments. Furthermore, the most intense ion fragment in the linear PS positive ion mass spectrum is the tropylium ($C_7H_7^+$) at m/z 91, because of its highest stability due to resonance effect. At a first glance, the cross-linked PS (cf. Figure 18.b) shows all the characteristic fragments of the polystyrene, in addition to the fact that the highest intensity peak is at m/z 91. However, differences in the relative intensities of these ion fragment peaks and the presence of oxidation already pointed out by XPS (see §6.3.2) can be remarked, as well as an intensity shift towards the m/z region below 65 amu (almost indiscernible in the proposed figure). Now, comparing the linear PS with the two pp-PS films (see Figure 18 a, c, and d), the above-mentioned characteristic molecular ions of PS are still traceable. The main difference between the conventionally polymerized PS and the films prepared in DBD concerns the inversed intensity ratio of the peaks 91^+ and 105^+, representing $C_7H_7^+$ and $C_8H_9^+$, respectively.

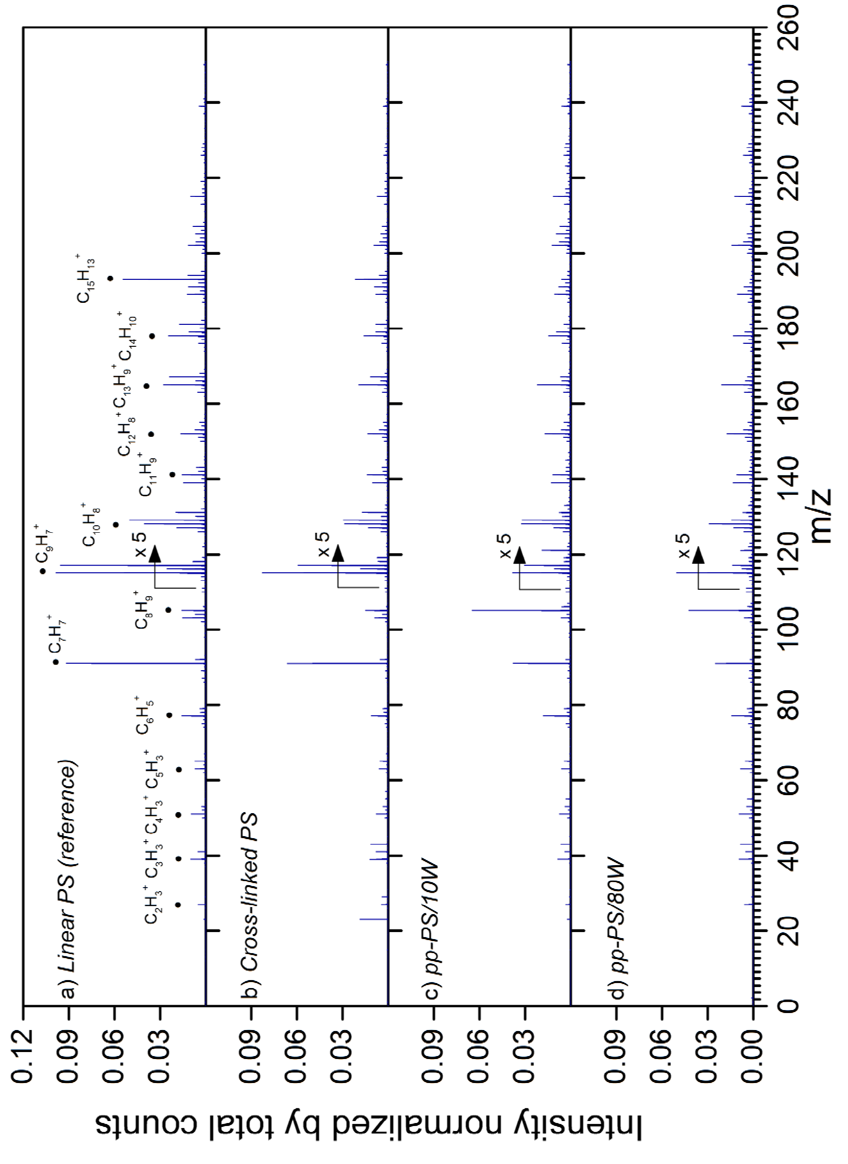

Figure 18. *Overview of the bulk-like positive ion mass spectra of the sample set used for this SIMS study, i.e. the conventionally polymerized PS, linear (reference) and cross-linked, and the plasma-deposited PS, pp-PS/10W and pp-PS/80W.*

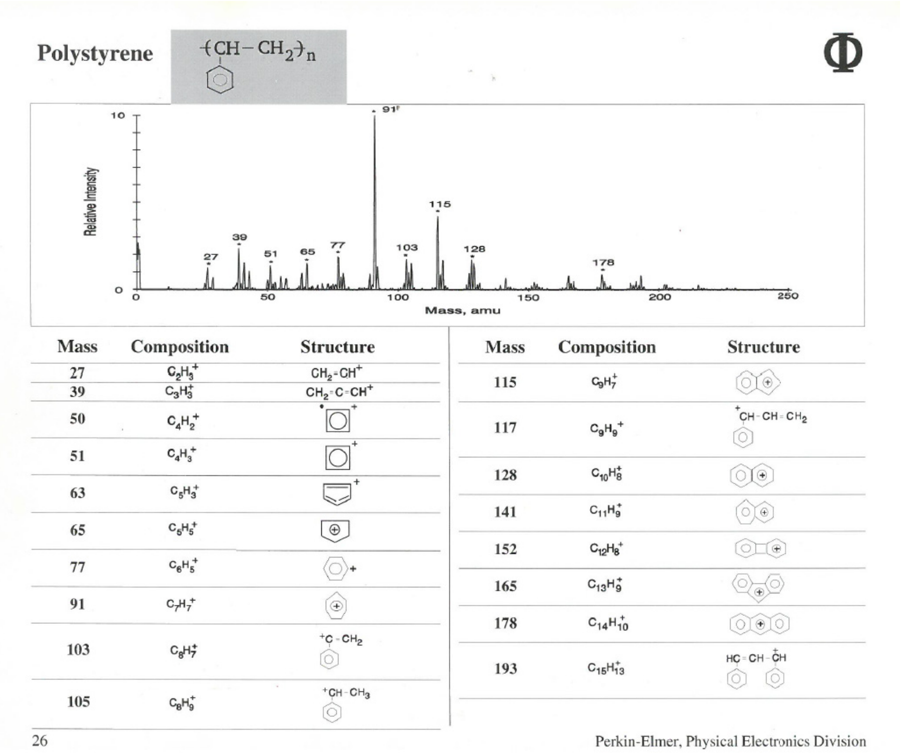

Polystyrene $-(CH-CH_2)_n-$

Mass	Composition	Structure
27	$C_2H_3^+$	$CH_2=CH^+$
39	$C_3H_3^+$	$CH_2=C=CH^+$
50	$C_4H_2^+$	
51	$C_4H_3^+$	
63	$C_5H_3^+$	
65	$C_5H_5^+$	
77	$C_6H_5^+$	
91	$C_7H_7^+$	
103	$C_8H_7^+$	$^+C-CH_2$
105	$C_8H_9^+$	$^+CH-CH_3$

Mass	Composition	Structure
115	$C_9H_7^+$	
117	$C_9H_9^+$	$^+CH-CH=CH_2$
128	$C_{10}H_8^+$	
141	$C_{11}H_9^+$	
152	$C_{12}H_8^+$	
165	$C_{13}H_9^+$	
178	$C_{14}H_{10}^+$	
193	$C_{15}H_{13}^+$	$HC=CH-\overset{+}{C}H$

26

Perkin-Elmer, Physical Electronics Division

Figure 19. *SSIMS spectrum in positive ion polarity of polystyrene, and the most characteristic secondary ions.*[37]

In the classical mass spectrometry literature, the $C_8H_9^+$ is postulated to be a methyl substituted of the tropylium ion.[39] This peculiar feature of the pp-PS positive ion mass spectra* reported in Figure 18 is observed in the overall plasma series, and it will constitute the keystone of the coming SIMS characterization. As in the case of the cross-linked PS, also the pp-PS deposits show O-uptake in their positive ion mass spectra*. For instance, in the m/z range from 0 to 210 amu, around 70 O-containing ion fragments are identified. However, other differences in the pp-PS mass spectra* are very subtle to be discerned by this preliminary analysis of the SIMS data. Thus, a more classical approach for the analysis of the SIMS positive ion mass spectra will be adopted. Indeed, several indicators of the structural properties of the coatings have been described in the SIMS literature, using generally ratios or normalized sums of secondary ion intensities, which are summarized in the feature paper published by Delcorte et al.[40] In this way, information concerning the degree of aromaticity, the branching and/or the cross-linking of the pp-PS films deposited at increasing plasma powers can be deduced. Such information has not to be intended in quantitative terms, since it derives from the comparison of the plasma-polymers with a known reference polymer, the linear PS.

A parameter that has been defined to evaluate the degree of aromaticity of polymers, such as the polystyrenes, consists in the sum of the normalized intensities of the aromatic fragments at m/z 77, 91, 105, 115, 128, 141, and 165.[41] More specifically, they represent all the secondary ions stabilized by resonance, starting from the single ring composed by six carbon atoms $C_6H_5^+$ at m/z 77. In the literature, another indicator is given by the intensity ratio of the ions $C_7H_7^+$ and $C_4H_7^+$ ($91^+/55^+$). It was proposed for the first time by Petrat et al. in the investigation of plasma-treated PS.[42] The choice of these two secondary ions is justified by the fact that the 91^+ represents the most characteristic ion of the polystyrene, as commented in Figure 18, and more generally of the aromatic polymers,[37] whereas the secondary ion $C_4H_7^+$ is one of the most intense in the aliphatic polymers.[34] Additionally, in the case of PS, the latter constitutes the aliphatic ion of the series $C_4H_y^+$ with the lowest degree of unsaturation, and simultaneously highest intensity. Both these indicators have been taken into consideration in this study. **Figure 20.a** depicts the sum of aromatics as a function of the plasma power, while **Figure 20.b** reports the ratio $C_7H_7^+/C_4H_7^+$. In both cases, for comparative purposes, the reference sample is shown on the left side of the graphs.

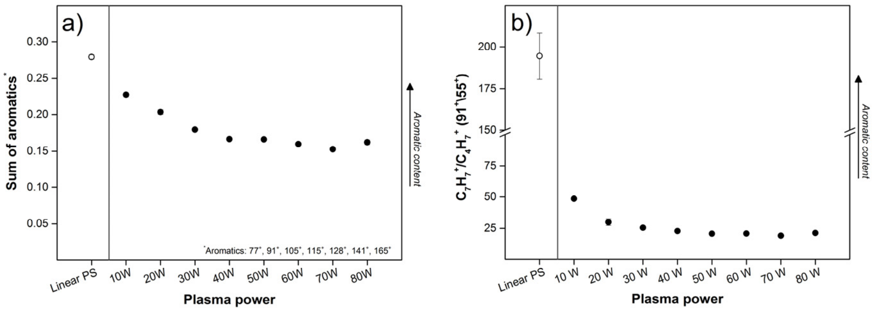

Figure 20. *Indicators expressing the integrity of the aromaticity in the pp-PS films compared to the linear PS as a function of the plasma power: a) Sum of the intensities of aromatics fragments normalized by total counts, and b) Intensity ratio* $C_7H_7^+/C_4H_7^+$.

The first indicator presented in Figure 20.a, and given by the sum of the intensities of the aromatic fragments, suggests a loss of the aromaticity content in the whole series of pp-PS deposits compared to the reference linear PS. Additionally, the aromaticity decreases gradually with increasing the plasma power from 10 W to 80 W. However, this decreasing trend of the aromatic content of the plasma-polymers as a function of the power injected in the discharge is the result of different contributions. Indeed, the intensity of 77^+ increases with the power, while those of 91^+ and 105^+ decrease. 115^+, 128^+, 141^+, and 165^+ remain constant along the investigated power range. Moreover, the relative intensity of these aromatics is higher for the linear PS, with the exception of the ions 77^+ and 105^+ that, instead, are more intense in the pp-PS films. In particular, the ion 105^+ is the most outstanding ion in all the mass spectra of those polymer films. Thus, the decreasing trend of the aromaticity indicator essentially mirrors the intensity drop of 105^+ and 91^+. The lower indicator values of the pp-PS films with respect to the linear PS can be explained by the lower relative intensities of 91^+, 115^+, 128^+, 141^+, and 165^+. Concerning the second indicator $C_7H_7^+/C_4H_7^+$ reported in Figure 20.b, it also suggests a decrease of the aromatic content of the plasma-polymer films compared to the conventionally polymerized counterpart, and with increasing power. Here, the final trend results from the decrease of 91^+ accompanied by the increase of 55^+, as expected from the definition of this SIMS parameter. This is in good agreement with the deductions based on the sum of aromatics, and more importantly with the XPS results (§6.3.2).

Insights about the cross-linking are hard to extract from the SIMS spectra. For instance, Oran et al. looked at the total secondary ion yield or total counts, in order to know the relative amount of the cross-linked character of a set of plasma-synthesized samples when varying the external plasma parameters.[32,43] In that work, it was taken into account that the emission probability of any secondary ion is a function of the chemical environment, phenomenon known as matrix effect. Nevertheless, the same conditions of SIMS analysis were supposed. Then, the total secondary ion yield is expected to decrease as the cross-linked character tends to increase.[44] However, the effects of the cross-linking and the branching are impossible to discern from each other. So, differences in total counts are interpreted indiscriminately in terms of branching and/or cross-linking. The corrected total counts of the positive ion mass spectra* of the pp-PS films are reported in **Figure 21.a**, as a function of the plasma power. Apparently, the branching and/or cross-linking increases with increasing power until reaching (roughly) the level of the reference linear PS at 80 W. However, any consideration based on this SIMS parameter is premature, considering the few elements known at this point of the SIMS investigation. Indeed, the total intensity of the mass spectra* of the plasma deposits may be influenced by the presence of oxidation, that moreover increases with the power, as pointed out by the XPS surface analyses (§6.3.2). This could determine an inversion between linear PS and pp-PS films, that could appear less branched and/or cross-linked (since the oxidation would enhance the probability of ionization of the latter samples). Moreover, other factors could influence the total counts, e.g. the polymerization degree. So, the GPC analyses indicated the presence of oligomers, that could induce an increase of the total intensity in the pp-PS samples with respect to the commercial linear PS (which contains oligomers too) if the relative amount is higher. However, the ratio of oligomers to the highly polymerized pp-PS remains unknown for the entire series of specimens. Another indicator of the cross-linked character is proposed by Oran,[43] and consists in the intensity ratio $C_7H_7^+/C_8H_9^+$ or $91^+/105^+$. Indeed, 91^+ and 105^+ are the most intense ions of the linear and plasma-polymerized PS, respectively. Thus, the first ion is attributed to a linear structure, whereas the second one to a more branched and/or cross-linked structure.

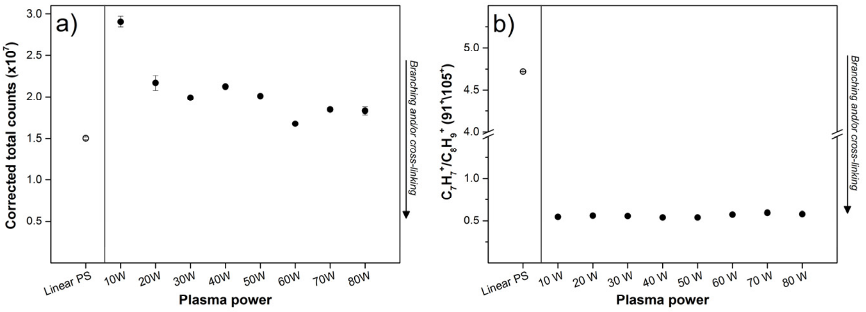

Figure 21. *Corrected total counts of the positive ion mass spectra* of the pp-PS films as a function of the plasma power (a), and the intensity ratio* $C_7H_7^+/C_8H_9^+$*(b). For comparison purposes, the reference linear PS is reported on the left side of the graphs.*

Now, in **Figure 21.b**, the linear PS looks less branched and/or cross-linked than the plasma-polymer series. Furthermore, the ratio $C_7H_7^+/C_8H_9^+$ remains constant with increasing the plasma power, because of the simultaneous decrease of both ions. On the contrary, this intensity ratio is expected to decrease with increasing the power, as a consequence of a more pronounced increase of 105^+ on the decrease of 91^+. This situation demonstrates properly that the investigation of the structural features of the plasma-synthesized polymers, such as aromaticity, branching and/or cross-linking, cannot be based on the mere comparison of selected peak intensities, ratios or sums of peak intensities. For instance, the effect of the oxidation on the ionization probability of the above-mentioned secondary ions 91^+ and 105^+ is unknown. So, a more systematic and scientist-independent data treatment is required, i.e. PCA. Before introducing the combined PCA/SIMS approach, some additional considerations about the fragmentation of the polymer chains and the presence of the monomer/dimer/trimer-related ions in the positive mass spectra need to be made.

Generally, the effects of branching and/or cross-linking in a polymer-based material determine an increase in the ratio of high mass fragments to low mass fragments.[43] For this reason, it was decided to compare the total intensities of the low and high m/z range of the "fingerprint" region of the positive ion mass spectra for the different pp-PS films, as shown in **Figure 22**.

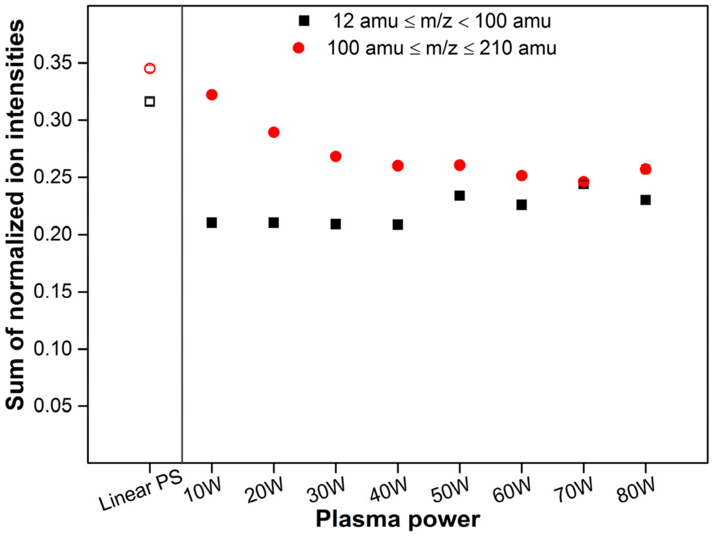

Figure 22. *Sum of the intensities normalized by total counts of the ion peaks in the m/z range from 12 amu to 100 amu (black squares), and from 100 amu (included) to 210 amu (red circles) for the pp-PS films, as a function of the plasma power. The reference sample is also depicted. Information about the polymer fragmentation is extracted.*

The low m/z range was fixed between 12 and 99 amu. So, it includes all the ion fragments from C^+ to the entire $C_7H_y^+$ series. This represents most of the sub-monomer mass region, and provides information about the repeat unit of the polymer, but also the eventual presence of contamination in the case of

SSIMS. In this study, spectral interferences due to surface contamination can be disregarded, thanks to the adopted protocol of reconstructed mass spectra (see §6.6.1). Instead, the high m/z range goes from 100 to 210 amu, and represents all the hydrocarbon fragments containing from 8 to 16 carbon atoms. Thus, it can be assumed as the oligomer mass region, in which the fragmentation of polymer chains ≥2 repeat units can be found.

Figure 22 shows a slight increase of the fragmentation of the pp-PS deposits in the low m/z region. It can be explained by the increase of the intensities of low mass $C_xH_y^+$ and $C_xH_yO^+$ ions, with the exception of 91^+. Ion $C_7H_7^+$ is responsible for the highest intensity of the reference PS sample in the mass range 0-100 amu, compared to the pp-PS specimens. On the other hand, the decrease of the fragmentation in the m/z region from 100 to 210 amu is essentially due to the decrease of the intensity of the $C_8H_9^+$ as a function of the plasma power. The gap between the pp-PS series and the linear PS is explainable by a higher intensity related to $C_xH_y^+$ ions of the latter in the oligomer region of the mass spectrum. The oxidation seems to be constant with increasing plasma power at high m/z ratio, and more pronounced in the sub-monomer region (in terms of number of O-based mass contributions).

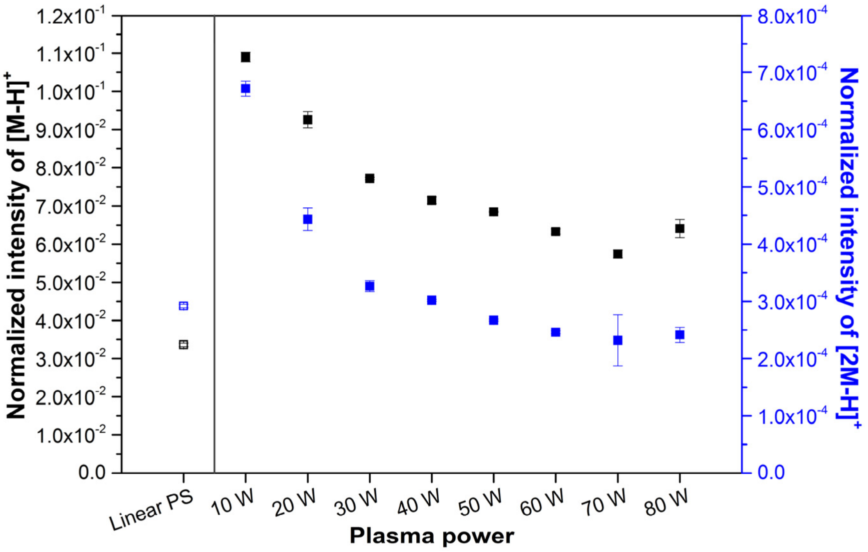

Figure 23. *Intensity of the protonated monomer (or repeat unit) of the polystyrene $[M+H]^+$ on the left y-axis (data in black) and intensity of the protonated dimer $[2M+H]^+$ on the right y-axis (data in blue) for the reference sample and the pp-PS deposits, as a function of the plasma power. The intensities are normalized by the total intensity of the mass spectrum*.*

Finally, **Figure 23** depicts the normalized intensity of the protonated monomer (black squares) and protonated dimer (blues squares) of PS. It was already mentioned that the 105^+ is the most intense ion in the plasma-polymer series. Furthermore, 105^+ decreases with increasing power. A similar behavior is observed for the dimer, whose intensity is lower in the linear PS compared to the pp-PS films synthesized at lower plasma powers. Instead, the trimer-related ion (**Figure 24**), or more specifically the deprotonated trimer $[3M\text{-}H]^+$ ($C_{24}H_{23}^+$ at m/z 311), is observed exclusively in the plasma-polymers obtained 10 and 20 W, in addition to the reference PS.

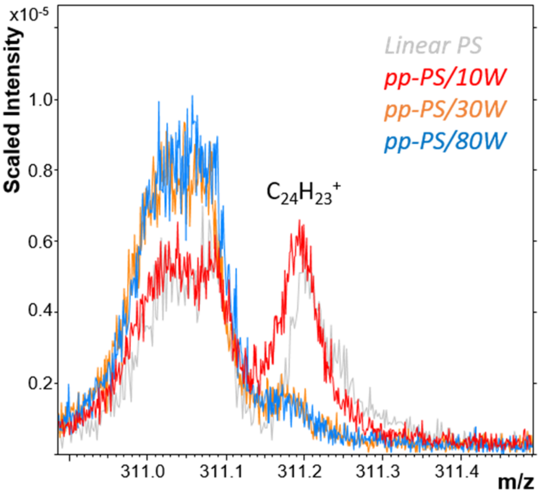

Figure 24. *Peak of the deprotonated trimer of the polystyrene* $[3M\text{-}H]^+$ ($C_{24}H_{23}^+$) *at m/z 311 for the reference linear PS (grey), and the pp-PS films deposited at 10 W (red), 30 W (orange), and 80 W (blue), respectively. The intensity is scaled by the total intensity of the mass spectrum*. Note that the ion* $[3M\text{-}H]^+$ *appears only in the linear PS and the plasma-polymer film prepared at 10 W.*

6.6.3.2. PCA study of pp-PS films and conventionally polymerized PS

Principal component analysis of the bulk-like positive ion mass spectra was conducted using the Spectragui code developed by NESAC/BIO (http://www.nb.uw.edu/). In order to perform the multivariate analysis, three molecular depth-profiles were acquired per sample, because of the high homogeneity of the plasma films. The calibration of the reconstructed mass spectra was based on the following PS ions: $C_4H_3^+$ (m/z 51), $C_5H_3^+$ (m/z 63), $C_6H_5^+$ (m/z 77), and $C_{10}H_8^+$ (m/z 128). Furthermore, a manual selection and integration of the peaks was made for the m/z range from 12 to 210 amu of the mass spectra* of the pp-PS films. The investigation of the chemical structure of the pp-PS films was first done by comparison with the conventionally polymerized counterparts, linear and cross-linked PS. In this case, the peak list consisted of ~170 hydrocarbon mass contributions, as well as ~70 O-containing secondary ions, since the pp-PS is oxidized. Then, in the PCA study of the plasma films, additional commercial polymers were included, namely poly (α-methyl styrene) (PAMS), poly (4-methyl styrene) (P4MS), and poly (4-vinylphenol) (PVP). Thus, in the latter case, the peak list was adjusted to the new set of samples, including 283 ions in the m/z range 12-210 amu. Before multivariate analysis, the dataset was normalized and mean-centered. The normalization to the total intensity of the reconstructed mass spectrum was performed in order to eliminate the variance produced by a systematic error due to the variation of the secondary ion formation efficiency, which depends on matrix effect, surface topography, charging effects and instrumental factors. The mean centering procedure ensures that the observed differences in samples were due to variations around the means and not to the variance of the means. The scores plots were obtained reporting each of the principal components versus the different samples of the given dataset (each one represented by three mass spectra*). The loadings plots were obtained reporting each of the principal components versus the mass-to-charge (m/z) ratio. In order to interpret the PCA results, loading thresholds have been set and carefully chosen in order to extract the most important variables (peaks) over the model. In fact, in each case, the chosen value assures that all the peaks (variables) having loading value under the threshold do not affect the samples (objects) arrangement in the scores plot, so they can be safely disregarded.

a. Study of the commercial samples "linear PS" and "cross-linked PS"

This first PCA aims for a better understanding of the chemical structure of the commercial cross-linked PS. Indeed, the XPS analysis (§6.3.2) pointed out a relatively high level of oxidation not related to surface contamination, totally unusual for the polystyrene. To this purpose, a comparison of the cross-linked PS with the reference linear PS is proposed. Furthermore, it is based on a peak list including all the hydrocarbon and O-based ion fragments in the m/z range from 12 to 210 amu.

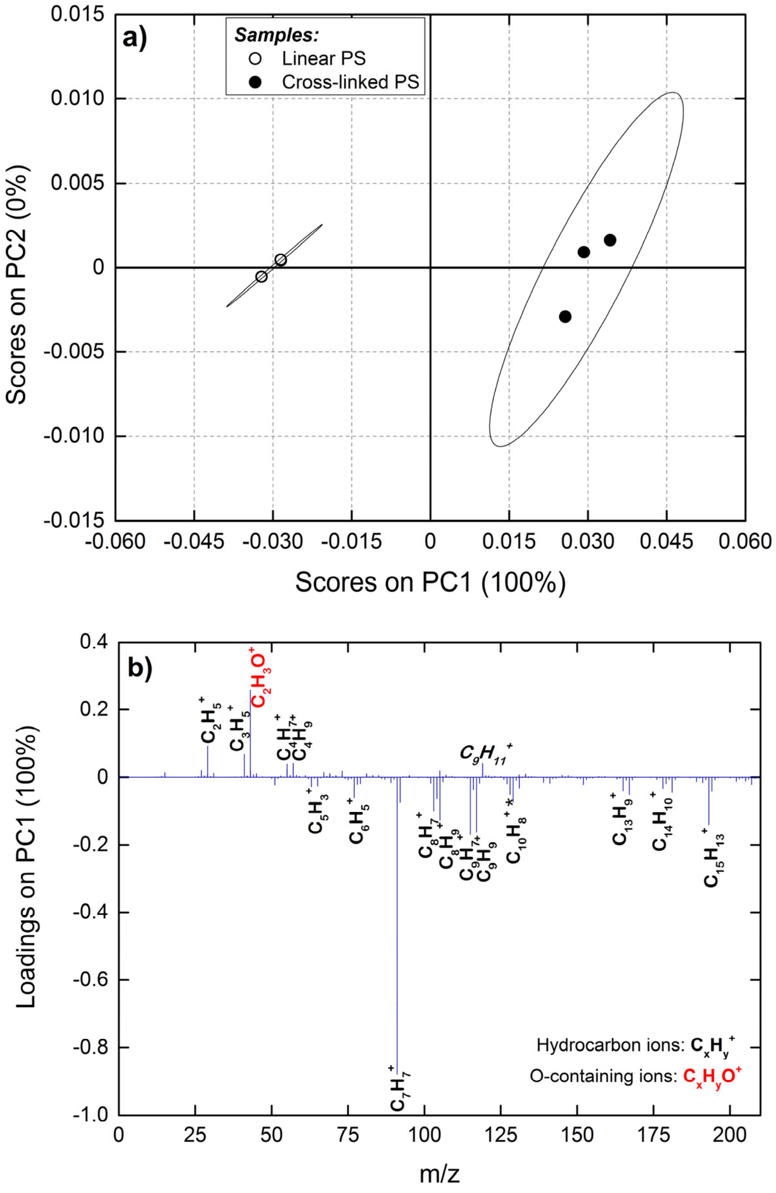

Figure 25. *a) PC2 versus PC1 scores plot obtained from the PCA applied to the ToF-SIMS positive ion mass spectra of the two commercial PS samples (linear and cross-linked). Three spectra have been acquired per sample. b) PC1 (100%) loadings plot with a threshold set at ±0.025. Only the most characteristic ion fragments of the polystyrene (within the fixed loading range) are reported in the graph. For a complete list of the loadings and the related secondary ions, one can refer to Table S2.*

Figure 25 shows the PC2 versus PC1 scores plot obtained from the PCA applied to the positive ion mass spectra* of the linear PS (open black circles) and the cross-linked PS (solid back circles). Three bulk-like mass spectra have been acquired per sample, because of the high reproducibility of the molecular depth-profiles. The ellipses reported in the scores plot represent a confidence limit of 95% for each polymer material. The cross-linked PS appears less homogeneous compared to the reference polystyrene.

PC1 discriminates the linear PS (negative scores) from the cross-linked PS (positive scores) (cf. Figure 25). The corresponding PC1 loadings plot is depicted in Figure 25. A loading threshold of 0.025 has been set in order to show the most influential ion fragments in the differentiation of the two samples. For the sake of simplicity, only the most typical secondary ions of the linear PS (loadings < 0) are indicated in Figure 25.[45] In other words, they are the most intense molecular ion fragment of each $C_xH_y^+$ series (with x=1, 2, 3, …, and y=1, 2, …, 2x+1), possessing an absolute loading value above the fixed threshold. A complete list of the most important PC1 loadings can be found in §6.9 (**Table S2**). In this PCA study, the ^{13}C-contribution to the different ion fragments has not been taken into account, since it does not bring essential information about the chemical and structural features of the investigated polymers. Concerning this contribution, only one example will be provided about the m/z 92.061 possessing a loading value of -0.073 (see Table S2), that counts two distinct mass contributions: $C_7H_8^+$ and $^{13}CC_6H_7^+$. According to the isotope cluster calculation, the abundance of the ions $C_7H_7^+$ (m/z 91), $^{13}CC_6H_7^+$ (m/z 92), and $^{13}C_2C_5H_7^+$ (m/z 93) is respectively of 92.7, 7.1, and 0.2. So, in the case of the linear PS, the main contribution to m/z 92.061 (8% of the $C_7H_7^+$ intensity) is attributed the ion $^{13}CC_6H_7^+$ (7%), and solely 1% to the ion $C_7H_8^+$. The appearance of the ion at m/z 92 in the negative loading list is linked to the fact that the related ion $C_7H_7^+$ is the most intense in the mass spectrum of the linear PS. Indeed, the reference linear PS is largely dominated by the tropylium ion ($C_7H_7^+$). In addition, the overall series of aromatics at m/z 77, 105, 115, 128, 141, and 165 characterizes the linear PS.[37] Thus, the peaks associated to the negative loadings illustrate the typical positive ion mass spectrum of the conventional polystyrene. On the other hand, the positive ion mass spectra* of the cross-linked PS are mainly dominated by the small O-containing ion $C_2H_3O^+$ (indicated in red), followed by a series of short aliphatic (almost) saturated ion fragments, such as $C_2H_5^+$, $C_3H_5^+$, and $C_4H_9^+$. The $C_2H_3O^+$ and $C_2H_5^+$ peaks (highest positive loadings) for the two commercial PS are depicted in **Figure 26 a,b**, whereas those of $C_7H_7^+$ and $C_9H_7^+$, associated to the highest negative loadings, are illustrated in **Figure 26 c,d**.

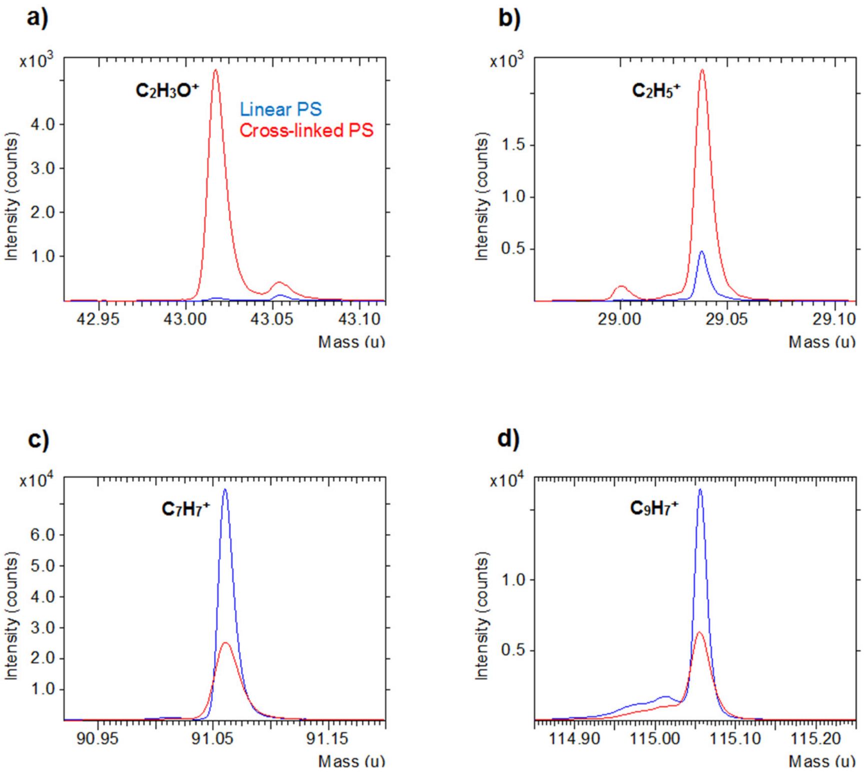

Figure 26. *Intensity of the secondary ions $C_2H_3O^+$, $C_2H_5^+$, $C_7H_7^+$, and $C_9H_7^+$ for the linear PS (blue) and cross-linked PS (red). The ions at m/z 43 and 29 (a, b) are related to the highest PC1 (100%) positive loadings of the PCA applied to the two commercial PS (linear and cross-linked), whereas the ions at m/z 91 and 115 (c, d) are related to the highest PC1 negative loadings (cf. Table S2).*

The positive ion mass spectra of the cross-linked PS show the classical signature of the polystyrene. All the aromatic ions are present, like for instance $C_7H_7^+$ and $C_9H_7^+$, but with lower intensity. However, the O-uptake suggested by the ion $C_2H_3O^+$ (highest positive loading) is confirmed by the fact that all the other oxidized fragment ions contained in the applied peak list possess also loadings > 0. When the loading threshold is lowered to 0.01, a series of O-containing ions with C_{1-5} and almost saturated can be found. The presence of additives containing oxygen atoms of relatively high molecular weight can be disregarded, since no molecular ions are identified at high m/z ratios of the acquired positive ion mass spectra (from 0 to 3000 amu).[ii] The last peculiar feature of the cross-linked PS concerns the ion $C_9H_{11}^+$ among the positive loadings > 0.025 (see Figure 25, where it is indicated in italic). This ion can be considered as an index of alkyl substitution of the aryl groups of the PS.[46] Indeed, if one looks at some poly (alkyl styrenes) mass spectra, such as those of the poly (2,4-dimethyl styrene) and the poly (2,5-dimethyl styrene) provided by the ION-TOF library, the peak at m/z 119 ($C_9H_{11}^+$) becomes the most intense one of the entire mass spectrum ($C_7H_7^+$: 25.06%, $C_9H_{11}^+$: 100%, and $C_7H_7^+$: 33.59%, $C_9H_{11}^+$: 100%, respectively)[iii].[45] All these observations can be summarized as follows: a) presence of small O-containing ions ($C_{1\text{-}5}$) with high H content, among them the most intense $C_2H_3O^+$, b) increased ratio of the small aliphatic ($C_{1\text{-}4}$) (almost) saturated ions to the aromatic ions, and c) increased intensity of the ion $C_9H_{11}^+$. They seem to be in rather good agreement with the synthesis of polystyrene in presence of a cross-linking agent, such as the divinylbenzene (DVB), as illustrated in **Figure 27**.[47] Indeed, the cross-linking induces an increase of the ratio of the aliphatic to aromatic fractions in the polymer structure, in addition to the introduction of di-substitution of the phenyl rings as demonstrated by the $C_9H_{11}^+$. Only the origin of the O-uptake remains unknown. However, one can state that the O-based functional groups are prevalently bonded to the aliphatic backbone of the polystyrene, as suggested by the ion $C_2H_3O^+$.

An additional PCA was run on the positive ion mass spectra* of both commercial polystyrenes by using a peak list made exclusively of hydrocarbon fragment ions. The aim of this study is to better understand the structural differences of the cross-linked PS with respect to the linear polystyrene, not related to the presence of oxidation pointed out by the first PCA. PC2 versus PC1 scores plot is reported in **Figure S6** (§6.9), where PC1 discriminates the linear PS (negative scores) from the cross-linked PS (positive scores). The most influential PC1 (almost 100% of the overall

---

[ii] It is very likely that the concentration of additives present in the commercial polymer is below the detection limits of the technique, so that they do not cause spectral interferences with the investigated polymer structure. In addition, it is worth noticing that additive molecules are known to segregate at the surface, where they could even evaporate in the UHV conditions required by the analysis. On the contrary, the SIMS measurements reported in this chapter concern the inner layers of the polymer samples (refer to §6.6.1), which consequently should be less influenced by the presence of such a molecules.

[iii] 11 keV Ar^+ ion beam was used to acquire the positive ion mass spectra of the alkyl-substituted polystyrenes. The samples were polymer thin films spin-coated onto silicon substrates.

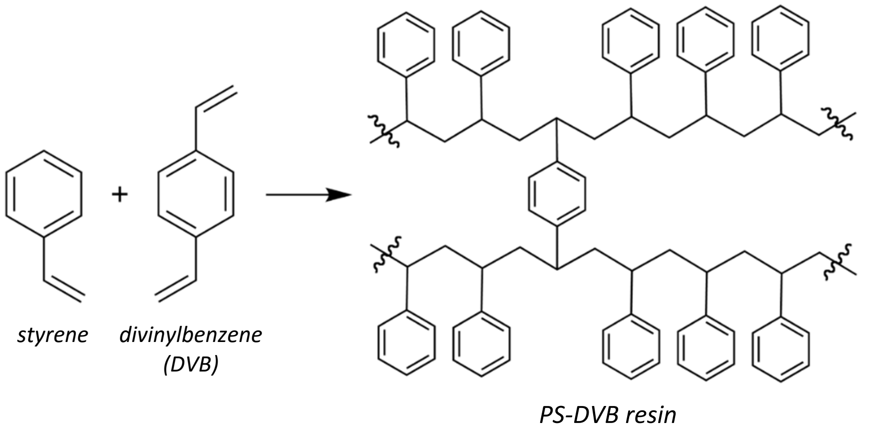

Figure 27. *Synthesis of a PS-DVB resin from the styrene monomer and 1-2% of cross-linking agent, the divinylbenzene (DVB).*[48]

variance) loadings are listed in **Table S3** (threshold: 0.025). The linear PS is mainly characterized by aromatic ions at $m/z \geq 91$, whereas the cross-linked PS is characterized by aliphatic ions at $m/z < 91$, and mainly saturated like $C_2H_5^+$ associated to the highest loading > 0, but also some unsaturated ones, such as $C_3H_3^+$, $C_2H_3^+$, and $C_4H_3^+$. These latter category of fragment ions is also typical of the classical polystyrene. Apparently, the cross-linking favors the emission of smaller aliphatic (un)saturated ions. Instead, a more linear polymer structure leads to an enhanced emission of bigger fragment ions (starting from the tropylium), mainly stabilized by resonance. Finally, in the cross-linked PS, such fragmentation at $m/z \geq 91$ is partly repressed, and replaced by the enhanced emission of the $C_9H_{11}^+$ ion due to the cross-links between adjacent polymer chains. Those results are in agreement with the previous PCA.

The last part of this PCA investigation of the two commercial PS samples focuses on the oxidation. Then, a third PCA was performed by creating a peak list of O-containing fragments in the m/z range from 12 to 210 amu. However, this comparison is made difficult by the presence of metastable ions that interfere with the O-based ions in the linear PS,[49,50] where the oxidation is minimal. Nevertheless, few conclusions can be drawn principally thanks to a careful observation of the SIMS spectra guided by the PCA results. Only the separation between the two polymers obtained in PC1 is reported in **Figure S7**. The linear PS is mainly characterized by the ion $C_7H_5O^+$, that suggests a low level of O-uptake of the polymer in presence of air. On the contrary, the cross-linked PS appears dominated by the $C_2H_3O^+$, as already pointed out by the first PCA. But also other small oxidized fragments with high H content, such as CH_3O^+ and $C_2H_5O^+$, are present. A second family of small O-based fragments (C_{2-4}) is highlighted by this PCA, i.e. ions containing two oxygen atoms whose origin cannot be directly related to the presence of additives since, as previously stated, no molecular ions are identified in the SIMS spectra.

b. *Comparative study of the pp-PS films, linear PS, and cross-linked PS*

A PCA study was conducted in order to compare the two conventionally polymerized PS and the plasma-polymer films along the overall spectral range 12 amu ≤ m/z ≤ 210 amu (including both hydrocarbon and O-based peaks). Only the comparison of the pp-PS films with the reference linear PS is shown in **Figure 28**. PC1 (85% of the overall variance) discriminates the reference from the pp-PS deposits, while PC2 (15% of the variance) points out the evolution of the chemical nature of the plasma films as a function of power.

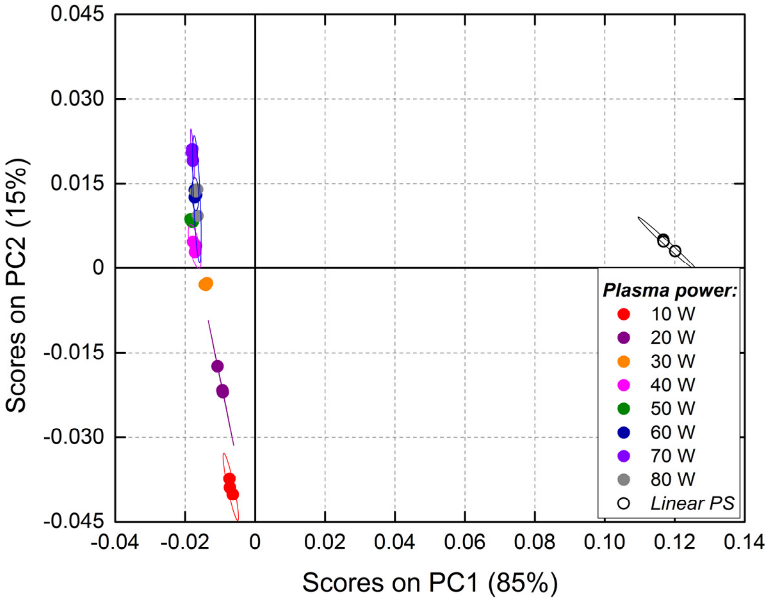

Figure 28. *PC2 versus PC1 scores plot obtained from the PCA applied to the ToF-SIMS positive ion mass spectra of the linear PS and the pp-PS films deposited in the plasma power range going from 10 W to 80 W.*

A detailed analysis of the PC2 loadings shows no relevant intervention of the linear PS in the separation along this principal component (refer to **Tables S4 and S5** for complete PC1 and PC2 loading lists). This evolution will be more clearly described by the PCA model proposed in the next section (point c), in order to avoid repetitions.

PC1 scores and loadings plots are reported in **Figure 29**. Positive loadings are associated to the linear PS. They show the typical positive ion mass spectrum of PS, reflecting the aromatic structure of the polymer, where the most outstanding peak is the tropylium ($C_7H_7^+$) ion. Among the negative loadings, representing the pp-PS films, dominate the protonated repeat unit of the PS, the ion $C_8H_9^+$, in addition to the ion $C_6H_5^+$ [iv] and a series of O-containing fragments. Ion $C_6H_5^+$ also represents the phenyl groups present in the polymer structure. Here, an important difference emerges between conventionally and plasma-polymerized PS, i.e. the inversed ratio of the ion intensities of 105^+ and 91^+. Concerning the oxidation, typical of the pp-PS films, the corresponding ions are either very small and linear, like $C_2H_3O^+$ and $C_3H_3O^+$, or bigger like $C_8H_9O^+$ and $C_9H_7O^+$, including an aromatic ring. This seems to indicate an O-grafting along the overall backbone of the polymer chains. It has already been proven that the oxidation increases with the power at the surface (cf. §6.3.2). Here, this is indicated by the decreasing trend of the PC1 negative scores (noticed thanks to the break of the y-scale). Lowering the loadings threshold, a third peculiar feature of the plasma-polymers can be observed: the increase of the aliphatic moieties in the polymer chains compared to the reference (e.g. refer to $C_2H_5^+$, $C_3H_7^+$, CH_3^+). It increases with increasing power, like in the case of the O-uptake. However, this is due to different phenomena occurring in the plasma, that will be discussed in §6.7.

The PCA model applied to the pp-PS films and the two conventionally synthesized polystyrenes (**Figure S8**) shows the following: PC1 separates the conventional PS from the plasma-polymers because of the (prevalent) aromatic structure of the first two samples, and the oxidized character of the latter; instead, PC2 assimilates the plasma films deposited at 10-30 W to the linear PS, being the most aromatic of the series, while the pp-PS films are similar to the cross-linked PS because of small O-containing ions (see $C_2H_3O^+$) and short aliphatic chains.

[iv] A contribution to the ion intensities of $C_8H_9^+$ ($[m+H]^+$) and $C_6H_5^+$ ($[m-C_2H_3]^+$ could be given by the presence of traces of unreacted styrene monomer (m) in the polymer film, which cannot be ruled out by the IR, GPC, and SIMS analyses.

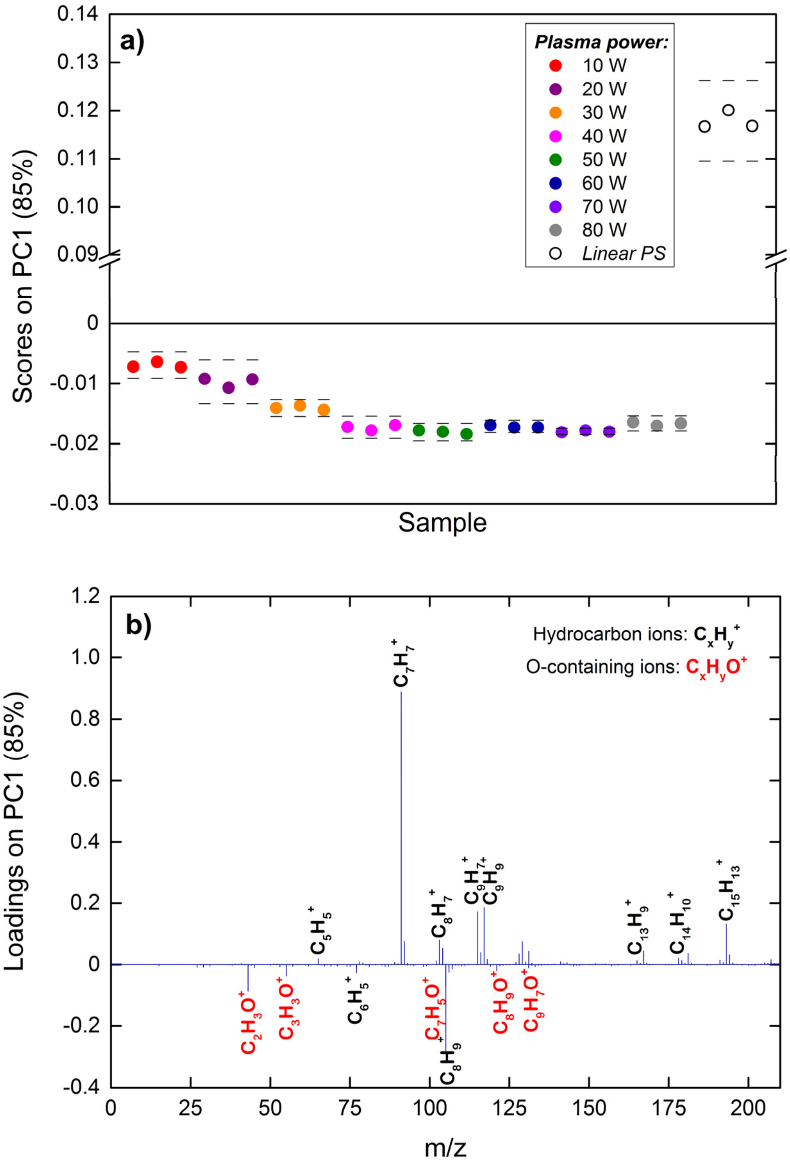

Figure 29. *a) PC1 (85%) scores plot of the PCA applied to the linear PS and the pp-PS films deposited by DBD at different plasma powers (10-80 W). b) The corresponding PC1 loadings plot as a function of the m/z ratio. The loading threshold has been set at ±0.01, but only the most characteristic ion fragments of the polystyrene (within the fixed loading range) are reported in the graph.*

In summary, these PCAs suggest a loss of aromaticity of the pp-PS films compared to the conventionally polymerized counterparts. The decrease of the aromatic content is accompanied by an increase of the cross-linking, inferred from an increase of short aliphatic ions with $C_{2\text{-}4}$. Conversely to the linear PS, the plasma-polymers are oxidized, and the oxygen content increases with increasing power. In the end, the ion $C_8H_9^+$ becomes the most characteristic in the pp-PS films. This fact could indicate a new structural feature in such plasma-polymers, and it will be investigated in the next SIMS section (§6.6.3.5) with the help of additional reference polymers.

In the end, in order to assess in SIMS the prevalence of mono-substitution of the aryl groups in the pp-PS deposits and the significant presence of methyl-substitution revealed by IR analysis, the evolution of the relative intensity of the ions $C_9H_{11}^+$ (119^+, PC1 positive loading) and CH_3^+ (15^+, PC1 negative loading) was checked (cf. **Figure S9**). Indeed, $C_9H_{11}^+$ can be related to the alkyl-substitution of the phenyl rings (as already discussed in point a), while CH_3^+ is indicative of the presence of $-CH_3$ groups in the polymer matrix. For the moment, it will be only noticed that the intensity of the first ion is much lesser in the plasma films with respect to the cross-linked PS. In the case of CH_3^+, the ion intensity of pp-PS is much higher than the linear PS and it increases with increasing power. The interpretation of these two different evolutions will be given in §6.7.

c. Study of the pp-PS films deposited by DBD

This PCA study focuses on the investigation of the chemical structure of the plasma deposits as a function of the power applied during the polymerization. To this purpose, the complete peak list from the m/z range 12-210 amu is applied, consisting both in hydrocarbon and oxidized fragments.

PC2 versus PC1 scores plot is shown in **Figure 30**. Only PC1 needs to be interpreted. PC2 is disregarded, because it describes the noise in the dataset. So, PC1 scores and loadings plots are illustrated in **Figure 31**. A comprehensive table of the PC1 loadings can be found in §6.9 (**Table S6**). Negative scores are associated to the lower plasma powers ranging from 10 to 30 W. More importantly, loadings < 0 indicates which SIMS peaks decrease in relative intensity with increasing power. Conversely, loadings > 0 point out the SIMS peaks whose relative intensity increases with increasing plasma power. In that respect, the highest negative loading is

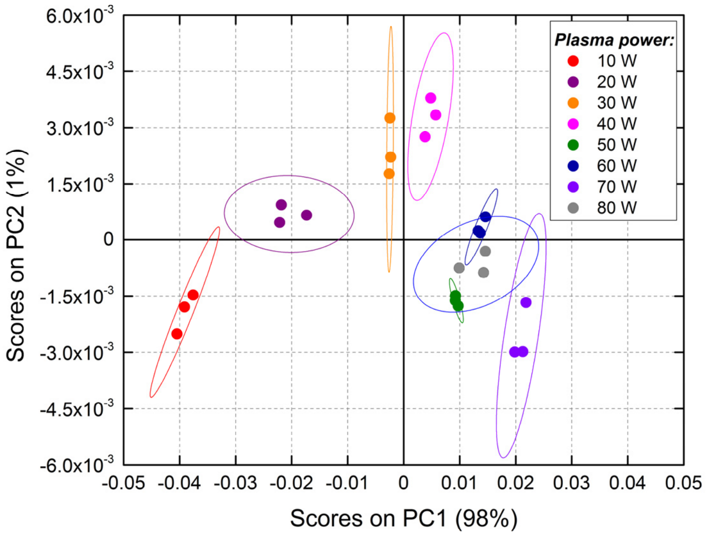

Figure 30. *PC2 versus PC1 scores plot obtained from the PCA applied to the ToF-SIMS positive ion mass spectra of the pp-PS films deposited by DBD in the plasma power range going from 10 W to 80 W.*

represented by the ion $C_8H_9^+$, that corresponds to the protonated repeat unit of the conventional PS. This is followed by the $C_7H_7^+$, the most characteristic fragment of PS. More generally, PS-like fragments with $m/z \geq 91$ are associated to loadings < 0, as well as the dimer-related fragment $C_{16}H_{15}^+$ at m/z 207 ([M-H]$^+$). So, the relative intensity of PS-like fragments decreases when the plasma power increases, as shown in **Figure 32.a** (reporting also the linear PS). Among the negative loadings one can find the oxidized ion $C_8H_9O^+$, that follows the decreasing intensity trend of $C_8H_9^+$. On the other hand, positive loadings are associated to smaller O-containing ions, such as $C_2H_3O^+$, $C_7H_5O^+$, and $C_3H_3O^+$, as well as smaller PS-like aliphatic fragments (see $C_3H_3^+$, $C_4H_3^+$, $C_5H_3^+$, $C_2H_3^+$), and the aromatic ion $C_6H_5^+$. These ion intensities increase with increasing power applied to the discharge, as depicted in **Figure 32.b**.

A possible explanation for these experimental evidences consists in a gradual loss of the aromaticity with increasing power, as suggested by the decrease of $C_7H_7^+$ and $C_8H_9^+$. An increase of the plasma power also induces an augmentation of the oxidation (seen in the comparison with the linear PS, **Figure 29.a**) and the cross-linking, since a higher fraction of smaller

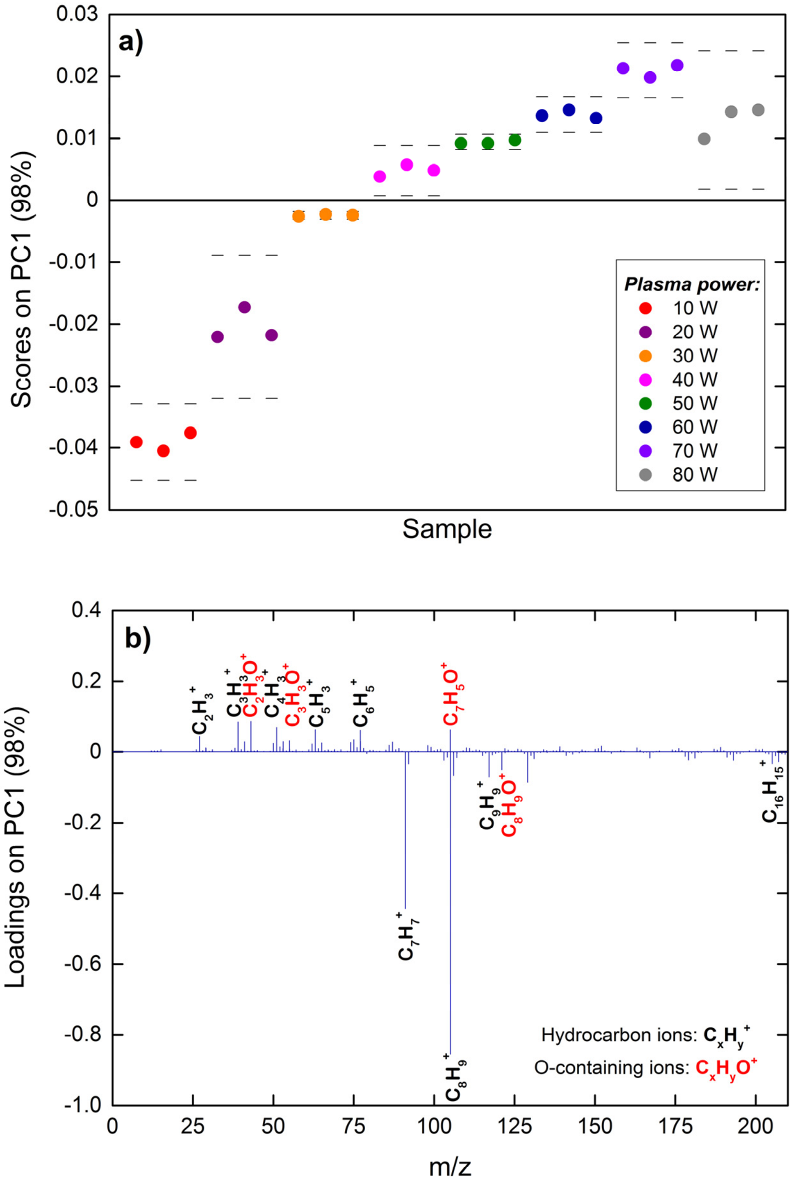

Figure 31. *a) PC1 (98%) scores plot of the PCA applied to the pp-PS films deposited by DBD at different plasma powers (10-80 W). b) The corresponding PC1 loadings plot as a function of the m/z ratio. The loading threshold has been set at ±0.025, but only the most characteristic ion fragments of the polystyrene (within the fixed loading range) are reported in the graph.*

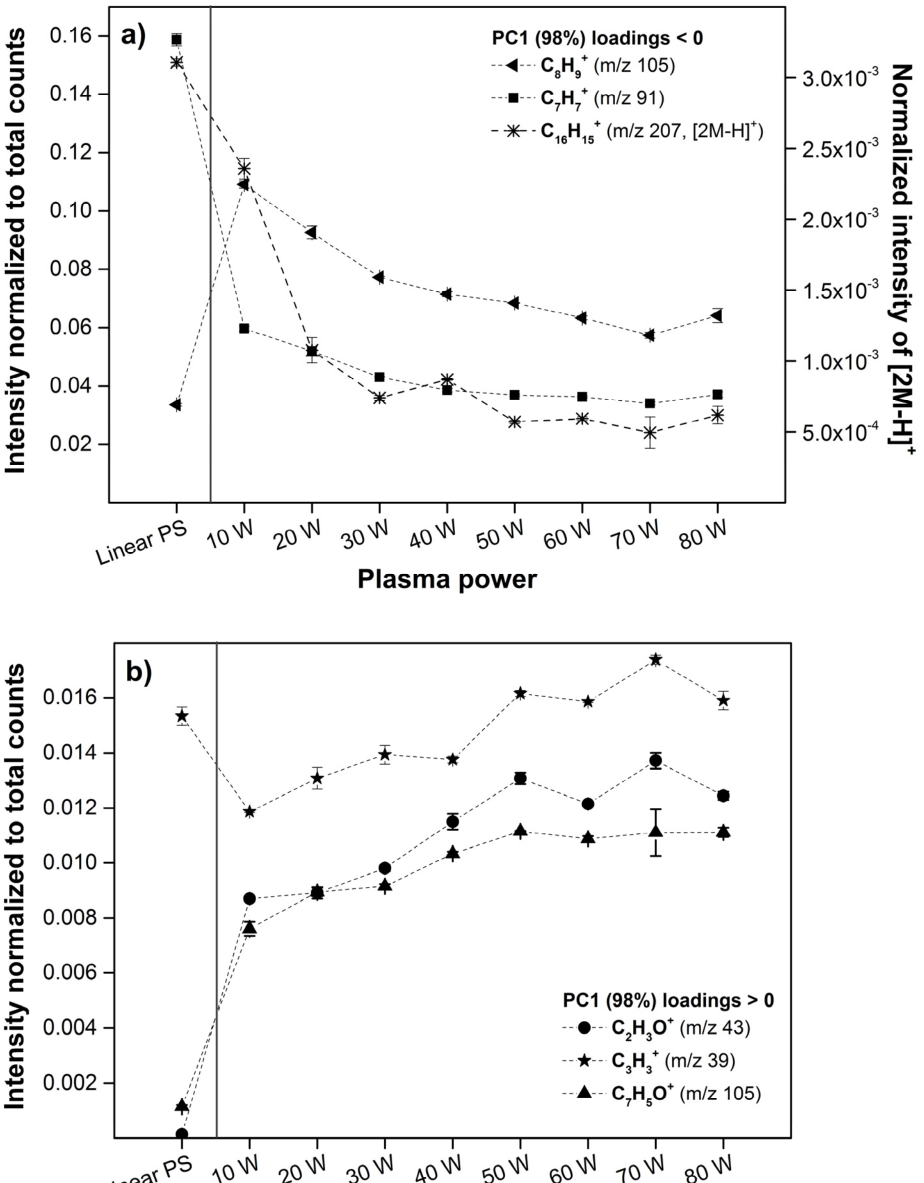

Figure 32. *Normalized intensities of some interesting secondary ions highlighted by the PC1 (98%) negative loadings (a) and positive loadings (b) obtained from the PCA applied to the pp-PS films synthesized at different plasma powers. The linear PS samples is reported separately (on the left side), and only for comparison purposes.*

hydrocarbon fragments emerges (<C_8) in the mass spectra. Additionally, PC1 scores of Figure 31 indicate that the general variation of the chemical structure as a function of power reaches a sort of saturation level towards 70-80 W.

6.6.3.3. PCA study of pp-PS ageing

This PCA study is focused on the exploration of the influence of the ageing process on the positive ion mass spectra of the pp-PS films. In order to perform it, a sample set obtained from a previous plasma polymerization, conducted in the same experimental conditions of this study (power ranging from 10 to 80 W; deposition time of 5 min), was chosen. The SIMS results obtained from these specimens were similar to those exposed in this chapter, showing a good reproducibility of the plasma conditions achieved with the home-made DBD device used at ULB. For this reason, such results are not presented here. The pp-PS films selected for the ageing study were conserved in Petri dishes until their SIMS characterization 5 months later. The exposure of the samples to the light was minimal during this time. The SIMS analytical conditions applied were the same of those described in §6.6.2, as well as the data treatment of §6.6.3.2. Moreover, the positive ion mass spectra used to run the PCA were reconstructed from the same in-depth region of the polymer films, in order to reliably compare the samples.

For clarity this PCA focuses on two different pp-PS films, pp-PS/20W and pp-PS/60W, analyzed by SIMS just after their polymerization (called "fresh"), and 5 months later ("aged"). This PCA uses the complete peak list between 12 and 210 amu, including both hydrocarbon and oxidized ion species. The related PC2 versus PC1 scores plot is shown in **Figure 33**. PC1 explains the effects of the applied plasma power on the chemical nature of the resulting films, already described in the previous section (refer particularly to point b of §6.6.3.2). This shows the excellent reproducibility of the plasma polymerization experiments conducted with the styrene monomer. The effect of ageing emerges in PC2, that captures only 2% of the total variance of the given dataset. **Figure 34** reports the PC2 versus PC1 loadings, so that the most outstanding ion fragments of each quadrant are the most characteristic of the corresponding samples shown in the scores plot of Figure 33. The aged samples are more oxidized as indicated by the O-containing ions (in red) $C_2H_3O^+$, $C_7H_5O^+$, and $C_3H_3O^+$ (loadings > 0.02), while the fresh samples are more characterized by the presence of aromatic ions (e.g. $C_8H_9^+$, $C_7H_7^+$, and $C_9H_9^+$). Moreover, a series of small aliphatic

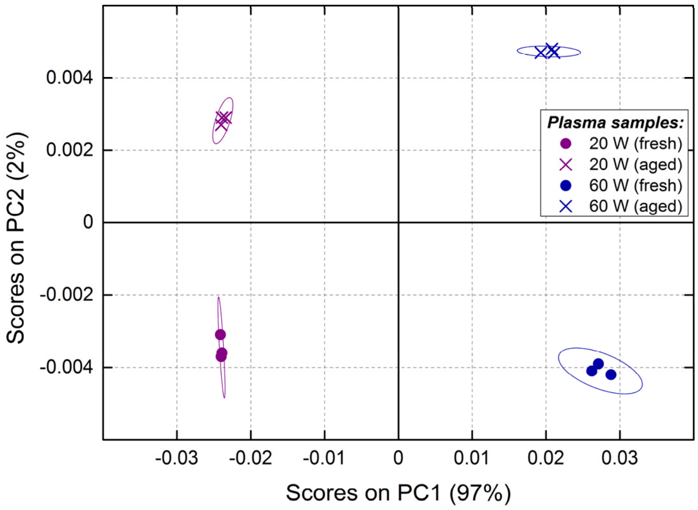

Figure 33. *PC2 versus PC1 scores plot of the PCA model obtained from the pp-PS films prepared at 20 and 60 W, both freshly synthesized ("fresh") and 5-month aged ("aged"). The PCA has been applied to the positive ion mass spectra obtained from the bulk-like region of the investigated polymers.*

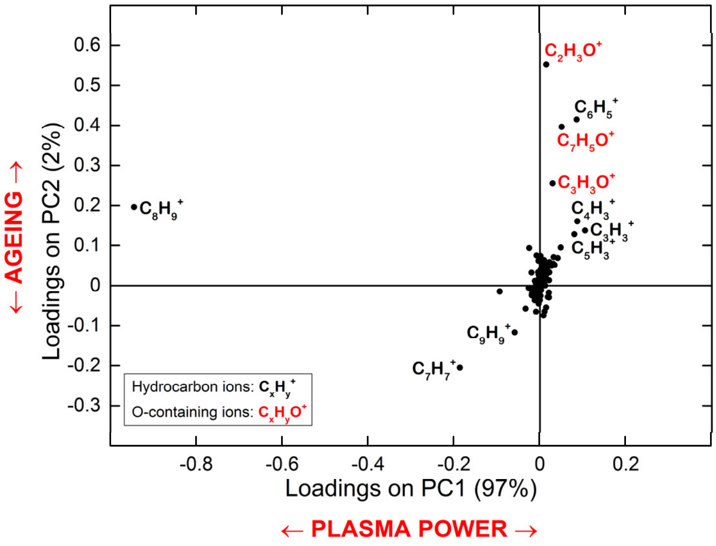

Figure 34. *PC2 (2%) versus PC1 (97%) loadings of the PCA model applied to the pp-PS films prepared at 20 and 60 W, freshly synthesized, and 5-month aged. PC1 separates the plasma powers, while PC2 discriminates the aged samples from the fresh ones.*

(un)saturated ions presents higher relative intensity in the plasma films after ageing. This could be ascribed to the increased cross-linking content in the aged polymers caused by the photo-oxidation,[51,52] due to the recombination of radical species with(out) oxygen formed by photolysis. On the other hand, the ion intensity of fragments like $C_8H_9^+$ and $C_6H_5^+$ increases slightly. A plausible explanation could lay in the chain scission induced by the polymer degradation under atmospheric conditions.

In summary, the effects of the ageing on the pp-PS mass spectra reconstructed in the sub-surface region are minimal compared to the chemical and structural differences determined by the plasma powers applied. This seems to suggest that pp-PS bulks are relatively stable at prolonged contact with the air. Nervertheless, this represents only an exploratory study. Hence, it should be interesting to understand the ageing process of these plasma deposits by the proposed SIMS/PCA methodology (for instance in terms of photo-oxidation, and thermal degradation).

6.6.3.4. Sputter yield volume calculation

The sputter yield volume Y (nm^3/PI) of the entire series of pp-PS films analyzed by SIMS was calculated following the protocol described in §4.3.2.3, in order to investigate its variation as a function of the plasma power. The SIMS crater depths were measured by using a stylus profilometer in 3D imaging mode (stylus: 0.7 μm, force: 0.3 mg, rastered area: 1000 x 1000 μm^2). For the profilometry technique, one can refer to §3.2. In addition, an averaged estimation of the crater depth was perfomed in correspondence of the SIMS analysis area of 200 x 200 μm^2, concentric to the crater size of 600 x 600 μm^2. The SIMS craters were measured after the XPS analyses. **Figure 35** reports the Y values of the pp-PS films as a function of the power (black solid squares). The values of sputter yield volume result from the average of three independent SIMS measurements. Because of the double-sided insulating tape used to fix the specimens to the XPS sample holder, it was not possible to recuperate the sample pp-PS/20W. This explains the absence of the point at 20 W. For comparison purposes, the sputter yield volume of the linear PS used as reference sample is reported in the graph (see the black open square). Furthermore, in order to get insights about the polymerization degree and/or the cross-linking content of the pp-PS deposits, the sputter yield volume of PS standards for GPC of different M_w (studied in chapter 4, §4.2), is also shown in Figure 35. For both measurement series, the sputtering was performed using a 10 keV Ar_{3000}^+ ion beam, but different sputter currents were applied. However, it is shown in §4.3 that the influence of the current on Y is negligible.

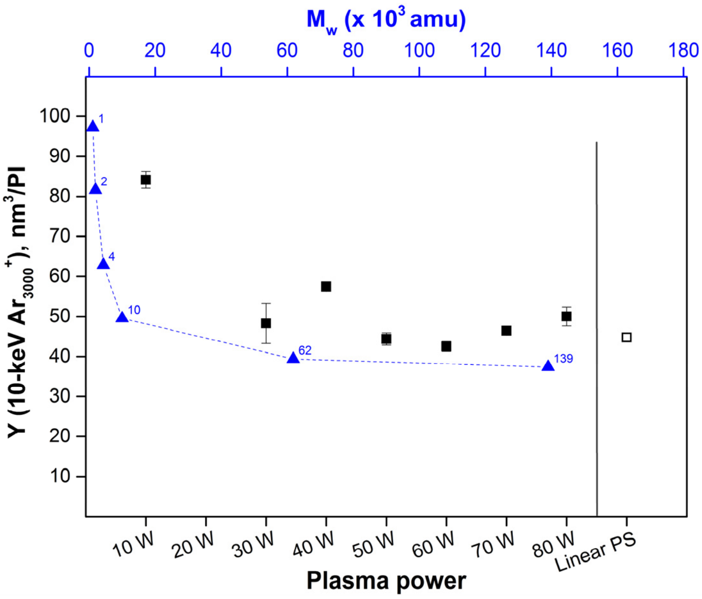

Figure 35. *Sputter yield volume (Y) of the pp-PS films deposited by DBD as a function of the plasma power (black solid squares). The reference linear PS is reported for comparison purposes on the left side of the graph (black open square). In addition, Y as a function of the* M_w *of PS standards for GPC is illustrated by the blue curve. The values in blue type are referred to the different* M_w *(x* 10^3*amu) of the polystyrene.*

Figure 35 shows a good agreement between the Y values of the reference linear PS, a polydisperse bulk polymer, and the PS standards with M_w > 50000 amu (considering an experimental error of ~10%). This seems reasonable since Y is independent of M_w for high polymerization degrees, as found out in §4.2.4. Furthermore, the pp-PS deposits synthesized at powers ≥ 30 W locate at the same level as the polydisperse PS. The presence of O-based functionalities in the pp-PS might induce an enhancement of the sputter yield volume (O content of ~7-9% determined by XPS) compared to the reference PS.[53] However, the extent of the O-uptake effect on Y remains within the experimental error. In any case, the oxidation of the pp-PS films, that increases with increasing power, cannot explain the gap between 10 W and the other powers. Y at 10 W is unexpectly high (almost a factor of 2 compared to the $\bar{Y}$ value of the remaining plasma-polymers). pp-PS/10W can be assimilated to PS 2k (composed by ~20 repeating units), strictly in terms of sputtered volume properties. This observation could be related to the presence of a much higher fraction of oligomers in the plasma films obtained at 10 W (refer to §4.2.4). For instance, the GPC analyses conducted on pp-PS/30W and pp-PS/60W only, suggested that the plasma films consist of a cross-linked matrix in which a certain amount of oligomers and monomers are trapped.

In conclusion, insights about the polymerization degree of plasma-polymers can be inferred from the Y calculation and comparison with proper calibration curves. In this particular case, the observations done for the pp-PS deposits are supported by the presence of oligomers proved by means of GPC measurements (refer to §6.5). However, the structure of the pp-PS differ from the one of the reference PS. Thus, the peculiar features of the pp-PS structure should be elucidated to interprete correctly the Y evolution as a function of the power. This will be attempted in the final SIMS section, by using PCA and new reference polymers.

6.6.3.5. PCA study of pp-PS films and PS derivatives

In order to elucidate the two most distinctive features of pp-PS synthesized near atmospheric pressure pointed out by SIMS characterization, i.e. positive ion mass spectra dominated by $C_8H_9^+$ and oxidation, additional reference polymers are taken into account. According to the methyl-substitution reported in the literature for certain polymers deposited by plasma at low pressure, among them the plasma-polymerized styrene studied by Prohaska et al.,[25] two commercial methyl-substituted PS have been selected to investigate this phenomenon: the poly (α-methyl styrene) (PAMS), and the poly (4-methyl styrene) (P4MS). Concerning the elucidation of the oxidized character of the pp-PS films, the poly (4-vinylphenol) (PVP) is commercially available as reference material. The chemical structures of these three polymers are shown in **Figure 36**.

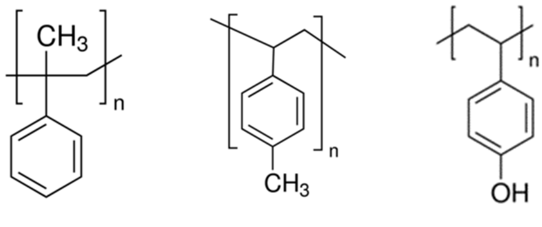

PAMS P4MS PVP

Figure 36. *Chemical structure of poly (α-methyl styrene) (PAMS), poly (4-methyl styrene) (P4MS), and poly (4-vinylphenol) (PVP), respectively.*

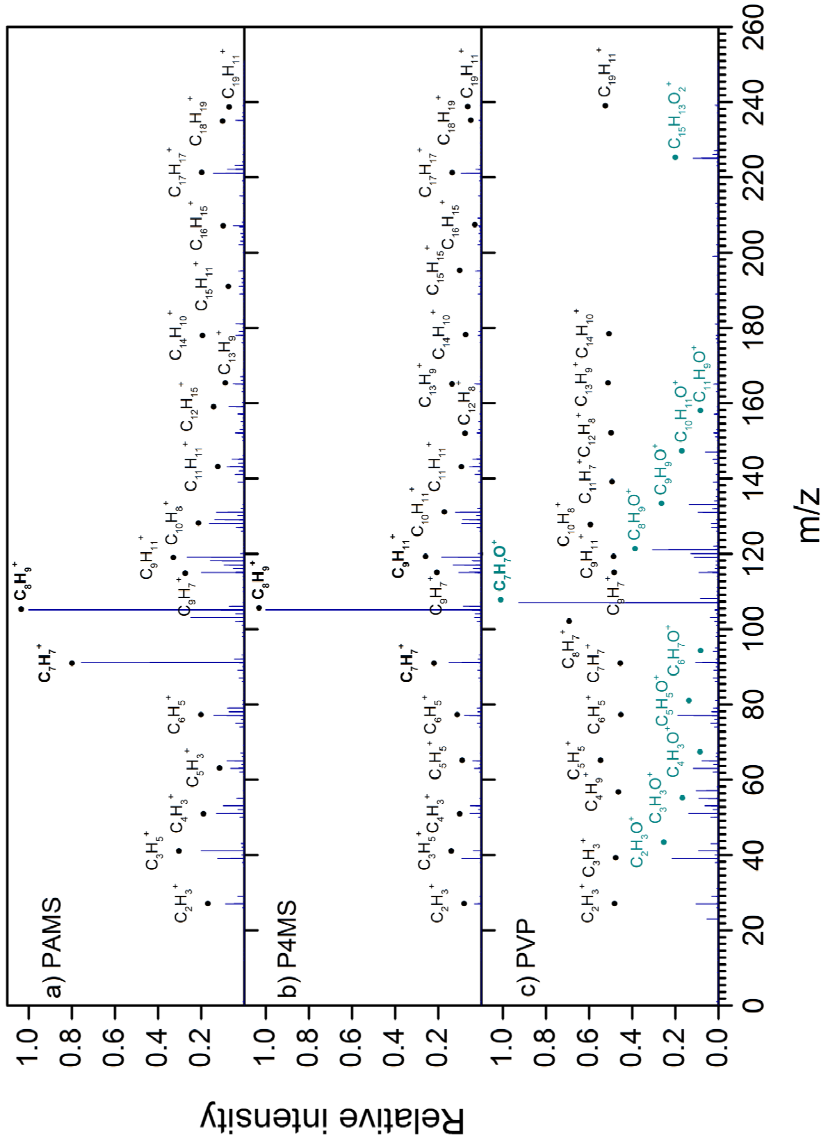

Figure 37. *SIMS positive ion mass spectra of: a) poly (α-methyl styrene) (PAMS), b) poly (4-methyl styrene) (P4MS), and c) poly (4-vinylphenol) (PVP).*

Figure 37 shows the typical positive ion mass spectra of the three additional reference polymers, normalized to the most intense peak. If a relative intensity threshold is set at 0.2 for all the references, the most outstanding peaks correspond to the ions $C_8H_9^+$, $C_7H_7^+$, $C_9H_{11}^+$ ($[M+H]^+$), $C_9H_7^+$, $C_3H_5^+$, for PAMS (Figure 37.a); $C_8H_9^+$, $C_9H_{11}^+$ ($[M+H]^+$), for P4MS (Figure 37.b); and $C_7H_7O^+$, $C_8H_9O^+$ ($[M+H]^+$), $C_3H_3^+$ for PVP (Figure 37.c). Furthermore, it is worth noticing that the mass spectra used in this section are reconstructed from the sub-surface region of the spin-coated reference films according to the protocol of §6.6.2, in order to avoid any surface organic contamination.

d. Comparative study of the pp-PS films, linear PS, cross-linked PS, PAMS, P4MS, and PVP

PCA was run with the overall series of PS structure-related polymers, namely the pp-PS films, linear PS, cross-linked PS, PAMS, P4MS, and PVP. The aim of this preliminary multivariate analysis is to know how the plasma-polymers locate among the commercial references to focus, at a second stage, on the most similar polymer structure.

The proposed PCA model is described by the first three principal components, representing together the 97% of the total variance of the given dataset. The corresponding 3D scores plot is depicted in **Figure 38**. In this graph, the most spread polymers for each PC are reported, in addition to the structural and chemical features (indicated between brackets) responsible of the observed separation. PC2 versus PC1 scores plot shows that PAMS is the closest polymer to the pp-PS deposits, where a total variance of 87% is described. Moreover, PVP and P4MS are differentiated substantially from the investigated plasma samples, in addition to the linear PS. Instead, the cross-linked PS is more assimilated to the pp-PS deposits. PC3 (explaining the remaining 10% of variance) separates the plasma films (as well as the cross-linked PS) from PAMS, and the other samples.

A more detailed analysis of the PC1 loadings (not reported) indicates a different type of oxidation in the plasma-polymers compared to the PVP. Indeed, the positive ion mass spectra of PVP are mostly dominated by the ions $C_7H_7O^+$ at m/z 107, and $C_8H_9O^+$ at m/z 121, whereas the pp-PS films are mainly characterized by the ions $C_2H_3O^+$ at m/z 43, and $C_7H_5O^+$ at m/z 105. More generally, the intensity of the O-containing ions in the pp-PS deposits tends to that of the PVP only for small fragments like the $C_3H_3O^+$ at m/z 55. Thus, the oxygen in the plasma-polymers is bonded to the backbone

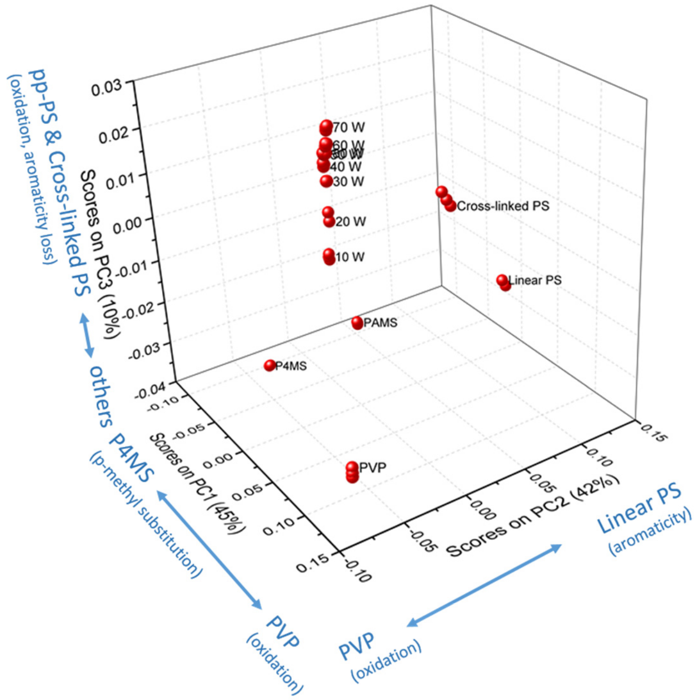

Figure 38. *3D scores plot (explaining the 97% of the overall variance) obtained from the PCA applied to the ToF-SIMS positive ion mass spectra of the pp-PS films synthesized at plasma powers ranging from 10 W to 80 W, the two commercial PS samples (linear and cross-linked), the two methyl-substituted PS (PAMS and P4MS), and the PVP. Three spectra have been acquired per sample.*

rather than to the phenyl ring. Moreover, it is hard to get insights about the kind of O-based functional groups present in the material, since different chemical functionalities produce common secondary ions.[43] Concerning the separation in PC1 between the plasma films and the P4MS, it is fundamentally due to the higher ion intensities of 105^+ and 119^+ in the case of the methyl-substituted PS. Then, it is possible to rule out the massive presence of para-methyl substitution of the aryl groups in the plasma-polymer network. This is in rather good agreement with the preliminary FT-IR analysis of the plasma samples. Regarding PC2, the discrimination of the linear PS and the pp-PS is based on the partial loss of aromaticity in the latter, indicated by the lower intensities of the ions 91^+, 115^+, 117^+, and 193^+. Finally, the PC3 separation of the pp-PS and cross-linked PS from the other samples is explainable by the oxidation (see $C_2H_3O^+$), common to both polymers, and the more irregular structure of the plasma films (see the increase of the $C_6H_5^+$ intensity, linked to a partial loss of the aromaticity that will be discussed in §6.9). The evolution of the chemical nature of the pp-PS films as a function of the power emerges in PC3, in terms of increase of the oxidation and decrease of the aromatic content.

In conclusion, this PCA study establishes a structural similarity between the pp-PS and the PAMS, even if the presence of oxidation remains a distinctive chemical feature of the plasma-polymer. This investigation permits also to exclude the prevalence of para-substitution of the aromatic rings by methyl and/or hydroxyl groups in the plasma films, that would lead to a different fragmentation pattern, exclusively in terms of relative ion intensities. Thus, the comparison of the pp-PS positive ion mass spectra with those of the PAMS constitutes the last step of this SIMS characterization, in order to draw the complete picture of the structure of the polymer deposits obtained by the plasma polymerization of the styrene monomer.

e. <u>Comparative study of the pp-PS films with the poly (alpha-methyl styrene)</u>

PCA is applied to the entire set of pp-PS films, and the poly (alpha-methyl styrene) or PAMS. The purpose is to elucidate the $-CH_3$ grafting occurring during the film growth indicated first by the FT-IR characterization (§6.4.2), and then by the SIMS analysis (§6.6.3.2, point b).

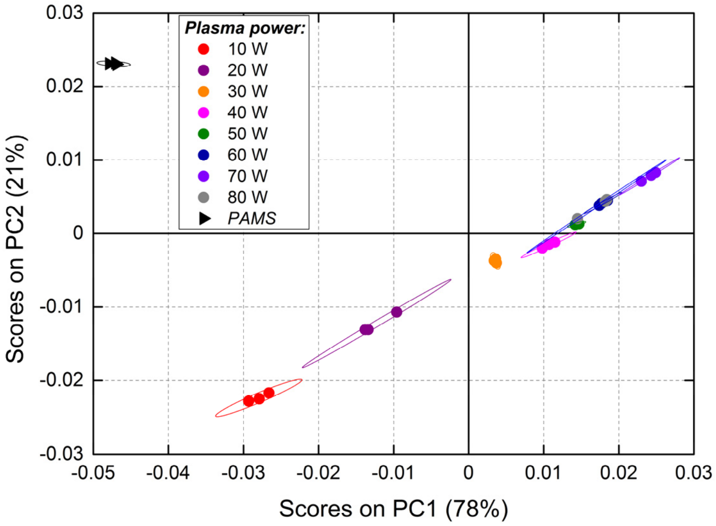

Figure 39. *PC2 versus PC1 scores plot obtained from the PCA applied to the ToF-SIMS positive ion mass spectra of the poly (alpha-methyl styrene) (PAMS) and the pp-PS films deposited at different plasma powers.*

PC2 versus PC1 scores plot is illustrated in **Figure 39**. Only PC1 will be described, because this study aims at the identification of the main differences and similarities between the two polymers. PC1 also captures the variation of the pp-PS structure as a function of power, that has been previously studied in §6.6.3.2 (point c). The PC1 loadings are listed in **Table 5**. Positive loadings are mostly representative of the plasma-polymers. They indicate that the pp-PS deposits are oxidized (highest negative loadings) and characterized by the presence of short aliphatic moieties in the polymer network, as suggested by ions like $C_5H_3^+$ at m/z 63, as well as the presence of phenyl groups derived from $C_6H_5^+$. Both features tend to increase with increasing plasma power. It is worth noticing that those ion intensities are very close to PAMS, as shown in **Figure 40.a.** Conversely, negative loadings indicate characteristic ion fragments of PAMS, that decrease with increasing power in the case of the pp-PS films. More specifically, the highest negative loadings are associated to 105^+ and 91^+, whose intensities in pp-PS films at low power are comparable to PAMS. However, peaks at higher m/z, such as 119^+ (representing the $[M+H]^+$ of PAMS), 143^+, 128^+, 207^+, 115^+ (in decreasing order of loading) are mostly characteristic of PAMS. This is illustrated in **Figure 40.b**, where a break scale is required to show the evolution of the much less intense 119^+ in the plasma series.

PCA seems to suggest that the mass spectra of pp-PS and PAMS can be assimilated more than PS, linear and cross-linked, in the sub-monomer region. Only this m/z region is really suited for the comparison of conventionally synthesized polymers with the plasma counterparts, the latter being deprived of repeat unit. In conclusion, this multivariate analysis points out that the methyl groups of the investigated plasma-polymerized PS are either bonded along the aliphatic backbone (rather than to the phenyl rings like in the case of P4MS), or constitute chain ends.

PC1 (78%) loading > 0 *30-80W*			**PC1 (78%) loading < 0** *10-20W & PAMS*		
Loading	**Mass**	**Peak**	**Loading**	**Mass**	**Peak**
0.159	43.019	$C_2H_3O^+$	-0.656	105.074	$C_8H_9^+$
0.127	105.036	$C_7H_5O^+$	-0.520	91.061	$C_7H_7^+$
0.067	77.039	$C_6H_5^+$	-0.242	119.091	$C_9H_{11}^+$
0.066	55.020	$C_3H_3O^+$	-0.183	41.039	$C_3H_5^+$
0.051	63.023	$C_5H_3^+$	-0.157	103.056	$C_8H_7^+$
0.037	51.023	$C_4H_3^+$	-0.150	118.079	$C_9H_{10}^+$
0.031	75.023	$C_6H_3^+$	-0.127	129.075	$C_{10}H_9^+$
0.031	39.023	$C_3H_3^+$	-0.115	131.093	$C_{10}H_{11}^+$
0.029	87.023	$C_7H_3^+$	-0.098	117.076	$C_9H_9^+$
0.027	74.014	$C_6H_2^+$	-0.097	143.094	$C_{11}H_{11}^+$
			-0.085	128.062	$C_{10}H_8^+$
			-0.079	207.131	$C_{16}H_{15}^+$
			-0.071	145.112	$C_{11}H_{13}^+$
			-0.067	159.132	$C_{12}H_{15}^+$
			-0.064	115.056	$C_9H_7^+$
			-0.057	106.077	$C_8H_{10}^+$
			-0.050	79.055	$C_6H_7^+$
			-0.042	181.112	$C_{14}H_{13}^+$
			-0.041	92.060	$C_7H_8^+$
			-0.030	116.061	$C_9H_8^+$
			-0.028	130.080	$C_{10}H_{10}^+$
			-0.027	157.115	$C_{12}H_{13}^+$
O-containing ions: $C_xH_yO_z^+$			-0.027	195.131	$C_{15}H_{15}^+$

Table 5. *List of the most influential PC1 loadings, and corresponding secondary ions, extracted from the PCA applied to the poly (alpha-methyl styrene) (PAMS), and the pp-PS films deposited by DBD at different plasma powers (10-80 W). A threshold value for the loadings of ±0.025 has been fixed. The corresponding loadings plot as a function of the m/z ratio can be found in supporting information (**Figure S10**).*

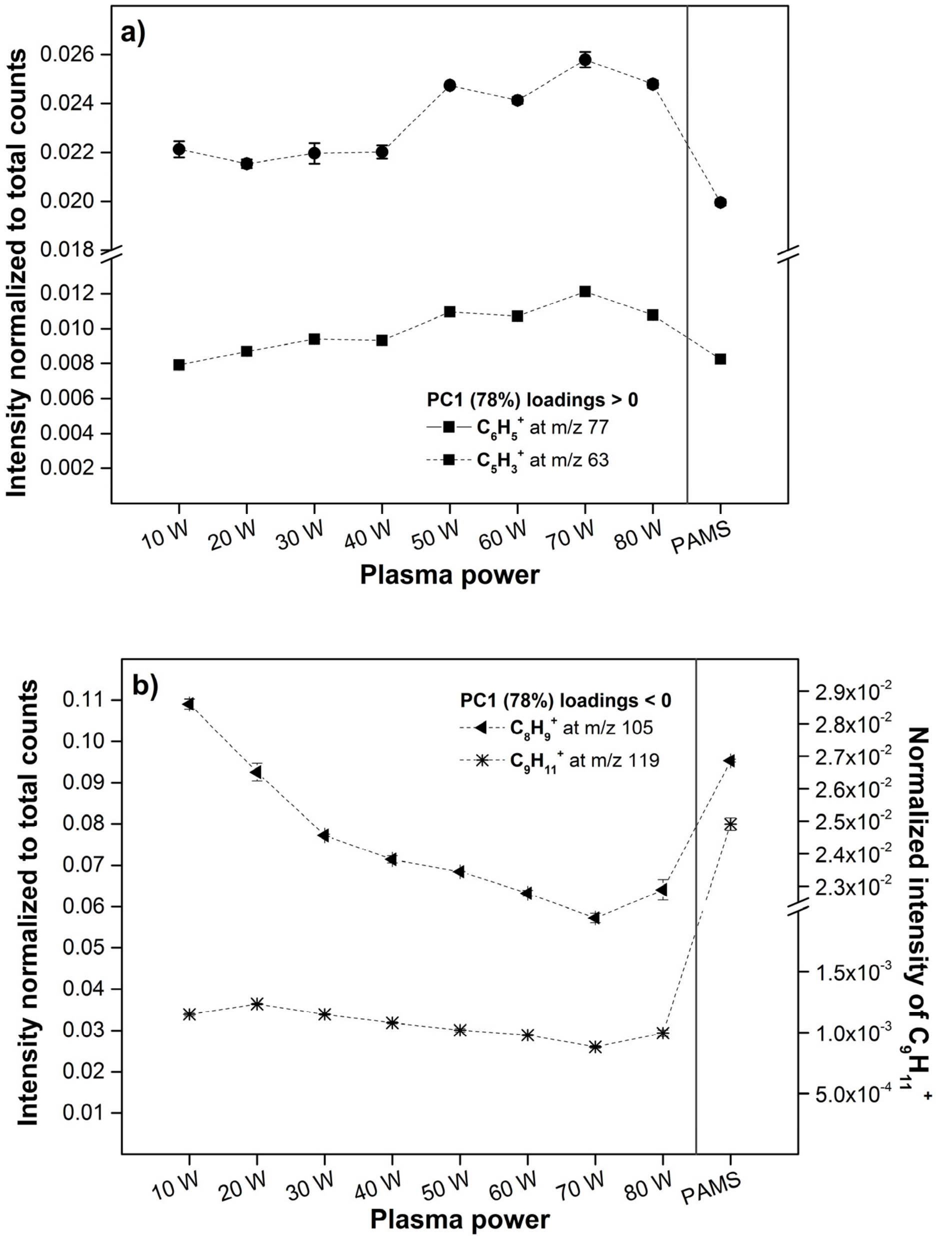

Figure 40. *Normalized intensities of some interesting secondary ions highlighted by the PC1 (78%) positive loadings (a) and negative loadings (b) obtained from the PCA applied to the pp-PS films synthesized at different plasma powers, and PAMS.*

6.7. Discussion

First, the cross-linked PS was investigated by the combined SIMS/PCA approach in order to assess the variation of the chemical structure with respect to the reference linear PS due to the cross-linking process (§6.6.3.2, point a). The study was conducted in the sub-surface region to disregard the spectral interference causes by the PDMS surface contamination, evidenced both in XPS and static-SIMS. The cross-linked PS shows the aromatic signature of the polystyrene, despite the fact that aromatic fragment ions, like for instance $C_7H_7^+$ (m/z = 91) and $C_9H_7^+$ (m/z = 115), are less intense. Conversely to the linear PS, the cross-linked counterpart contains a relatively high percentage of oxygen, as demonstrated at the surface by XPS and static-SIMS, and along the depth by SIMS molecular depth-profiling. The origin of the O-uptake remains unknown, since the manufacturer did not provide any information about the cross-linking procedure adopted, and more in general about the synthesis of the material. The SIMS characterization of the bulk reveals that the grafting of oxygen mostly occurs along the aliphatic backbone (detection of small $C_{1-5}H_xO_y^+$ ions, where the most outstanding is $C_2H_3O^+$). In addition, XPS analysis highlights a preponderant presence of C_{aliph}-OR functional groups at the sample surface, when the contribution to the O 1s peak given by the PDMS contamination is subtracted (cf. Figure 8). The presence of additives of high M_w contributing to the oxygen detection in the SIMS positive ion mass spectra of the bulk-like region can be disregarded, since no molecular ions (intended as the entire additive molecule protonated or deprotonated) appear at the highest m/z ratios (spectra recorded up to 3000 amu). SIMS mass spectra of the bulk of the cross-linked PS also show an increased secondary ion yield ratio of aliphatic (un)saturated C_{1-4} ions to the aromatic ones at m/z > 91 amu. This leads to the hypothesis that the cross-linking has very likely been performed by addition of a cross-linking agent, such as the divinylbenzene (DVB) commonly utilized by the polymer industry in these cases. Indeed, the use of DVB causes a sort of dilution of the aromatic content in favor of the aliphatic saturated moieties, and consequently of the emission of smaller aliphatic ions to the detriment of the bigger aromatic ions. This hypothesis seems to be corroborated by the increased XPS ratio $\underline{C}C_{aliph}$/ $\underline{C}C_{arom}$ (0.66) compared to the linear PS (0.54) (results not shown in Table 3), accompanied by a noticeable decrease of the shake-up satellite (of ~3 times, refer to Table 3). Furthermore, the intensity increase of the secondary ion $C_9H_{11}^+$ is observed, that can be related to the alkyl-substitution of the aryl groups. This is in rather good agreement with the small IR band observed at 797 cm^{-1} (Figure 11), indicating the para-substitution of the phenyl groups that can be explained by the use of 1-2% of DVB (prevalently the para-isomer) to induce the cross-linking of the polymer matrix (refer to Figure 27).

Then, the pp-PS films were compared with the conventionally polymerized counterparts (cross-linked and not) in §6.6.3.2, point b, looking at their bulks in order to avoid the influence of the surface contamination (demonstrated in XPS), and more importantly the post-oxidation. The SIMS/PCA investigation reveals the inversed intensity ratio of the tropylium ion $C_7H_7^+$ (m/z = 91) and the postulated methyl-substituted tropylium ion $C_8H_9^+$ (m/z = 105). The tropylium ion is the most characteristic of both the conventional PS, whereas its methyl-substituted $C_8H_9^+$ becomes the most intense in the mass spectra of the overall plasma series (followed in intensity by $C_7H_7^+$ and $C_6H_5^+$ as illustrated in Figure 18). Hence, the ion $C_8H_9^+$ represents a peculiar structural feature of the pp-PS films deposited by plasma at sub-atmospheric pressure. This observation has been already reported for the pp-PS films deposited in DBD near atmospheric pressure[v] by Merche and co-workers using Ar or He as plasmagen gas.[5] Also the plasma polymerizations of the styrene monomer at low pressure carried out by Leggett and collaborators[vi] in 1995,[33] and more recently by Oran[vii],[32,43] show the same spectral feature. Leggett and al. considered the $91^+/105^+$ ratio as an indicator of the cross-linked character of the plasma-deposited films (it decreases with increasing branching and/or cross-linking). Following the protocol proposed by Leggett et al.,[33] Oran applied the $91^+/105^+$ intensity ratio to evaluate the augmentation of the cross-linked and/or branched content in the films synthesized from the styrene monomer by asymmetrical pulsed plasma as a function of the power and the duty cycle.[32,43] However, in this work the $91^+/105^+$ ratio decreases in the case of the plasma films compared to the linear PS (thus the cross-linking and/or branching increases), but conversely to what is expected, it remains constant with increasing plasma power (see Figure 21.b, §6.6.3.1). This suggests a more complex situation, where additional factors need to be taken into account,

---

[v] SSIMS spectra acquired on a PHI-Evans-TFS-4000 MMI (TRIFT 1) spectrometer with a source of 12 keV Ga^+ primary ions (600 pA).

[vi] SSIMS spectra acquired with a quadrupole mass spectrometer by using 3.5 keV Xe^+ primary ions.

[vii] A TOF.SIMS IV instrument was used with a 10 keV Cs^+ primary ion beam (0.75 pA).

like for instance the oxidized character pointed out by the IR bulk characterization and quantified by XPS at the surface (from ~7% to ~9%). Indeed, the presence of oxidation can play an important role influencing the probability of ionization of secondary ions. This factor was not present in the plasma deposits prepared by Oran, which, being synthesized at low pressure and then analyzed in-situ, were lacking of oxygen.[32] The O-uptake of films obtained from the styrene monomer plasma-polymerized in similar experimental conditions than those employed in this study was also detected by Merche and collaborators thanks to XPS, static-SIMS and FT-IR characterization.[5] In that work, the authors speculated that the O-uptake occurs during the plasma polymerization and/or it is due to post-polymerization oxidation in the air, since radical species remain trapped in the film after plasma deposition.[18] Optical emission spectroscopy (OES) of the Ar/DBD carried out by Merche shows Ar lines, together with impurities of nitrogen and small peaks OH, but not O at 777 nm.[5] In this investigation, SIMS molecular depth-profiling demonstrates that relatively thick plasma films, like pp-PS/70W (maximum thickness of ~8 μm, see Figure 10 of §6.4.1), show constant signals of O-containing fragment ions in the inner layers (after a few tens of nm from the air/polymer interface) of the film down to the interface with the silicon substrate. This is coherent with the IR analyses (Figure 13), that demonstrate a significant oxidation of the bulk of all the plasma films. Only in the outermost polymer layers, an increase of the O-based ions is observed in depth-profiles acquired a few hours later the plasma deposition. This seems to indicate that the O-uptake evidenced by the PCA study of the bulk-like region is fundamentally occurring in the reactor during the growth phase of the polymer deposit, rather than being the result of post-oxidation in the air. Moreover, from XPS and PCA (Figure 29) the oxidation appears to increase with increasing power, probably as a consequence of the augmentation of the radicals formed in the polymer and those from the O_2 molecules.

Furthermore, pp-PS films show an increase of the ratio of the aliphatic to aromatic fractions compared to the linear PS. Thus, they are more assimilated to the cross-linked PS, especially at higher powers. Moreover, the O-based functional groups seem to be grafted along the polymer aliphatic (un)saturated backbone, rather than to the phenyl rings. This can be partly confirmed by the comparison with the fragmentation pattern of the poly (vinyl phenol) or PVP, where -OH groups are linked to the aromatic rings (§6.6.3.5). XPS analysis elucidates that C-OH or alcohol groups are predominant at the surface of the pp-PS films, and that the oxidation increases of around 2% at the expense of the aromaticity (represented by the shake-up satellite) with increasing plasma power from 10 to 80 W (Figure 8 and 9). This could suggest an oxidative functionalization of the phenyl rings with subsequent disruption of the aromaticity, as described by Potter et al.[18] However, a concomitant fragmentation of the styrene monomer in the plasma medium, leading to the loss of aromatic rings[54],[viii] and the O-grafting to the aliphatic moieties of the polymer in growth cannot be excluded. Unfortunately, OES conducted on the Ar/styrene discharge used in this study did not evidence the presence of any fragmentation products of the styrene monomer.[ix] These results are in rather good agreement with Merche's Ph.D. thesis (not shown).[55] This is supposed to be due to a strong dilution of the styrene in the more emissive Ar plasmagen gas. Emissive species of styrene are $C_4H_2^+$ (506.8 nm), CH· (431.4 nm), H_α and H_2 reported in the work of Chen and Yang,[56] while Z. Li et al. individuate C_6H_6, CH, and C_2, among others.[26] Both cases deal with only styrene discharges. The decrease of the aromatic content in the plasma-polymers is confirmed in the bulk by IR characterization where, according to Prohaska[25] and Chen,[20] it is also possible to determine that the aromaticity decreases as a function of the power (see the A3027/A2927 ratio defined in §6.4.2 as the ratio of the peak heights of the ν (aromatic CH) at 3027 cm^{-1} to the ν_{as} (aliphatic CH_2) at 2927 cm^{-1}). However, in IR the discrimination between aromaticity and unsaturation is problematic.

An important difference between cross-linked PS and pp-PS emerges through the $C_9H_{11}^+$ ion at m/z 119. Indeed, the alkyl-substitution (more precisely in position -para as elucidated by IR) of the cross-linked PS, due to the use of the cross-linking agent DVB, leads to an augmentation of small aliphatic saturated ions with respect to the linear PS, such as CH_3^+ or $C_2H_5^+$. Conversely, in the case of the pp-PS films, the increased intensity of CH_3^+ does not follow the $C_9H_{11}^+$ and $C_2H_5^+$. This is compatible with the prevalence of mono-substitution of the aryl groups found out in the IR analyses and a more unsaturated polymer backbone. This experimental evidence seems to indicate that the higher intensity of CH_3^+ with respect to the linear PS is related to the methyl-substitution of the plasma-polymer (i.e. branching)

[viii] According to Yasuda, two types of C=C can be found in styrene: aromatic C=C with bond energy of 2.7 eV, and alkene with relatively high bond energy of 6.4 eV, thus more difficult to break.[26]

[ix] OES measurements were not conducted during the plasma deposition of the polymer samples studied in this chapter, but at a later stage.

and/or the higher density of chain-ends, the latter being influenced by the cross-linking and the branching (impossible to discern each other).

The influence of the power applied to the plasma on the chemical structure of the pp-PS deposits was investigated in more details by SIMS/PCA in §6.6.3.2 (point c). The evolution of the polymer structure in the given interval of powers show a saturation level towards 70-80 W. Four are the "key" ions that permit to summarize the structural variations of the pp-PS as a function of power: $C_8H_9^+$ (105^+), $C_7H_7^+$ (91^+), $C_6H_5^+$ (77^+), and CH_3^+ (15^+) (in decreasing order of m/z ratio). Increasing the power, $C_8H_9^+$ and $C_7H_7^+$ decrease, in addition to the other PS-like fragment ions with $m/z \geq 91$ (included $C_9H_{11}^+$ or 119^+, previously mentioned in the comparison with the cross-linked PS). Conversely, the aromatic ion $C_6H_5^+$ (related to the phenyl ring) at m/z 77 increases, as well as a series of small aliphatic ions ($C_3H_3^+$, $C_4H_3^+$, $C_5H_3^+$, $C_2H_3^+$), and the CH_3^+. Small O-containing ions ($C_2H_3O^+$, $C_7H_5O^+$, $C_3H_3O^+$) increase with increasing power, while bigger oxidized ions like $C_8H_9O^+$ decreases. This mirrors the increase of the aliphatic fraction in the polymer matrix with the increase of power. Concerning the methyl-substitution, it is already reported in the literature the case of the plasma-polymerized styrene since 1966[1], but also for other polymer materials like the plasma-polymerized vinylferrocene[3] or the 2-vinylpyridine.[2] In the particular case of plasma-polymerized styrene at low pressure, Prohaska hypothesized a structure similar to the poly (α-methyl styrene) or poly (β-methyl styrene) on the basis of IR characterization.[25] Here, the comparison of the fragmentation pattern in the sub-monomer region of two methyl-substituted PS derivatives, i.e. PAMS and P4MS, seems to corroborate the fact that the $-CH_3$ groups are bonded to C_α, C_β, C_γ, and so on, but not to the phenyl rings. This is in agreement with the prevalence of mono-substitution observed in IR (refer to §6.4.2, point D). However, pp-PS films lack of repeat unit, being characterized by an irregular structure, cross-linked and branched. Thus, the high concentration of $-CH_3$ groups could be explained by the branching (refer to §6.4.2, point B). In this context, the polymerization degree can also play an important role. Indeed, GPC analyses carried out at 30 W and 60 W revealed the presence of oligomers (2-20 repeat unit if compared to the PS standards), although the plasma films are well polymerized as demonstrated by the undissolved polymer matrix after several hours of immersion in the solvent and heating (§6.5). This is also compatible with a high cross-linked character of the polymer deposited in the DBD at sub-atmospheric pressure. The significant presence of oligomers at 10 W can be supported by the estimation of the sputter yield volume (almost a factor of 2 with respect to 80 W, cf. Figure 35 of §6.6.3.4). This higher presence of oligomers could determine a higher density of -CH_3 chain ends, so that a significant contribution to the methyl-substitution observed in IR comes from the degree of polymerization. This factor, in combination with the -CH_3 grafting along the polymer backbone, might explain the inversed ratio $91^+/105^+$ that characterizes the plasma-deposited styrene films. Additionally, $C_8H_9^+$ (105^+) and $C_7H_7^+$ (91^+) decrease with power, because of a polymer network more cross-linked. A higher cross-linked and/or branched content (established in XPS, IR, and SIMS), also leads to an increase of the emission probability of smaller fragment ions, like the aromatic $C_6H_5^+$ (77^+) and the aliphatic CH_3^+ (15^+). The higher presence of oligomers at lower powers might explain the higher relative intensity of the dimer-related ion $[2M+H]^+$ at m/z 207 (as well as $[M+H]^+$,) as illustrated in Figure 23 (§6.6.3.1), and the $[3M-H]^+$ ion only at 10 W and 20 W (Figure 24). Additionally, the stability of the plasma samples has been tested after a 5-months ageing, showing a very slight increase of the oxidation and the preservation of the $91^+/105^+$ ratio.

In conclusion, all these experimental evidences point to an enhancement of the fragmentation of the styrene monomer with increasing the plasma power, and consequently a reduction of the aromaticity content in the resulting polymer deposits,[43,57] accompanied by an increase of the branching/cross-linking and oxidized content, and a diminution of the oligomer trapped in the polymer structure.

6.8. Conclusion

This study demonstrates the possibility to probe the actual chemical structure of plasma-polymers, looking at the bulk thanks to the application in ToF-SIMS depth-profiling of massive Ar cluster ion beams (Ar_n^+) as sputter sources. Indeed, SIMS analysis of the inner layers of plasma coatings is exempted from spectral interferences due to post-oxidation in air and organic surface contamination. In this work, for the first time, the elucidation of the most outstanding chemical and structural features related to the sub-surface of plasma-deposited styrene films near atmospheric pressure, and as a function of the injected power, have been successfully conducted by the combined dynamic-SIMS/PCA approach. To this purpose, plasma coatings have been comparatively studied with the conventionally polymerized counterparts, i.e. linear and cross-linked PS. Additional commercial reference polymers have been considered, in order to clarify the origin of the methyl-substitution reported by Jesch et al. in 1966 for plasma-synthesized styrene coatings in a glow discharge on the basis of infrared absorption techniques. Briefly, the high concentration of -CH_3 groups in the polymer matrix is ascribed to branching or grafting of $CH_3\cdot$ radicals to active sites (prevalently in position α, β, γ) along the aliphatic backbone (also forming chain ends by termination reactions), and a relatively high fraction of trapped oligomers. The oligomer contribution (whose presence has been proved by GPC) has been supported by an original study based on the M_w dependence of the sputter yield volume Y of PS standards. The overall SIMS experimental evidences suggest a milder fragmentation of the monomer at lower powers, leading to a higher conservation of the aromaticity and a lesser branched and/or cross-linked content. These two main features have been confirmed by an independent IR bulk characterization of the specimens, as well as the O-uptake that mainly occurs during the plasma polymerization under sub-atmospheric pressure. XPS analyses of the surface of the plasma coatings have demonstrated the gradual increase of the O-uptake to the detriment of the aromaticity with increasing power. This is in rather good agreement with the SIMS and IR bulk characterizations. In this respect, it should be interesting to perform XPS depth-profiling with large Ar_n^+ ion sputtering to probe the chemical composition of the sub-surface region for a direct comparison with the SIMS mass spectra obtained in this study. Furthermore, a more detailed investigation of the oxidation could be attempted by SIMS molecular depth-profiling in negative ion polarity, which was not performed in this work due to the poor information content provided about unsaturation, aromaticity, cross-linking, and branching.

6.9. Supporting information

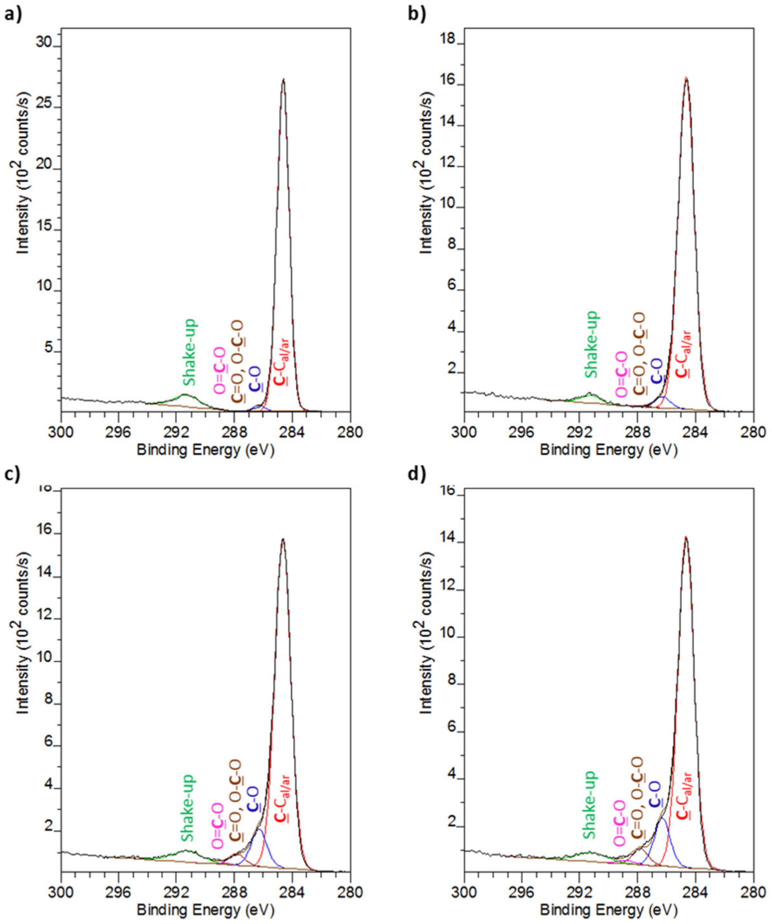

Figure S1. *Fitting of the C 1s photoelectron peak for (a) linear PS, (b) cross-linked-PS, (c) pp-PS/10W, and (d) pp-PS/80W.*

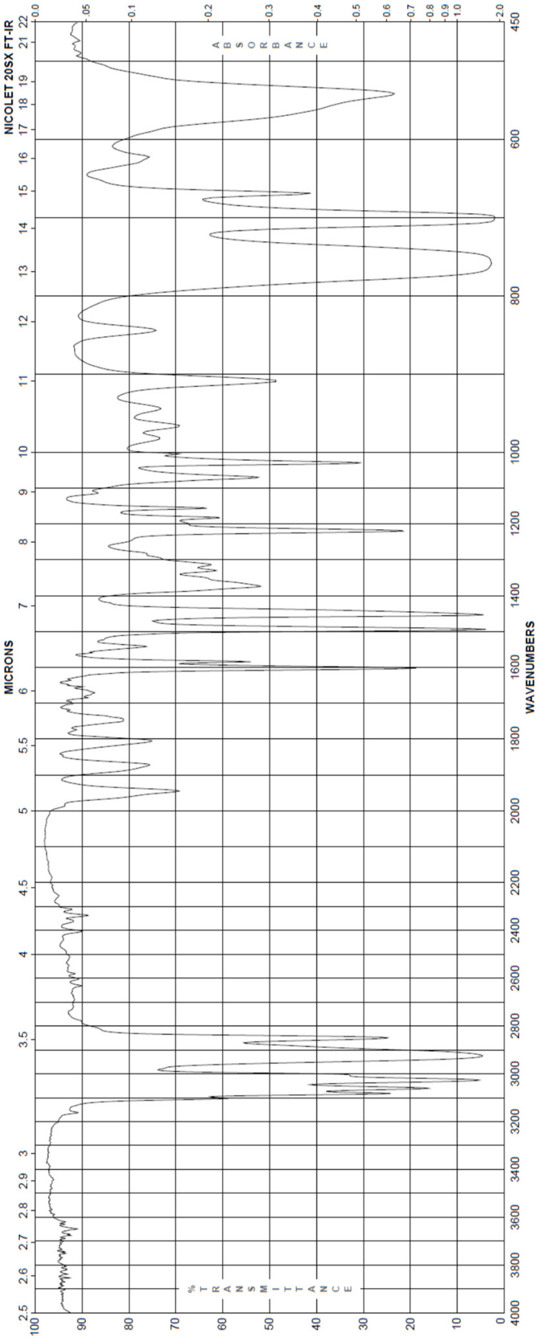

Figure S2. *FT-IR spectrum of polystyrene (M_w=1000 g/mol) from www.sigmaaldrich.com.*

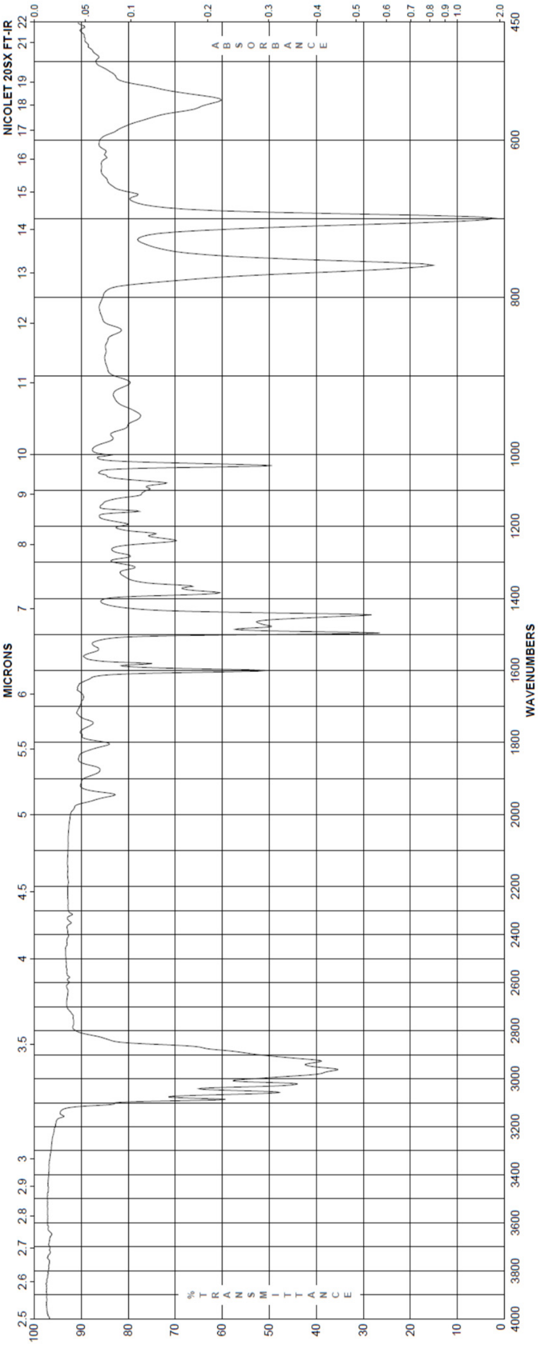

Figure S3. *FT-IR spectrum of poly (alpha-methyl styrene) (PAMS) (M_w ~10000 g/mol) from www.sigmaaldrich.com.*

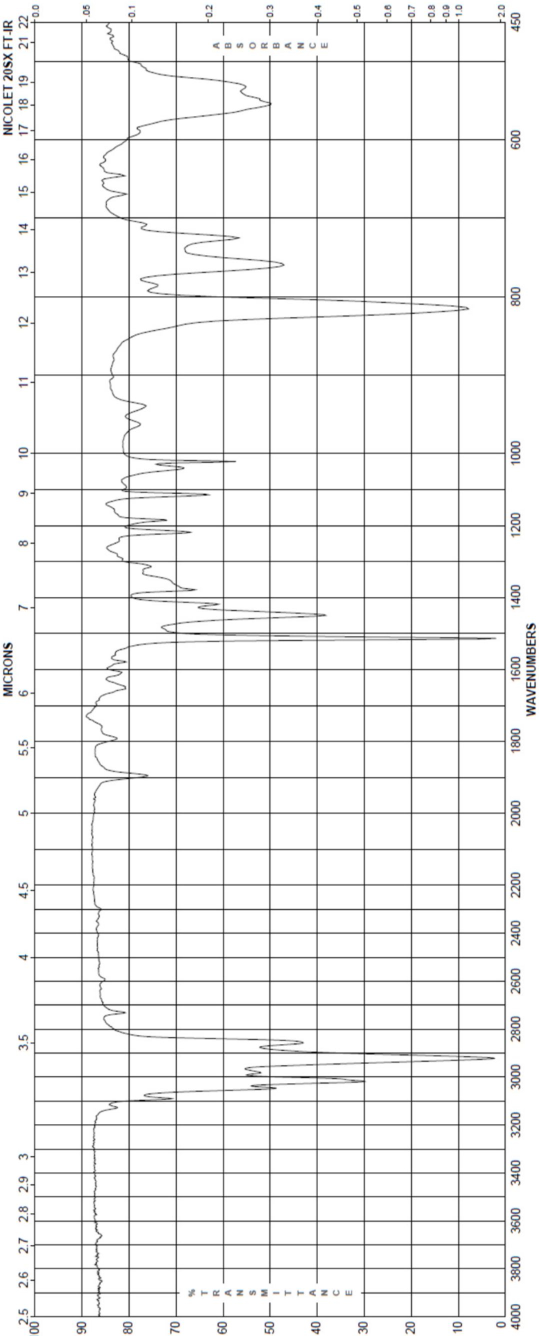

Figure S4. *FT-IR spectrum of poly (4-methyl styrene) (P4MS) (M_w ~70000 g/mol) from www.sigmaaldrich.com.*

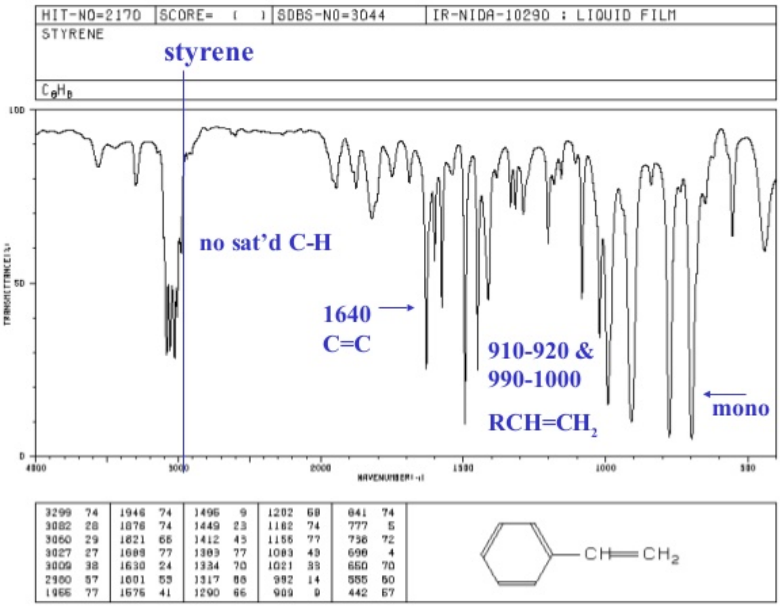

HIT-NO=2170 | SCORE= ( ) | SDBS-NO=3044 | IR-NIDA-10290 : LIQUID FILM

STYRENE

C_8H_8

3299	74	1946	74	1496	9	1202	68	841	74
3082	28	1876	74	1449	23	1182	74	777	5
3060	29	1821	66	1412	45	1156	77	758	72
3027	27	1689	77	1303	77	1083	49	698	4
3009	38	1630	24	1334	70	1021	33	650	70
2980	57	1601	53	1317	88	992	14	555	60
1966	77	1576	41	1290	66	909	9	442	67

Figure S5. *IR spectrum of styrene from SDBS website.*[23]

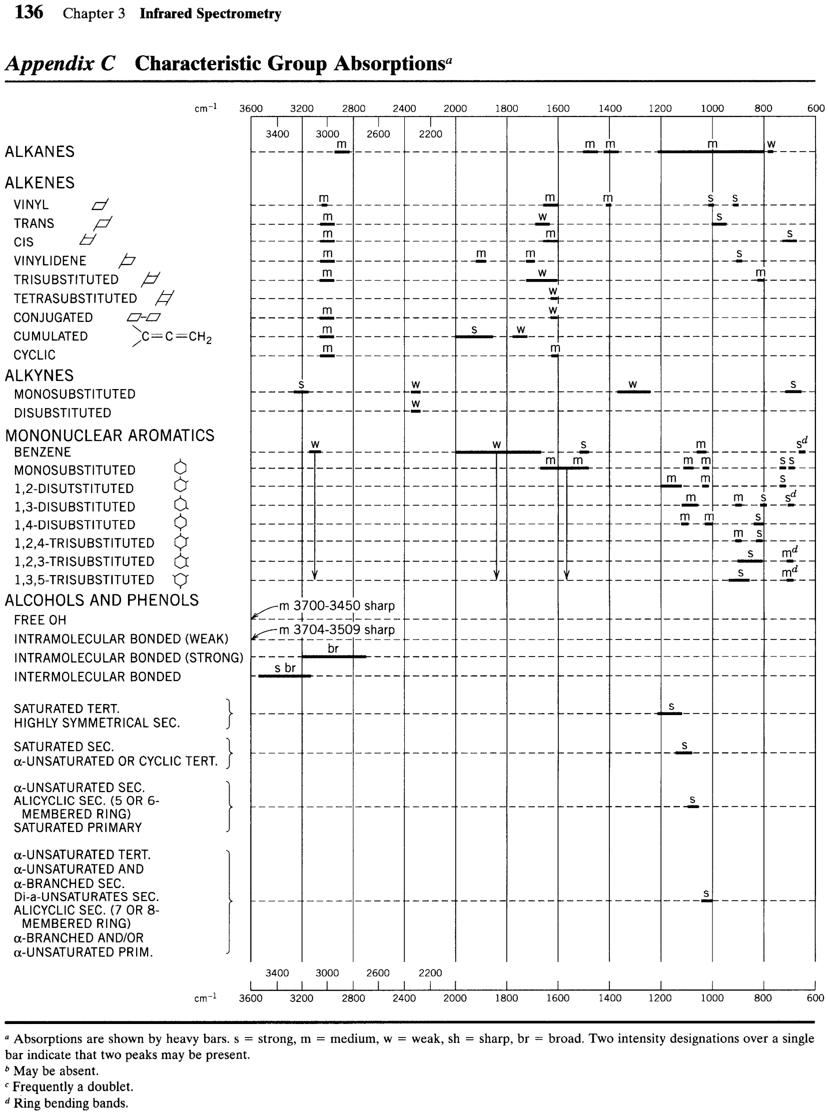

136 Chapter 3 **Infrared Spectrometry**

***Appendix C* Characteristic Group Absorptions**[a]

[a] Absorptions are shown by heavy bars. s = strong, m = medium, w = weak, sh = sharp, br = broad. Two intensity designations over a single bar indicate that two peaks may be present.

[b] May be absent.

[c] Frequently a doublet.

[d] Ring bending bands.

Table S1. *IR correlation table from "Spectrometric identification of organic compounds" of Silverstein et al.*[58]

PC1 (100%) loading > 0 *Cross-linked PS*			**PC1 (100%) loading < 0** *Linear PS*		
Loading	**Mass**	**Peak**	**Loading**	**Mass**	**Peak**
0.257	43.020	$C_2H_3O^+$	-0.879	91.060	*$C_7H_7^+$
0.093	29.039	$C_2H_5^+$	-0.170	115.056	*$C_9H_7^+$
0.068	41.040	$C_3H_5^+$	-0.162	117.075	*$C_9H_9^+$
0.042	57.071	$C_4H_9^+$	-0.140	193.110	*$C_{15}H_{13}^+$
0.041	119.091	$C_9H_{11}^+$	-0.127	105.079	*$C_8H_9^+$
0.039	55.057	$C_4H_7^+$	-0.099	103.056	*$C_8H_7^+$
			-0.073	92.061	$C_7H_8^+$
			-0.073	129.073	$C_{10}H_9^+$
			-0.063	104.062	$C_8H_8^+$
			-0.060	77.039	*$C_6H_5^+$
			-0.051	167.091	$C_{13}H_{11}^+$
			-0.050	128.062	*$C_{10}H_8^+$
			-0.044	181.110	$C_{14}H_{13}^+$
			-0.040	194.111	$C_{15}H_{14}^+$
			-0.039	165.071	*$C_{13}H_9^+$
			-0.035	116.060	$C_9H_8^+$
			-0.032	178.078	*$C_{14}H_{10}^+$
Most characteristic PS ions: *$C_xH_y^+$			-0.031	131.092	$C_{10}H_{11}^+$
O-containing ions: $C_xH_yO_z^+$			-0.027	63.023	*$C_5H_3^+$

Table S2. *List of the most influential PC1 loadings, and corresponding molecular ion fragments, extracted from the PCA obtained on the ToF-SIMS positive ion mass spectra of the two commercial PS samples (linear and cross-linked). A loading threshold of ±0.025 has been fixed.*

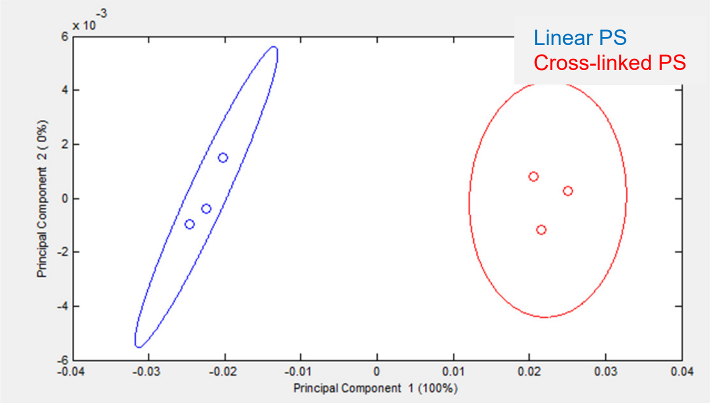

Figure S6. *PC2 versus PC1 scores plot obtained from the PCA applied to the ToF-SIMS positive ion mass spectra of the two commercial PS samples (linear and cross-linked), and based on a peak list constituted exclusively of hydrocarbon ions in the m/z range 0-210 amu.*

PC1 (100%) loading > 0 *Cross-linked PS*			**PC1 (100%) loading < 0** *Linear PS*		
Loading	**Mass**	**Peak**	**Loading**	**Mass**	**Peak**
0.244	29.039	$C_2H_5^+$	-0.839	91.060	*$C_7H_7^+$
0.234	41.040	$C_3H_5^+$	-0.193	193.110	*$C_{15}H_{13}^+$
0.135	39.023	*$C_3H_3^+$	-0.139	117.075	*$C_9H_9^+$
0.112	119.091	$C_9H_{11}^+$	-0.099	115.056	*$C_9H_7^+$
0.109	27.023	*$C_2H_3^+$	-0.077	103.056	*$C_8H_7^+$
0.109	57.071	$C_4H_9^+$	-0.074	104.062	$C_8H_8^+$
0.108	55.057	$C_4H_7^+$	-0.067	92.061	$C_7H_8^+$
0.055	53.040	$C_4H_5^+$	-0.061	167.091	$C_{13}H_{11}^+$
0.052	51.023	*$C_4H_3^+$	-0.059	181.110	$C_{14}H_{13}^+$
0.050	43.055	$C_3H_7^+$	-0.059	194.111	$C_{15}H_{14}^+$
0.049	67.058	$C_5H_7^+$	-0.043	129.073	$C_{10}H_9^+$
0.035	15.022	CH_3^+	-0.027	105.079	*$C_8H_9^+$
			-0.025	207.129	$C_{16}H_{15}^+$
			Most characteristic PS ions: *$C_xH_y^+$		

Table S3. *List of the most influential PC1 loadings, and corresponding secondary ions, extracted from the PCA obtained on the positive ion mass spectra of the two commercial PS samples (linear and cross-linked), and based on a peak list constituted exclusively of hydrocarbon ions in the m/z range 0-210 amu (refer to Figure S1). A loading threshold of ±0.025 has been fixed.*

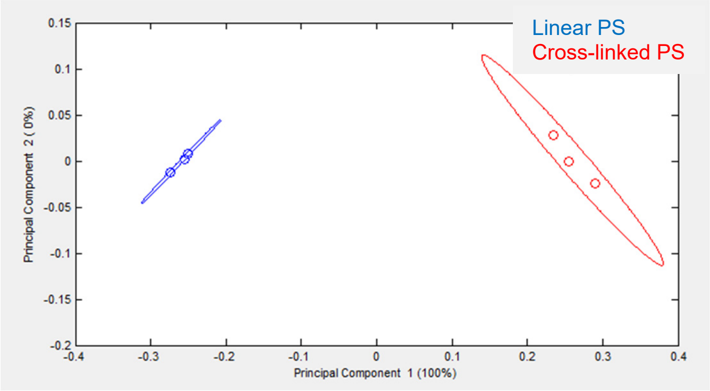

Figure S7. *PC2 versus PC1 scores plot obtained from the PCA applied to the ToF-SIMS positive ion mass spectra of the two commercial PS samples (linear and cross-linked), and based on a peak list constituted exclusively of O-containing ions in the m/z range 0-210 amu.*

PC1 (85%) loading > 0			**PC1 (85%) loading < 0**		
Linear PS			*10-80 W*		
Loading	**Mass**	**Peak**	**Loading**	**Mass**	**Peak**
0.888	91.060	*$C_7H_7^+$	-0.281	105.078	*$C_8H_9^+$
0.186	117.075	*$C_9H_9^+$	-0.087	43.020	$C_2H_3O^+$
0.171	115.056	*$C_9H_7^+$	-0.069	105.035	$C_7H_5O^+$
0.132	193.111	*$C_{15}H_{13}^+$	-0.037	55.020	$C_3H_3O^+$
0.080	103.056	*$C_8H_7^+$	-0.027	77.039	*$C_6H_5^+$
0.076	92.061	$C_7H_8^+$	-0.025	106.076	$C_8H_{10}^+$
0.075	129.074	$C_{10}H_9^+$	-0.020	121.070	$C_8H_9O^+$
0.054	104.062	$C_8H_8^+$	-0.014	107.051	$C_7H_7O^+$
0.046	167.092	$C_{13}H_{11}^+$	-0.011	131.052	$C_9H_7O^+$
0.044	131.091	$C_{10}H_{11}^+$			
0.041	116.060	$C_9H_8^+$			
0.038	181.109	$C_{14}H_{13}^+$			
0.036	128.062	$C_{10}H_8^+$			
0.033	194.110	$C_{15}H_{14}^+$			
0.022	178.078	*$C_{14}H_{10}^+$			
0.020	65.039	*$C_5H_5^+$			
0.018	118.078	$C_9H_{10}^+$			
0.017	207.129	$C_{16}H_{15}^+$			
0.015	191.089	$C_{15}H_{11}^+$			
0.014	165.071	*$C_{13}H_9^+$			
0.014	179.088	$C_{14}H_{11}^+$			
0.013	102.046	$C_8H_6^+$			
0.011	141.077	$C_{11}H_9^+$			
0.011	130.077	$C_{10}H_{10}^+$	Most characteristic PS ions: *$C_xH_y^+$		
0.010	78.045	$C_6H_6^+$	O-containing ions: $C_xH_yO_z^+$		

Table S4. *List of the most influential PC1 loadings, and corresponding secondary ions, extracted from the PCA obtained on the ToF-SIMS positive ion mass spectra of the linear PS and the pp-PS films deposited by DBD at different plasma powers (10-80 W). A loading threshold of ±0.01 has been fixed.*

PC2 (15%) loading > 0 40-80 W & Linear PS			**PC2 (15%) loading < 0** 10-30 W		
Loading	**Mass**	**Peak**	**Loading**	**Mass**	**Peak**
0.087	39.023	*$C_3H_3^+$	-0.931	105.078	*$C_8H_9^+$
0.071	51.023	*$C_4H_3^+$	-0.270	91.060	*$C_7H_7^+$
0.071	43.020	$C_2H_3O^+$	-0.074	106.076	$C_8H_{10}^+$
0.064	63.023	*$C_5H_3^+$	-0.073	129.074	$C_{10}H_9^+$
0.057	77.039	*$C_6H_5^+$	-0.056	121.070	$C_8H_9O^+$
0.049	105.035	$C_7H_5O^+$	-0.034	117.075	*$C_9H_9^+$
0.043	27.023	*$C_2H_3^+$	-0.033	205.110	$C_{16}H_{13}^+$
0.034	75.023	$C_6H_3^+$	-0.025	207.129	$C_{16}H_{15}^+$
0.030	65.039	*$C_5H_5^+$	-0.021	179.088	$C_{14}H_{11}^+$
0.030	41.040	$C_3H_5^+$	-0.020	107.051	$C_7H_7O^+$
0.029	53.039	$C_4H_5^+$	-0.019	92.061	$C_7H_8^+$
0.028	87.023	$C_7H_3^+$	-0.013	191.089	$C_{15}H_{11}^+$
0.026	74.014	$C_6H_2^+$	-0.011	206.114	$C_{16}H_{14}^+$
0.025	55.020	$C_3H_3O^+$	-0.010	131.091	$C_{10}H_{11}^+$
0.025	50.014	$C_4H_2^+$	-0.010	181.109	$C_{14}H_{13}^+$
0.024	115.056	*$C_9H_7^+$			
0.022	62.014	$C_5H_2^+$			
0.019	86.014	$C_7H_2^+$			
0.017	152.061	*$C_{12}H_8^+$			
0.017	98.014	$C_8H_2^+$			
0.016	139.059	$C_{11}H_7^+$			
0.015	52.030	$C_4H_4^+$			
0.013	189.069	$C_{15}H_9^+$			
0.013	99.022	$C_8H_3^+$			
0.013	78.045	$C_6H_6^+$			
0.013	76.030	$C_6H_4^+$			
0.012	89.038	$C_7H_5^+$			
0.011	163.054	$C_{13}H_7^+$			
0.011	110.014	$C_9H_2^+$			
0.011	38.014	$C_3H_2^+$			
0.011	102.046	$C_8H_6^+$	Most characteristic PS ions: *$C_xH_y^+$		
0.010	29.002	CHO^+	O-containing ions: $C_xH_yO_z^+$		

Table S5. *List of the most influential PC2 loadings, and corresponding secondary ions, extracted from the PCA obtained on the ToF-SIMS positive ion mass spectra of the linear PS and the pp-PS films deposited by DBD at different plasma powers (10-80 W). A loading threshold of ±0.01 has been fixed.*

PC1 (98%) loading > 0 *40W - 80W*			**PC1 (98%) loading < 0** *10W - 30W*		
Loading	**Mass**	**Peak**	**Loading**	**Mass**	**Peak**
0.087	43.020	$C_2H_3O^+$	-0.855	105.078	$*C_8H_9^+$
0.085	39.023	$*C_3H_3^+$	-0.444	91.060	$*C_7H_7^+$
0.069	51.023	$*C_4H_3^+$	-0.086	129.074	$C_{10}H_9^+$
0.063	63.023	$*C_5H_3^+$	-0.071	117.075	$*C_9H_9^+$
0.062	105.035	$C_7H_5O^+$	-0.068	106.076	$C_8H_{10}^+$
0.061	77.039	$*C_6H_5^+$	-0.051	121.070	$C_8H_9O^+$
0.044	27.023	$*C_2H_3^+$	-0.034	92.061	$C_7H_8^+$
0.035	75.023	$C_6H_3^+$	-0.033	205.110	$C_{16}H_{13}^+$
0.032	55.020	$C_3H_3O^+$	-0.028	207.129	$C_{16}H_{15}^+$
0.029	53.039	$C_4H_5^+$			
0.029	41.040	$C_3H_5^+$			
0.028	87.023	$C_7H_3^+$			
0.027	74.014	$C_6H_2^+$	Most characteristic PS ions: $*C_xH_y^+$		
0.026	65.039	$*C_5H_5^+$	O-containing ions: $C_xH_yO_z^+$		

Table S6. *List of the most influential PC1 loadings, and corresponding secondary ions, extracted from the PCA obtained on the ToF-SIMS positive ion mass spectra of the pp-PS films deposited by DBD at different plasma powers (10-80 W). A loading threshold of ±0.025 has been fixed.*

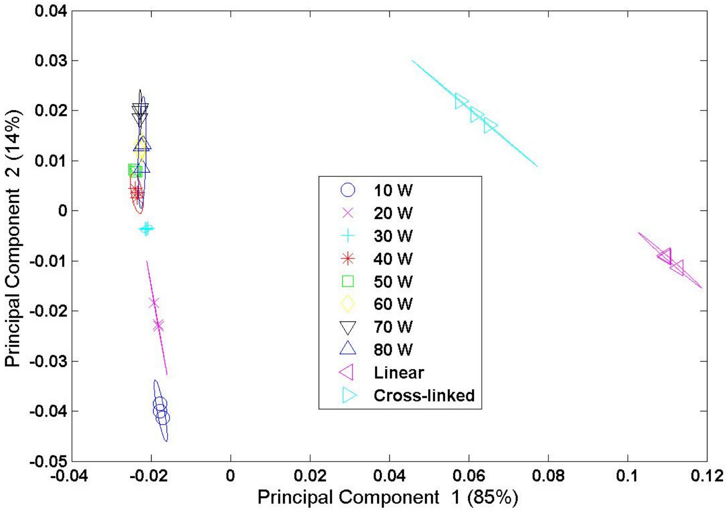

Figure S8. *PC2 versus PC1 scores plot obtained from the PCA applied to the ToF-SIMS positive ion mass spectra of the two conventionally polymerized polystyrenes (linear and cross-linked), and the plasma-synthesized polymer at different powers (10-80 W).*

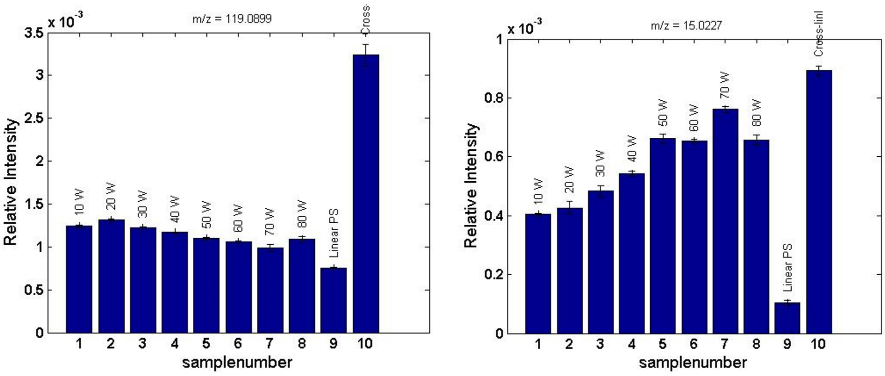

Figure S9. *Intensity normalized by total counts (relative intensity) of the secondary ions* $C_9H_{11}^+$ *(m/z = 119.0899) and* CH_3^+ *(m/z = 15.0227), respectively, for the entire series of pp-PS deposits and the two commercial PS.*

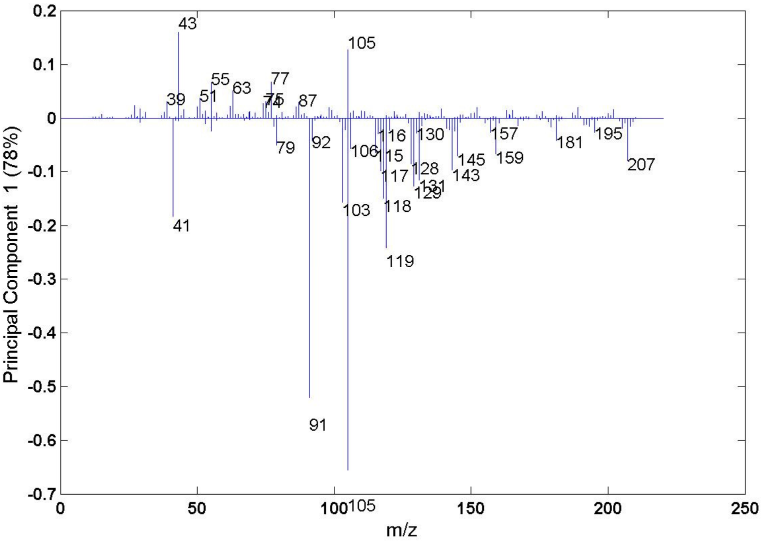

Figure S10. *PC1 (78%) loadings plot of the PCA applied to the poly (alpha-methyl styrene) (PAMS), and the pp-PS films deposited by DBD at different plasma powers (10-80 W). The loading threshold has been set at ±0.025. The nominal masses are reported, while the corresponding ion attributions can be found in Table 5.*

6.10. References

[1] K. Jesch, J. E. Bloor, P. L. Kronick. Structure and physical properties of glow discharge polymers. I. Polymers from hydrocarbons. *J. Polym. Sci. A-1* **1966**, *4*, 1487.

[2] K. W. Bieg, D. K. Ottesen, *Plasma polymerization*, M. Shen and A. T. Bell, Eds., ACs Symp. Ser., **1979**, 108-128.

[3] M. F. Dautartas. Studies of plasma polymerized vinylferrocene thin films. Ph.D. Thesis, University of Minnesota, **1982**.

[4] Polystyrene sheet: Material information.
http://www.goodfellow.com/E/Polystyrene-Sheet.html

[5] D. Merche, C. Poleunis, P. Bertrand, M. Sferrazza, F. Reniers. Synthesis of polystyrene thin films by means of an atmospheric-pressure plasma torch and a dielectric barrier discharge. *IEEE Transactions on Plasma Science* **2009**, *37*, 951.

[6] D. Merche, Synthèse et caractérisation de couches de polystyrène et de polystyrène sulfoné obtenues par polymérisation-plasma à pression (sub)-atmosphérique, Université libre de Bruxelles, **2011**.

[7] A. A. Howling, J.-L. Dorier, C. Hollenstein, U. Kroll, F. Finger. Frequency effects in silane plasmas for plasma enhanced chemical vapor deposition. *Journal of Vacuum Science & Technology A* **1992**, *10*, 1080.

[8] B. Andries, G. Ravel, L. Peccoud. Electrical characterization of radio-frequency parallel-plate capacitively coupled discharges. *Journal of Vacuum Science & Technology A* **1989**, *7*, 2774.

[9] N. Spiliopoulos, D. Mataras, D. E. Rapakoulias. Power dissipation and impedance measurements in radio-frequency discharges. *Journal of Vacuum Science & Technology A* **1996**, *14*, 2757.

[10] M. A. Sobolewski, J. G. Langan, B. S. Felker. Electrical optimization of plasma-enhanced chemical vapor deposition chamber cleaning plasmas. *Journal of Vacuum Science & Technology B* **1998**, *16*, 173.

[11] B. Andries, G. Ravel, L. Peccoud. Electrical characterization of radio-frequency parallel-plate capacitively coupled discharges. *Journal of Vacuum Science & Technology A* **1989**, *7*, 2774.

[12] M. A. Sobolewski, R. G. Ridgeway, M. D. Bitner, D. Sinatore, P. T. Hurley. Power coupling and utilization efficiencies of silicon-depositing plasmas in mixtures of H_2, SiH_4, Si_2H_6, and Si_3H_8. *Journal of Vacuum Science & Technology A* **2014**, *32*, 041307.

[13] M. Long. Power efficiency oriented optimal design of high density CCP and ICP sources for semiconductor RF plasma processing equipment. *IEEE transactions on plasma science* **2006**, *34*, 443.

[14] M. Hołub. On the measurement of plasma power in atmospheric pressure DBD plasma reactors. *International Journal of Applied Electromagnetics and Mechanics* **2012**, *39*, 81.

[15] H.-E. Wagner, R. Brandenburg, K. V. Kozlov, A. Sonnenfeldc, P. Michela, J.F. Behnkea. The barrier discharge: Basic properties and applications to surface treatment. *Vacuum* **2003**, *71*, 417, and references herein.

[16] C. D. Wagner, L. E. Davis, M. V. Zeller, J. A. Taylor, R. H. Raymond, L. H. Gale. Empirical atomic sensitivity factors for quantitative analysis by electron spectroscopy for chemical analysis. *Surface and Interface Analysis* **1981**, *3*, 211.

[17] G. Beamson, D. Briggs. *High Resolution XPS of Organic Polymers: The Scienta ESCA 300 Database*, John Wiley & Sons, Chichester, **1992**.

[18] W. Potter, A. J. Ward, R. D. Short. The stability of plasma polymers: Part I, A preliminary XPS study of the photostability of plasma polymerised styrene and methyl methacrylate. *Polymer Degradation and Stability* **1994**, *43*, 385.

[19] I. Retzko, J. F. Friedrich, A. Lippitz, W. E. S. Unger. Chemical analysis of plasma-polymerized films: The application of X-ray photoelectron spectroscopy (XPS), X-ray absorption spectroscopy (NEXAFS) and fourier transform infrared spectroscopy (FTIR). *Journal of Electron Spectroscopy and Related Phenomena* **2001**, *121*, 111.

[20] M. Chen, T.-C. Yang, Z.-G. Ma. Plasma polymerization of styrene with controlled particle energy. *Journal of Polymer Science Part A: Polymer Chemistry* **1998**, *36*, 1265.

[21] B. H. Stuart, *Infrared spectroscopy: Fundamentals and applications*, John Wiley & Sons, Chichester, **2004**, 74.

[22] J. Coates, *Interpretation of infrared spectra, A practical approach. Encyclopedia of analytical chemistry*, John Wiley & Sons, Chichester, **2000**, p. 8.

[23] SDBSWeb: http://www.aist.go.jp/RIODB/SDBS/

[24] http://webbook.nist.gov/chemistry; The experimental details about the IR spectrum acquisition can be found here: http://webbook.nist.gov/cgi/cbook.cgi?ID=C100425&Type=IR-SPEC&Index=2

[25] G. W. Prohaska, E. D. Johnson, J. F. Evans. Preparation and characterization of plasma-polymerized styrene thin films. *Journal of Polymer Science: Polymer Chemistry Edition* **1984**, *22*, 2953.

[26] Z. Li, X. Gillon, M. Diallo, L. Houssiau, J.-J. Pireaux. Plasma diagnostic and analysis for the styrene polymerization by low pressure inductively-coupled plasma. *Proc. 19th Int. Symp. Plasma Chem.* **2009**, 1.

[27] G. Varsányi, *Assignments for vibrational spectra of 700 benzene derivatives*, Hilger, London, **1974**.

[28] S. Eufinger, W. J. Van Ooij, K. D. Conners. DC-plasma polymerization of hexamethyldisiloxane part II. Surface and interface characterization of films deposited on stainless-steel substrates. *Surface and Interface Analysis* **1996**, *24*, 841.

[29] D. Cossement, F. Renaux, D. Thiry, S. Ligot, R. Francq, R. Snyders. Chemical and microstructural characterizations of plasma polymer films by time-of-flight secondary ion mass spectrometry and principal component analysis. *Applied Surface Science* **2015**, *355*, 842.

[30] C. Poleunis, N. Médard, P. Bertrand. Additive quantification on polymer thin films by ToF-SIMS: aging sample effects. *Applied Surface Science* **2004**, *231*, 269.

[31] U. Oran, S. Swaraj, J. F. Friedrich, W. E. S. Unger. Surface analysis of plasma-deposited polymer films by Time of Flight Static Secondary Ion Mass Spectrometry (ToF-SSIMS) before and after exposure to ambient air. *Surface and Coatings Technology* **2005**, *200*, 463.

[32] U. Oran, S. Swaraj, J. F. Friedrich, W. E. S. Unger. Surface analysis of plasma-deposited polymer films, 1. *Plasma Processes and Polymers* **2004**, *1*, 123.

[33] G. J. Leggett, B. D. Ratner, J. C. Vickerman. Characterization of plasma-deposited styrene films by XPS and static SIMS. *Surface and Interface Analysis* **1995**, *23*, 22.

[34] J. C. Vickerman, D. Briggs, *The Wiley static SIMS library*, John Wiley and Sons, Manchester, **1999**.

[35] A. G. Shard, R. Havelund, M. P. Seah, S. J. Spencer, I. S. Gilmore, N. Winograd, D. Mayo, T. Miyayama, E. Niehuis, D. Rading, R. Moellers. Argon cluster ion beams for organic depth profiling: results from a VAMAS interlaboratory study. *Analytical Chemistry* **2012**, *84*, 7865.

[36] J. C. Vickerman, D. Briggs, *ToF-SIMS: materials analysis by mass spectrometry* Second Edition, IM Publications LLP and SurfaceSpectra Limited, Chichester, UK **2013**, 656.

[37] J. G. Newman, B. A. Carlson, R. S. Michael, J. F. Moulder, T. A. Hohlt, *Static SIMS handbook of polymer analysis,* Perkin-Elmer Corporation, Eden Prairie (MN), **1991**, 26.

[38] J. G. Newman, B. A. Carlson, R. S. Michael, J. F. Moulder, T. A. Hohlt, *Static SIMS handbook of polymer analysis,* Perkin-Elmer Corporation, Eden Prairie (MN), **1991**, VI.

[39] D. Kuck. Mass spectrometry of alkylbenzenes and related compounds. Part I. Gas-phase ion chemistry of alkylbenzene radical cations. *Mass Spectrometry Reviews* **1990**, *9*, 187.

[40] A. Delcorte, V. Cristaudo, M. Zarshenas, D. Merche, F. Reniers, P. Bertrand. Chemical analysis of plasma-treated organic surfaces and plasma polymers by secondary ion mass spectrometry. *Plasma Processes and Polymers* **2015**, *12*, 905.

[41] Y. De Puydt, D. Léonard, P. Bertrand, *Metallized Plastics 3: Fundamental and Applied Aspects*, A static SIMS study of the chemical modifications induced by plasma and flame treatments at the surface of polyolefins. K. L. Mittal, Plenum Press, New York, **1992**, 225.

[42] F. M. Petrat, D. Wolany, B. C. Schwede, L. Wiedmann, A. Benninghoven. Comparative in situ ToF-SIMS/XPS study of polystyrene modified by argon, oxygen and nitrogen plasmas. *Surface and Interface Analysis* **1994**, *21*, 402.

[43] U. Oran. Surface chemical characterization of plasma-chemically deposited polymer films by time of flight static secondary ion mass spectrometry. Ph.D. Thesis, Free University, Berlin, **2005**.

[44] U. Oran. Surface chemical characterization of plasma-chemically deposited polymer films by time of flight static secondary ion mass spectrometry. Ph.D. Thesis, Free University, Berlin, **2005**, 40 and 53.

[45] B. C. Schwede, T. Heller, D. Rading, E. Niehuis, L. Wiedmann, A. Benninghoven. *The Münster High Mass Resolution Static SIMS Library.* ION-TOF: Münster, **1999**, Print edition VI.3, Volume II: Polymers.

[46] D. Kuck. Mass spectrometry of alkylbenzenes and related compounds. Part I. Gas-phase ion chemistry of alkylbenzene radical cations. *Mass Spectrometry Reviews* **1990**, *9*, 209.

[47] C. H. Huck, G. K. Bonn. Poly (styrene-divinylbenzene) based media for liquid chromatography. *Chemical Engineering & Technology* **2005**, *28*, 1457.

[48] https://en.m.wikipedia.org/wiki/Peptide_synthesis#Solid-phase_synthesis

[49] A. Delcorte, B. G. Segda, P. Bertrand. ToF-SIMS analyses of polystyrene and dibenzanthracene: evidence for fragmentation and metastable decay processes in molecular secondary ion emission. *Surface Science*, **1997**, *381*, 18.

[50] A. G. Shard, I. S. Gilmore. Analysis of metastable ions in the ToF-SIMS spectra of polymers. *International Journal of Mass Spectrometry*, **2008**, *269*, 85.

[51] https://en.wikipedia.org/wiki/Photo-oxidation_of_polymers

[52] J. F. Rabek, *Photostabilization of Polymers: Principles and Application*, Elsevier Science Publisher LTD, London & New York, **1990**, Chapter 1.

[53] C. M. Mahoney. Cluster secondary ion mass spectrometry of polymers and related materials. *Mass Spectrometry Reviews* **2010**, *29*, 247.

[54] H. Yasuda. *Plasma polymerization.* Academic Press, London, **1985**.

[55] D. Merche, Synthèse et caractérisation de couches de polystyrène et de polystyrène sulfoné obtenues par polymérisation-plasma à pression (sub)-atmosphérique, Université libre de Bruxelles, **2011**, Chapter 5, 133.

[56] M. Chen, T.-C. Yang. Diagnostic analysis of styrene plasma polymerization. *Journal of Polymer Science Part A: Polymer Chemistry* **1999**, *37*, 325.

[57] I. Retzko. Pulsplasmapolymerisation von Acetylen, Ethylen, 1,3-Butadien und Styrol. Ph.D. Thesis, Free University, Berlin, **2001**.

[58] R. M. Silverstein, F. X. Webster, *Spectrometric identification of organic compounds*, John Wiley & Sons, New York, **1996**, 136.

CHAPTER 7
Conclusions and perspectives

I. Main results

In this thesis, ToF-SIMS was successfully applied to investigate the chemical and structural characteristics of plasma-treated and plasma-synthesized polymers under (sub-)atmospheric pressure. It constitutes a suitable tool to obtain information about properties such as unsaturation, branching and/or cross-linking, functionalization, and aromatic and/or aliphatic content, from the outermost layers of the polymer down to the bulk or the interface with the substrate. Part of this valuable information is out of reach of XPS, which is the most commonly used technique for surface chemical characterization of polymeric materials in plasma treatment and/or plasma polymerization. Furthermore, any detailed variation of the chemical structure along depths of tens of nm cannot be revealed by XPS, unless it is coupled with a sputtering source conceived for sensitive organic materials as the polymers.

Preliminary fundamental studies on polymer SIMS depth-profiling by massive Ar clusters were conducted on model systems constituted by well characterized monodisperse (conventionally-polymerized) polymers (i.e. PS and PMMA), in order to exploit this knowledge, at a later stage, for experimental planning and quantification of depth-profiles of plasma-treated and plasma-synthesized polymeric films. Firstly, the effects of the polymer molecular weight M_w (10^3 – 1,5 x 10^5 amu) and the Ar cluster size (1500, 3000, 5000 atoms/cluster) on the efficiency of the sputtering process were investigated.

- The experiments showed that the sputtering yield volume Y (nm^3/primary ion) decreases with the increase of the molecular weight M_w for a selected cluster size and, at constant molecular weight, Y decreases with increasing cluster size. The variation as a function of M_w levels off for M_w > 5 x 10^4 amu.
- The trend of Y versus M_w seems to be related to the variation of the glass transition temperature (T_g) as a function of the polymerization degree of the investigated polymers. This would suggest that the mobility of the

oligomer chains is a determining parameter in the dependence of Y on M_w.

The dependence of Y on the M_w of polystyrene will find later an application in the corroboration of the strong presence of oligomers in the polymer matrix of plasma-deposited coatings from the styrene monomer. Generally, an accurate knowledge of the sputtering rates and their variation along the depth of polymeric films are important for the conversion of the sputter time scale in depth. Thus, the second contribution on polymer depth-profiling focused on the investigation of the effects of the thickness of thin films of PS and PMMA with low M_w, and the substrate nature (hard vs soft) on the sputtering efficiency.

- For the first time on polymer systems, a remarkable thickness dependence of Y was experimentally demonstrated in the nanoscale (~15-230 nm) with low M_w PS and PMMA on silicon supports. Y shows a steep decay in the region below 90 nm for both PS 4k and PMMA 4k, then it levels off (ΔY is estimated to ~20%).
- The absence of the $\Delta Y(d)$ for ultrathin polymer layers of PS 4k on a soft substrate leads to hypothesize a mechanistic nature of the observed phenomenon involving the reflection of the Ar cluster energy at the interface with the hard silicon substrate and its confinement in the polymer layer. A physical "2-layer" model was developed to describe the thickness dependence of Y, which is based on the energized volume of the target material by the primary ion impact. In the current form, the proposed model already describes satisfactorily the Y-nanoconfinement. Nevertheless, it could be refined by considering a larger number of intermediate layers between interface and bulk of the polymer film.
- The influence of the M_w on the thickness dependence of Y was highlighted as well. An increase of M_w leads to a decrease of $\Delta Y(d)$, due presumably to the larger extent of entanglements and lower end-chain density.

The modifications induced by an atmospheric Ar-D_2O post-discharge in LDPE films were successfully evidenced by using ToF-SIMS, both at the sample surface and along the depth. The methodological developments established for the SIMS analyses, and the main results are reported here:

- D_2O vapor was employed in this experiment to discriminate the influence of the water deliberately injected into the post-discharge from the environmental humidity, owing to the isotopic resolution of SIMS. Then, tracing the D_2O reactivity with the polyolefin substrate was made possible by the appearance of new secondary ions $C_xH_yD_z^+$ and $C_xH_yD_zO_m^+$ in the positive ion mass spectra of the modified polyethylene, derived from H-D exchange reactions and O-uptake during the plasma treatment.

- Depth-profiling experiments were conducted in dual beam mode, by using alternately a 10 keV Ar_{5000}^+ cluster beam (2 eV/atom) for the sputtering and a 30 keV Bi_5^+ ion beam for the analysis. In these SIMS conditions, minimal damage of the sample was ensured and an extremely mild erosion was achieved, which permitted to probe extreme surface modifications of the treated polyethylene involving solely the top ten nm. The erosion depth was confirmed by the implantation profile of the Bi_5^+ ions used for the analysis in the polymeric material.
- The H-D exchange was investigated by the elaboration of a mathematical parameter, the deuteration ratio (R_D), defined by the sum of the deuterated PE monomer ions $C_2H_xD_y^+$ divided by the sum of all the monomer ions (including $C_2H_5^+$). This indicator permitted to perform an internal normalization, that could circumvent matrix effects related to the surface oxidation. Thanks to this parameter, the quantification of the deuteration was conducted as a function of the plasma treatment parameters, such as the duration and the sample-torch distance. It was found that the most important deuteration occurs at 5 mm of distance, with 25% of deuterated monomer units at the surface. Ultra-shallow molecular depth-profiling pointed out that the fraction of deuterated monomer units is reduced by a factor >2 over a depth of ~3 nm.
- The oxidative functionalization of LDPE surfaces as a function of the parameters “sample-torch distance” (3, 5, 7 and 10 mm) and “treatment time” (30, 60 and 300 s) was studied by the combined approach SSIMS/PCA. Two different oxidation trends for the treated LDPEs were found out as a function of time depending on the distance from the torch: type I for 3-7 mm, where the functionalization decreases with increasing time, and type II for 10 mm, where the oxidation behaves inversely. By tracing the reactivity of the water vapor, ToF-SIMS could follow the gradual decrease of the oxidation efficiency related to D_2O with increasing the distance from the torch and to evidence the prevalent reactivity of the atmospheric O_2 and H_2O at distances >7 mm. The observed effect of time on the LDPE modifications for both oxidation trends as a function of

distance was explained by the competition between plasma-induced ablation and functionalization.

- The in-depth modifications of the LDPE as a function of the parameters "sample-torch distance" (3, 5, 7 and 10 mm) and "treatment time" (30, 60 and 300 s) were investigated by combining dynamic-SIMS and the recently introduced Wavelet-PCA approach. The data processing by Wavelet-PCA was made possible thanks to the collaboration with Professors N. Tuccitto and A. Licciardello from University of Catania, who developed this particular procedure. 10 keV Ar_{3000}^+ ions (3 eV/atom) were selected for the sputtering of the sample surface, while 30 keV Bi_5^+ ions were used for collecting the mass spectra. The selected analytical protocol permitted to probe the gradual transition of a functionalized and damaged polymer at the surface to a native material along the first ten of nm.

The new SIMS methodology proposed in this thesis for the chemical and structural characterization of plasma-treated polyethylene films under atmospheric conditions demonstrates the feasibility to accurately probe the nature and degree of functionalization, simultaneously at the surface and in the inner layers (few tens of nm), and to control it for the desired applications.

ToF-SIMS depth-profiling with large Ar clusters was also employed to elucidate the actual chemical structure of plasma-deposited films from the styrene monomer in a reactor of dielectric barrier discharge (DBD) type, under sub-atmospheric pressure. The power applied to the plasma was varied in the range 10 W - 80 W, in order to establish its influence on the chemistry of the synthesized polymer. The methodological improvements of the traditional SIMS characterization of plasma-deposited styrene coatings, and the main results obtained from this study can be summarized as follows:

- Molecular depth-profiling of the plasma films, after exposure to air, was performed with 10 keV Ar_{3000}^+ projectiles. Then, positive ion mass spectra were reconstructed by computer processing from the relative profiles in the inner region of the aromatic coatings, where they appear to be homogenous and free of adventitious contamination and post-polymerization oxygen incorporation in air. The resulting mass spectra were considered to be more representative of the actual chemical structure of the films under growth in the plasma chamber. Finally, PCA was applied to the whole set of mass spectra for the extrapolation of the chemical and structural character of the investigated polymer, as a reliable method of data treatment compared to the “blind” utilization of the traditional SIMS structural indicators (also attempted in this work).

- Plasma coatings were comparatively studied with the conventionally polymerized counterparts, i.e. linear and cross-linked PS. Additional reference polymers (PAMS, P4MS, PVP) were included to elucidate some peculiar chemical and structural features evidenced from the comparison with the conventional PS. Most of the SIMS experimental evidences were corroborated by IR and XPS analyses of the same specimens.
- The SIMS results evidenced a higher conservation of the aromaticity and a lesser branched and/or cross-linked content for the polymer coatings deposited at lower powers, suggesting a milder fragmentation of the precursor at low power regime. These two main features were confirmed by IR bulk characterization of the films. In addition, SIMS demonstrated that O-uptake occurs during the plasma polymerization under sub-atmospheric pressure, and that it gradually increases at the expense of the aromaticity with increasing power. This is in rather good agreement with the XPS surface analyses and IR bulk characterizations.
- A significant methyl-substitution was found in plasma-polymerized films from the styrene monomer by SIMS analysis, and confirmed by IR. The SIMS characterization ascribed this feature to branching or grafting of $CH_3^\bullet$ radicals to active sites, mostly in position α, β, γ along the aliphatic backbone, in addition to a relatively high fraction of trapped oligomers. The oligomer contribution, pointed out by gel permeation chromatography, was corroborated by a more original SIMS depth-profiling study based on the M_w dependence of the sputter yield volume (Y) of PS standards for GPC.

II. Perspectives

The methodologies applied in this thesis for the surface and in-depth molecular characterization of plasma-treated and plasma-synthesized polymers led to interesting results. Nevertheless, additional analyses and experiments could be planned/defined to improve the understanding of the two investigated systems. Moreover, further research could be undertaken in both case studies in order to contribute to the elucidation of the mechanisms underlying the plasma-induced modification of polymers and the plasma polymerization under (near) atmospheric pressure.

- Concerning the fundamental studies on polymer depth-profiling with large Ar clusters, further investigations could be devoted to elucidating the effect of the substrate nature (hard vs soft, different hydrophilicity, etc.) on the thickness dependence of Y with model polymers, such as PS and PMMA standards. This study could be extended to plasma-polymers, where the thickness of the films is, for instance, a function of the deposition time. In the latter case, interesting features could be highlighted because of the covalent grafting of the plasma films to their supports (determining their well-known adhesion strength).
- In the context of the study of the plasma-induced modifications in LDPE films exposed to an atmospheric Ar-D_2O post-discharge, the monitoring of the H-D exchange could be attempted in FT-IR as well (although the concentration of deuterated CH_2-groups within the sampling depth is low). Indeed, the H-D substitution of the CH_2-groups in the polymer produces well detectable shifts of the characteristic IR signals of polyethylene, such as ν_{as} ($CH_2 \rightarrow CD_2$) = 727 cm^{-1} and ν_s ($CH_2 \rightarrow CD_2$) = 765 cm^{-1}, and δ ($CH_2 \rightarrow CD_2$) = 383 cm^{-1}.[1] IR can determine the global amount of H-D substitution in contrast to SIMS, which gives a more detailed information about the process. Therefore, it should be interesting to compare the complementary results of these two techniques.
- In light of the results of the study on the LDPE films modified by an atmospheric Ar-D_2O post-discharge, showing the presence of type I and II samples (see the previous section "Main results"), it would be worthy a further investigation of the transition from one to the other typology of functionalization in order to better understand the chemistry underlying this process. The control of the environmental humidity could be performed to determine the impact of this parameter on the resulting plasma-induced functionalization of the polymer films.
- A more detailed investigation of the oxidation induced in polyethylene films by the water vapor injected into the post-discharge of an atmospheric Ar plasma torch could be performed by ^{18}O-isotopic labelling (i.e. the use of $H_2(18\text{-}O)$). This expedient could enable the discrimination of the contributions to the polymer functionalization, even at very small sample-torch distances, from the water vapor injected in the post-discharge, and from the atmospheric O_2 and H_2O. However, the prices of heavy-oxygen labeled water were prohibitive in the framework of this thesis.

- Based on the established protocol for the characterization of plasma-treated polyethylene, future work could address other kinds of plasma treatments of polymers under atmospheric conditions.

- A study of the post-treatment ageing behavior of the (sub-)surface region of LDPE films functionalized by an atmospheric Ar-D_2O post-discharge could be undertaken, in order to better understand the chemical/physical interactions of the active species of the post-discharge at the interface with the polymer substrate.

- In the chemical characterization of plasma-polymerized styrene films, the complementarity between SIMS and XPS should be strengthened. Because the SIMS analyses were conducted in the inner layers of the plasma-deposited coatings to prevent any spectral interference coming from air post-oxidation and/or surface organic contamination, it would be useful to perform in-depth characterization by XPS as well. Then, reliable relations between SIMS and XPS results could be directly established. However, this would imply the implementation in the XPS instrumentation of a "damageless" sputter source for sensitive polymer samples as the gas cluster ion beams (GCIB), which unfortunately are not widespread in the analytical laboratories of surface characterization. Additionally, gel permeation chromatography could potentially provide valuable information about the role played by the significant fraction of oligomers trapped in the polymer matrix. In this respect, the analysis of the whole set of plasma films deposited at different powers, previously used in the SIMS investigation, should be beneficial. In order to favor the (complete) dissolution of the polymer layer on the Si support by applying more adequate conditions, the wet chemical etching in HF solution of films deposited on substrates covered by thermal silicon oxide could be first attempted. This expedient is reported in the literature to detach (ultra)thin films from silicon supports, and it should permit to compare more reliably the GPC results from different specimens.[2] The accurate determination of the molecular weight distributions of the plasma films as a function of the power could be used to elucidate their influence on the observed variations in the relative SIMS intensities, which cannot be done with conventionally polymerized PS standards. Moreover, SSIMS analysis of the oligomers desorbed from the plasma film could be performed after their deposition on very clean substrates, since a slight surface contamination definitely compromises the analytical results as already mentioned in this work. This could permit to get the SIMS signature of the low M_w species.

- The plasma-polymerized styrene coatings studied in this thesis were characterized by oxidation, that very likely took place during the film growth as suggested by SIMS and IR bulk characterization. The oxygen incorporation alters the polymer structure in many ways, like for instance destroying the aromaticity when the oxygen binds to the phenyl group. The O-uptake also influences the probabilities of secondary ion formation in SIMS, so that matrix effects need to be taken into account. Both of these factors made the SIMS characterization presented in this thesis more challenging. A more detailed investigation of the observed oxidation could be attempted by SIMS molecular depth-profiling in negative ion polarity. On the contrary, the reduction of the oxygen partial pressure in the plasma chamber is desired to gain a better understanding of the influence of the oxidation on the chemical structure of the aromatic deposits (in terms of aromatic and aliphatic contents, branching and/or cross-linking, …).

- Because of the presence of aromatic rings in the plasma coatings obtained from the styrene monomer, the investigation of the unsaturation of the polymer backbone by SIMS was impossible. The synthesis of coatings from aliphatic monomers, such as e.g. ethylene, could alleviate this issue and help to determine the influence of the aromaticity on the estimation of the unsaturated content.

- The plasma polymerization of the styrene monomer could be conducted by using a different noble carrier gas, like for instance helium, to investigate its impact on the polymer chemistry. According to the literature, He carrier gas leads to plasma-deposited styrene films which are less unsaturated, cross-linked and/or branched, and with a higher degree of aromaticity.[3,4]

- The influence of other external plasma parameters could be investigated by the methodology described in this thesis, like for example the monomer flux. Eventually, plasma-polymerized styrene could be deposited on different kinds of substrates, insulating and metallic, to influence the nature of the discharge, and consequently the chemical character of the deposits to be probed by SIMS.

- It is worth noticing that the ToF-SIMS characterization could further help to elucidate the polymerization mechanism under (sub-)atmospheric pressure if the investigated chemistry of the films, as a function of the external plasma parameters, is correlated to a systematic study of the plasma phase. To this purpose, atmospheric mass spectrometry, gas chromatography and optical emission spectroscopy measurements of the plasma medium are necessary.

- The thermal stability and the photo-sensibility of the plasma-deposited styrene films as a function of the power (or any other parameter) could be monitored by the combined (dynamic-)SIMS/PCA approach.
- A systematic study of the ageing of pp-PS films obtained under different plasma conditions could be undertaken, as shown by the promising preliminary results of section 6.6.3.3.
- The study of the cross-linking process of plasma-deposited styrene films near atmospheric pressure could be carried out by introduction of cross-linking agents like DVB. A well-defined cross-linked conventional polystyrene would be required for this investigation. The discrimination of the cross-linking induced by the addition of DVB and the one intrinsically linked to the plasma polymerization process could be attempted in the low power regime, where the retention of the chemical structure of the monomer is higher.
- Surface and in-depth molecular characterization of plasma copolymers under (near) atmospheric pressure by using SIMS coupled to PCA could be very challenging. An example could be given by the use of styrene as chain-extending monomer and a functional group bearing monomer. The retention of the chemical functionalities of the monomer and other specific chemical features of the deposited coatings could be searched by SIMS.

---

[1] S. Wettmarshausen, H. Min, W. Unger, C. Jäger, G. Hidde, J. Friedrich. Significance of hydrogen - deuterium exchange at polyolefin surfaces on exposure to ammonia low-pressure plasma. *Plasma Chemistry and Plasma Processing* **2011**, *31*, 551, and references herein.

[2] I. Amin, M. Steenackers, N. Zhang, A. Beyer, X. Zhang, T. Pirzer, T. Hugel, R. Jordan, A. Gölzhäuser. Polymer carpets. *Small* **2010**, *6*, 1623.

[3] D. Merche. Synthèse et caractérisation de couches de polystyrène et de polystyrène sulfoné obtenues par polymérisation-plasma à pression (sub)-atmosphérique. Ph. D. Thesis, Université libre de Bruxelles, **2011**.

[4] D. Merche, C. Poleunis, P. Bertrand, M. Sferrazza, F. Reniers. Synthesis of polystyrene thin films by means of an atmospheric-pressure plasma torch and a dielectric barrier discharge. *IEEE Transactions on Plasma Science* **2009**, *37*, 951.

Publications and scientific communications derived from this thesis

Journals

- Cristaudo V., Poleunis C., Czerwinski, B. & Delcorte A. (**2014**). Ar Cluster Sputtering of Polymers: Effects of Cluster Size and Molecular Weights. *Surface and Interface Analysis*, 46(S1), 79-82.
- Delcorte A., Cristaudo V., Lebec V., & Czerwinski B. (**2014**). Sputtering of polymers by keV clusters: Microscopic views of the molecular dynamics. *International Journal of Mass Spectrometry*, 370, 29-38.
- Cristaudo V., Collette S., Poleunis, C., Reniers F., & Delcorte A. (**2015**). Surface Analysis and Ultra-Shallow Molecular Depth-Profiling of Polyethylene Treated by an Atmospheric Ar-D_2O Post-Discharge. *Plasma Processes and Polymers*, 12(9), 919-925.
- Delcorte A., Cristaudo V., Zarshenas M., Merche D., Reniers F., & Bertrand P. (**2015**). Chemical Analysis of Plasma-Treated Organic Surfaces and Plasma Polymers by Secondary Ion Mass Spectrometry. *Plasma Processes and Polymers*, 12(9), 905-918.
- Cristaudo V., Collette S., Tuccitto N., Poleunis C., Melchiorre L. C., Licciardello A., Reniers F., & Delcorte A. (**2016**), Molecular Surface Analysis and Depth-Profiling of Polyethylene Modified by an Atmospheric Ar-D_2O Post-Discharge, *Plasma Processes and Polymers*, 13(11), 1106-1119.

Oral presentations

- Cristaudo V., Poleunis C., Czerwinski B., & Delcorte A., Ar Cluster Sputtering of Polymers: Effects of Cluster Size and Molecular Weights, *SIMS XIX: 19th International Conference on Secondary Ion Mass Spectrometry*, Jeju (Korea), 29 Sept. – 4 Oct. 2013.

- Cristaudo V., Collette S., Merche D., Poleunis C., Reniers F., & Delcorte A., Chemical Surface and 3D Characterization of Plasma-Treated and Plasma-Polymer Films, *IAP Symposium: Fundamentals of Plasma – Surface Interactions*, Antwerp (Belgium), 8 Nov. 2013.

- Cristaudo V., Poleunis C., & Delcorte A., Large Argon Cluster Sputter Yields: Effect of the Thickness of Polymer Thin Layers, *SIMS Europe 2014 Workshop*, Muenster (Germany), 8-9 Sept. 2014.

- Cristaudo V., Melchiorre L. C., Collette S., Poleunis C., Reniers F., & Delcorte A., ToF-SIMS Investigation of Polyethylene Modified by an Atmospheric Ar-D_2O Post-Discharge, *SIMS XX: 20th International Conference on Secondary Ion Mass Spectrometry*, Seattle (USA), 13-18 September 2015.

- Cristaudo V., Melchiorre L. C., Collette S., Poleunis C., Reniers F., & Delcorte A., Etude par ToF-SIMS de la modification du polyéthylène dans la post-décharge d'un plasma atmosphérique Ar-D_2O, *Workshop & Réunion des utilisateurs francophones TOF-SIMS (ION-TOF)*, Mons (Belgique), 9-10 March 2016.

- Cristaudo V., Collette S., Poleunis C., Tuccitto N., Licciardello A., Reniers R., & Delcorte A., SIMS/PCA Approach for The Investigation of the Oxidation of LDPE Films Exposed to an Atmospheric Ar/D_2O Post-Discharge, *IMCN Ph.D. Students' Day*, LLN, 20 May 2016.

- Cristaudo V., Collette S., Poleunis C., Tuccitto N., Licciardello A., Reniers R., & Delcorte A., SIMS/PCA Approach for The Investigation of the Oxidation of LDPE Films Exposed to an Atmospheric Ar/D_2O Post-Discharge, *IAP Workshop: Organic surface modifications by plasmas and plasma-polymers*, Nancy (France), 9 June 2016.

Poster presentations

- Cristaudo V., Poleunis C., Czerwinski B., Lebec V., Yunus S., Collette S., Merche S., Reniers F., Kalaskar D., Demoustier S., Dupont C., & Delcorte A., Development of 3D Molecular Characterization of Organic Surfaces Using Cluster SIMS, *Visit of the IMCN Scientific Advisory Committee*, LLN, 13 March 2014.
- Cristaudo V., Poleunis C., Czerwinski B., & Delcorte A., SIMS Molecular Depth-Profiling of Polymers: Effects of Ar Cluster Size and Polymer Molecular Weight, *IMCN Ph.D. Students' Day*, LLN, 23 May 2014.
- Cristaudo V., Collette S., Poleunis C., Reniers F., & Delcorte A., ToF-SIMS Study of the Reactivity of Water and Deuterated Water with LDPE Films in an Atmospheric Argon Plasma Torch, *IAP Workshop: Plasma Diagnostics*, Reims (France), 10-12 June 2014.
- Cristaudo V., Collette S., Poleunis C., Reniers F., & Delcorte A., ToF-SIMS Study of the Reactivity of Deuterated Water with LDPE Films in an Atmospheric Argon Plasma Torch, *SIMS Europe 2014 Workshop*, Muenster (Germany), 8-9 Sept. 2014.
- Cristaudo V., Melchiorre L. C., Collette S., Reniers F., & Delcorte A., ToF-SIMS Investigation of Polyethylene Modified by an Atmospheric Ar-D_2O Post-Discharge, *IMCN Ph.D. Students' Day*, LLN, 22 May 2015.
- Cristaudo V., Collette S., Poleunis C., Reniers F., & Delcorte A., A ToF-SIMS Study of the Polyethylene Chemical Modification Induced by an Atmospheric Ar-D_2O Post-Discharge, *IAP Workshop – 22nd International Symposium on Plasma Chemistry (ISPC 22)*, Antwerp (Belgium), 5-10 July 2015.
- Cristaudo V., Merche D., Reniers F., & Delcorte A., A New ToF-SIMS Approach for Characterization of Plasma-Deposited Polystyrene under Sub-Atmospheric Pressure, *SIMS XX: 20th International Conference on Secondary Ion Mass Spectrometry*, Seattle (USA), 13-18 September 2015.